ESTE EXEMPLAR CORRESPONDE A REDAÇÃO FINAL DA TESE DEFENDIDA POR DANIEL GRANDO STROPPA E APROVADA PELA COMISSÃO JULGADORA EM 07 / 11 / 11

Antonio José Ramirez
ORIENTADOR

UNIVERSIDADE ESTADUAL DE CAMPINAS
FACULDADE DE ENGENHARIA MECÂNICA
COMISSÃO DE PÓS-GRADUAÇÃO EM ENGENHARIA MECÂNICA

Daniel Grando Stroppa

Modelamento de Nanocristais pelo Uso de Técnicas Avançadas de QHRTEM

Campinas, 2011

158/2011

Daniel Grando Stroppa

Modelamento de Nanocristais pelo Uso de Técnicas Avançadas de QHRTEM

Tese apresentada ao Curso de Doutorado da Faculdade de Engenharia Mecânica da Universidade Estadual de Campinas, como requisito para a obtenção do título de Doutor em Engenharia Mecânica.

Área de concentração: Materiais e Processos de Fabricação

Orientador: Prof. Dr. Antonio José Ramirez Londono

Campinas

2011

FICHA CATALOGRÁFICA ELABORADA PELA
BIBLIOTECA DA ÁREA DE ENGENHARIA E ARQUITETURA - BAE - UNICAMP

Grando Stroppa, Daniel
G764m Modelamento de nanocristais pelo uso de técnicas avançadas de QHRTEM / Daniel Grando Stroppa. -- Campinas, SP: [s.n.], 2011.

Orientador: Antonio Jose Ramirez Londono.
Tese de Doutorado - Universidade Estadual de Campinas, Faculdade de Engenharia Mecânica.

1. Microscopia eletrônica de transmissão de alta resolução. 2. Caracterização de materiais. 3. Cristais - Crescimento. I. Ramirez Londono, Antonio Jose. II. Universidade Estadual de Campinas. Faculdade de Engenharia Mecânica. III. Título.

Título em Inglês: Nanocrystals modeling by advanced QHRTEM techniques
Palavras-chave em Inglês: Transmission electron microscopy of high resolution, Materials characterization, Crystals - Growth
Área de concentração: Materiais e Processos de Fabricação
Titulação: Doutor em Engenharia Mecânica
Banca examinadora: Carlos Kenichi Suzuki, Daniela Zanchet, Caue Ribeiro de Oliveira, Paulo Fernando Papaleo Fichtner
Data da defesa: 07-11-2011
Programa de Pós Graduação: Engenharia Mecânica

UNIVERSIDADE ESTADUAL DE CAMPINAS
FACULDADE DE ENGENHARIA MECÂNICA
COMISSÃO DE PÓS-GRADUAÇÃO EM ENGENHARIA MECÂNICA
DEPARTAMENTO DE ENGENHARIA DE MATERIAIS

TESE DE DOUTORADO

Modelamento de Nanocristais pelo Uso de Técnicas Avançadas de QHRTEM

Autor: Daniel Grando Stroppa
Orientador: Prof. Dr. Antonio José Ramirez Londono

A banca Examinadora composta pelos membros abaixo aprovou esta tese:

Prof. Dr. Antonio José Ramírez Londono (Presidente)
FEM/UNICAMP

Prof. Dr. Carlos Kenichi Suzuki
FEM/UNICAMP

Profa. Dra. Daniela Zanchet
IQ/UNICAMP

Prof. Dr. Caue Ribeiro de Oliveira
EMBRAPA/São Carlos

Prof. Dr. Paulo Fernando Papaleo Fichtner
UFRGS/Porto Alegre

Campinas, 07 de novembro de 2011

Este projeto contou com o apoio financeiro das seguintes agências:

Conselho Nacional de Desenvolvimento Científico e Tecnológico - CNPq
Bolsa de Mestrado
Processo: 130418/2008-0

Fundação de Amparo à Pesquisa do Estado de São Paulo – FAPESP
Bolsa de Doutorado Direto no País
Processo: 2007/07837-2

Deutscher Akademischer Austausch Dienst – DAAD
Estadias de Pesquisa na Alemanha para doutorandos
Processo: A/09/76658

"As respostas não podem ser encontradas
em escritos alheios
ou em palavras vindas de mentes enviesadas."
Charles "Chuck" Schuldiner

Agradecimentos

Ao orientador e amigo *Antonio Ramirez*, por todo o suporte nos projetos realizados, pela motivação, pela liberdade em criar e pelo aprendizado, acadêmico ou não, ao longo destes anos. Mais importante que os frutos científicos conseguidos, ficará a sua influência na minha formação como pesquisador, profissional e pessoa.

Ao co-orientador *Edson Leite*, pelos ensinamentos fundamentais e pelo suporte desde a iniciação científica. Se hoje tenho prazer em pesquisar, devo isto aos desafios e às possibilidades que tive trabalhando contigo.

Ao *Luciano Montoro*, por todo o suporte prestado, pelo aprendizado proporcionado e especialmente pela paciência dispendida nos projetos nos quais trabalhamos juntos.

Aos inúmeros colaboradores que suportaram este projeto, especialmente as equipes *LNNano-CNPEM*, *LIEC-UFSCar*, *Ernst Ruska Centre*, *Universitat Jaume I* e *Paris Sud Université*. Se existe mérito neste trabalho, este deve ser dividido entre as diversas cabeças que pensaram e trabalharam ao meu lado para obtê-lo.

A equipe CPG-Unicamp, pela presteza e cordialidade no suporte necessário durante o curso de doutorado.

A todos os amigos e aos colegas de trabalho no *LNNano* e *LNLS*, pelas dicussões científicas e não-científicas que tornaram excelentes o ambiente de trabalho e a vida em Campinas. Espero que vocês não percam o horário do almoço daqui em diante!

Aos amigos da *UFSCar*, que desde a graduação tem me propiciado momentos fantááárdigos.

Aos amigos de *Campinas*, pela companhia, pelo suporte nesta caminhada e pela música nossa de todos os dias.

Aos amigos ao redor do globo, pelo aprendizado cultural e pelos bons momentos que tivemos: *Saeedeh*, *Laura*, *Miana*, *Bergoi*, *Marialilia*, *Mirko*, *Ester*, *Yuji*, *Raffa*, *Roberto*, *Leo*, *Milan*.

Aos mestres que motivaram meu fascínio pela ciência desde a infância: *Fernando*, *Eiko*, *Ricardo*, *João*, *Adenilson.*

A minha *família*, pelo suporte incondicional, pelos valores e exemplos, e por representar sempre um porto seguro. Dedico-lhes este trabalho, pois o valorizam mesmo sem entendê-lo, apenas pelo apreço que deposito nele. Em especial, dedico esta tese à memória de meu avô *Arcidio Stroppa*, que teria se orgulhado muito por esta conquista.

Resumo

O desenvolvimento de tecnologias baseadas em nanoestruturas é dependente da criação de modelos confiáveis que possam suportar a obtenção de materiais com características controladas. Neste contexto, o aprimoramento de técnicas de caracterização quantitativa e com alta resolução espacial é fundamental para o melhor entendimento das correlações entre a configuração de síntese, a morfologia e as propriedades resultantes de materiais nanoestruturados.

Esta tese apresenta a avaliação e a aplicação de diferentes técnicas de Microscopia Eletrônica de Transmissão de Alta Resolução Quantitativa (QHRTEM) visando a extração de informações relacionadas à estrutura tridimensional e à segregação de espécies dopantes em nanocristais individuais de óxidos semicondutores dopados (Sb:SnO_2 e Gd:CeO_2). Os resultados experimentais combinados a cálculos teóricos proporcionaram a obtenção de informações referentes à distribuição de energia superficial e aos mecanismos de crescimento de cristais envolvidos na evolução temporal dos sistemas estudados.

A descrição de tais aspectos de sistemas nanocristalinos explicita a importância das técnicas QHRTEM, tanto no contexto do desenvolvimento e aplicação do modelamento de nanocristais, quanto para o avanço das teorias fundamentais que descrevem o comportamento dos materiais em escala nanométrica. Neste sentido, os resultados presentes nesta tese constituem significativos avanços para o entendimento das características dos materiais em escala atômica e para a posterior manipulação destas segundo o preceito da engenharia de materiais no desenvolvimento de novas tecnologias.

Palavras chave: Caracterização Quantitativa de Nanocristais, Mecanismo de Crescimento, Segregação de Dopantes, Técnicas HRTEM.

Abstract

Technologies based on nanostructured materials depend on the development of reliable models which can support the fabrication of nanocrystals with highly controlled features. In this scenario, advances on high resolution quantitative techniques are required in order to improve the description of the nanostructured systems, especially the correlations among the nanocrystals synthesis parameters, the resultant morphology and the system properties.

This PhD thesis presents the evaluation and use of different Quantitative High Resolution Transmission Electron Microscopy (QHRTEM) techniques aiming the three-dimensional morphology and the dopant species segregation characterization of individual oxide nanocristals ($Sb:SnO_2$ e $Gd:CeO_2$). In addition, the combined use of such techniques and theoretical calculations provided valuable insights on the surface energy distribution and growth mechanisms present on the analyzed nanocrystalline systems.

The obtained high resolution quantitative characterization results indicate that QHRTEM techniques are priceless tools for both the nanocrystal modeling procedures development and application, and for the improvement of fundamental theories that describe the materials features at nanoscale. In this scenario, this thesis presents significant advances on the nanomaterials characteristics description and, consequently, on their further manipulation aiming novel technologies development according to the materials engineering approach.

Keywords: Nanocrystals Characterization, Dopant Segregation, Growth Mechanism, HRTEM techniques

Lista de Figuras

Lista de Tabelas

Lista de Abreviaturas e Siglas

Letras Latinas

(h,k,h) – Índices De Miller

[X] – Concentração

A(u) – Função de Aberturas

$\mathbf{A_i}$ – Dimensão 2D

B(u) – Função de Aberração

$\mathbf{C_{10}}$ – Defocus

$\mathbf{C_{30}}$ – Aberração Esférica

$\mathbf{C_c}$ – Aberração Cromática

$\mathbf{C_s}$ – Aberração Esférica

D – Densidade de Energia Superficial

$\mathbf{d_i}$ – Distância Em Relação Ao Centro

e – Carga Elementar

$\mathbf{E_a}$ – Energia de Ativação

$\mathbf{E_s}$ – Energia Superficial Associada a Áreas

$\mathbf{E_i}$ – Energia Superficial

$\mathbf{E_l}$ – Energia Superficial Associada a Arestas

$\mathbf{E_m}$ – Energia de Ativação

$\mathbf{E_v}$ – Energia Superficial Associada a Vértices

G – Energia Livre

g – Vetor de Espalhamento Complexo

H – Entalpia

k – Constante de Velocidade

$\mathbf{K_b}$ – Constante de Boltzmann

$\mathbf{L_i}$ – Dimensão 1D

$\mathbf{N_A}$ – Número de Avogrado

P – Fator Estérico

r – Constante Universal dos Gases

$\mathbf{r_i}$ – Taxa de Formação

S – Entropia

T – Temperatura

u – Freqüência Espacial

U(u) – Função Envelope

V – Volume

$\mathbf{V_g}$ – Volume Global

W – Parâmetro de Wulff

W* – Parâmetro de Wulff Equivalente

$\mathbf{W_i}$ – Parâmetros de Wulff Parciais

Z – Número Atômico

Letras gregas

θ – Ângulo Axial

Ω – Ângulo Sólido

λ – Comprimento De Onda

Ψ – Função De Onda

μ - Massa Reduzida

χ – Modulação De Fase

σ – Seção De Choque

γ – Tensão Superficial

(α, β, γ) – Ângulo Referência em uma Célula Unitária

Abreviaturas

0D – Zero Dimensional

1D – One Dimensional

2D – Two Dimensional

3D – Three Dimensional

ABF – Annular Bright Field

ADF – Annular Dark Field

APFIM – Atom Probe Field Ion Microscopy

AR – Aspect Ratio

ATO – Antimony-Doped Tin Oxide

BF – Bright Field

CBED – Convergent Beam Electron Diffraction

CCD - Charged-Couple Device

CL – Cathodoluminescence

CLR – Core Loss Region

CTF – Contrast Transfer Function

DOF – Degree of Freedom

EELS – Electron Energy Loss Spectroscopy

EMS – Electron Microscopy Suite

FEG – Field Emission Gun

FFT – Fast Fourier Transform

FSR – Focal Series Reconstruction

FTO – Fluorine-Doped Tin Oxide

FWHM – Full Width at Half Maximum

GMM – Gaussian Mixture Models

GPA – Geometric Phase Analysis

HAADF – High Angle Annular Dark Field

HOLZ – High Order Laue Zone

HREELS – High Resolution Electron Energy Loss Spectroscopy

HRTEM – High Resolution Transmission Electron Microscopy

HSTEM – High Resolution Scanning Transmission Electron Microscopy

ITO – Indium-Doped Tin Oxide

LLR – Low Loss Region

MAADF – Medium Angle Annular Dark Field

MOSFET – Metal-Oxide Semiconductor Field Effect Transistor

MSA – Multivariate Statistical Analysis

MTF – Modulation Transfer Function

NCSI – Negative C_s Imaging

NPS – Noise Power Spectrum

OA – Oriented Attachment

OR – Ostwald Ripening

Qdisk – Quantum Disk

QHRTEM – Quantitative High Resolution Transmission Electron Microscopy

SCEM – Scanning Confocal Electron Microscopy

SEM – Scanning Electron Microscopy

SNR – Signal to Noise Ratio

SPM – Scanning Probe Microscopy

STEM - Scanning Transmission Electron Microscopy

TEM - Transmission Electron Microscopy

THF – Tetrahydrofuran

WPOA – Weak Phase Object Approximation

XEDS – X-ray Energy Dispersive Spectroscopy

XPS – X-ray Photoelectron Spectroscopy

XRD – X-ray Diffration

ZA – Zone Axis

ZLP – Zero Loss Peak

Sumário

1. Introdução e Objetivos Gerais

1.1. Introdução Geral

A engenharia de novos materiais e de dispositivos baseados em nanoestruturas requer modelos confiáveis para a descrição das correlações entre os parâmetros de síntese, a morfologia e as propriedades resultantes do material. O modelamento de nanocristais (WANG *et al.*, 2003; BARNARD *et al.*, 2006, 2008, 2010) apresenta-se como uma ferramenta essencial para a predição e controle das características de sistemas nanoestruturados, especialmente os obtidos por processos de síntese do tipo *bottom-up* (LEITE, 2004), nos quais os nanocristais são empregados como blocos de montar para a obtenção de estruturas funcionais em meso- e macro-escala.

O fundamento do modelamento de nanocristais está na descrição de maneira simplificada dos sistemas avaliados, sendo os componentes destes representados por modelos geométricos com morfologia e distribuição de energia determinados em função dos parâmetros de síntese e do ambiente reacional. A partir desta representação é também possível a descrição da evolução de tais sistemas tendo em vista os mecanismos de interação entre os nanocristais. Deste modo é vislumbrada a avaliação e a posterior manipulação das propriedades de um sistema nanoestruturado por meio de alterações na configuração de síntese em função das correlações bem determinadas pelo modelo proposto.

Um dos desafios presentes no modelamento de nanocristais é relativo à avaliação da segregação de espécies atômicas para sistemas nanocristalinos dopados e a avaliação dos seus efeitos. Dada a influência da concentração local de dopantes na distribuição de energia superficial (XIA *et al.*, 2009a; SINGH *et al.*, 2010), e na morfologia esperada para os cristais no equilíbrio termodinâmico (HERRING, 1951), a análise quantitativa da segregação de dopantes é indispensável para o desenvolvimento e para a validação de modelos descritivos para sistemas nanocristalinos. Tal análise requer técnicas avançadas de caracterização que propiciem dados quantitativos com alta resolução espacial.

As técnicas baseadas em microscopia eletrônica de transmissão (TEM) se destacam dentre as ferramentas de caracterização de materiais aplicadas na análise de amostras nanocristalinas devido à possibilidade da obtenção de imagens de alta resolução, padrões de difração de elétrons e de análises espectroscópicas com um mesmo aparato experimental (WILLIANS *et al.*, 1996).

Esta característica multifuncional aliada a procedimentos de simulação permite análises quantitativas mais precisa devido à complementaridade dos dados extraídos (KIRKLAND, 1998).

Avanços recentes nas técnicas de TEM e nas metodologias teóricas que suportam a avaliação dos dados obtidos indicam a possibilidade de que sistemas nanocristalinos sejam caracterizados de modo quantitativo e com alta resolução espacial. Neste contexto, o desenvolvimento de metodologias que aliem experimentos e cálculos teóricos é fundamental para o suporte do modelamento de nanocristais e o seu posterior uso e consolidação na fabricação de dispositivos baseados em nanoestruturas.

1.2. Objetivos

O objetivo geral deste projeto é a avaliação de ferramentas e metodologias baseadas em TEM para a caracterização de nanoestruturas, sendo visada a extração de informações necessárias ao modelamento de nanocristais. As técnicas inclusas neste contexto são pertencentes à microscopia eletrônica de transmissão de alta resolução (HRTEM) e microscopia eletrônica de transmissão de alta resolução por varredura (HRSTEM). O foco das análises é a extração de informações quantitativas e com alta resolução espacial a respeito da morfologia tridimensional e da distribuição de dopantes nos nanocristais avaliados.

Os objetivos específicos deste projeto são:

a) Caracterização da morfologia e da segregação de dopantes em nanocristais de óxidos semicondutores dopados (Sb:SnO_2 e Gd:CeO_2) pelo uso combinado de técnicas avançadas de HR(S)TEM e ferramentas teóricas.

b) Proposição de um modelo para a descrição *ab initio* da distribuição de átomos dopantes em nanocristais individuais.

c) Correlação entre resultados obtidos a partir da caracterização quantitativa realizada por meio de técnicas TEM e o mecanismo de crescimento dos sistemas nanocristalinos estudados.

2. Introdução a TEM

2.1. Introdução às Técnicas HRTEM

A obtenção de imagens HRTEM é baseada na interferência entre duas ou mais componentes difratadas de um feixe de elétrons espalhado por uma amostra fina. Para amostras cristalinas, as condições específicas de difração com ângulos bem determinados decorrentes da estrutura periódica geram padrões de interferência também periódicos. Deste modo, a formação da imagem HRTEM é dada pelos planos atômicos que difratam em uma determinada condição de imagem. É imprescindível notar que as imagens formadas em HRTEM são decorrentes da interferência dos feixes difratados sob a atuação da lente objetiva, sendo os eventuais pontos observados não necessariamente referentes às posições atômicas na amostra.

A análise das imagens obtidas por HRTEM é simplificada ao considerarmos os elétrons acelerados no feixe como ondas planas e a amostra como um objeto capaz de alterar a amplitude e a fase destas segundo a interação com o potencial periódico da rede cristalina. O efeito que a amostra exerce sobre a fase e amplitude de uma onda plana incidente é descrita por diferentes fenômenos físicos simultâneos. A alteração da fase de uma determinada onda plana é dada pela interação com os potenciais atômicos, descritos para átomos individuais pelo potencial de Wentzel (RÜHLE *et al.*, 2003), que são usualmente tratados se considerando o potencial projetado da rede cristalina. A alteração na amplitude de uma determinada onda plana é dada por uma série de eventos, como espalhamentos dos elétrons a alto ângulo (absorção) e interações inelásticas.

A contribuição dos eventos que alteram a amplitude das ondas planas incidentes não é considerada na avaliação de imagens HRTEM, dadas algumas características da técnica e aproximações dos modelos usualmente utilizados. Tais características incluem o baixo ângulo de espalhamento dos elétrons ($>10^{-2}$ rad), a ocorrência de difração em regime cinemático com pequena variação de amplitude e a consideração da amostra como um objeto fino, sendo desconsiderada a propagação transversal devida ao espalhamento. Esse conjunto de considerações é usualmente chamado de *Weak Phase Object Approximation* (WPOA) e constitui a base do teorema de formação linear de imagens (WALTON *et al.*, 1986).

Assumindo o mecanismo linear de formação imagens, a função de onda dos elétrons após a interação com a amostra pode ser descrita pela equação 2.1a. Tal equação é obtida pela solução da equação de Schrödinger dependente no tempo assumindo o comprimento de onda de De Broglie, que leva a um caso particular da equação de Helmholtz com solução do tipo onda estacionária.

$$\Psi(x,y) = A(x,y).\ \exp\left(i\varphi(x,y)\right) \qquad \textbf{Equação 2.1a}$$

onde **ψ** denota a função de onda bidimensional no plano de saída da amostra, **A** a amplitude e **φ** a fase pós a interação com a amostra. Contudo, para a maioria das amostras reais, a descrição da função de onda de saída não pode ser feita diretamente a partir da equação 2.1a por não serem válidas as aproximações assumidas na WPOA. Nestes casos a avaliação pode ser realizada pela abordagem de potenciais periódicos segundo a descrição de Bloch ou pelo método Multislice (COWLEY *et al.*, 1957), no qual a interação do feixe com a amostra é descrita a partir de sua segmentação em fatias que podem ser consideradas pela aproximação WPOA. Informações mais detalhadas do método Multislice são apresentadas no Anexo A.

A propagação dos elétrons após a interação com a amostra, usualmente representada por meio de uma função de onda de saída, é mediada pela lente objetiva e recebe contribuições expressivas em função da configuração do sistema óptico e do sistema de aquisição. Tais contribuições são representadas pela função de transferência de contraste (CTF).

O processo de propagação e interferência da função de onda pode ser descrito matematicamente como uma operação de transformada de Fourier (FFT), que resulta em uma função de onda no espaço recíproco ($\psi(u)$) e é referente ao plano focal posterior da lente objetiva, e por uma transformada Fourier inversa (FFT^{-1}), que descreve a função de onda no espaço real no plano imagem da lente objetiva. Usualmente as componentes da CTF são tratadas no espaço recíproco e incluem as aberrações coerentes, decorrentes das imperfeições da lente objetiva, e também as aberrações incoerentes, decorrentes de uma série de outros fatores experimentais microscópio. A separação das contribuições na CTF é ilustrada na Figura 2.1a.

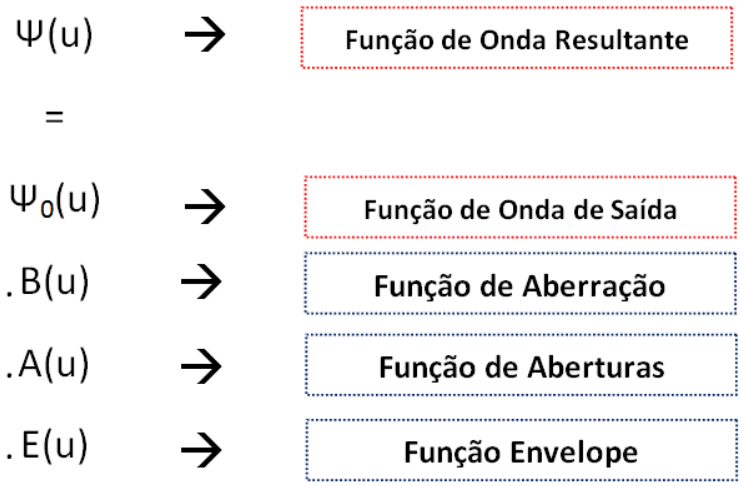

Figura 2.1a: Esquematização da separação das componentes da CTF.

A função de aberrações (B(u)) representa a distorção decorrente da atuação da lente objetiva na fase da função de onda dos elétrons. Tal influência se deve a distorções e assimetrias intrínsecas do campo magnético. O efeito das aberrações na CTF é descrito pelas nas Equações 2.1b e 2.1c em função do vetor de espalhamento complexo (g). Um sumário das aberrações (KRIVANEK *et al.*, 1999) é apresentado na Tabela 2.1a e o efeito do defocus (C_{10}) e da aberração esférica (C_{30}) na CTF são apresentados na Figura 2.1b.

$$g = g_x + ig_y; \qquad \omega = \lambda g; \qquad B(\omega) = e^{(-2\pi i \chi(\omega))} \qquad \textbf{Equação 2.1b}$$

$$\chi(\omega) = \frac{1}{\lambda} Re\left(\frac{1}{2} C_{10}\omega\bar{\omega} + \frac{1}{2} C_{12}\bar{\omega}^2 + \frac{1}{3} C_{21}\omega\bar{\omega}^2 + \frac{1}{3} C_{23}\omega\bar{\omega}^3 + \right.$$

$$+ \frac{1}{4} C_{30}\omega^2\bar{\omega}^2 + \frac{1}{4} C_{32}\omega\bar{\omega}^3 + \frac{1}{4} C_{34}\bar{\omega}^4 + \frac{1}{5} C_{41}\omega^2\bar{\omega}^3 + \frac{1}{5} C_{43}\omega^2\bar{\omega}^3 + \qquad \textbf{Equação 2.1c}$$

$$\left. + \frac{1}{5} C_{45}\bar{\omega}^5 + \frac{1}{6} C_{50}\omega^3\bar{\omega}^3 + \frac{1}{6} C_{52}\omega^2\bar{\omega}^4 + \frac{1}{6} C_{54}\omega\bar{\omega}^5 + \frac{1}{6} C_{56}\omega\bar{\omega}^6 + \cdots \right)$$

Tabela 2.1a: Sumário das aberrações coerentes

Nome	Codigo	Simetria
Defocus	C_{10}	-
Astigmatismo	C_{12}	2
Coma	C_{21}	1
Astigmatismo	C_{23}	3
Aberração esférica	C_{30}	-
Estrela	C_{32}	2
Astigmatismo	C_{34}	4
Coma	C_{41}	1
Lóbulo	C_{43}	3
Astigmatismo	C_{45}	5
Aberração esférica	C_{50}	-
Estrela	C_{52}	2
Roseta	C_{54}	4
Astigmatismo	C_{56}	6

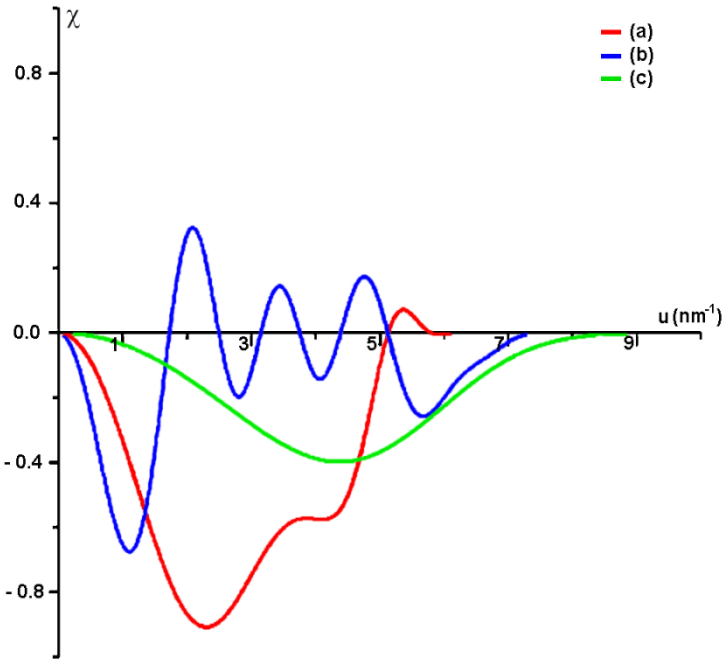

Figura 2.1b: Exemplos de funções de transferência de contraste para diferentes configurações de aberrações coerentes. a) C_{30} = 1.2mm e C_{10} = 59 nm, b) C_{30} = 1.2mm e C_{10} = 178 nm, c) C_{30} = 0.01 mm e C_{10} = 6 nm.

A Figura 2.1b explicita a CTF para diferentes freqüências espaciais com a alteração das aberrações coerentes C_{10} e C_{30}. De maneira simplificada, tal comportamento pode ser entendido como a transferência de informações de diferentes freqüências espaciais, ou espaçamentos periódicos no espaço real, e está diretamente relacionado com o contraste obtido nas imagens. A partir dos cálculos das CTF para diferentes configurações experimentais incluindo os valores de aberrações, é possível a otimização das condições de imagem (SCHERZER *et al.*, 1949), a extração de informações após o primeiro zero da CTF e a obtenção de imagens reconstruídas por meio de séries focais e/ou de inclinação.

A função de aberturas A(u) se refere a atuação das aberturas físicas do microscópio, que restringem a passagem de componentes do feixe de elétrons espalhados a alto ângulo. Apesar de tais componentes serem referentes às informações de maior freqüência espacial (justificado pela relação de Bragg), estas contém maior influência das aberrações dada a dependência polinomial com u. Deste modo, a correta configuração de aberturas é um dos fatores que leva ao aumento da resolução espacial em HRTEM.

A função envelope E(u) é composta de diversas componentes relacionadas a parâmetros experimentais e atua como uma componente de amortecimento na CTF. Os fatores mais importantes que compõem a função envelope são relacionados à estabilidade e à característica de emissão pontual do filamento (coerência espacial) (O'KEEFE *et al.*, 2005), à distribuição de energia dos elétrons emitidos pela fonte (coerência temporal) (BARTHEL *et al.*, 2008) e ao deslocamento e vibração da amostra (MÖBUS, 1994).

O último fato a ser levado em consideração na formação das imagens de HRTEM é a contribuição do sistema de aquisição de imagens. Recentes estudos (THUST, 2009) indicam que a diferença entre o contraste teórico avaliado por simulação multislice de imagens HRTEM e o contraste observado experimentalmente, referida usualmente como fator de Stobbs, é devida à função de transferência (MTF) e ao ruído eletrônico (NPS) do sistema de aquisição de imagens.

De maneira geral, a avaliação quantitativa de imagens HRTEM pressupõe o conhecimento dos parâmetros do sistema experimental. No entanto, devido às aproximações efetuadas nos modelos utilizados na descrição das interações que constituem a caracterização por HRTEM, o uso ferramentas teóricas para a simulação e análise de imagens é imprescindível.

2.2. HRTEM techniques applied to Nanocrystals Modeling

HRTEM techniques applied to Nanocrystals Modeling: towards an "atom-by-atom" description (STROPPA *et al.*, 2011a)

D. G. Stroppa, L. A. Montoro, E. R. Leite, A. J. Ramirez

Publicado no livro *Materials Characterization*, WIT Press, Southampton, 41-53, **2011**.

Abstract

The development of technologies based on nanostructures presents a wide range of challenges for materials scientists and engineers, including the attainment of well-controlled synthesis procedures, the improvement of characterization techniques down to the atomic scale resolution, and the conception and validation of reliable models that can describe materials properties as function of their morphology and fabrication process. A relevant topic in this scenario is the correlation among the spatial distribution of chemical elements, the surface energy configuration, the growth mechanism, and the resultant nanocrystal 3D morphology.

This work presents an overview on the use of advanced HRTEM techniques for the quantitative analysis of nanocrystals and how these results can be used to implement nanocrystals models, which can analytically describe the material features on atomic level. The presented findings show the combined use of experimental data and theoretical tools, such as image simulation and *ab initio* surface energy calculations, for the advanced quantitative characterization of nanocrystalline systems.

The combination of experimental and theoretical efforts on HRTEM characterization represents a powerful tool for the nanocrystals 3D morphology elucidation with atomic resolution and the chemical/structural properties assessment in a quantitative way. Thereby, it is presented as the stepping stone towards the development of novel approaches to describe nanostructured systems.

Introduction

Nanotechnology has been considered one of the most promising branches on the scientific development since the 60's (FEYNMAN, 1960) and its contributions to various fields are notorious nowadays. The "nano" suffix and its effects became an intrinsic subject of materials science and technology on the last few years as the unique properties from nanometer scale are becoming increasingly relevant in those fields.

The traditional materials engineering perspective (CALLISTER, 1949), depicted in Figure 2.2a, can also be applied for the analysis of nanostructured systems. This approach considers that the design of materials aiming an optimum performance requires the complete understanding of the correlation among the processing routes parameters, the materials structure and the resultant properties. However, regarding nanostructured systems, this correlation may be stated as the interrelationship among the synthesis parameters, the atomic scale morphology and the energy configuration (BURDA *et al.*, 2005). As the surface area to volume ratio is enhanced for such systems, unique properties related to the surface energy distribution become relevant. These properties are related to the unique performance of nanomaterials (KOLMAKOV *et al.*, 2004).

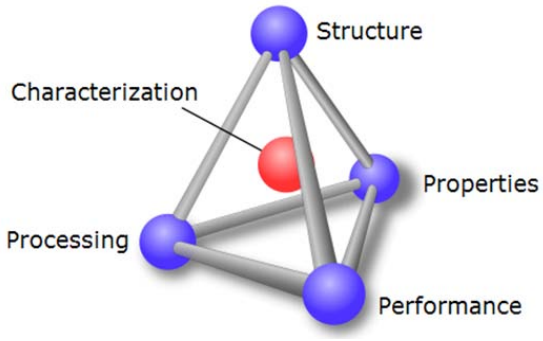

Figure 2.2a: Engineering approach for describing and correlating materials features.

Materials characterization plays a crucial role on the development of reliable models for the description and the design of nanostructured materials with specific features for countless technological areas. Apart from the specific questions that different characterization techniques may answer, there are three general issues that can be highlighted as the most relevant questions for the nanostructured materials modeling and design.

The first one is related to the morphology characterization at the atomic scale. As mentioned before, it is vital to assess the nanomaterials structure with high resolution in order to evaluate its correlation with the system properties. The ultimate goal in this sense is the "atom-by-atom" description of nanocrystals, which would be specially required for the determination of atomic species segregation on alloyed/doped materials (SHIBATA *et al.*, 2004) and the high resolution strain state analysis of nanostructures (BRUNE *et al.*, 1998).

The second issue is related to the nanocrystals surface structure and its dependency on the synthesis environment and chemical species. This aspect is intrinsically correlated to the nanocrystals morphology and, consequently, to the material surface energy distribution and properties (YANG *et al.*, 2008).

The third relevant point is the interrelation between the nanocrystals and the system growth behavior (DALMASCHIO *et al.*, 2010). These aspects represent crucial issues for the understanding and optimization of synthesis methodology as they are closely related to the nanostructured system stability and long term reliability (YU *et al.*, 2003).

As describing the properties and behavior of each nanocrystal in an actual nanostructured system represents an overwhelming many-bodies problem, simplified models are needed for the engineering of nanomaterials in a reliable manner. Nanocrystal modeling (BARNARD, 2010) is a wide approach where nanostructured systems components are described as building blocks with specific morphology, energy distribution, and interaction mechanisms. In these terms, the development of accurate models may be a fundamental tool for nanocrystals and mesocrystals shapes prediction, design and control of growth processes, and the resulting properties tuning of an unlimited number of systems.

The development of reliable modeling methodologies represents a hard task for materials scientists and engineers due to involved challenges, especially when quantitative high resolution characterization analyses are required. Even though advanced characterization techniques based on electron microscopy, scanning probe microscopy and synchrotron radiation are feasible and complimentary in this scenario, limitations (BRUNDLE *et al.*, 1992) associated to each one of them prevent their isolated use a for reliable analysis. The most relevant limitations of high resolution techniques are summarized on Table 2.2a:

Table 2.2a: Most relevant limitations from high resolution characterization tools

ISSUE	EFFECT
Sample Preparation	modification on the sample original features
Sample Stability	characteristics changes during analysis
Energy Resolution	spectroscopic signature may have overlaps
Signal to Noise Ratio	poor detection system sensitivity
Sampling	lack of statistical representativeness
Averaging	lack of features from individual particles
Data Analysis	deconvolution, modeling and fitting

Although continuous improvements on the characterization instrumentation and methodologies enhance the individual techniques performance, the combined use different available experimental techniques and theoretical approaches are widely used to overcome the inherent limitations of the quantitative analysis of nanosized systems.

Transmission Electron Microscopy (TEM) based techniques stand out among other characterization techniques for nanostructured systems due to the possibility of a comprehensive and versatile approach including high resolution imaging, diffraction and spectroscopy. This multipurpose characteristic allied with simulation procedures provides complementary information that can be used to improve the analysis precision.

Recent developments on the TEM instrumentation and analysis methods allowed outstanding advances on nanoscience and nanotechnology (HAWKES, 2008). The spherical aberration (Cs) correction (HAIDER *et al.*, 1998) can be considered among the most influential improvements on both high resolution TEM (HRTEM) and high resolution scanning TEM (HRSTEM) due to a number of factors. For HRTEM, the Cs-correction of the objective lens resulted in the drastic improvement on achievable spatial resolution, the possibility of larger gaps in the pole piece for *in situ* experiments, and new imaging modes (JIA *et al.*, 2004a) due to fine tuning of the aberration coefficients. For HRSTEM, the Cs-correction of the condenser lens leads to an improvement on the achievable spatial resolution due to the probe size reduction and the effective beam current increase.

In addition to the instrumental TEM improvements, the development of more accurate models to describe the image formation and to support the TEM image simulation (STADELMANN, 1987) provides a more reliable interpretation of experimental data.

This work presents an overview on the HRTEM techniques state of art with several examples which indicate the development of such characterization tools towards the quantitative high resolution analysis of nanocrystalline materials.

HRTEM and HRTEM image simulation

HRTEM image formation is based on the incident electron beam scattering by a thin sample. The technique is especially relevant for very thin crystalline samples, where the interaction of the several diffracted beams forms an interference patterns. As the diffracted components correspond to particular oriented periodic spacings on the sample, their interference may appear as a 2D periodic image which cannot be directly interpreted. The direct interpretation unfeasibility is mainly related to the HRTEM interference pattern dependency with the sample thickness and with the microscope configuration, especially the defocus value. However, the use of HRTEM image simulation can provide information about the sample crystalline arrangement.

HRTEM image simulation is a crucial step in HRTEM characterization, which supports the atomic structure analysis. Multislice method (COWLEY *et al.*, 1957) is the most widely used image simulation procedure and consists in the electrons wave function calculation after the electron beam interaction with the sample projected potential. Imaging distortions due to the lens aberrations, microscope instabilities and detection system defects (THUST, 2009) may be included in order to better reproduce the experimental imaging condition.

The HRTEM imaging and image simulation combination has provided numerous examples of successful materials characterization. Remarkable examples can be noticed on the determination and refinement of crystalline structures (KILAAS *et al.*, 2001) and the quantitative evaluation of the chemical composition along the thin films interface (TILLMANN *et al.*, 2002).

Figure 2.2b illustrates the combination of HRTEM imaging and image simulation on the evaluation of an anomalous anisotropic growth mechanism for SnO_2 nanocrystals (STROPPA *et al.*, 2011b). The used approach provided an unambiguous characterization of the growth mechanism and its preferential direction, which would not be feasible from direct imaging only.

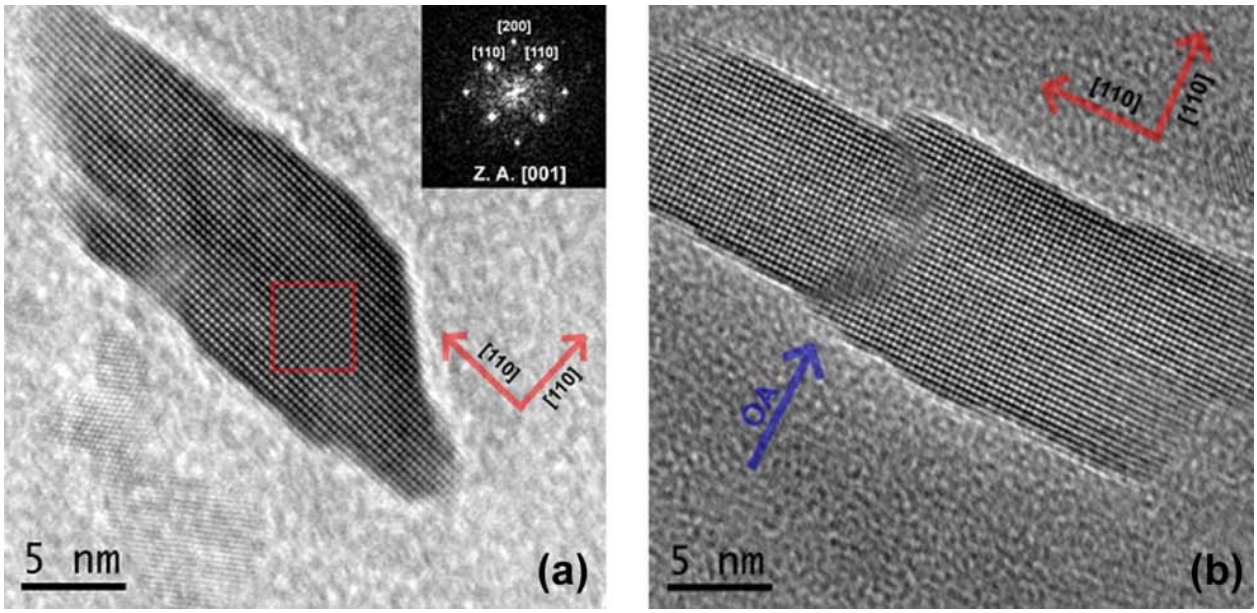

Figure 2.2b: (a) SnO_2 nanocrystal HRTEM image with an indexed FFT inset and a HRTEM multislice simulation (red square). (b) Oriented Attachment along the [110] is identified as the main growth mechanism. [From ref. (STROPPA *et al.*, 2011b), Copyright © 2011 by RSC Publishing, reprinted with permission of authors.]

In addition, the accurate determination of nanocrystals 3D morphology by HRTEM simulation of nanocrystals (STROPPA *et al.*, 2011c) can be used to indirectly extract quantitative dopant segregation information (STROPPA *et al.*, 2009) from systems where conventional analytical techniques are impracticable due to several experimental restrictions. Figure 2.2c depicts the 3D morphological modeling for Sb:SnO_2 nanocrystals with different dopant contents. The nanocrystals models were compared to the Wulff (HERRING, 1951) constructions based on *ab initio* surface energy calculations, providing the dopant atoms segregation for individual particles and its dependency with the doping level (STROPPA *et al.*, 2011d).

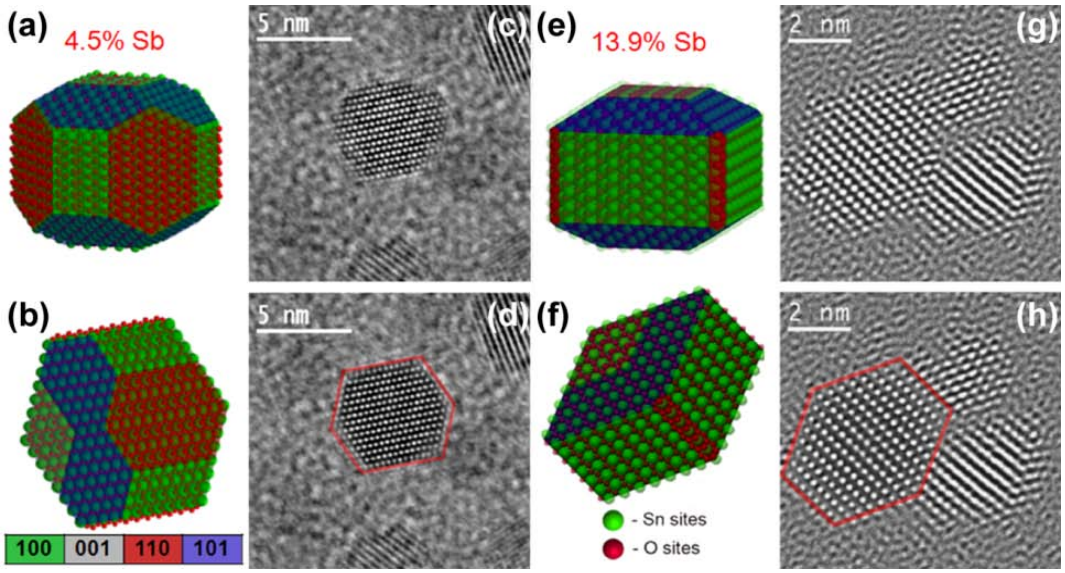

Figure 2.2c: (a), (e) Trimetric and (b), (f) [111] zone-axis oriented views for the Sb-doped nanocrystals geometric model. (c), (g) Original HRTEM images and (d), (h) superimpositions with the simulated HRTEM images. [Adapted from ref. (STROPPA *et al.*, 2009), Copyright © 2009 by ACS Publications, reprinted with permission of authors.]

The presented examples depict the synergism between the HRTEM imaging and theoretical methods such as HRTEM image simulation and *ab initio* surface energy calculations. Therefore, this combination presents a remarkable potential as a tool for unveiling important nanocrystalline systems features, such as 3D morphology, dopant segregation, surface energy distribution, and growth mechanisms.

Focal Series Reconstruction and Geometric Phase Analysis

Although the HRTEM image simulation can support accurate nanocrystals 3D morphology analyses, it is not always feasible to use such procedure to precisely evaluate the position of individual atoms or atomic columns in crystalline structures. To extract information which is directly related to the atomic positions, such as strain/stress state, a refinement on the HRTEM analysis is needed.

Focal Series Reconstruction (FSR) (THUST *et al.*, 1996) is a proposed calculation which is applied for the electron wavefunction restoration on the HRTEM imaging process and allows obtaining the sample projected potential without the interference of the microscope optical aberrations. The FSR implementation is based on the acquisition of a set of images under different objective lens defocus conditions, which is subsequently submitted to a restoration procedure that estimates the contrast transfer function (CTF) and the aberration coefficients implicated on the imaging process.

A number of successful uses of FSR aiming a straightforward image interpretation (BARTHEL *et al.*, 2010), the correction of residual aberration (KIRKLAND *et al.*, 2004), and the improvement of the HRTEM technique spatial resolution (BIGGEMANN *et al.*, 2008) have been already described in the literature. An example which illustrates the image improvement when FSR method is applied to structural analysis is depicted on Figure 2.2d. These images show the comparison between an original HRTEM image and a phase image of the reconstructed wavefunction.

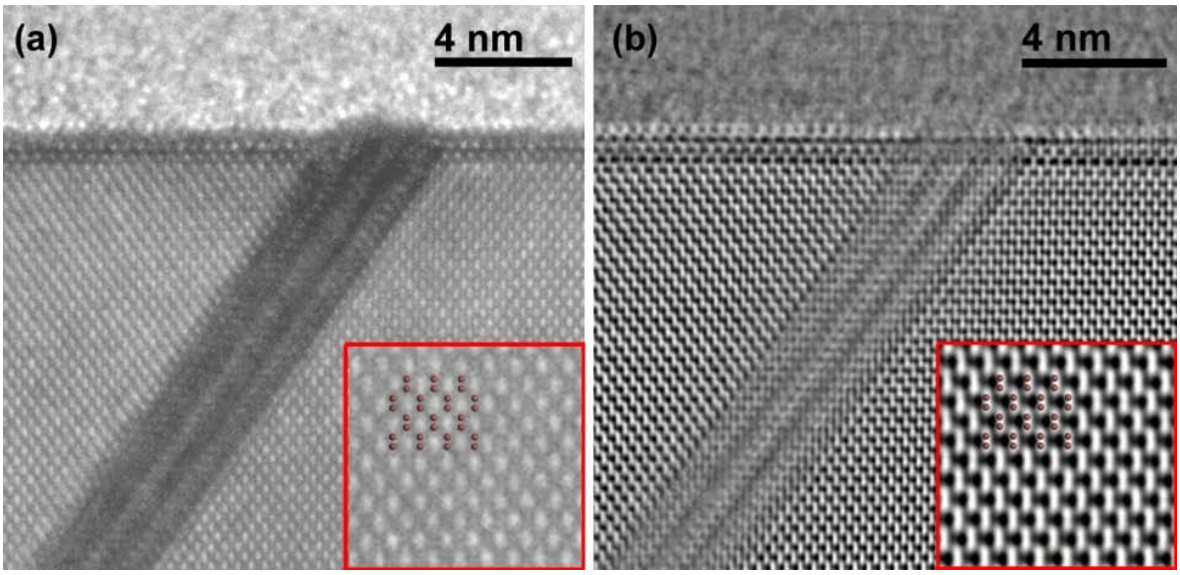

Figure 2.2d: (a) Example of an original HRTEM image and (b) the output from a FSR restoration from a $CoSi_2$ sample. The insets exhibit a higher magnification detail with the crystal structure superimposition.

Geometric Phase Analysis (GPA) (KRET *et al.*, 2001) is a methodology for measuring and mapping structural displacement fields on HRTEM images using a reference lattice. Its application to HRTEM image analysis allows the local lattice distortion evaluation, which can be directly related to the local strain state. This method has been effectively employed to study strain fields in semiconductors and metals (HYTCH *et al.*, 2003).

The GPA implementation is based on the reciprocal space evaluation of a HRTEM image with respect to a reference undistorted lattice image, either obtained from a different region in the analyzed sample or from an image simulation procedure. As a spatial frequency spread around the characteristic lattice parameters frequencies is existent on strained samples, the determination of lattice distortions can be performed by the comparison with a reference image. The distorted components can be extracted on the reciprocal space and further translated to real space components through an inverse Fourier transform. Such analysis can be performed for two non-collinear spatial frequencies, resulting in a projected 2D distortion description of the sample which can be related to its 2D strain/stress state.

The GPA application is reported on the literature as an efficient tool to calculate strain maps on microelectronic components (HUE *et al.*, 2008) and for the strain state analysis on individual nanocrystals (JOHNSON *et al.*, 2008). A typical output from a GPA analysis is the distortion map from the analyzed HRTEM image, as exemplified on Figure 2.2e, which includes the perpendicular, parallel and rotational strain components.

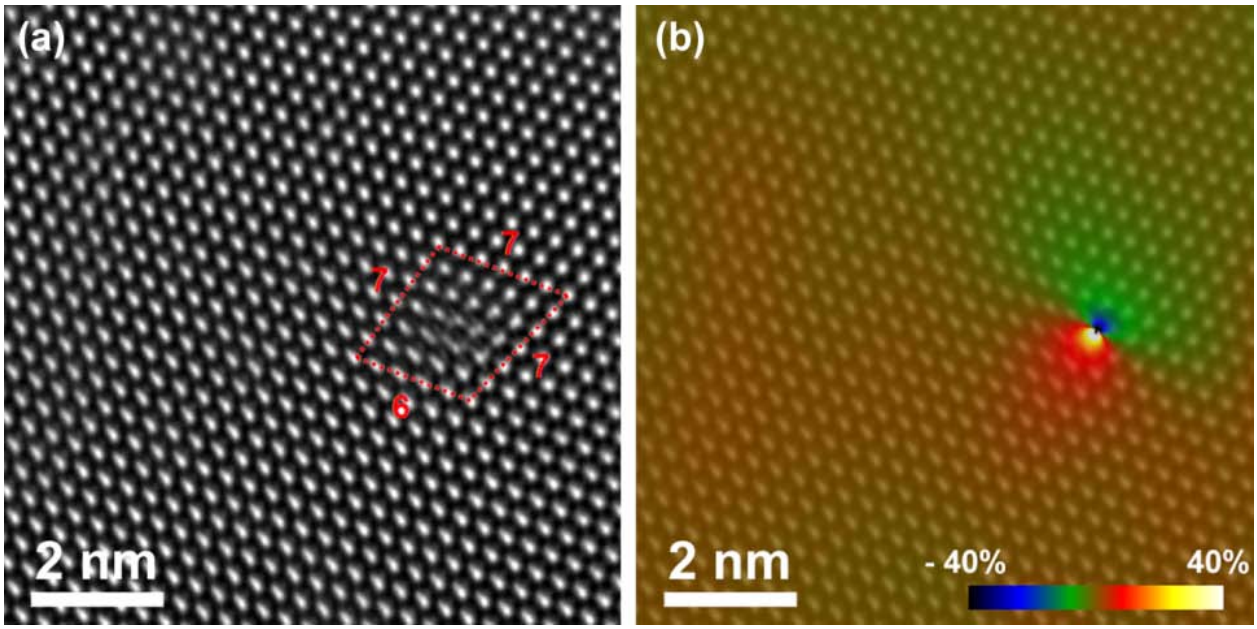

Figure 2.2e: (a) Original Cs-corrected HRTEM image and (b) distortion mapping from a single dislocation on a CeO_2 sample.

An example of the combined user of FSR and GPA is presented on Figure 2.2f (MONTORO *et al.*, 2009). Cross-section HRTEM images of epitaxially grown $Si_{1-x}Ge_x$:Si(001) alloyed islands were used to characterize in a self-consistent way the strain configuration and the local chemical composition with high spatial resolution. By the combination of projected 2D chemical composition mapping from two different cross-sectioned zone-axis views, [100] and [110], it was possible to infer chemical composition in a three-dimensional fashion (MONTORO *et al.*, 2010).

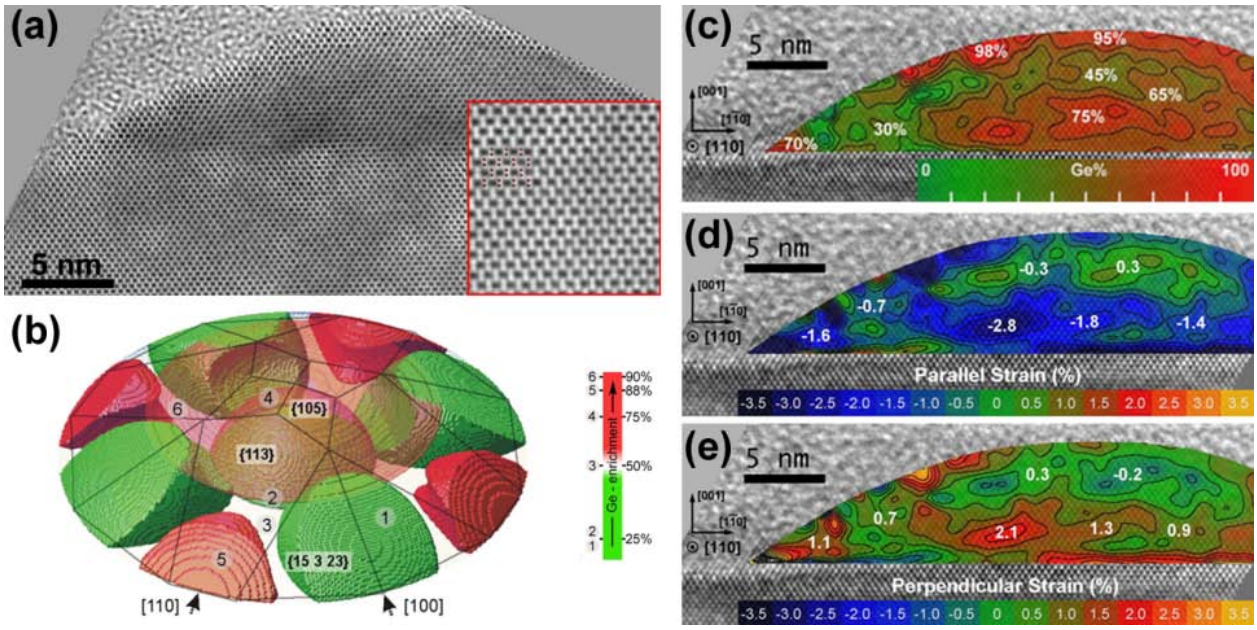

Figure 2.2f: (a) FSR reconstruction from a Si-Ge island including a higher magnification detail on the inset. (b) A simplified 3D chemical reconstruction was obtained after the strain chemical mapping of several Si-Ge islands at different zone-axis. An example from a single island: (c) chemical composition map, (d) parallel and (e) perpendicular strain projections. [Adapted from refs. (MONTORO *et al.*, 2009; MONTORO *et al.*, 2010), Copyright © 2009 by ACS Publications, reprinted with permission of authors.]

The successful application of this technique to quantify the elastic behavior of the Si-Ge:Si(001) system shows that this methodology arises as a remarkable tool for accurate chemical and elastic state evaluation, which can be applied to several strained alloyed nanostructures, such as epitaxial islands, nanowires, nanocrystals, and thin films.

A Novel approach for HRTEM imaging

The improvement of HRTEM characterization depends on the comprehensive understanding of the underlying image formation theory. An important imaging condition representation is given by the Contrast Transfer Function (CTF), which represents how the spatial frequencies are transmitted through microscope imaging system.

Since the 40's, microscopists have been trying to improve the CTF characteristics by tuning the instruments parameters during the experiments or by the posterior treatment of the images. The main goal in this sense is to extend information transfer for high spatial frequencies. The most remarkable improvements were achieved by using induced defocus values on the objective lens in order to compensate its inherent positive spherical aberration coefficient (SCHERZER *et al.*, 1949). However, a ground-breaking evolution happened with the Cs-correction possibilities.

At a first glance, the use of Cs-correction adds an additional degree of freedom to the microscope tuning, allowing the CTF direct improvement for high spatial frequencies and improving the microscope information limit. A comparison between the HRTEM images from the same sample obtained by conventional and Cs-corrected microscopes, which is presented on Figure 2.2g clearly shows the image enhancement provided by the aberration corrector hardware.

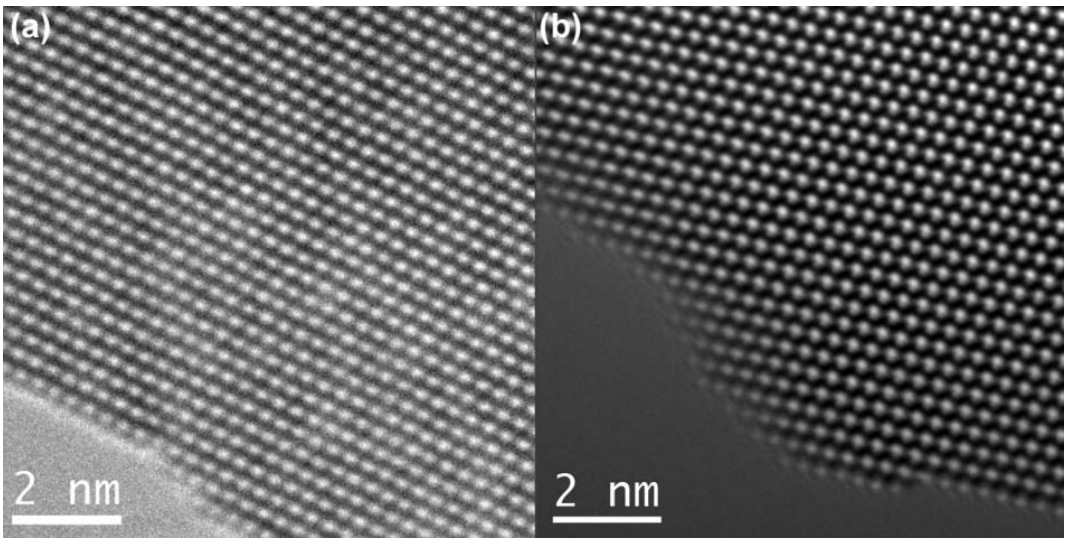

Figure 2.2g: Raw HRTEM images from the same CeO_2 nanocrystal from a (a) standard TEM microscope (1.25 Å information limit) and from a (b) Cs-corrected microscope (0.8 Å information limit).

A detailed investigation (JIA *et al.*, 2010) of the electron scattering on the dynamical regime pointed out that non-linear contributions would enable the achievement of enhanced contrast transfer for low-Z elements by the use of negative Cs values. The Negative Cs Imaging (NCSI) (JIA *et al.*, 2004a) aims the contrast maximization at high frequencies by the microscope parameters optimization, including defocus and Cs adjustments. The NCSI application allowed some unique measurements including the high resolution assessment of light elements atomic columns information, such as occupancy next to crystalline defects (JIA *et al.*, 2003) and sub-angstrom displacement in magnetic domain walls (JIA *et al.*, 2008).

Examples of NCSI HRTEM characterization for CeO_2 sintered and nanocrystalline samples are depicted on Figure 2.2h. Although the contrast for Oxygen columns is observed in both images, the direct analysis of a bulk-like sample HRTEM image (Figure 2.2ha) is unfeasible due to a combination of factors. As the accurate thickness estimation is not achievable by HRTEM image simulation for this specific combination of crystalline system and imaging conditions, the intensity distribution cannot be directly associated to the Oxygen columns scattering. A solution for this issue is the sample projected potential assessment by the FSR application on NCSI HRTEM images (Figure 2.2hb).

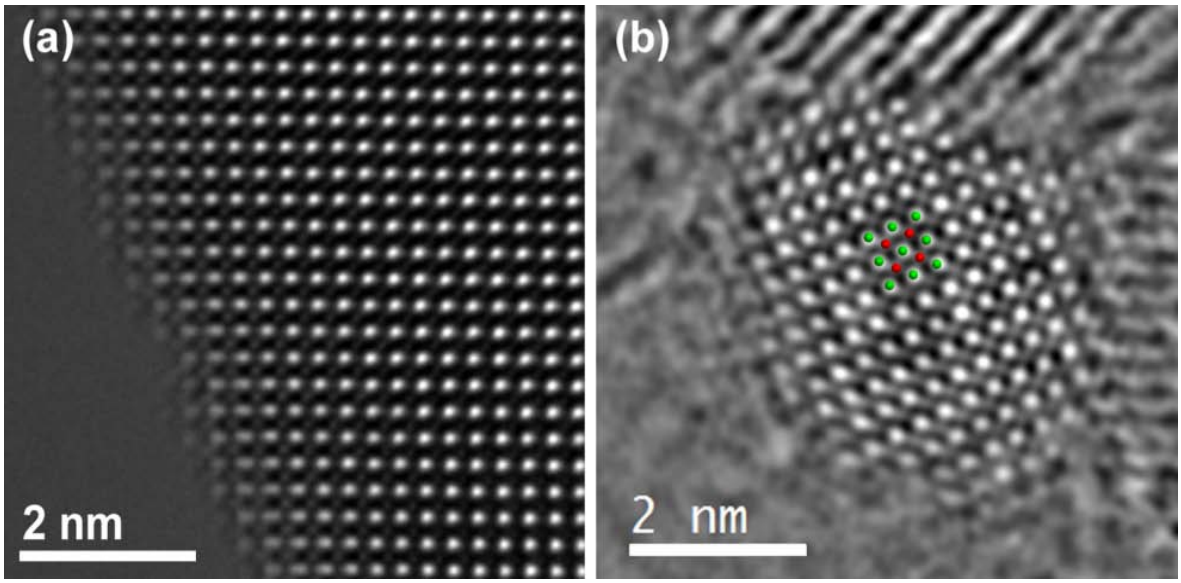

Figure 2.2h: (a) NCSI HRTEM image from a CeO_2 bulk-like sample on the [100] ZA and (b) FSR from NCSI HRTEM images from a CeO_2 nanocrystal on the same ZA orientation including a unit cell superimposition.

Concluding Remarks

State of art HRTEM techniques indicate that their use in conjunction with theoretical procedures for HRTEM image simulation and data analysis represents a vital tool for the quantitative evaluation of nanostructured systems. The depicted examples illustrate how this technique can simplify, or even present completely novel approaches, a number of materials characterization challenges where a quantitative high resolution assessment is required.

The current development of HRTEM instrumentation and related methodologies indicates that its importance on materials characterization will grow on this decade, especially due to the novel possibilities achieved by aberration correction implementation and by on-growing combined use with HRSTEM imaging and spectroscopy techniques.

Acknowledgements

The authors acknowledge the financial support of the Brazilian research funding agencies FAPESP and FINEP; the German research funding agency DAAD. The authors would also like to thank the Ernst Ruska Centre staff at the Forschungszentrum Jülich and the QFA staff at the Universitat Jaume I for the fruitful discussions and scientific support.

2.3. Introdução às Técnicas HRSTEM

A diferenciação entre a obtenção de imagens em modo HRTEM e em microscopia eletrônica de transmissão de alta resolução em modo varredura (HRSTEM) é dada por quatro fatores: a configuração do sistema óptico para a obtenção de alta colimação no feixe, a dinâmica de análise baseada na varredura do feixe, a influência do sistema óptico no sinal transmitido e a configuração de detectores utilizada.

A configuração das lentes condensadoras e de suas respectivas aberturas no modo STEM é feita de maneira a se obter um feixe paralelo e com pequena dimensão. O ajuste do sistema óptico é realizado visando o equilíbrio entre a dimensão da sonda e a sua corrente eletrônica. Estes dois fatores são determinantes na resolução espacial e na relação sinal-ruído (SNR) em modo STEM. Deste modo, a configuração do sistema óptico é feito em função das medidas as serem realizadas (JAMES *et al.*, 1999), considerando a distinção entre as técnicas analíticas (espectroscópicas) e os modos de obtenção de imagens com alta resolução espacial.

Os microscópios que operam no modo STEM apresentam um conjunto adicional de bobinas defletoras que controla a deflexão do feixe e a posterior correção de inclinação, assim resultando em um processo de varredura no qual o feixe tem incidência axial sobre a amostra. Tal configuração propicia a análise da amostra a cada ponto de varredura, sendo avaliados os diferentes tipos de interação que ocorrem devido à incidência do feixe.

Diferentemente do modo HRTEM, no qual as informações são majoritariamente extraídas do padrão de interferência entre componentes do feixe difratadas pela amostra, nos modos HRSTEM as informações referentes a diferentes tipos de interações entre o feixe e a amostra podem ser detectados e analisados independentemente. Desta forma, os sinais espalhados pela amostra podem adquiridos sem a necessidade de intermédio de lentes objetivas.

As técnicas HRSTEM são classificadas de acordo com os diferentes eventos de espalhamento eletrônico durante a interação dos elétrons do feixe com a amostra. Tais eventos são diretamente relacionados ao ângulo de espalhamento e, conseqüentemente, aos tipos e à disposição dos detectores utilizados na aquisição de sinal.

O detector usado em configuração de Campo Escuro Anular em Alto Ângulo (HAADF) é destinado à coleção de elétrons espalhados em alto ângulo, usualmente acima de 80 mrad, relativos ao espalhamento Rutherford com os núcleos atômicos presentes na amostra. O detector usado em configuração Anular Dark Field (ADF) é utilizado para a coleção de elétrons espalhados em ângulos intermediários, usualmente entre 10 e 80 mrad, e que são, de modo geral, relativos aos sinais difratados pela amostra. O detector usado em configuração Bright Field (BF) é destinado à coleção de elétrons espalhando em ângulos menores que 10 mrad, incluindo assim os elétrons que não interagiram com a amostra e os que sofreram interações inelásticas com espalhamento de baixo ângulo. Adicionalmente, um espectrômetro pode ser utilizado para a separação dos elétrons, sobretudo os espalhados em baixo ângulo, em função da energia perdida nas interações com a amostra e sua posterior detecção. Tal procedimento constitui a base da espectroscopia por perda de energia de elétrons (EELS) (EGERTON, 2009).

As técnicas baseadas em STEM apresentam três vantagens em relação às técnicas análogas em TEM. A primeira está relacionada à interpretação das imagens, dada a possibilidade da correlação direta entre a localização das interações detectadas e a formação da imagem pixel a pixel durante a varredura. A segunda está relacionada à possibilidade da obtenção de imagens formadas a partir de elétrons espalhados a altos ângulos em regime HAADF. Devido ao mecanismo de espalhamento a alto ângulo, tais imagens contêm contraste de número atômico (Z-Contrast) (PENNYCOOK *et al.*, 1991, 1996) e podem ser obtidas em condições em que o contraste difração é minimizado. A terceira está relacionada às técnicas analíticas com alta resolução espacial, como EELS e XEDS (WATANABE *et al.*, 2006), que possibilitam a obtenção de informações composicionais e/ou de estrutura eletrônica.

A primeira aproximação para a quantificação do sinal HAADF é realizada a partir do espalhamento de elétrons por um núcleo carregado pelo modelo de espalhamento de Rutherford, cuja seção de choque diferencial pode ser quantificada pela Equação 2.3a.

$$\frac{d\sigma(\theta)}{d\Omega} = \frac{e^4 . Z^2}{16(E_o)^2 \sin^4 \frac{\theta}{2}} \qquad \textbf{Equação 2.3a}$$

Na Equação 2.3a, a seção de choque diferencial em função do ângulo sólido ($d\sigma(\theta)/d\Omega$) é descrita em função do número atômico do átomo espalhador (Z), da energia do feixe incidente (E_o) e do ângulo de espalhamento em relação à direção de propagação do feixe de elétrons (θ). A integração da seção de choque para um determinado intervalo de ângulos θ indica que o número de eventos de espalhamento deve ser proporcional ao quadrado do número atômico do núcleo espalhador. Modelos teóricos mais refinados e complementados com dados semi-empíricos indicam que tal dependência tem potência aproximada de 1.7 (HILLYARD *et al.*, 1995).

A avaliação de imagens HAADF com alta resolução espacial requer a avaliação dos espalhamentos a alto ângulo promovidos por uma coluna de átomos alinhados ao invés da avaliação de interação de espalhamento entre os elétrons do feixe e um núcleo isolado. Em tais casos, especialmente para átomos pesados, a consideração de dois fatores se torna necessária. A primeira refere-se à ocorrência de tunelamento ao longo da coluna, que seria análogo à focalização do feixe eletrônico após as primeiras interações com a amostra, levando assim à alteração do sinal espalhado. A segunda se refere à consideração da influência da temperatura do sistema nas posições atômicas, dada a oscilação dos átomos em torno da posição de equilíbrio para temperaturas diferentes de zero (LEVI *et al.*, 1979; XU *et al.*, 1991). Tal combinação de fatores leva a uma complexa dependência não linear entre o sinal detectado, o número atômico dos núcleos espalhadores e a espessura da amostra. Deste modo, a avaliação quantitativa acurada de imagens obtidas por HAADF só é possível por meio de simulações de imagem, de maneira similar ao realizado com imagens HRTEM pelo método multislice. Apesar da existência de softwares comerciais (BARTHEL, 2010; KOCH *et al.*, 2011) para a realização de tais simulações, o modelo para a descrição da formação de imagens HAADF com alta resolução encontra-se atualmente em desenvolvimento.

A análise EELS baseia-se na avaliação do espalhamento inelástico que ocorre na interação do feixe de elétrons com a amostra, que usualmente apresentam ângulos de espalhamento menores que 5 mrad quando em regime cinemático. A detecção é realizada por meio de um espectrômetro, constituído por um prisma magnético e um sistema de aberturas, que seleciona elétrons segundo a sua energia. O espectro EELS, que apresenta o número de eventos detectados em função da perda de energia, pode ser correlacionado com eventos de espalhamentos inelástico e, posteriormente, com as características da amostra.

O espectro EELS (EGERTON, 2008) pode ser dividido em três regiões em função da perda de energia dos elétrons. A primeira é denominada Zero-Loss Peak (ZLP) e representa as perdas de energia até 10 eV, referentes aos elétrons que não sofreram interação com a amostra ou tiveram perdas de energia referente à vibrações térmicas da rede cristalina (fônons). A intensidade integrada do ZLP é usualmente três ordens de grandeza maior que as demais regiões para amostras finas, como requerido para a realização de EELS. A largura do ZLP à meia altura indica o desvio em energia dos elétrons e a máxima resolução em energia do experimento.

A segunda região é denominada Low-Loss region (LLR) e representa perdas de energia entre 10 eV e 50 eV. As interações de presentes nesta região são referentes à formação de plásmons, ao *gap* semicondutor, às transições inter-bandas e a geração de radiação Cherenkov. A relação entre a intensidade dos picos de plásmons e o ZLP indica a espessura da amostra em função da seção de choque inelástica para a formação de plásmons para o material da amostra. De um modo geral, a LLR contém informações referentes à estrutura eletrônica da amostra.

A terceira região é denominada Core-Loss Region (CLR) e representa perdas de energia maiores que 50 eV, que são usualmente referentes a transições eletrônicas características dos tipos atômicos presentes na amostra. A perda de energia registrada para os elétrons na região CLR está relacionada às energias de ligação dos elétrons presentes na amostra, sendo utilizada na identificação de tipos atômicos na amostra e em sua quantificação. Deste modo, a posição dos picos na CLR é análoga às bordas de absorção de Raios X e indica a presença de elétrons com energias características segundo a configuração eletrônica do material. O valor da integração dos picos na CLR é proporcional ao número de eventos de transição eletrônica característica após a ionização da amostra pelo feixe, sendo diretamente relacionado com a concentração da espécie atômica que apresenta tal transição em função da seção de choque para tal evento.

A quantificação de espécies atômicas (RIEGLER *et al.*, 2010) é iniciada pela subtração de espectro de fundo, relacionado a eventos de espalhamento múltiplo em menores energias e usualmente modelado como função do tipo decaimento exponencial. Em seguida, os picos referentes a determinadas transições eletrônicas são integrados e a quantificação relativa é obtida a partir da seção de choque de ionização para cada tipo de transição, avaliadas a partir de cálculos teóricos (POWELL, 1989).

2.4. STEM techniques applied to Nanocrystals Modeling

HRSTEM techniques - High Resolution Imaging and Spectroscopy Side by Side (STROPPA *et al.*, 2011e)

D. G. Stroppa, L. F. Zagonel, L. A. Montoro, E. R. Leite, A. J. Ramirez

Aceito para publicação na revista *ChemPhysChem*, **2011**.

Abstract

This work presents an overview on the High Resolution Scanning Transmission Electron Microscopy (HRSTEM) techniques and exemplifies the novel quantitative characterization possibilities that emerged from recent advances on these methods. The synergistic combination of atomic resolution imaging and spectroscopy provided by HRSTEM is highlighted as a unique feature which can provide a comprehensive analytical description of materials properties at the nanoscale. State-of-art High Angle Annular Dark Field (HAADF) and Annular Bright Field (ABF) examples are depicted, as well as the use of X-ray Energy Dispersive Spectroscopy (XEDS) and Electron Energy Loss Spectroscopy (EELS) for probing samples properties at atomic scale. In addition, promising techniques such as Cathodoluminescence (CL), Confocal HRSTEM and diffraction mapping are introduced. The presented examples and results point out that HRSTEM related techniques will be fundamental tools for a comprehensive properties assessment at the atomic scale.

Introduction

Nanoscience is becoming increasingly relevant for the development of novel technologies as the systems' nanoscale configuration and properties assessment becomes more accessible. The developments on both theory and experiments provided an improved understanding about the underlying phenomena and their role on nanomaterials properties (BARNARD, 2010). A significant part of this advance and on the further use of distinguished properties that are obtained at nanoscale are due to the progress of characterization techniques.

The quantitative analysis of nanostructured systems requires remarkable efforts due to the high resolution characterization techniques inherent restrictions (BRUNDLE *et al.*, 1992). In this scenario, the combination of theoretical and experimental tools has been shown to be effective for a comprehensive description of nanomaterials features (STROPPA *et al.*, 2011d).

Transmission electron microscopy (TEM) techniques can be highlighted among the characterization techniques due to their versatility on the quantitative data retrieval from nanostructured samples. More specifically, high resolution scanning transmission electron microscopy (HRSTEM) techniques have shown unprecedented characterization possibilities due to the combination of high resolution imaging, diffraction and spectroscopy in a single experiment (COLLIEX *et al.*, 2009). This characteristic allows the mapping of different electron interactions events on the sample, which implies on the possibility of probing features with accurate localization. In this sense, HRSTEM techniques point towards the materials properties quantitative characterization with atomic resolution (TRASOBARES *et al.*, 2011).

Scanning transmission electron microscopy (STEM) is based on the electron scattering analysis as a focused beam scans over a thin sample. Even though STEM is approximately as old as TEM and SEM techniques (PENNYCOOK *et al.*, 2011), some recent instrumental developments greatly enhanced its performance and supported a reasonable number of breakthrough results. Among these advances are the spherical aberration (Cs) and chromatic aberration (Cc) corrector (BATSON *et al.*, 2002; PENNYCOOK *et al.*, 2009; KRIVANEK *et al.*, 2009), the monochromator implementation (KRIVANEK *et al.*, 2009) and the improvement of the synchronous systems for data acquisition (HEIDELMANN *et al.*, 2009).

Besides the instrumental enhancements, several theoretical tools were developed and implemented in order to improve the characterization possibilities and to provide more reliable quantitative analysis. Among them are the more accurate image simulation and spectrum analysis procedures (BERTONI *et al.*, 2008; BARTHEL *et al.*, 2009), and the implementation of deconvolution models (GLOTER *et al.*, 2003; ISHIZUKA *et al.*, 2003) and multivariate statistical analysis (MSA) (BOSMAN *et al.*, 2006) for an improved information extraction from raw data.

The aforementioned improvements on STEM techniques are mostly related to two fundamental criteria which define the characterization efficiency: spatial resolution and energy resolution. The spatial resolution is related to the beam size and the interaction events delocalization, which dictates how fine the sample assessed details could be. The state-of-art STEM microscopes are currently near the 50 pm spatial resolution (PENNYCOOK *et al.*, 2011). The energy resolution on spectroscopic techniques is related to the possibility of distinguishing the different inelastic interactions between the electron beam and the sample by their inherent energy losses. The most advanced STEM microscopes present energy resolution better than 0.1 eV (MOOK *et al.*, 1999). The role of spatial and energy resolutions on STEM can be better understood by analyzing how information is extracted by each related technique and how experimental configuration affects data acquisition.

The use of STEMs as versatile electron scattering experimental setups with high resolution imaging capability is enhancing the nanostructured systems quantitative analysis possibilities. The following sections present an overview on the state-of-art HRSTEM techniques and their application on the quantitative analysis from nanocrystalline materials.

Imaging Modes and Image Simulation

Figure 2.4a presents a schematic illustration of a STEM, including the most relevant detectors for imaging and spectroscopic techniques. STEM techniques can be generally described as the sequential scan of a focused electron beam over a selected region of the sample and the simultaneous use of annular detectors, which select electrons with different scattering angles with

respect to the original beam propagation. The pixel by pixel data acquisition provided by these detectors is used to reconstruct STEM images.

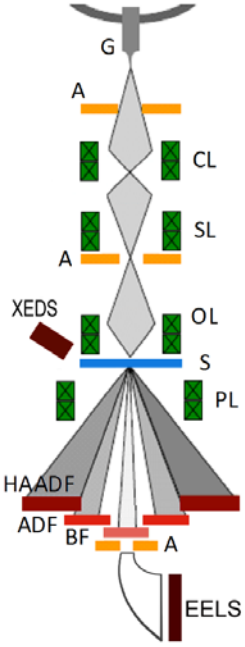

Symbol	Component
G	Electron Gun
A	Apertures
CL	Condenser Lenses
SL	Scanning Lenses
OL	Objective Lens
S	Sample
PL	Projector Lenses
BF	Bright Field Detector
ADF	Annular Dark Field Detector
HAADF	High Angle ADF Detector
XEDS	X-rays Detector
EELS	EELS Spectrometer

Figure 2.4a: STEM microscope schematic diagram depicting the main detectors and spectrometers standard positioning.

The major advantage from STEM techniques experimental setup is that it allows acquiring images using electrons that undergone different interactions, such as diffraction and Rutherford scattering, and provide information related to the physical phenomena that occur during the electron-sample interaction.

The high angle annular dark field (HAADF) imaging mode in STEM is based on the detection of incoherent quasi-elastic electron scattering by the atoms nuclei, which is usually the predominant contribution for scattering angles higher than 80 mrad (HILLYARD *et al.*, 1995). A first approximation of these scattering events by the Rutherford model indicates that their cross-section is dependent on the squared atomic weight (Z^2). However, the occurrence of channelling effect as the electrons travel through the sample requires a much more complex analysis for the reliable quantitative analysis of the HAADF signal (VAN AERT *et al.*, 2009).

The combination of optimized HRSTEM instrumental configuration and enhanced models for the evaluation of incoherent electron scattering allow novel approaches for the determination of chemical species on single-layered materials (LUYSBERG *et al.*, 2009), the heavy atoms impurities detection on nanowires (ALLEN *et al.*, 2008), and the nanocrystals 3D morphology assessment. (ZHANG *et al.*, 2010; LEBEAU *et al.*, 2010). An application of HAADF imaging for the characterization of CeO_2 nanocrystals is presented on Figure 2.4b. The depicted analysis approach (STROPPA *et al.*, 2011f) uses the HAADF signal intensity dependence with the atomic columns weight to retrieve the nanocrystals dimensions along the zone axis. The major advantage from this methodology is the possibility of 3D morphology characterization from a single HAADF-HRSTEM image.

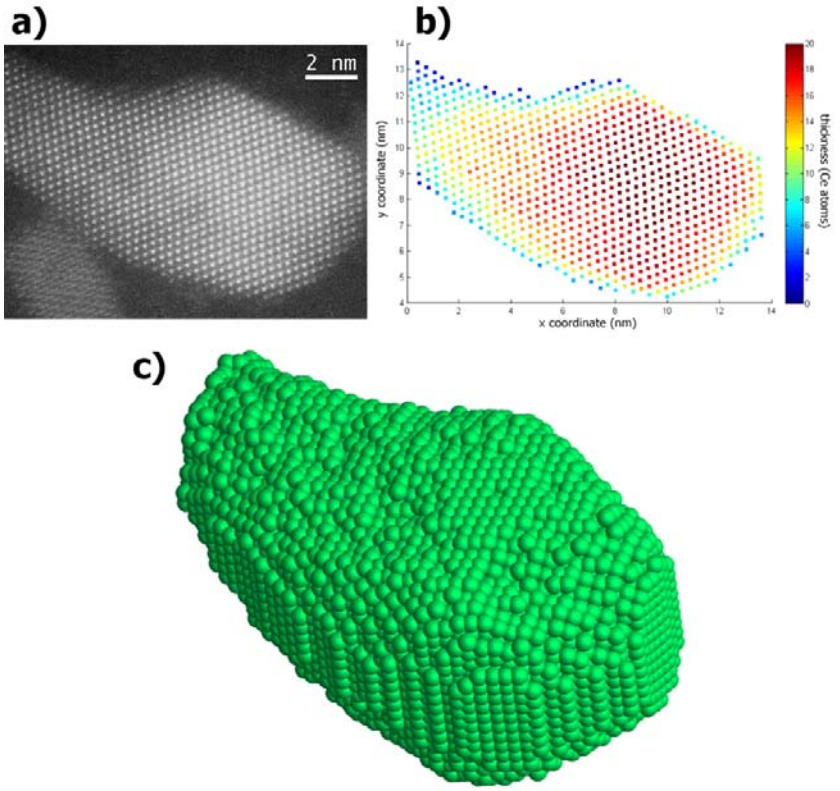

Figure 2.4b: a) As-obtained HAADF-HRSTEM image from a CeO_2 nanocrystal (300 kV, 80-230 mrad collection angle, 0.136 nm pixel size). b) The thickness map is obtained after the peaks integrated intensities histogram fitting (10 pixels integration mask, Multiple Gaussian fitting). c) 3D morphological model obtained after the reconstruction considering the CeO_2 crystallographic structure symmetry operations. The estimated error from the thickness evaluation is ± 1 atom.

The state-of-art HAADF-HRSTEM points toward the nanocrystals 3D reconstruction from either a set of images or from single images in particular cases where the nanostructures crystallographic symmetry can be effectively used in combination with the HAADF intensities profile. In this scenario, the enhanced analysis and simulation procedures applied to HAADF imaging and the improvements on the HAADF-tomography spatial resolution are likely to merge into an effective tool for the characterization of nanocrystals at the atomic scale (VAN AERT *et al.*, 2011). One of the main advantages of HAADF imaging mode in tomography is the diffraction contrast suppression at oriented zone axes (LU *et al.*, 2010).

The combination of HAADF characterization and the electron scattering analysis from other angular ranges has been increasingly applied on the extraction of additional features from crystalline samples. One example is the designed use of specific angle ranges for selecting high order Laue zones (HOLZ), which can provide information about atomic species ordering along the electron beam direction2 (HUANG *et al.*, 2010). In addition, the medium angle annular dark field (MAADF) has been applied to 3D defects analysis in STEM-tomography (SHARP *et al.*, 2008).

The information extraction from the low angle scattering analysis also presents novel possibilities, especially for the lighter atomic species. The combination of HAADF and annular bright field (ABF) allowed the direct imaging of oxygen (FINDLAY *et al.*, 2011a) and hydrogen (FINDLAY *et al.*, 2011b; ISHIKAWA *et al.*, 2011) atomic columns on Al_2O_3 and VH_2, respectively, and provided the unambiguous identification of chemical species on single-layered BN (KRIVANEK *et al.*, 2010).

Image simulation procedures represent an essential tool for the evaluation of obtained images and for the extraction of quantitative information from them. The state-of-art multislice image simulation procedures provides the identification of a single high-Z dopant atom (SOHLBERG *et al.*, 2004), the relative chemical composition evaluation (MOLINA *et al.*, 2009), and the dopant atoms location inside an oriented atomic column. (BORISEVICH *et al.*, 2006; MITTAL *et al.*, 2011).

High Resolution Spectroscopy

The HRSTEM spectroscopy techniques focus on the direct acquisition of quantitative information from a number of signals generated during the incident electron beam scanning over the sample. After proper collection, these signals can be used for the construction of properties maps that are presented together with HRSTEM imaging results. The simultaneous acquisition of high resolution images and spectroscopic signals allows the attainment of quantitative data with accurate localization, which is the main advantage of HRSTEM and represents a unique feature among the characterization techniques.

Among the signals generated during the interaction of an electron beam with matter, the characteristic X-rays and the low-angle scattered electrons are the most commonly used in spectroscopy analysis by HRSTEM. The characteristic X-rays detection is performed by an additional detector placed as close as possible to the sample in order to maximize the collection angle, as illustrated in Figure 2.4a. The acquisition of low-angle scattered electrons and the practice of electron energy-loss spectroscopy (EELS) require a spectrometer with dispersive optics in order to sort the collected electrons according to their energy loss due to inelastic interactions with the sample.

XEDS

Although X-ray energy dispersive spectroscopy (XEDS) technique on STEM already presented the possibility of atomic resolution spectroscopy by the use of an optimized experimental setup (D'ALFONSO *et al.*, 2010), the combined use of high brightness electron guns, Cs-corrected STEM microscopes (PENNYCOOK *et al.*, 2009), enhanced X-ray detectors (FEI, 2010), and the application of statistical methods on data treatment (BOSMAN *et al.*, 2006; WATANABE *et al.*, 2010) have recently pushed the atomic resolution characterization possibilities (CHU *et al.*, 2010; OHNISHI *et al.*, 2011). In addition to the above-mentioned collection angle optimization, these enhancements are mainly related to two other features that determine the XEDS analysis efficiency.

The first one is the compromise between the probe size and the effective beam current, which defines the spectroscopy spatial resolution and X-ray signal output, respectively. The use of Cs-correction hardware for the probe formation improvement allowed a more efficient beam focusing and the use of larger apertures due to reduced aberration influence, resulting thus in a larger effective electron density.

The second one is the relationship between the signal-to-noise ratio (SNR) and the dwell time for each collected spectrum, which plays a major role on the quantification accuracy/precision and on the required data acquisition time. The use of MSA on XEDS datasets containing numerous spectra with poor SNR allowed the quantitative analysis with enhanced accuracy and precision (BOSMAN *et al.*, 2006). The successful analysis from low SNR XEDS spectra points toward the reduction of the dwell time, providing thus a faster data acquisition and reduced sample degradation.

Figure 2.4c presents a successful atomic resolution chemical mapping from a $SrTiO_3$ sample by the use of XEDS - HRSTEM spectroscopy. The combined use of a high brightness field emission gun (FEG) and an optimized XEDS detection system are the key aspects for such measurement. In addition to the aforementioned advances which supported the atomic resolution spectroscopy, XEDS related techniques were substantially enhanced by an improved model that allows an accurate absolute quantification of the spectra by the use of more general standard samples (WATANABE *et al.*, 2006). Finally, the current characterization possibilities indicate that high resolution XEDS analysis may be applicable to almost all elements of the periodic table.

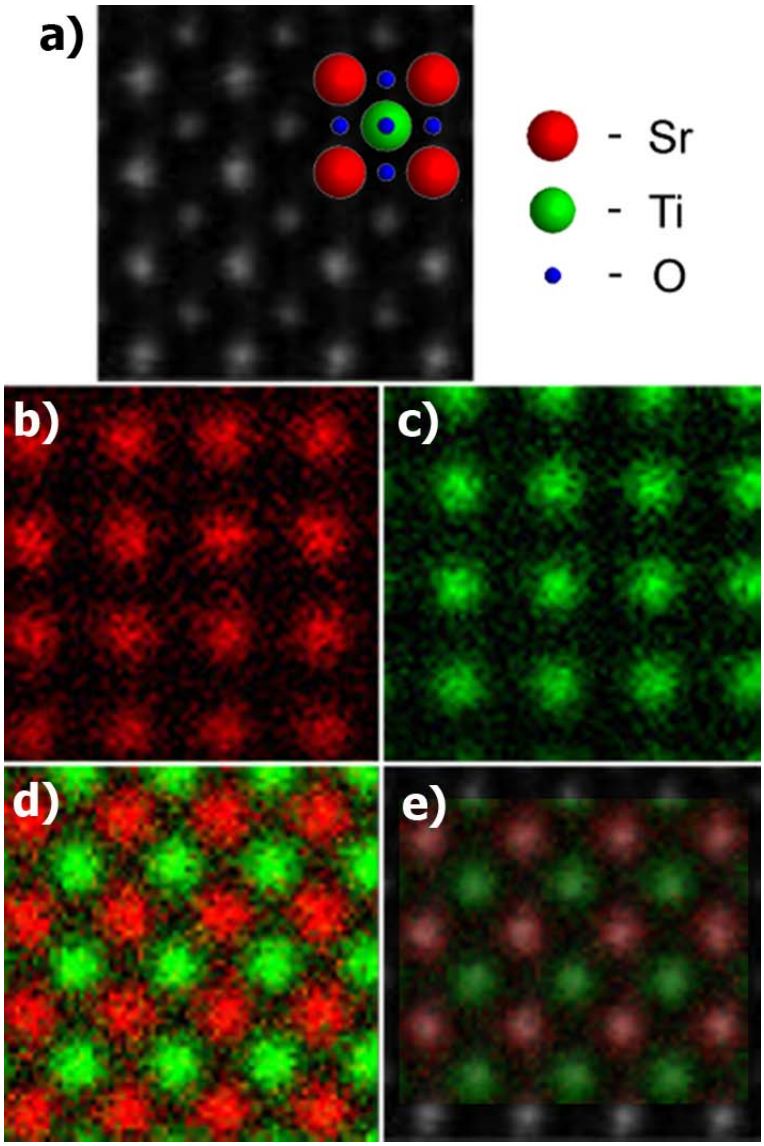

Figure 2.4c: Simultaneous atomic resolution imaging and XEDS spectroscopy. a) HAADF-HRSTEM image with a $SrTiO_3$ unit cell superimposed, b) Sr and c) Ti peaks integrated values were combined to generate the d) composition map. e) Its comparison with the high resolution HAADF image clearly presents the signal localization and points to the possibility of atomic columns XEDS spectroscopy. (Courtesy of FEI Company, results obtained by ChemiSTEM™ Technology) (FEI, 2010)

EELS

The analysis of low-angle scattered electrons on HRSTEM experiments provides a variety of information about localized interaction phenomena associated to inelastic electron scattering events (EGERTON, 2009)**.** Although analogous spectroscopy techniques based on synchrotron radiation, such as XAFS, are able to extract similar information, HRSTEM-EELS presents the possibility of probing such features with enhanced spatial resolution (HITCHCOCK *et al.*, 2008).

The identification and quantification of inelastic scattering events require thin samples in order to minimize effects from multiple scattering. The optimum sample thickness is determined by the interaction cross-section for the inelastic scattering event which is going to be analysed and is usually in the range of few nanometers (TANUMA *et al.*, 2011). Besides an adequate sample condition, the use of an adequate instrumental configuration is mandatory for the attainment of reliable HRSTEM-EELS results. The spatial resolution is not only determined by the probe size, but also by the stability of the electron probe and its propagation through the sample and by the inelastic scattering localization and multiple scattering effects (EGERTON, 2009). In addition, similarly to XEDS, the HRSTEM-EELS analysis requires the beam current maximization in order to improve the signal to noise ratio.

Regarding to the EELS spectra, the low-angle scattered electrons can be classified in three general groups according to their energy-loss. The Zero-loss peak (ZLP) comprises the electrons with null or negligible energy losses, the Low-loss (LLR) region include the electrons that presented energy losses up to 50 eV, and the Core-loss (CLR) region contains the electrons with energy losses higher than 50 eV. As the inelastic scattering signal intensity decreases as function energy-loss, the different above- cited groups have distinct magnitudes. For thin samples, reduction factors of 10^1 and 10^3 are expected on the peaks maximum intensity when comparing the ZLP to the LLR and to the CLR, respectively.

The ZLP comprises the transmitted beam component with minor energy transfer to sample, mostly given by the phonon interaction. The ZLP full width at half maximum (FWHM) refers to the beam energy spread which can be used as input on deconvolution algorithms to increase EELS energy resolution (ISHIZUKA *et al.*, 2003). In addition, an estimation of sample thickness

profile can be obtained by the comparison of the ZLP and LLR integrated signals (IAKOUBOVSKII *et al.*, 2008).

The LLR comprises the transmitted beam component which interacted with valence electrons, mostly as a plasmon generation interaction. Despite the signal delocalization (up to few nm) (MULLER *et al.*, 1995), the high resolution LLR spectroscopy is shown to be achievable with the use of adequate instrumental setup (LAZAR *et al.*, 2010). Among the applications of LLR spectroscopy are the dielectric function mapping (ZHANG *et al.*, 2010; ESPINOSA-MAGAN *et al.*, 2009), the bonding hybridization type mapping (BOSMANA *et al.*, 2009), the valence configuration determination (VERLEYSEN *et al.*, 2010), the optical properties and bandgap assessment (STÖGER-POLLACH, 2008), and the interface properties measurement (YAMAZAKI *et al.*, 2011). The combination of ZLP deconvolution and monochromator hardware has been successfully used on the surface plasmon mapping in metallic nanoparticles (NELAYAH *et al.*, 2007; ROSSOUW *et al.*, 20011). In addition, LLR analysis has shown to be applicable on cryo-microscopy for water measurement on biological materials (YAKOVLEV *et al.*, 2010) and on gas phase analysis for the quantitative analysis of gas mixtures (CROZIER *et al.*, 2010).

The CLR comprises the transmitted beam component which undergone interaction with core electrons. As these interactions are much more localized than LLR (typically few Å) (MULLER *et al.*, 1995), atomic resolution chemical maps analysis are feasible by CLR scattering signal analysis. However, an optimized experimental setup is required in order to obtain atomic resolution imaging and spectroscopy simultaneously (KIMOTO *et al.*, 2008).

The spectral imaging using selected energy intervals has been successfully applied to identify atomic columns composition on interfaces (KIMOTO *et al.*, 2007; MULLER *et al.*, 2008; COLLIEX *et al.*, 2010) and on crystalline defects (KURATA *et al.*, 2009) with atomic resolution. This methodology has been also used to deal with challenging problems in materials chemistry, such as chemical composition mapping of individual Ce-Zr pyrochlore catalytic nanocrystals with atomic resolution. The combined results from HAADF-HRSTEM imaging and HREELS spectroscopy for the chemical mapping of individual $Ce_2Zr_2O_8$ nanocrystals is depicted in Figure 2.4d. (TRASOBARES *et al.*, 2011).

Although atomic resolution chemical mapping is still a developing field, few CLR analysis approaches have presented great perspectives on materials characterization. Some examples are the bond type mapping on BN complex (ARENAL *et al.*, 2008) and the valence mapping on Co-doped ZnO nanostructures (WANG *et al.*, 2010b).

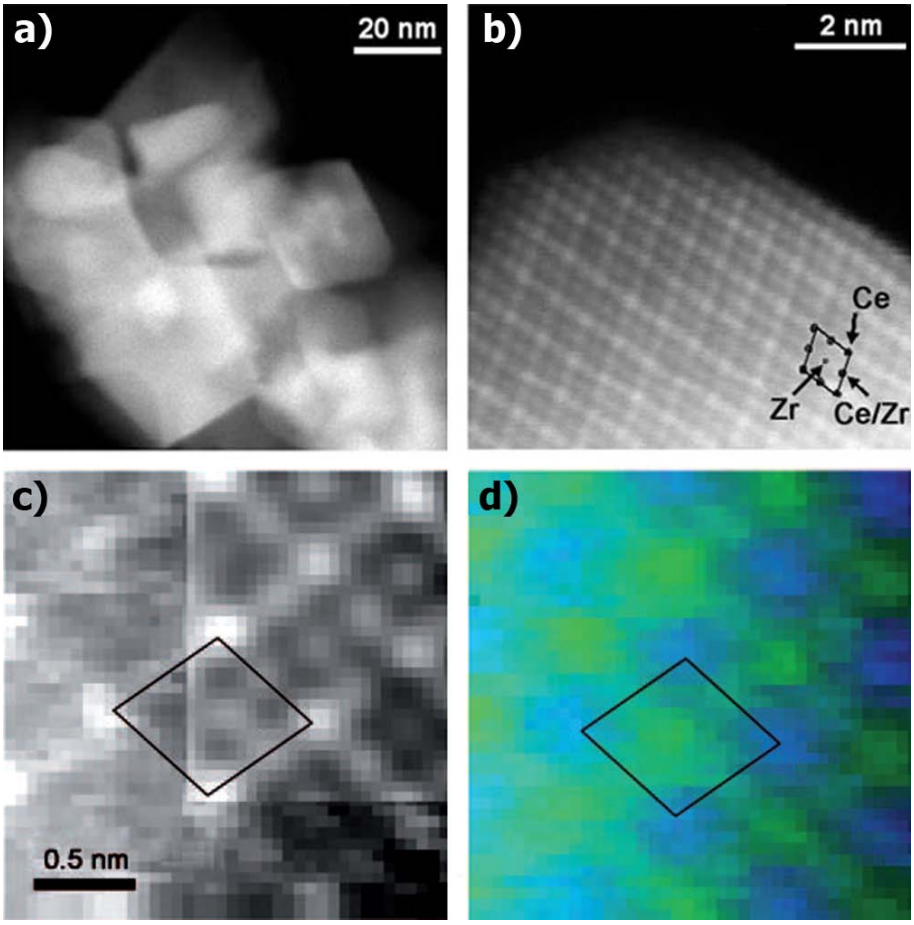

Figure 2.4d: a) HAADF image of the $Ce_2Zr_2O_8$ sample. b) HAADF-HRSTEM image from a nanocrystal. The atomic positions are highlighted according to a superstructure model. c) HAADF signal acquired simultaneously with the EELS signal. The inset image corresponds to the experimental data treated with a low-pass filter. d) Experimental atomic resolution chemical map. The quantification was performed by the Zr-$M_{2,3}$ and Ce-$M_{4,5}$ EELS peaks integration. The color map indicates the Zr (green) and Ce (blue) positions. (Adapted from (TRASOBARES *et al.*, 2011).

Novel approaches on HRSTEM

In addition to the advances on more usual imaging and spectroscopy techniques, some methodologies associated to HRSTEM evolve towards the nanomaterials atomic resolution characterization. The following subsections present an overview on them.

Cathodoluminescence

In recent years, the growing importance of nanostructured semiconductors, such as III-V nanowires, is renewing the interest in cathodoluminescence (CL) (LIM *et al.*, 2009). Instrumentation advances increased the achievable spatial and spectral resolution to about 1 nm and 5 meV, respectively (ZAGONEL *et al.*, 2011). In addition, improvements can be expected in near future due to the advantages from low voltage STEM featuring spherical and chromatic aberration correctors. Moreover, the development of efficient CL detectors tends to push the current measurement limits to a new level.

The effective spatial and spectral resolutions on CL measurements associated to STEM are greatly dependent and limited by sample features. This is due to the secondary effect based on the recombination of electron-hole pairs excited by the electron beam, which results in CL signal delocalization (GUSTAFSSON, 2010). Additionally, the CL peaks can also be arbitrarily broad depending on the sample band structures as seen on standard photoluminescence experiments.

Figure 2.4e shows a characterization of GaN quantum disks (QDisk) and AlN barriers stack grown in a nanowire by the combined use of HAADF-STEM imaging and CL spectroscopy (ZAGONEL *et al.*, 2011). Similarly to EELS, the CL spectrum image is obtained by scanning the electron probe and acquiring simultaneously both HAADF signal and CL spectrum for each pixel. Single QDisks can be readily distinguished on the image HAADF images and, by selecting different wavelengths in the spectrum image, the light emission from single QDisks can be resolved. A correlation between QDisks size and emission energy can be extracted for each QDisk (ZAGONEL *et al.*, 2011).

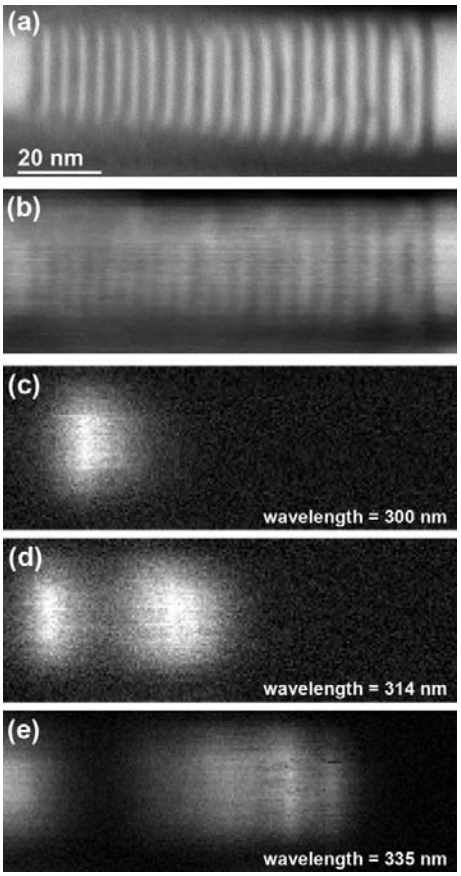

Figure 2.4e: a) HAADF-HRSTEM image showing the QDisk stack in the middle of the NW. b) HAADF image acquired simultaneously with the CL spectrum image. c) to e) show energy filtered images obtained from the spectrum image at 300, 314 and 335 nm, respectively, which correspond to energies values below the GaN band gap. (Adapted from (ZAGONEL *et al.*, 2011))

Scanning Confocal Electron Microscopy

The nanostructures 3D morphology reconstruction is a current challenge on materials characterization, especially when high resolution information on chemical species segregation is required (STROPPA *et al.*, 2009, STROPPA *et al.*, 2011d). Besides the HRSTEM tomography (VAN AERT *et al.*, 2011) and the HAADF-HRSTEM images reconstruction based on the recorded intensities (LEBEAU *et al.*, 2011; STROPPA *et al.*, 2011f), Scanning Confocal Electron Microscopy (SCEM) on STEM mode is shown to be a suitable technique for extracting structural information along the imaging zone axis.

The SCEM technique (MITSUISHI *et al.*, 2010) is based on the analysis of electron microscopy images acquired under different defocus, either by the change on the condenser lens excitation or the controlled change on the sample positioning (TAKEGUCHI *et al.*, 2008).

Theoretical studies (BORISEVICH *et al.*, 2006; EINSPAHR *et al.*, 2011) supported by image simulation procedures and experiments using different imaging modes on STEM regime (XIN *et al.*, 2009; HASHIMOTO *et al.*, 2011) indicate that SCEM technique can provide spatial resolution up to 1 nm along the zone axis and can unveil the depth localization of heavy atoms (Bi) on a lighter matrix (Si). The SCEM state of art presents the high resolution depth profile analysis for nanocrystals (XIN *et al.*, 2009; XIN *et al.*, 2010) by the use of STEM optimized optical systems including Cs-correction. Further advance is expected by the use of novel Cc-correction hardware and improved analysis methods (HOVDEN *et al.*, 2010).

Diffraction mapping

In addition to the imaging and spectroscopy approaches, STEM experimental configuration can be applied for the crystalline structure mapping with high spatial resolution by the analysis of local diffraction patterns. Although it is analogous to TEM Selected Area Diffraction technique, the STEM mode with a parallel electron beam provides the mapping possibility during the scan procedure and a higher spatial resolution can be achieved (GANESH *et al.*, 2010). Similarly, the Convergent-Beam Electron Diffraction (CBED) mapping can be performed on STEM by altering the optical system in order to attain a small and convergent probe (SEYRING *et al.*, 2011).

High resolution applications of diffraction mapping techniques include the local Ge concentration determination in Si/SiGe nanostructures (RUH *et al.*, 2010), the lattice distortions evaluation on InP nanowires containing an axial screw dislocation (TIZEI *et al.*, 2011), and the strain mapping in MOSFET devices (UESUGI *et al.*, 2011; DIERCKS *et al.*, 2011). In addition, improved grain orientation mapping on polycrystalline materials has been demonstrated by the use of precession-enhanced electron diffraction (MOECK *et al.*, 2011). Moreover, the diffraction analysis on STEM mode is currently providing new information about the electron scattering process on crystalline materials (KOURKOUTIS *et al.*, 2011; KIMOTO *et al.*, 2011).

Outlook

Recent advances on HRSTEM present a number of unique possibilities for materials characterization. This is easily noticed as the combination of high resolution imaging and spectroscopy becomes more usual for the extraction of chemical and structural information of a wide range of nanostructured systems.

In this scenario, the support provided by HRSTEM tools is shown to be invaluable for solving a handful of question on various fields within materials science, chemistry and physics. At the same time, great perspectives are drawn by the current progresses on related hardware and analysis techniques, whose point out HRSTEM will consolidate its condition as an essential tool for nanoscience and nanotechnology.

Acknowledgement

The authors acknowledge the financial support of the Brazilian research funding agencies FAPESP, CNPq and FINEP; the German research funding agency DAAD. The authors would also like to thank the Ernst Ruska Centre staff at Forschungszentrum Jülich and the STEM group staff at Université Paris-Sud for the fruitful discussions and scientific support.

3. Análises Quantitativas pelo uso de HRTEM

3.1. Metodologia para Avaliação da Segregação de Dopantes em Nanocristais

A descrição de sistemas nanostruturados constitui um desafio relevante para as metodologias de caracterização de materiais, sendo muitos dos avanços instrumentais neste ramo impulsionados pela melhoria da resolução espacial nas análises realizadas (BRUNDLE *et al.*, 1992). Dada a necessidade da extração de informações quantitativas com resolução atômica, o contexto do modelamento de nanocristais apresenta requerimentos extremos aos métodos de caracterização de materiais.

As limitações experimentais na caracterização quantitativa com alta resolução se apresentam ainda mais relevantes para a análise de sistemas nanocristalinos dopados. Em tal contexto, o modelamento de nanocristais requer informações acerca da distribuição de átomos dopantes com alta resolução para que seja possível uma avaliação mais criteriosa acerca da morfologia e da distribuição de energia superficial.

Apesar dos recentes avanços na instrumentação e nas metodologias de análise de diversas técnicas de caracterização de materiais, especialmente as associadas à HR(S)TEM e apresentadas no Capítulo 2, o mapeamento de espécies atômicas com resolução atômica ainda é severamente limitado e requer a utilização de técnicas de caracterização complementares e o extensivo suporte de cálculos teóricos. Adicionalmente, tal mapeamento em nanocristais apresenta restrições mais rigorosas referentes à estabilidade da amostra durante a medida. Dois pontos críticos neste aspecto são a estabilidade mecânica do substrato porta-amostra e a estabilidade dos nanocristais, sendo deste modo restritas metodologias que envolvam varreduras de longa duração e/ou com alta densidade de energia incidente sobre a amostra.

O Capítulo 3.2 apresenta de uma metodologia indireta proposta para a extração de informações acerca da segregação de dopantes pela análise da morfologia dos nanocristais suportada por HRTEM e simulações de imagens. A consideração inicial utilizada é a de que a morfologia esperada para o equilíbrio termodinâmico pode descrever o comportamento de determinados sistemas nanocristalinos obtidos em condições estritas.

De maneira geral, a morfologia de nanocristais obtidos por rotas *bottom-up* é definida pelas condições termodinâmicas e cinéticas do ambiente de crescimento. Em respeito às condições termodinâmicas, é esperado que o sistema evolua até atingir o valor mínimo de energia livre de Gibbs (G), definida para temperatura e pressão constantes na Equação 3.1a.

$$G = H - TS, \qquad \textbf{Equação 3.1a}$$

sendo H a entalpia, T a tempertura e S a entropia do ambiente de síntese e crescimento. A componente entálpica inclui as contribuições da composição química, da estrutura cristalina e de parte significativa da energia superficial, enquanto a componente entrópica inclui a contribuição energética referente à distribuição de espécies atômicas e da segregação de fases cristalinas.

As condições cinéticas atuam como fatores limitantes em relação à evolução do sistema em direção à minimização de energia livre de Gibbs esperada para o equilíbrio termodinâmico. Inclusas nos fatores cinéticos estão as contribuições de solventes, de espécies iônicas presentes em solução, da concentração dos precursores e a de suas mobilidades no meio reacional.

A primeira aproximação adotada no modelo proposto para a descrição da segregação de dopantes em nanocristais é a de que o fator determinante na morfologia dos nanocristais é dado pela energia superficial. Neste sentido, de acordo com o teorema de Wulff (WULFF, 1901), a configuração geométrica de um sistema em equilíbrio termodinâmico será dada pela minimização da energia superficial total. Tal consideração restringe o uso da metodologia para sistemas nos quais os fatores cinéticos sejam predominantes e cujas contribuições não possam ser aproximadas em termos de variação da distribuição de energia superficial.

A base da metodologia proposta é a comparação do facetamento de nanocristais reais, caracterizado por HRTEM e simulações de imagem, com a geometria de equilíbrio segundo o teorema de Wulff, que define a morfologia poliédrica por meio facetas localizadas a distâncias proporcionais a sua densidade de energia superficial. Deste modo, a morfologia dos nanocristais é diretamente correlacionada com a distribuição de energia superficial de suas facetas, que por sua vez é dependente da família cristalográfica das facetas e da concentração de espécies dopantes.

A segunda condição presente na metodologia proposta é a possibilidade da avaliação do sistema nanocristalino em relação à dependência da densidade de energia superficial para diferentes famílias cristalográficas em função da concentração de átomos dopantes. A escolha do sistema Sb:SnO_2 e da utilização de cálculos *ab initio* foi devida à possibilidade da descrição do comportamento de crescimento de nanofios de SnO_2 a partir de cálculos similares para a distribuição de energia superficial (BELTRAN *et al.*, 2003). Os cálculos *ab initio* presentes nesta tese foram realizados pelos colaboradores da UJI, A. Beltran e J. Andres, enquanto a síntese dos nanocristais de Sb:SnO_2 foi realizada pelos colaboradores do LIEC, T. G. Conti e R. O. da Silva.

Duas características inerentes ao modelo de cálculo *ab initio* foram consideradas no desenvolvimento da metodologia proposta. A primeira foi a realização de cálculos *in vacuo*, sendo desta forma desconsideradas as interações das superfícies com o meio reacional, e a segunda foi a utilização do modelo de *bulk* truncado, no qual a energia superficial é avaliada a partir de estruturas semi-infinitas incluindo cortes referentes às famílias cristalográficas pertinentes tendo em vista o facetamento experimentalmente observado.

Embora os valores absolutos obtidos para as densidades de energia superficial calculadas sejam inapropriados para uso direto devido à estabilização de superfície pelo meio reacional, a metodologia proposta emprega a razão entre os valores calculados para a correlação com a razão entre as distâncias entre facetas. Deste modo, sendo a síntese do sistema Sb:SnO_2 realizada sem a presença de surfactantes de alta especificidade e as facetas avaliadas não apresentarem diferenças extremas em relação à polaridade, a utilização da razão entre os valores obtidos pelos cálculos *in vacuo* foi considerada uma aproximação válida para a avaliação apresentada. De modo similar é justificada a adequação do uso de modelos de *bulk* truncado, dado que a contribuição de arestas e vértices é reduzida ao ser considerada a razão entre as energias superficiais calculadas.

Uma discussão mais elaborada a respeito da aplicabilidade dos cálculos *ab initio* para energia superficial no suporte da metodologia proposta é apresentada no Capítulo 3.4. Contudo, não existe nenhuma restrição *a priori* em relação ao uso de demais métodos que possam apresentar a correlação entre a energia superficial para diferentes planos cristalográficos em função da concentração de espécies dopantes. Os detalhes da metodologia proposta e do modelo de cálculo são apresentados nos Capítulo 3.2 e no Anexo B.1.

3.2. Unveiling the Chemical and Morphological Features of Sb:SnO_2 Nanocrystals

Unveiling the Chemical and Morphological Features of Sb-SnO_2 Nanocrystals by the Combined Use of High Resolution Transmission Electron Microscopy and *ab initio* Surface Energy Calculations (STROPPA *et al.*, 2009)

Daniel G. Stroppa, Luciano A. Montoro, Armando Beltran, Tiago G. Conti, Rafael O. da Silva, Juan Andres, Elson Longo, Edson R. Leite, Antonio J. Ramirez.

Publicado na revista *Journal of the American Chemical Society*, 131, 14544-14548, **2009**.

Abstract

Modeling of nanocrystals supported by advanced morphological and chemical characterization is a unique tool for the development of reliable nanostructured devices, which depends on the ability to synthesize and characterize materials on the atomic scale. Among the most significant challenges in nanostructural characterization is the evaluation of crystal growth mechanisms and their dependence on the shape of nanoparticles and the distribution of doping elements. This paper presents a new strategy to characterize nanocrystals, applied here to antimony-doped tin oxide (Sb-SnO_2) (ATO) by the combined use of experimental and simulated high resolution transmission electron microscopy (HRTEM) images and surface energy *ab initio* calculations. The results show that the Wulff construction can not only describe the shape of nanocrystals as a function of surface energy distribution but also retrieve quantitative information on dopant distribution by the dimensional analysis of nanoparticle shapes. In addition, a novel three-dimensional evaluation of an oriented attachment growth mechanism is provided in the proposed methodology. This procedure is a useful approach for faceted nanocrystal shape modeling and indirect quantitative evaluation of dopant spatial distribution, which are difficult to evaluate by other techniques.

Introduction

The development and implementation of new applications for nanostructured materials is, in many cases, closely linked to the ability to describe, model, and control nanocrystal morphology during the synthesis process, especially by the bottom-up approach (LEITE *et al.*, 2004). Hence, the successful application of nanocrystals as building blocks for the development of novel materials requires control over the shape and the assembly of those nanocrystals. Crystal modeling (WANG *et al.*, 2003; BARNARD *et al.*, 2006, 2008) is therefore a unique tool due to its wide application in the prediction of crystal shapes, growth process, and the resulting properties of an unlimited number of systems.

A key subject in materials chemistry and a major issue in crystal modeling, particularly for nanocrystals synthesis, is the strong influence of the chemical environment and synthesis parameters that determine the surface chemistry and crystal morphology. Several cases reported in the literature show that organic and/or inorganic additives (PUNTES *et al.*, 2001; POLLEUX *et al.*, 2005; YANG *et al.*, 2008) and solvents (GRUBBS, 2007) can determine crystal growth and final morphology. Those studies indicate that additives act as selective poisoning agents, shifting the configuration of the nanocrystal surface energy, defining crystal habit and preferential growth directions. However, the role of synthesis parameters on the resulting nanocrystal features is complex and still not fully understood.

In recent years, advanced tools (HANSEN *et al.*, 2002; ARSLAN *et al.*, 2005; JINSCHEK *et al.*, 2008; SCHAMM *et al.*, 2008; HUANG *et al.*, 2009) have been developed for nanocrystal characterization in order to obtain accurate chemical, structural, and morphological information, such as crystallographic habit, surface chemistry, and growth mechanisms from self-assembled arrangements. Although a number of techniques based on X-ray (HUANG *et al.*, 2009; (RENAUD *et al.*, 2003), scanning probe microscopy (MORALES *et al.*, 2008), and transmission electron microscopy (TEM) (JIA *et al.*, 2004a; FERRER *et al.*, 2007; MULLER *et al.*, 2008) have been successfully applied to retrieve compositional and morphological information about nanostructures, several challenges still remain, especially with regard to three-dimensional reconstruction and chemical mapping.

In this work we present a novel approach based on high resolution transmission electron microscopy (HRTEM) characterization and surface energy *ab initio* calculation (BELTRAN *et al.*, 2003) (atomistic simulation). By combining information from HRTEM images of faceted nanocrystals, Wulff construction (HERRING, 1951; MARKS, 1983), and surface energies obtained by atomistic simulation for selected facets, the 3D morphological and compositional features of ATO nanocrystals and their growth mechanisms were elucidated.

Among the transparent conductive oxides (TCO) (MINAMI, 2005), SnO_2 and its doped forms, such as FTO (fluorine-doped SnO_2) (RAKHSHANI *et al.*, 1998), ITO (indium-doped SnO_2) (GRANQVIST *et al.*, 2002) and ATO (antimony-doped SnO_2) (TERRIER *et al.*, 1997), have received special attention due to their unique electro-optical properties with applications in catalysis (KOWAL *et al.*, 2009; LEE *et al.*, 2008), electronics (DASGUPTA *et al.*, 2008), optics (LUFF *et al.*, 1997), and as gas sensors (WANG *et al.*, 2008). The Antimony-doped Tin Oxide (Sb:SnO_2) (ATO) nanocrystalline system (DA SILVA *et al.*, 2009) was chosen for this work because of the limitations for its comprehensive characterization by conventional and advanced techniques. These limitations are due to the reduced dimensions, small difference between the atomic weight of Sn and Sb, and the structural and chemical instability of these nanoparticles, which preclude long-duration TEM and/or scanning transmission electron microscopy (STEM) analyses, for example. However, the proposed methodology should not be seen as exclusive to the study of ATO system, for it can also be applied to other faceted-nanostructured crystalline systems.

Experimental Section

The ATO nanocrystals were synthesized in a glovebox under a controlled atmosphere by the benzyl alcohol method (NIEDERBERGER *et al.*, 2006b). For an $18\%_{atom}$ Sb doping concentration (nominal composition), a total of 5.47 mmol of $SnCl_4$ (99.995%) and 1.01 mmol of $SbCl_3$ (99.99%) were stirred in a vessel with 40 mL of benzyl alcohol, after which the reaction vessel was removed from the glovebox and heated at 150ºC for about 48h in a silicone bath. ATO nanoparticles were collected by centrifugation, washed twice with tetrahydrofuran, and stocked in a concentrated tetrahydrofuran (THF) dispersion.

TEM samples were prepared by dripping diluted ATO solution onto copper grids covered with a thin amorphous carbon film (~5 nm). HRTEM characterization was performed on a JEM-3010 URP TEM at 300 kV with a LaB_6 electron gun and equipped with a 1024 × 1024 thermoelectrically cooled charged-couple device (CCD) camera and a X-ray energy-dispersive spectroscopy (XEDS) detector.

Wulff construction (HERRING, 1951; MARKS, 1983) was applied to build theoretical crystals by using the *ab initio* calculated surface energies and the SnO_2 $P4_2/mnm$ crystal structure. HRTEM multislice simulated images of theoretical ATO nanocrystals were obtained by use of JEMS software (STADELMANN, 1987).

Surface energy calculations (BELTRAN *et al.*, 2003) for ATO nanocrystals were performed with the CRYSTAL06 program package. Oxygen atoms were described by the standard 6-31G* basis sets and the Tin and Antimony centers in the PS-21G* scheme (DOVESI *et al*, 2005), where PS stands for Durand-Barthelat's nonrelativistic large effective core potential (DURAND *et al.*, 1975). Becke's three-parameter hybrid nonlocal exchange functional (BECKE, 1993) combined with the Lee-Yang-Parr gradient-corrected correlation functional (B3LYP) (LEE *et al.*, 1988) was used.

Full optimization of the cell parameters (a and c) and internal coordinate (u) for the bulk SnO_2 was carried out. The low index (110), (101), (100), and (001) surfaces were modeled by unreconstructed (truncated bulk) slab models by use of the calculated equilibrium geometry. Because these surfaces have a different number of atoms in each layer, the low-index surfaces were modeled with different thicknesses in the *z*-direction but periodic in *x*- and *y*-directions. After the corresponding convergence test on the undoped systems, slab models containing nine SnO_2 layers for the (110), (100), and (101) surfaces and eleven layers for the (001) surface were selected. For the models used here, the top and bottom planes are equivalent in symmetry so the substitution of Sn for Sb atoms was done on both sides of each slab model. Supercells were used to model the lower percentages of doping (~7%). A complete relaxation of all the atoms in each model was performed.

Results

X-ray diffraction (XRD) analysis of synthesized ATO indicated highly crystalline nanocrystals with SnO_2 cassiterite tetragonal structure (see Appendix B – supporting information). No other crystalline phases were revealed by the XRD analysis, indicating the complete incorporation of Sb in the SnO_2 structure. The broad XRD peaks indicate small crystalline domains with dimensions of approximately 5 and 4 nm for (110) and (101) planes, respectively, as evaluated by Scherrer's equation, suggesting the presence of elongated crystals.

HRTEM images show that the nonaqueous synthesis route produces highly dispersed and crystalline ATO nanoparticles, as presented in Figure 3.2aa. The evaluation of size distribution shown in Figure 3.2ab reveals elongated particles with a mean length of 4.2 nm, mean width of 3.2 nm and mean aspect ratio of 1.3.

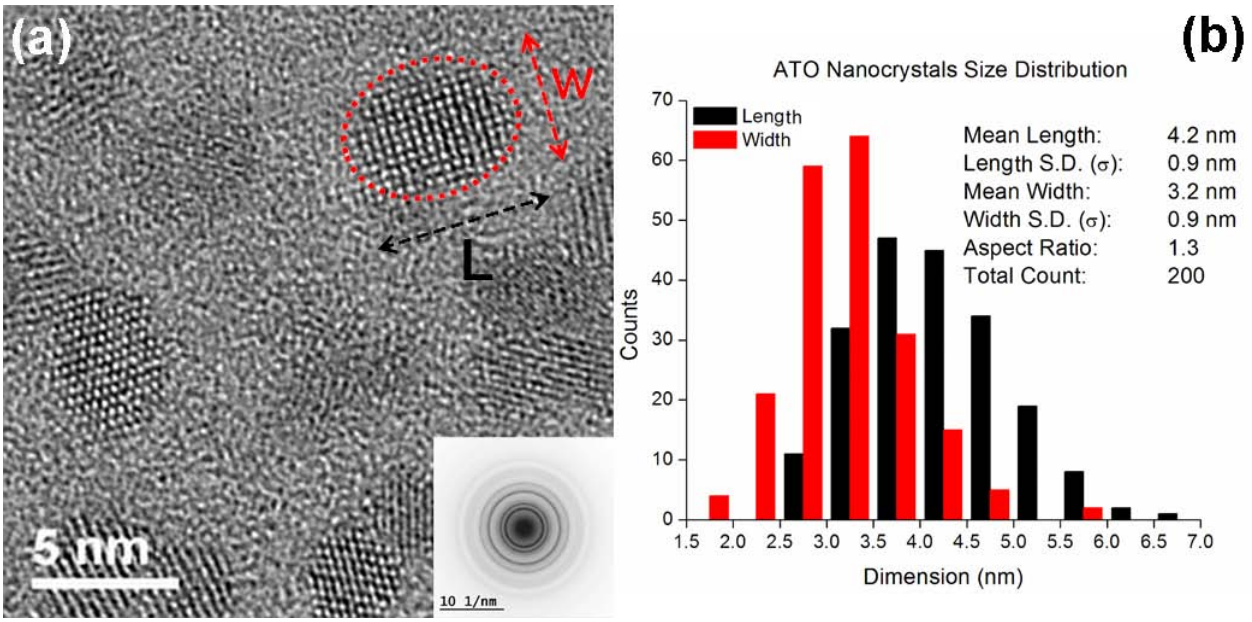

Figure 3.2a: Typical HRTEM image of ATO nanocrystals and size distribution histogram. (a) HRTEM image of representative ATO ($Sb:SnO_2$) nanocrystals, where the inset shows the electron diffraction pattern and the dashed lines exemplify the measured length and width. (b) Size distribution histogram, where the red and black bars represent the width and length, respectively. The inset text indicates the mean sizes with their respective standard deviations and the aspect ratio for a total count of 200 particles.

The electron diffraction pattern of ATO nanoparticles depicted in Figure 3.2a also indicates a SnO_2 cassiterite tetragonal structure with $P4_2/mnm$ spatial group symmetry. Measured interplanar distances are in excellent agreement with the XRD results and the previously reported crystallographic characterization (MCCARTHY *et al.*, 1989).

The HRTEM analysis of ATO samples indicated two relevant morphological aspects: (a) the formation of faceted nanocrystals, and (b) the occurrence of oriented attachment as the growth mechanism for a significant number of particles, as illustrated in Figures 3.2ba, 3.2bb. and 3.2bc shows a representative HRTEM image of ATO samples and the fast Fourier Transform (FFT), which indicates the particle orientation along the [111] zone axis. An HRTEM multislice simulation of SnO_2 $P4_2/mnm$ crystal structure under the experimental image conditions is shown in Figure 3.2bc (dashed box). It is important to point out that the reported morphological features of the ATO nanocrystals are directly related to the presence and distribution of Sb dopant. SnO_2 nanocrystals obtained by a similar synthetic route do not present a faceted shape (BA *et al.*, 2005).

Soluble ions play a major role during crystallization, particularly in crystal shape, as previously reported for $CaCO_3$ (TITILOYE *et al.*, 1993). This effect is explained by the reduction of particle surface energy due to the substitution of native surface ions by foreign ones. The analyses suggest that the addition of Sb modifies the SnO_2 surface energy, leading to crystal shape modifications. In order to validate this assumption, the Wulff construction (HERRING, 1951; MARKS, 1983) was chosen as the model to evaluate ATO nanocrystal faceting based on surface energy *ab initio* calculations for different exposed crystallographic planes and Sb concentrations.

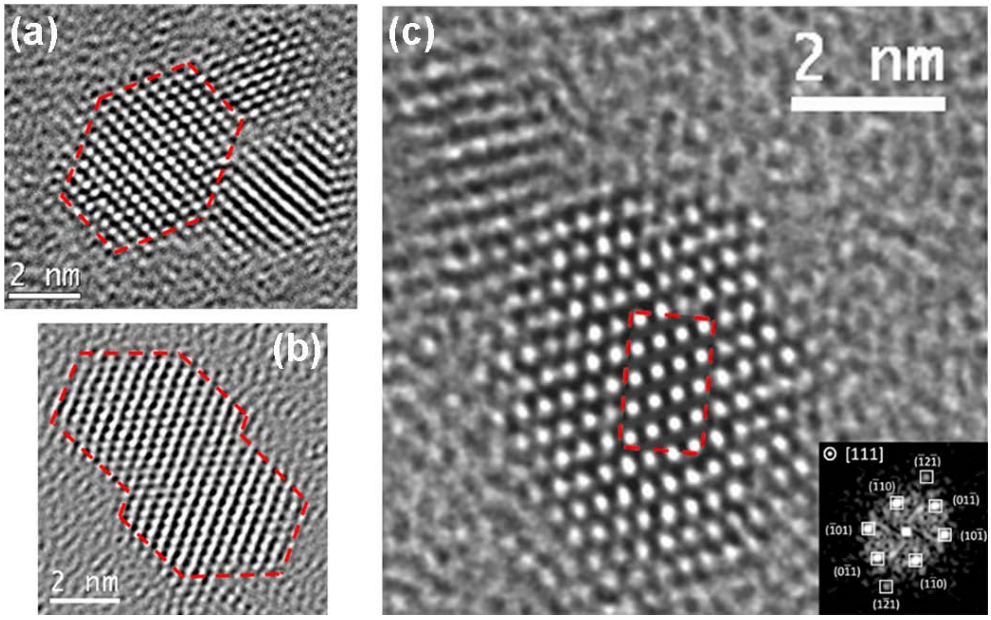

Figure 3.2b: HRTEM images of ATO nanocrystals. (a,b) HRTEM images of faceted ATO (Sb-SnO_2) nanocrystals, showing oriented attachment growth. The red dashed lines highlight the projected facet boundaries. (c) HRTEM image of faceted ATO nanocrystal. The dashed red box indicates the superimposed image of the simulated HRTEM multislice. (Inset) Fast Fourier Transform, which indicates the particle alignment along the [111] zone axis.

According to Wulff's rule (WULFF, 1901), which determines the equilibrium crystal shape by minimizing surface energy for a given enclosed volume, the crystal morphology can be thermodynamically predicted by use of the surface energy of different facets. Thus, the crystal shape can be derived from a geometrical construction where the distance of the facet from an arbitrary origin is proportional to the respective crystallographic plane surface energy. The *ab initio* calculated surface energies for different crystalline planes and Sb concentrations are presented in Figure 3.2c, as well as the Wulff construction for different Sb contents. Due to the substitutional character of Sb in the ATO structure, the dopant concentration is quantized according to available exposed sites.

The results of the calculations shown in Figure 3.2c indicate that the surface energy for different exposed crystalline planes is highly dependent on the Sb concentration, leading to dependence of the nanocrystal habit on the dopant content. In addition, preferential segregation

toward different exposed crystalline planes can be inferred due to modifications of the nanocrystal habit as a function of dopant content, especially in highly doped systems. Therefore, both qualitative and quantitative information can be extracted from HRTEM images of faceted and crystalline nanosystems by evaluating the aspect ratio for different crystalline planes within the Wulff construction.

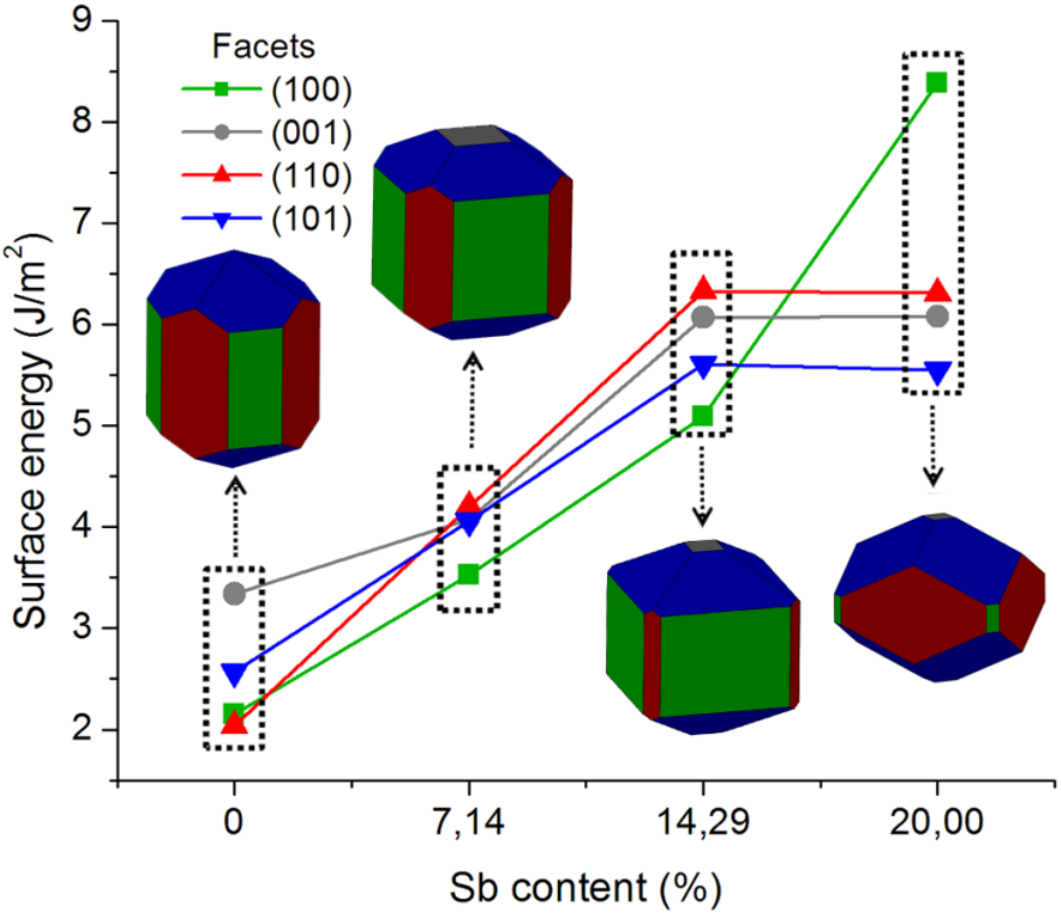

Figure 3.2c: Surface energies for different Sb contents and Wulff constructed nanocrystals for each dopant content considering a homogeneous Sb distribution. The figure shows the *ab initio* calculated surface energies for the selected crystalline planes with different Sb contents. The facets on the constructed Wulff crystals are indicated by a color code.

Based on projected two-dimensional HRTEM image of ATO nanocrystals observed along the [111] zone axis, a hypothetical nanocrystal shape is proposed. The actual HRTEM images

provide the exact number of atomic columns on the oriented ATO nanocrystals and hence provide precise information regarding their projected dimensions. In this specific case, the exposed (100), (110), (111), and (101) facets were successfully reconstructed on the basis of HRTEM image of the particle due to the [111] oriented tetragonal crystalline structure. Only the possibly exposed (001) facet could not be directly evaluated because it does not substantially modify the projected dimensions of the ATO nanoparticle HRTEM image when observed along the [111] zone axis. However, simulated HRTEM images of the proposed nanocrystal atomic arrangement provide information about all the facets considered (see Appendix B – supporting information). Thus, it is possible to infer the habit of the actual ATO nanocrystals from an iterative process based on the combined use of HRTEM characterization, Wulff construction, and HRTEM multislice image simulation.

Figures 3.2da and 3.2db present the proposed ATO nanocrystal atomic arrangement with a superimposed Wulff construction and the multislice simulated HRTEM image (STADELMANN, 1987), respectively. Figures 3.2dc and 3.2dd compare the nanocrystal multislice simulated HRTEM image (c) and the experimental image (d). The remarkable agreement between the images supports the proposed nanocrystal habit.

Dimensional analysis of the proposed ATO nanocrystal indicates the surface energy ratio for the different exposed crystallographic planes of the experimental ATO nanocrystals. Therefore, a comparison of these surface energy values and the *ab initio* calculated ones provides the dopant content on those exposed facets. Table 3.2a presents the absolute distances of the proposed Wulff-constructed facets of the ATO nanocrystal, the surface energy values, and the estimated Sb content for the exposed crystalline planes. Both surface energy and dopant content of each facet were evaluated by the use of Wulff construction dimensions, mean Sb content retrieved by XEDS measurements, and *ab initio* calculated surface energies. A detailed description of this methodology is presented on the supporting information (see Appendix B – supporting information). Finally, the estimated Sb concentrations of the exposed facets of the proposed ATO nanocrystal were quantized on the basis of available Sn atomic sites on these crystallographic planes. This evaluation of the Sb content on the exposed facets, presented in Table 3.2a, indicates a preferential segregation of Sb toward the (100) and (110) facets and a dopant depletion at the (001) facets of the ATO nanocrystals.

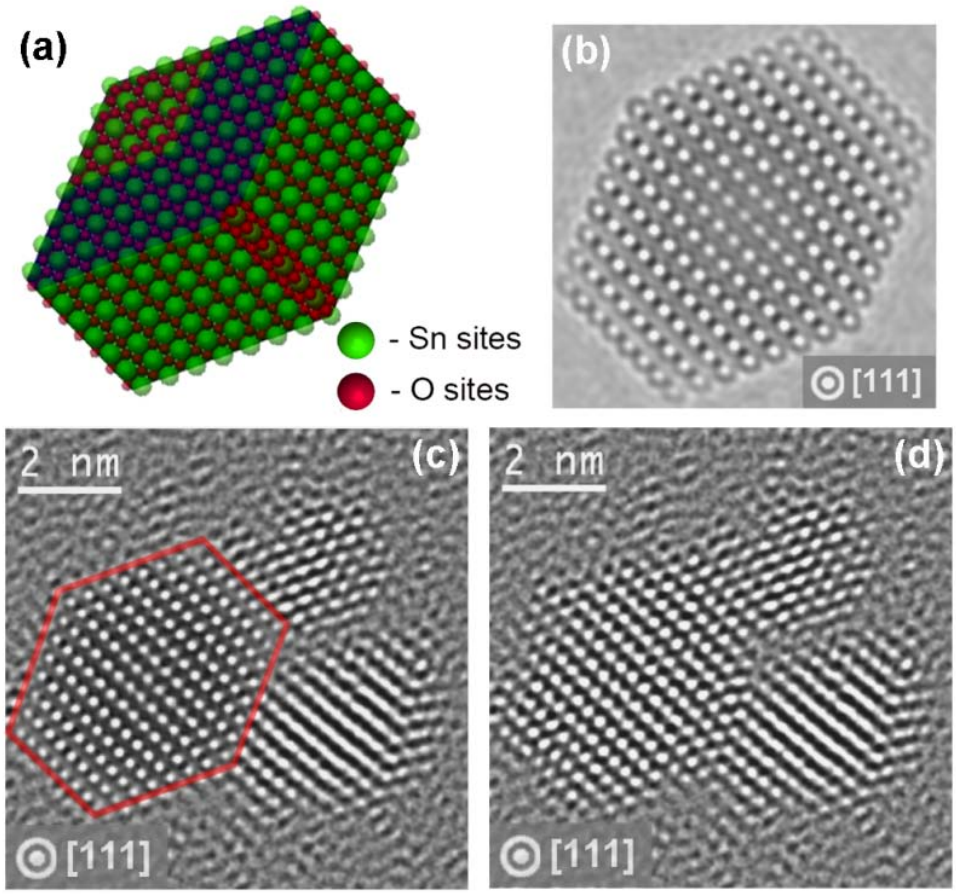

Figure 3.2d: Proposed and actual ATO nanocrystals observed along the [111] zone axis. (a) Proposed ATO ($Sb:SnO_2$) nanocrystal habit superimposed on its Wulff construction. (b) Multislice simulated HRTEM image obtained from the proposed nanocrystal habit. (c,d) Comparison of the nanocrystal multislice simulated HRTEM nanocrystal image (c) and the experimental HRTEM image (d).

Table 3.2a: Evaluation of Surface Energy and Sb Content for the ATO Nanocrystal Habit

exposed plane	distance (nm)	surface energy (J/m^2)	$\%_{atom}Sb$
(001)	1.73	4.65	8.0
(101)	2.08	5.54	14.2
(100)	1.90	5.18	15.3
(110)	2.50	6.87	16.1

As previously shown, the ATO nanocrystal self-assembling process occurs through oriented attachment (OA) growth (PENN *et al.*, 1998a, 1998b, 1999). OA is a statistical process related to the collision rate among nanocrystals in suspension and to the reduction of surface energy driven by the area minimization of high-energy facets (LEITE *et al.*, 2003). It has been recently reported as the predominant growth mechanism for an increasing number of materials and has called the attention of scientists as a suitable technique for processing mesocrystals and anisotropic nanomaterials (TANG *et al.*, 2002; COLFEN *et al.*, 2005; FANG *et al.*, 2006; NIEDERBERGER *et al.*, 2006a; MELDRUM *et al.*, 2008; ZHOU *et al.*, 2008). Several growth kinetic models (ZHANG *et al.*, 2004; RIBEIRO *et al.*, 2005) have been developed that considers OA as a common step in the nanocrystal growth mechanism, even in systems with high solubility in which Ostwald ripening is the predominant growth mechanism (RATKOVICH *et al.*, 2007).

Figure 3.2bb shows a pair of coalesced ATO nanocrystals, self-organized through OA growth. This oriented ensemble was evaluated by the use of previously proposed nanocrystal model and simulated HRTEM images in order to investigate the OA growth mechanism. Figures 3.2ea and 3.2eb present the atomic arrangement of an ATO nanocrystal ensemble superimposed with its Wulff construction and the results of HRTEM multislice image simulation, respectively. Figures 3.2ec and 3.2ed compare the multislice simulated HRTEM image of the ensemble (c) and the experimental image (d).

The remarkable agreement between the experimental HRTEM image and the simulated image of the proposed ATO nanocrystal assembly allows for an accurate evaluation of the OA mechanism. [100] and [101] were observed as the preferential growth directions for the ATO nanoparticles. Figure 5c corresponds to an example of (100) facet oriented attachment. The OA growth process along the [100] and [101] directions is congruent with the predicted attachment configurations (see Appendix B – supporting information) and with the higher expected collision rate for the (100) and (101) facets as a result of their larger exposed facet area. In the proposed nanocrystal habit, more than 78% of the total surface area corresponds to (100) and (101) facets.

The combined use of HRTEM characterization, HRTEM image multislice simulation and *ab initio* calculations provided information on the 3D habit and surface chemical composition of faceted nanocrystals by correlation of the crystal faceting and the dopant-dependent surface energy of exposed facets.

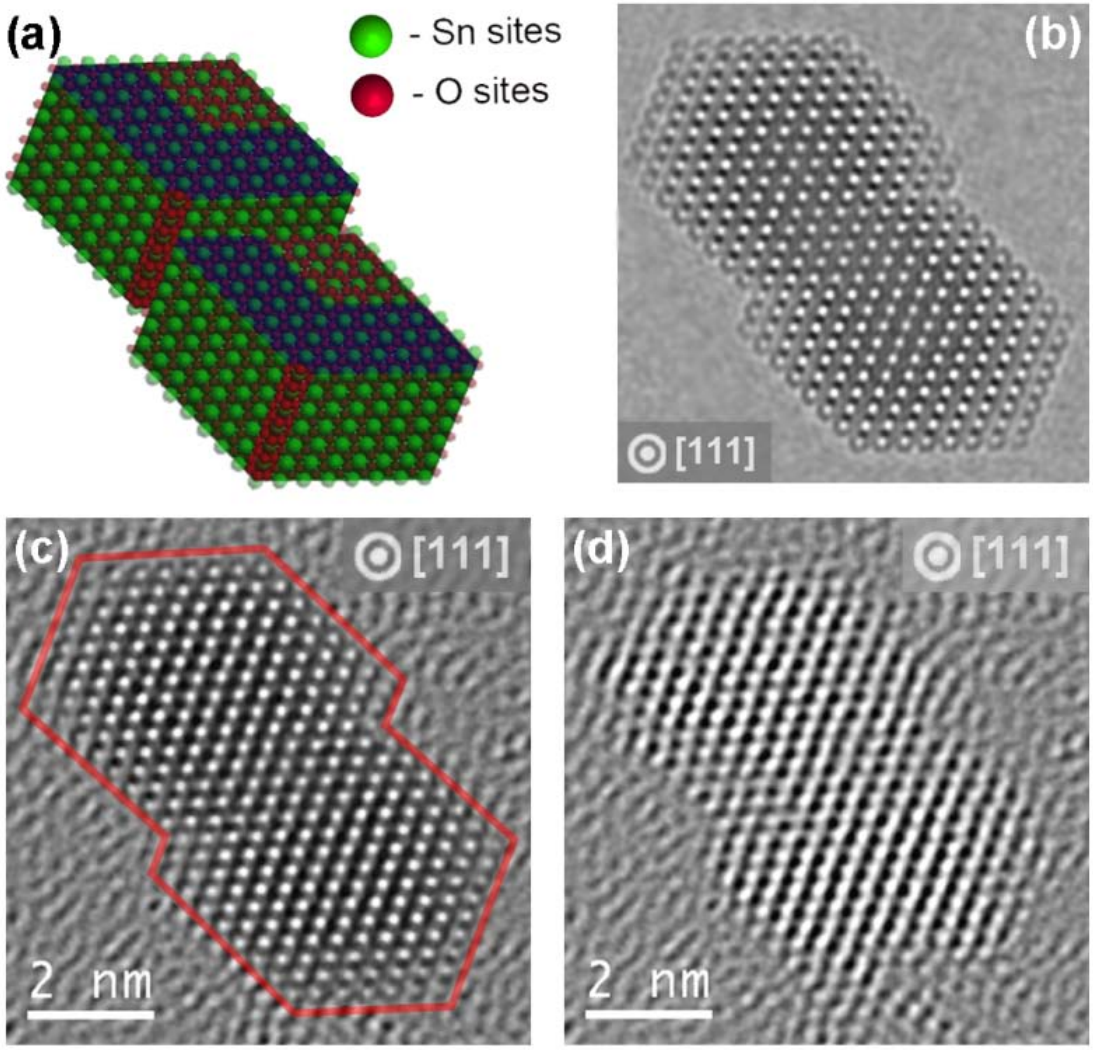

Figure 3.2e: Proposed ATO nanocrystal ensemble and its simulated HRTEM image. (a) Atomic arrangement of the ATO (Sb-SnO_2) nanocrystal ensemble superimposed on its Wulff construction. (b) Multislice simulated HRTEM image obtained from the proposed nanocrystal ensemble. (c,d) Comparison of the simulated nanocrystal image and the experimental image.

Concluding Remarks

Based on indirect quantitative measurements, this methodology is a novel approach for the evaluation of surface dopant distribution on nanoparticles. It is a powerful tool for the analysis of nanocrystals, where usual quantitative techniques such as X-ray photoelectron spectroscopy (XPS), X-Ray energy dispersive spectroscopy (XEDS), high angle annular dark field (HAADF), and electron energy loss spectroscopy (EELS) would require a much greater effort and/or would be restricted by system dimensions and/or small atomic weight differences between the material elements (SUN *et al.*, 2002).

In addition, the combined use of surface energy *ab initio* calculations and Wulff construction applied to nanocrystal modeling was applied successfully to study the oriented attachment growth mechanism in ATO nanocrystals and can be used to carry out such studies in a number of nanostructured systems. Modeling hypothetical nanocrystals as building blocks with known surface energy distribution and faceting enables one to produce a three-dimensional description of the oriented attachment growth mechanism, which can be further investigated by HRTEM imaging and HRTEM multislice image simulation.

Acknowledgements

We acknowledge the financial support of the Brazilian research funding agencies FAPESP, CNPq, and FINEP.

3.3. Segregação de Dopantes para a Estabilização da Estrutura Cristalina

O desenvolvimento de metodologias para a extração de informações quantitativas a respeito da segregação de dopantes em nanocristais remete à possibilidade de melhoria no entendimento no mecanismo de formação e evolução de sistemas nanocristalinos e seu posterior modelamento. Neste sentido, a metodologia proposta no Capítulo 3.2 representa uma aproximação que pode ser utilizada na caracterização de sistemas que apresentam restrições em relação às metodologias diretas que visam a quantificação de espécies atômicas com alta resolução espacial.

Além de ilustrar o uso da caracterização morfológica combinada aos cálculos *ab initio* para energia superficial na avaliação da inter-relação entre a morfologia, a distribuição de energia superficial e a segregação de dopantes, os resultados obtidos remetem à segregação de dopantes como um mecanismo adicional para a redução de energia superficial de um sistema nanocristalino. Neste contexto, a segregação de dopantes atua juntamente com a alteração de morfologia, a variação local de parâmetros de rede, a reestruturação de superfícies e o crescimento de cristais como mecanismo de redução da energia livre de Gibbs em sistemas nanocristalinos. (CAO, 2004)

Uma consideração pertinente à minimização de energia em sistemas nanocristalinos, e conseqüentemente ao modelo proposto, é referente à dimensão temporal dos eventos envolvidos nos mecanismos citados anteriormente. Um limitante para parte dos fatores considerados fundamentais para que o sistema atinja o equilíbrio termodinâmico pode ser representado pela taxa de difusão de espécies atômicas, pois esta rege a estabilização da morfologia e a mobilidade de espécies dopantes. Uma descrição cinética da difusão por meio do deslocamento de vacâncias pode ser vislumbrada pela lei de Arrhenius (KITTEL, 2004), que relaciona a constante de velocidade (k) à energia de ativação para a movimentação de átomos a sítios livres ($E_m \sim 1$ eV) e à energia livre referente a temperatura ambiente ($k_bT = 0.026$ eV). Contudo, para sistemas cristalinos de com dimensões reduzidas, tem-se uma maior taxa efetiva de difusão devido à abundância de sítios livres ao longo da superfície. A título de comparação, o sistema

nanocristalino de Pd com dimensão média de 5 nm apresenta 45% dos átomos na superfície (NÜTZENADEL *et al*, 2000).

Neste contexto, o tempo característico para eventos de *hopping* em nanocristais isolado pode ser estimado na ordem de nanosegundos (RATSCH *et al.*, 1998), o que torna factível a consideração de equilíbrios termodinâmicos locais para sistemas nanostruturados reais considerando a duração típica dos procedimentos de síntese. Contudo, tal argumento tem em vista apenas as restrições cinéticas baseadas em difusividade atômica e indica que esta não deve ser determinante na minimização de energia total de sistemas no escopo supracitado.

Outra parte fundamental das restrições cinéticas é dada pelo efeito de outras espécies químicas presentes no meio reacional, tal como íons livres, solventes e surfactantes, que determinam as relações de interação entre os nanocristais. No contexto de sistemas nanocristalinos, é usual que a morfologia seja dada pela configuração de síntese e que o fator determinante seja o efeito de espécies químicas ligadas ou adsorvidas nas superfícies do material ao longo das fases de nucleação e crescimento (XIA et al, 2009a). Contudo, avanços nos modelos de cálculos teóricos *ab initio* apresentam a possibilidade da avaliação da energia livre incluindo espécies ligadas (TUTUIANU *et al*, 2006). Neste caso, a contribuição de espécies químicas no meio reacional como uma restrição cinética à evolução de um sistema nanocristalino é passível de ser tratada como uma componente termodinâmica caso o sistema seja considerado como um nanocristal e sua vizinhança, sendo as espécies adsorvidas descritas em termos de variação da energia superficial. No entanto, os estudos presentes nesta tese abordam o desenvolvimento dos modelos de avaliação dos sistemas nanocristalinos e não os cálculos teóricos *ab initio*. Desta maneira é considerada uma boa aproximação a utilização da razão entre os valores obtidos para energia superficial *in vacuo*.

No Capítulo 3.4 é apresentada a avaliação da segregação de dopantes de dois sistemas $Sb:SnO_2$ com diferentes níveis de dopagem pela utilização da metodologia apresentada no Capítulo 3.2. Os resultados indicam a variação no padrão de segregação de dopantes em função da composição geral, que remete diretamente à migração de espécies dopantes para facetas pertencentes a planos cristalinos determinados. Tal comportamento é discutido sob a ótica da minimização da energia livre de Gibbs para nanocristais individuais.

3.4. Dopants segregation analysis on $Sb:SnO_2$ nanocrystals

Dopants segregation analysis on $Sb:SnO_2$ nanocrystals (STROPPA *et al.*, 2011d)

Daniel G. Stroppa, Luciano A. Montoro, Armando Beltran, Tiago G. Conti, Rafael O. da Silva, Juan Andres, Edson R. Leite, Antonio J. Ramirez.

Publicado na revista *Chemistry: A European Journal*, 17, 11515-11519, **2011**.

Abstract

The development of reliable nanostructured devices is intrinsically dependent on the description and manipulation of materials' properties at the atomic scale. Consequently, several technological advances are dependent of improvements on the characterization techniques and on the models used to describe nanosized materials properties as function of the synthesis parameters. The evaluation of doping elements distribution on the nanocrystals is directly linked to fundamental aspects that defines the materials properties, such as surface energy distribution, nanoparticles shape and crystal growth mechanism. However, this is still one of the most challenging tasks in materials characterization due to required spatial resolution and due to other various restrictions from quantitative characterization techniques, such as sample degradation and signal-to-noise ratio.

This paper addresses the dopant segregation characterization for two Antimony-doped Tin Oxide ($Sb:SnO_2$) systems with different Sb-doping level by the combined use of experimental and simulated high-resolution transmission electron microscopy (HRTEM) images and surface energy *ab initio* calculations. The applied methodology provided three-dimensional models with geometrical and compositional information, which were demonstrated to be self-consistent and correspondent to the systems mean properties. The results evidence that the dopant distribution configuration is dependent of the system composition and that dopant atoms redistribution may be an active mechanism for the overall surface energy minimization.

Introduction

Nanostructured materials have become key ingredients for the development and implementation of novel technologies due to some unique properties that are enhanced as the surface area to volume ratio increases. The engineering of such nanostructured materials requires reliable models that can describe how the synthesis process parameters are related to the nanocrystals features, especially for the bottom-up synthesis approach (LEITE, 2004). In addition, as the successful use of nanostructured materials as building blocks requires control over the nanocrystals properties, the crystal modeling (WANG *et al.*, 2003; BARNARD *et al.*, 2006, 2008, 2010) has become a fundamental tool due to its use on the prediction of crystal shapes, growth process, and the resulting properties of an unlimited number of systems.

A major issue in crystal modeling is to describe how synthesis parameters and the chemical environment influence the nanocrystals morphology and surface energy distribution. Some studies report that the surface energy distribution is dependent of the local composition for doped systems (XIA *et al.*, 2009b; SINGH *et al.*, 2010). This relationship indicates the importance of dopant segregation analysis on nanocrystals, which requires advanced characterization procedures with the high spatial resolution.

In recent years, advanced tools (HUANG *et al.*, 2009; JINSCHEK *et al.*, 2008; ARSLAN *et al.*, 2005; SCHAMM *et al.*, 2008; HANSEN *et al.*, 2002) have been developed for nanocrystal characterization in order to obtain accurate chemical, structural and morphological information, such as crystallographic habit, surface chemistry, and growth mechanisms from self-assembled arrangements. Although a number of techniques based on X-ray (HUANG *et al.*, 2009; RENAUD *et al.*, 2003), scanning probe microscopy (MORALES *et al.*, 2008), and transmission electron microscopy (TEM) (MONTORO *et al.*, 2009; MULLER *et al.*, 2008; JIA *et al.*, 2004a) have been successfully applied to retrieve compositional and morphological information from nanostructures, several challenges remain, especially with regard to three-dimensional reconstruction and chemical mapping.

In this work we characterized the $Sb:SnO_2$ system with different Sb contents in order to describe the dopant segregation, surface energy distribution and crystal habit as function of the nanocrystals composition. The applied methodology (STROPPA *et al.*, 2009) combines

information from HRTEM images of faceted nanocrystals, Wulff construction (HERRING, 1951; MARKS *et al.*, 1983), and surface energies *ab initio* calculation (BELTRAN *et al.*, 2003) (atomistic simulation) for selected facets.

Results and Discussion

XRD and electron diffraction analysis of synthesized Sb:SnO_2 nanocrystals indicated that both materials present SnO_2 cassiterite tetragonal structure with P_{42}/mnm spatial group symmetry (MACCARTHY *et al.*, 1989). No other crystalline phases were revealed by the XRD analysis, indicating the complete incorporation of Sb in the SnO_2 structure (see Appendix B – supporting information).

The XEDS spectra quantification (see Appendix B – supporting information) indicated an average Sb content of 4.5 ± 0.8 % and of 13.9 ± 1.4 % for approximately 500 nanocrystals synthesized with $7\%_{Atom}$ and $18\%_{Atom}$ Sb doping concentration (nominal composition), respectively.

The HRTEM analysis of Sb:SnO_2 samples indicated the formation of faceted nanocrystals for both compositions, as illustrated in Figure 3.4a. Figure 3.4aa and 3.4ab show representative HRTEM images from the $7\%_{Atom}$ and $18\%_{Atom}$ Sb:SnO_2 samples, respectively. The Fast-Fourier Transform (FFT) indexation indicated a [111] zone axis orientation for both examples and the HRTEM multislice simulations of the SnO_2 P_{42}/mnm crystal structure under the experimental image conditions (dashed boxes) was used to check the accuracy of the HRTEM characterization.

Based on the projected two-dimensional HRTEM images of Sb:SnO_2 nanocrystals and the allowed symmetry operations for the SnO_2 crystallographic structure, a nanocrystal model was proposed for both the analyzed compositions. The refinement of such models was performed by an iterative procedure of HRTEM image simulation of the complete nanocrystal model and the comparison with the experimental images.

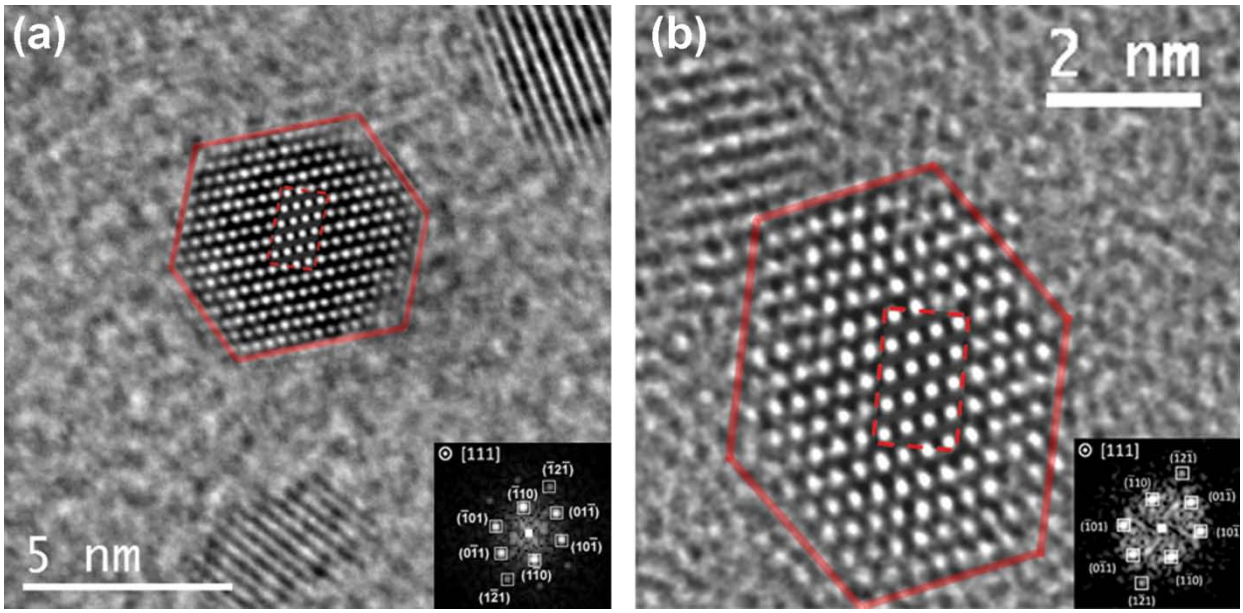

Figure 3.4a: HRTEM images and FFT indexation from a) 4.5%atom Sb-doped and b) 13.9%atom Sb-doped nanocrystals. The red continuous lines indicate the nanocrystals faceting and the dashed red lines indicate the results from multislice image simulation for the experimental imaging conditions.

The remarkable agreement between experimental (3.4bc and 3.4bg) and simulated (3.4bd and 3.4bh) HRTEM images is presented on Figure 3.4b. Consequently, it is indicated that the proposed nanocrystals models (3.4ba and 3.4bd) can accurately describe the nanocrystals morphology for the analysed samples. These morphologies were observed for several [111] oriented nanocrystals, indicating that the 3D modeling can be assumed valid to describe the samples faceting behaviour.

As the experimental data suggest that different dopant contents implies in different nanocrystal morphologies, Wulff construction (HERRING, 1951; MARKS *et al.*, 1983) was applied to correlate the nanocrystals faceting and surface energy for different exposed crystallographic planes and Sb concentrations. According to Wulff's rule (HERRING, 1951) which determines the equilibrium crystal shape by minimizing the surface energy for a given enclosed volume, the crystal morphology can be thermodynamically predicted using the surface energy from different crystallographic families.

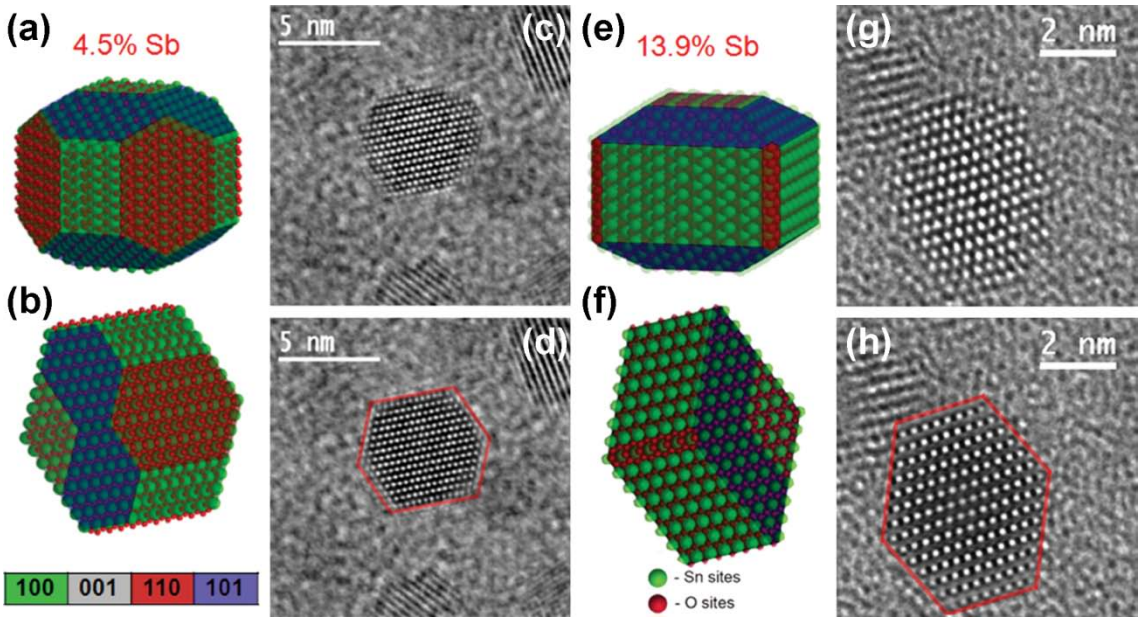

Figure 3.4b: a) Trimetric and b) [111] zone axis oriented view for the 4.5%atom Sb-doped nanocrystals geometric model. c) Original HRTEM image from 4.5%atom Sb-doped nanocrystals and d) superimposition with the geometric model simulated HRTEM image. e) Trimetric and f) [111] zone axis oriented view for the 13.9%atom Sb-doped nanocrystals geometric model. g) Original HRTEM image from 13.9%atom Sb-doped nanocrystals and h) superimposition with the geometric model simulated HRTEM image.

The thermodynamic equilibrium consideration is a required approximation as the Wulff rule regards to the minimum energy configuration. However, given the nanocrystals typical dimensions and the characteristic atomic diffusion time scale considering the synthesis temperature, it is reasonable to assume thermodynamic equilibrium conditions within the nanocrystals surrounding volume.

The *ab initio* calculated surface energies for different Sb:SnO_2 crystalline planes and Sb concentrations are presented in Figure 3.4c. A Wulff construction is presented for each Sb composition assuming that it is homogeneously distributed at the considered facets. These results suggest that the crystal morphology evolves as a function of Sb total content in order to minimize the total surface energy.

Crystallographic Plane		Sb dopant amount ($\%_{atom}$) 0.00	7.14	14.29	20.00	Surface Energy (J/m^2)
	{100}	2,15	3,53	5,09	8,39	
	{001}	3,34	4,08	6,07	6,08	
	{110}	2,04	4,20	6,33	6,31	
	{101}	2,57	4,06	5,61	5,55	

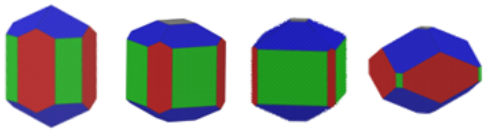

Wulff Construction

Figure 3.4c: Results from the surface energy *ab initio* calculation for different Sb-doping levels and crystallographic families. A Wulff construction is presented for each set of energies considering the homogeneous dopant distribution

It is important to notice that a reliable analysis of surface energy absolute values must include the effect of adsorbant species. However, the material synthesis was performed in a chemical environment free of addictives, and the existent counter-ion and solvent did not present relevant selective-facet adsorption. Additionally, as the performed analysis takes into account the surface energy ratio for different crystallographic planes, the adsorbant species influence is reduced and can be neglected for this specific system. Moreover, the use of the surface energy ratio on this analysis also reduces inherent errors related to bulk truncated model applied on the surface energy values evaluation, including the edges and surface stress energy contributions.

The qualitative and quantitative information on dopant segregation was retrieved by the nanocrystal models geometrical analysis under the light of the surface energy *ab initio* calculations (STROPPA *et al.*, 2009). Figure 3.4d presents the Sb:SnO_2 nanocrystal models information for both analyzed systems, including the geometric parameters, the surface energy values, and the estimated Sb content for the exposed crystalline planes.

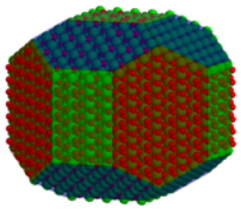

Surface Energy Density:
3.94 J/mm^3

ATO 4.5% Sb

Wulff parameter: 1.3159

Facet	Distance (nm)	Surface Area (nm^2)	Energy (J/m^2)	Sb Content (%)
[100]	2.85	17.12	3.78	8.3
[001]	2.40	10.48	3.13	0.0
[110]	2.62	34.68	3.45	4.7
[101]	2.63	43.60	3.44	4.2

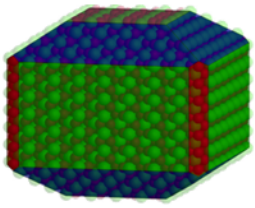

Surface Energy Density:
8.10 J/mm^3

ATO 13.9% Sb

Wulff parameter: 2.7047

Facet	Distance (nm)	Surface Area (nm^2)	Energy (J/m^2)	Sb Content (%)
[100]	1.90	32.16	5.18	15.3
[001]	1.73	10.66	4.65	8.0
[110]	2.50	3.80	6.87	16.1
[101]	2.08	21.60	5.54	14.2

Figure 3.4d: Characterization summary including morphological and dopant segregation information for both analyzed Sb:SnO_2 compositions.

In order to evaluate the Figure 3.4d data consistency and statistical representativeness, two approaches were applied. The first one is a first-principle geometric derivation that was used to correlate the ratio between the surface energy density values and the Wulff parameter (RW), which is completely described on support information (see Appendix B – supporting information). The comparison between the theoretical and experimental RW values revealed an agreement higher than 99.6%, indicating that the geometrical model and the surface energy evaluation from both the systems are self-consistent.

The second approach is a comparison between the experimental particle size distributions and the projected dimensions of the geometric models, which can be used to infer the results statistical adequacy for the studied samples description. This analysis is depicted on support information (see Appendix B – supporting information) and its results indicate that the nanocrystals models mean projected dimensions for low-order zone axes are approximately 10% higher than the measured crystal size mean dimensions.

The quantitative analysis presented on Figure 3.4d indicates that the nanocrystals morphologies provide a useful insight about the dopant distribution regarding facets from different crystallographic families. In addition, the dopant atoms segregation behavior is shown to be dependent on the system overall composition. A decisive argument to rationalize these quantitative results is given by the thermodynamic of mixing (LEWIS *et al.*, 1961) which can be evaluated from the Gibbs free energy as show in Equation 3.4a, where H is the enthalpy, T is the synthesis temperature, and S is the entropy.

The entropic contribution corresponds to the mixing entropy, which approximation is shown in Equation 3.4b, where x is the dopant concentration.

$$G = H - TS \qquad \textbf{Equation 3.4a}$$

$$T.S_{mix}(x) = - kT\,[x.\ln(x) + (1-x).\ln(1-x)] \qquad \textbf{Equation 3.4b}$$

The mixing entropy values were calculated for the nanocrystals models with the two evaluated compositions ($4.5\%_{atom}$ and $13.9\%_{atom}$ Sb) considering both the homogeneous and the characterized non-homogeneous dopant distribution cases. The results are nearly identical, with $T.S_{mix}$ approximately equals to 2.0×10^{-18} J per nanocrystal.

The comparable entropic contribution on the Gibbs free energy from the homogeneous and the non-homogeneous chemical distributions indicates that the driving force for dopant segregation is predominantly originated from an enthalpic contribution. In fact, the enthalpic term is dominated by the overall surface energy (SHCHUKIN *et al.*, 1995), which can be evaluated by the *ab initio* calculated energies for different crystallographic planes and their respective surfaces areas for the analyzed systems. The total surface energy for both evaluated systems is approximately 3.6×10^{-16} J per nanocrystal. This result indicates that the enthalpic contribution on the Gibbs free energy is at least two orders of magnitude higher than the entropic one.

Conclusion

The combination of HRTEM characterization and surface *ab initio* calculations for surface energy indicated that a semi-empirical quantitative analysis of dopant segregation on nanocrystals is feasible. The obtained results indicated that the dopant segregation is dependent on the overall dopant content and that the surface energy configuration plays a major role on the nanocrystals morphological features.

An interpretation for the heterogeneous distribution is that the dopant atoms tend to diffuse preferentially to facets belonging to determined crystallographic planes in order to minimize the overall surface energy, compensating thus the nanocrystals energy excess from facets, edges and vertexes. The Gibbs free energy evaluation indicates that the enthalpic component, which includes the surface energy, is the most relevant driving force for the dopant segregation.

Experimental Section

Sb:SnO_2 nanocrystals with two different Sb contents, 18%atom and 7%atom Sb doping concentration (nominal composition), were synthesized in a glovebox under a controlled atmosphere by the benzyl alcohol method (NIEDERBERGER *et al.*, 2006b; DA SILVA *et al.*, 2009). Stoichiometric amounts of $SnCl_4$ (99.995%) and $SbCl_3$ (99.99%) were stirred in a vessel with benzyl alcohol, after which the reaction vessel was removed from the glovebox and heated at 150ºC for about 48h in a silicone bath. Sb:SnO_2 nanoparticles were collected by centrifugation, washed and stocked in tetrahydrofuran.

HRTEM characterization was performed using a JEM-2010 URP TEM at 200 kV with a LaB_6 electron gun and equipped with a 1024×1024 thermoelectrically cooled CCD camera and a XEDS detector. TEM samples were prepared by dripping diluted Sb:SnO_2 solution onto copper grids covered with a thin amorphous carbon film.

The nanocrystals analysis methodology applied in this work is described in detail elsewhere.18 The nanocrystals models were constructed using the MEGACELL software (STROPPA *et al.*, 2011c). HRTEM simulated images of the nanocrystals models were obtained using JEMS software (STADELMANN *et al.*, 1987). The quantitative analysis was carried out

by the comparison between the nanocrystal models and a set of Wulff construction (HERRING, 1951; MARKS, 1983) using *ab initio* calculated surface energies for different dopant concentrations and crystalline planes.

Surface energy calculations for Sb:SnO_2 nanocrystals were performed with the CRYSTAL06 program package (DOVESI *et al*, 2005). Oxygen atoms were described by the standard 6-31G* basis sets and the Tin and Antimony centres in the PS-21G* scheme, where PS stands for Durand-Barthelat's non-relativistic large effective core potential (DURAND *et al.*, 1975). Becke's three-parameter hybrid nonlocal exchange functional (BECKE, 1993) combined with the Lee-Yang-Parr (LEE *et al.*, 1988) gradient-corrected correlation functional (B3LYP) was used. Full optimization of the cell parameters (a and c) and internal coordinate (u) for the bulk SnO_2 was carried out. The low index (110), (101), (100) and (001) surfaces were modelled by unreconstructed (truncated bulk) slab models using the calculated equilibrium geometry. Because these surfaces have a different number of atoms in each layer, the low-index surfaces were modeled with different thicknesses in the z-direction but periodic in x- and y-directions. After the corresponding convergence test on the undoped systems, slab models containing nine SnO_2 layers for the (110), (100), and (101) surfaces and eleven layers for the (001) were selected. A complete relaxation of all the atoms in each model was performed in order to evaluate the surface stress contribution on the surface energy value.

Acknowledgements

The authors acknowledge the financial support of the Brazilian research funding agencies FAPESP and FINEP.

3.5. Avaliação *ab initio* da Segregação de Dopantes

Os resultados obtidos pela aplicação da metodologia descrita no Capítulo 3.2 apresentam uma perspectiva positiva para o modelamento de nanocristais dada a obtenção de informações referentes à morfologia, segregação de espécies atômicas e distribuição de energia superficial. Adicionalmente, a demonstração presente no Anexo B2 indica que o modelo de cálculo é auto-consistente. Contudo, três restrições substanciais são existentes em relação à aplicabilidade da metodologia proposta em escala mais ampla.

A primeira restrição é referente à quantificação confiável da variação da energia superficial em função da concentração de dopantes incluindo o efeito das espécies químicas presentes no ambiente reacional.

A segunda restrição é decorrente da falta de representatividade estatística dos resultados da metodologia na representação do comportamento médio do sistema dado o número limitado de nanocristais analisados. Embora a análise presente no Anexo B2 indique que os casos avaliados no Capítulo 3.4 se situam próximos das dimensões médias dos nanocristais que constituem os sistemas em questão, tal argumento não garante que o facetamento, e conseqüentemente a relação entre as energias superficiais avaliadas, sejam representativos. Contudo, a análise de diversos nanocristais seria custosa devido ao modelo de cálculo ser aplicado a partir das características de um nanocristal específico.

A terceira restrição é decorrente à medição da concentração geral de espécies dopantes, que apresenta uma imprecisão considerável para a análise de segregação de dopantes. Apesar de técnicas com alta precisão na quantificação de espécies atômicas serem disponíveis, de acordo com a revisão apresentada no Capítulo 2 e com as perspectivas descritas no Capítulo 3.7, a aplicação de tais procedimentos ainda não é viável devido à complexidade dos experimentos necessários.

Com o intuito de superar parte das restrições supracitadas, um modelo para a predição de segregação de dopantes foi idealizado e avaliado. Tal modelo, descrito em detalhe e discutido no Capítulo 3.6, utiliza como informações de entrada uma ou mais geometrias poliédricas selecionadas e fixas que possam descrever os componentes do sistema nanocristalino estudado e

funções numéricas que descrevam a variação da energia superficial em função da concentração de espécies dopantes. Neste caso não existe restrição *a priori* em relação à aos métodos utilizados para a obtenção de tais informações.

O modelo proposto realiza a avaliação de um determinado sistema para passos incrementais de concentração total de dopantes e é baseado na minimização da distorção das condições calculadas em relação à condição de Wulff, e conseqüentemente à condição de mínima energia livre. Dado o caráter incremental de dopagem, a metodologia não requer inicialmente uma medida precisa da concentração total de dopantes dado que os resultados apresentam de maneira mais geral o comportamento do sistema na vizinhança do nível de dopagem estimado. Adicionalmente, a implementação do modelo como um algoritmo iterativo torna sua aplicação viável para numerosas configurações geométricas iniciais, o que torna viável a avaliação de diversos componentes em um determinado sistema nanocristalino.

Os resultados obtidos são apresentados no Capítulo 3.6 e indicam que o modelo proposto é equivalente à rotina de cálculos apresentada no Capítulo 3.2. Uma versão mais geral deste modelo, na qual a geometria de entrada é considerada um parâmetro livre e pode variar para diferentes concentrações globais de dopantes, foi proposta e testada. Contudo, não foi obtida uma descrição satisfatória que condissesse com os resultados semi-empíricos. A finalidade desta investigação foi a avaliação da configuração mais provável de um nanocristal em função de sua composição, sendo inclusas a previsão da morfologia, da segregação de dopantes e da distribuição de energia superficial mais prováveis segundo a minimização da energia livre do sistema. A provável justificativa para a falha do modelo preliminar proposto é a desconsideração dos fatores relacionados à nucleação e ao crescimento dos nanocristais, como a disponibilidade de materiais precursores, que são fundamentais para a definição da distribuição de dimensões dos nanocristais.

O desenvolvimento deste modelo mais geral é previsto dentro das perspectivas futuras relacionadas a este projeto.

3.6. A thermodynamic approach to predict dopant atoms segregation on nanocrystals

Thermodynamic approach to predict dopant atoms segregation on nanocrystals (STROPPA *et al.*, 2011g)

Daniel G. Stroppa, Luciano A. Montoro, Antonio Campelo, Lourdes Gracia, Armando Beltran, Juan Andres, Edson R. Leite, Antonio J. Ramirez.

Submetido para publicação, **2011**.

Abstract:

This work describes a methodology for the evaluation of dopant atoms segregation on faceted nanocrystals based on first principles calculations of surface energy as function of dopant content for different crystalline planes. Starting from an arbitrary nanocrystal geometrical configuration, an iterative calculation procedure for incremental doping levels is performed to verify the most likely dopant segregation state as a function of the nanocrystal overall composition. Sb-doped SnO_2 nanocrystals have been selected as case study and the calculated dopant segregation patterns for two systems with different geometries (4.5%atom and 13.9%atom dopant content) were analyzed and compared with results obtained by HRTEM characterization. The measured and the calculated dopant atoms distributions are in a good agreement, with an overall deviation value below 7%.

The consistent use of nanostructured components on novel technologies requires the ability to design and synthesize materials with highly controlled features in a reproducible way. Although a number of accomplishments are reported in this direction (XIA *et al.*, 2009a), the development of improved methodologies for nanocrystals processing is required in order to fully exploit unique materials properties that arise at nanoscale (CAO, 2004; BARNARD, 2010).

Progress on the nanosized systems manipulation can only be achieved if nanocrystals characteristics are reliably described by models which can correlate the systems features to the environmental variables, such as the synthesis parameters and materials operational conditions. These models development and improvement require the combination of experimental and theoretical approaches due to the current limitations on the available characterization methodologies.

Even though the nanomaterials characterization techniques have presented breakthrough advances towards the high resolution information assessment (URBAN, 2008; MULLER *et al.*, 2008; DALFONSO *et al.*, 2010; KRIVANEK *et al.*, 2010), the quantitative analysis at atomic scale still restricted for a number of nanocrystalline systems. Among the reasons for this are the sample preparation difficulties and the degradation during the tests. In addition, the description of nanostructured systems by the use of high spatial resolution analysis can be deceptive as the available techniques usually provide a relatively small sampling, which may not represent the system accurately.

Although the atoms segregation analysis has been addressed for few nanocrystalline materials (SHIBATA *et al.*, 2004; STROPPA *et. al.*, 2011d; ABEL *et al.*, 2011), a methodology that provides high resolution quantitative information for a representative number of nanocrystals is not currently available. As the retrieval of statically representative data on the dopant segregation behavior from individual nanocrystals by the available experimental approaches would require tremendous efforts, a complementary theoretical approach is required.

First principle calculations have been widely used together with experimental techniques in a synergic manner. More specifically on materials science scope, this combination is especially required on the study of nanostructured systems as many remarkable properties are related to extremely small size (BARNARD *et al.*, 2008) and time scales (RATSCH *et al.*, 1998;

BARNARD, 2010), which usually prevent the exclusive use of experimental approaches. Therefore, the theoretical modeling of materials based on first principle calculations is fundamental in order to support, improve and extend the experimental results on the nanosized systems characterization.

Nanostructured materials features, such as morphology, growth mechanism, and a number of interesting properties depend greatly on the surface energy distribution (YANG *et al.*, 2008; DA SILVA *et al.*, 2011). The *ab initio* evaluation of surface energy distribution on nanocrystalline materials is still a great challenge for theoreticians due to the extensive number of factors that must be taken into account: bulk structure and exposed facets crystallography, chemical environment and atomic species distribution for doped materials. Although the dependency between surface energy and dopant atoms concentration for selected crystallographic planes is already elucidated (BELTRAN *et al.*, 2003), the dopant segregation occurrence within individual nanocrystals requires a more extensive analysis if accurate quantifications of the dopant atoms distribution and of the total surface energy are intended.

This work presents a novel model for the combined evaluation of dopant atoms segregation and surface energy distribution for faceted nanocrystals after *ab initio* surface energy calculations for different doping levels and crystallographic planes. It considers the thermodynamic equilibrium for incremental doping levels on a nanoparticle with an arbitrary polyhedral geometry in order to evaluate the most likely dopant distribution according to the Gibbs free energy minimization.

Wulff theorem (HERRING, 1951) states that the crystalline materials morphology is defined by the surface energy distribution if the system is in thermodynamic equilibrium. For such condition, the nanocrystals shape is a geometric configuration in which the free energies of different facets (E_i) contribute in such a way to generate a minimum total free energy (G) for a fixed volume. This geometric configuration occurs if the ratio between each E_i and its correspondent facet distance (d_i) to an arbitrary crystal center is a constant value, namely the Wulff parameter (W).

On real systems, the crystals morphology evolves through a number of mechanisms until a minimum free energy state is reached. Equation 3.6a presents the free energy quantification, where H is the enthalpy, T is the system temperature, and S is the entropy.

$$G = H - TS \qquad \textbf{Equation 3.6a}$$

While the entropic contribution (S) is related to the atomic species and crystalline phases distribution, the enthalpic contribution (H) is given by the overall chemical composition, the crystalline structure, and the surface energy. For doped systems in which crystalline phases segregation is not likely to occur, the entropic contribution to the free energy corresponds to the mixing entropy (S_{mix}), which approximation is shown in Equation 3.6b, where x is the dopant concentration.

$$S_{mix}(x) = - k [x.\ln(x) + (1-x).\ln(1-x)] \qquad \textbf{Equation 3.6b}$$

As $S_{mix}(x)$ cannot be higher than 0.7k, its contribution to nanostructured systems at room temperatures is negligible when compared to the enthalpic contribution. In such scenario, for a given composition and crystalline structure, the surface energy is the key component that defines the free energy and the nanocrystals structure, consequently (CAO, 2004).

The surface energy, which refers to the number of unmet chemical bonds at the nanocrystal surface, is intrinsically dependent of the exposed crystallographic planes at the nanocrystal facets and the dopant content in each one of them (CAO, 2004). In addition, different components present in the nanocrystals environment may alter the surface energy distribution if they are site selective. For such case, adsorbant species such as free ions, solvent and surfactant molecules need to be included on the surface energy evaluation. Other relevant aspects that modify the structure periodicity, such as the lattice parameters relaxation and the surface reconstruction, and the excess energy from edges and vertices may be also taken into account (GONG *et al.*, 2006).

So far, not all the above-cited aspects can be integrated simultaneously in a calculation model for the surface energy distribution. Although this issue restricts the free energy evaluation in a general manner, first principles calculations of surface structures successfully provided a good approximation on the theoretical predictions for resultant morphologies on a number of systems (BARNARD, 2010). After such results, *ab initio* calculations results were found to be suitable for the present methodology development. However, there is no restriction regarding the use of other surface energy calculation approaches for its application.

In addition to the surface energy evaluation, the nanocrystals morphology evaluation via Wulff theorem requires the analyzed system to be in thermodynamic equilibrium. This consideration requires the careful evaluation of some aspects which may determine the system behavior. However, defining the nanocrystal and its close surroundings as the thermodynamic system for the equilibrium analysis, instead of the whole synthesis environment, may be more suitable approximation due to the more probable local equilibrium. This is justified given the typical diffusion time scale on nanosized materials for typical synthesis temperatures, which may allow the atoms to diffuse within a nanocrystal towards the minimum free energy configuration.

Regardless of the thermodynamic system choice, a feasible equilibrium approximation requires that the chemical species solubility and diffusion coefficient on the reaction environment are not major restrictions to the system evolution toward the minimum energy configuration within the synthesis timeframe.

Even though it seems restrictive, the thermodynamic equilibrium consideration provided good approximation for the morphology description of several nanocrystalline systems (DA SILVA et al., 2010; LONGO *et al.*, 2011). These findings motivate its use on the dopant distribution analysis given by the present methodology.

Figure 3.6a presents a schematic representation of the proposed model for dopant atoms segregation. Its steps are thoroughly discussed on the following subsections.

The first step comprises the evaluation of surface energy density dependency with the dopant content for different crystallographic planes (BELTRAN *et al.*, 2004). Figure 3.6b summarizes the results from *ab initio* surface energy calculations for Sb-doped SnO_2 and illustrate the free energy dependence with the dopant content (E_i ($\%Z_i$)), which was obtained for

each crystallographic plane by the linear fit of the calculated energies within low-doping regime (0:14.29%) given its adequacy to the experimental doping levels used on the upcoming comparison.

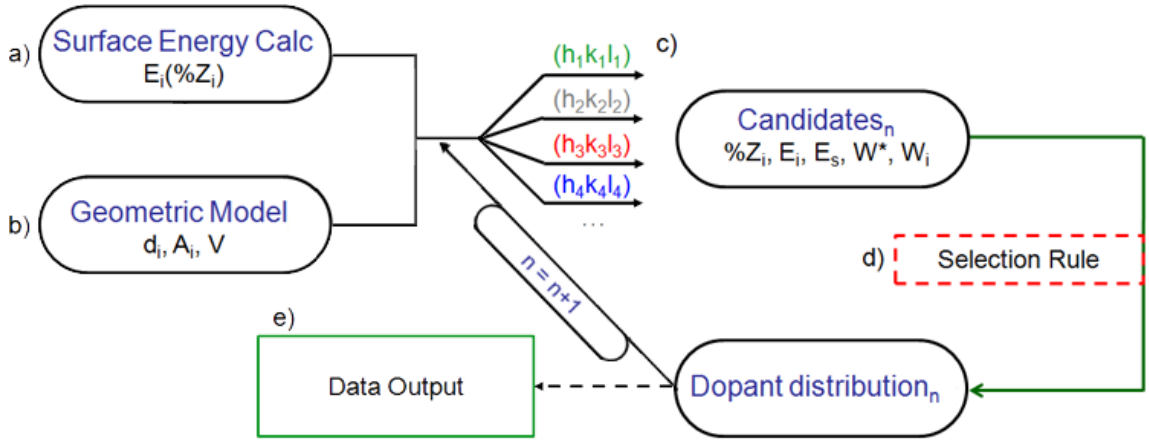

Figure 3.6a: Schematic representation of the proposed evaluation methodology and its five subdivisions: a) *ab initio* Surface Energy Calculations, b) Geometric Model, c) Possible Doping Configurations, d) Calculations and Selection Rule, and e) Iteration and Results Output.

a) *ab initio* Surface Energy Calculations

Surface energy calculations were performed with the CRYSTAL06 program package. Oxygen atoms were described by the 6-31G* basis sets and the Sn and Sb centers by the scheme PS-21G*. Becke's three-parameter hybrid non-local exchange functional combined with the B3LYP was used. Full optimization of the cell parameters and internal coordinates for the bulk SnO_2 were carried out and the studied surfaces were modeled by unreconstructed slab models using the calculated equilibrium geometry. Slab models containing nine SnO_2 layers for the (110), (100), and (101) surfaces and eleven layers for the (001) were selected. A complete relaxation of all the atoms was performed in each model. Details from the *ab initio* surface energy calculations are reported elsewhere (BELTRAN *et al.*, 2004).

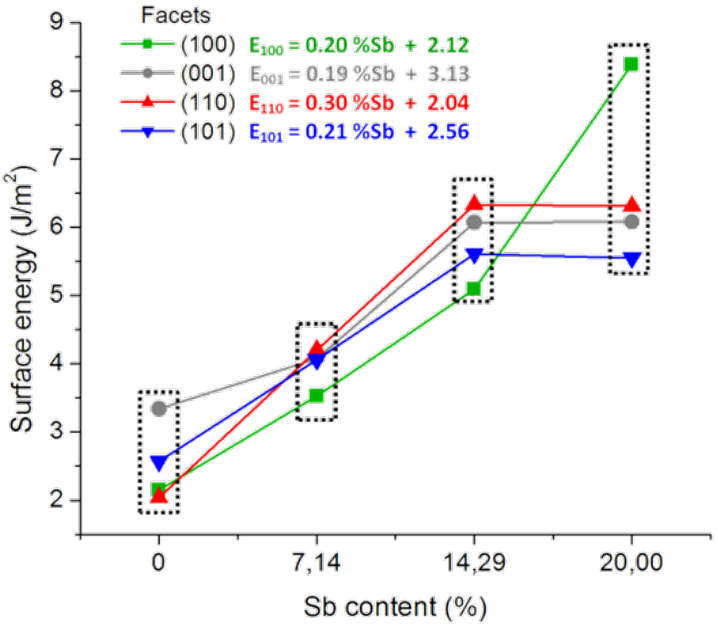

Figure 3.6b: *ab initio* calculations results for the surface energy of different crystallographic planes as function of the Sb dopant content. The obtained E_i ($\%Z_i$) functions are indicated for each evaluated crystallographic family.

b) Geometric Model

The second step comprises the geometric parameters input which define the fixed crystal shape considered for calculations. The required information includes the facets distance to the crystal center (d_i), the facets area (A_i) and the crystal volume (V). This work used the geometries obtained after the HRTEM analysis of two different Sb-doped SnO_2 systems, with an average 4.5 and 13.9 $\%Sb_{atom}$ respectively. The HRTEM dimensions were rounded to the closest crystalline plane considering the SnO_2 unit cell structure. Table 3.6a presents the geometric parameters from both the structures used in this study. Details from the HRTEM characterization and the geometric model determination are reported elsewhere (STROPPA *et al.*, 2009; STROPPA *et al.*, 2011d).

Table 3.6a: Geometric parameters for the 4.5 and 13.9 %atom Sb-doped SnO_2 nanocrystals

	Composition	4.5 $\%Sb_{atom}$			13.9 $\%Sb_{atom}$		
	Geometric Parameters	d (nm)	A (nm^2)	V (nm^3)	d (nm)	A (nm^2)	V (nm^3)
Crystalline planes	{100}	2.85	19.47	100.38	1.90	29.20	45.16
	{001}	2.49	11.32		1.76	11.31	
	{110}	2.69	34.42		2.35	7.32	
	{101}	2.65	47.41		2.12	20.16	

c) Possible Doping Configurations

The third step determines the possible dopant atoms (n) distribution configurations considering the facets included in the model. The implemented algorithm starts from a single dopant atom condition (n = 1) and a cumulative distribution is assumed for iterations.

Each iterative step consists on a single atom increment in the total dopant amount and a limited redistribution among different facets is considered through the degree of freedom (DOF) parameter. The DOF parameter indicates the maximum number of dopant atoms which could migrate from each facet to the others in order to generate a more stable configuration. Although the real nanocrystals doping level do not occur as incremental fashion, this approach is related to the consideration that there are no abrupt changes on the atoms distribution for neighbor dopant overall contents, which is represented by the use of low DOF values. DOF values ranging from 0 to 5 were tested in order to check the algorithm convergence and the results indicated that the optimum value for the analyzed system is 3.

d) Calculations and Selection Rule

The fourth step comprises the evaluation of dopant concentration ($\%Z_i$) and surface energy values (E_i) for the crystal facets for each dopant atoms distribution configuration generated on the previous step. $\%Z_i$ is calculated for each facet using the number of dopant atoms on the distribution (n_i), Ai and the surface atom density from the evaluated facets. Finally, the surface energy contribution from each facet (E_i) is calculated using the E_i ($\%Z_i$) functions illustrated on Figure 3.6b.

At this point, the geometric parameters d_i, A_i, V and surface energy E_i value from each of the possible dopant atoms distributions are determined. The most likely doping configuration is selected among the candidates by the comparison of the Wulff parameter equivalent (W*) and the Wulff parameters (W_i), retrieved for each facet by the relation between E_i and d_i. ($W_i = E_i / d_i$).

As the geometric parameters input and the dopant distribution configurations are arbitrary, the Wulff proportionality should not occur for most of the evaluated configurations. However, as a consequence of Wulff theorem, the thermodynamically favorable configuration is the one closer to have a unique Wi value. The Wulff parameter equivalent W* is an alternative approach to indicate the minimum energy configuration for a system given its total surface energy (Es) and volume V, which derivation is shown in Figure 3.6c.

$$\frac{E_s}{V} = \frac{\sum_i E_i A_i}{\sum_i \frac{d_i}{3} A_i} = 3 \frac{\sum_i E_i A_i}{\sum_i \frac{E_i}{W^*} A_i} = 3W^*$$

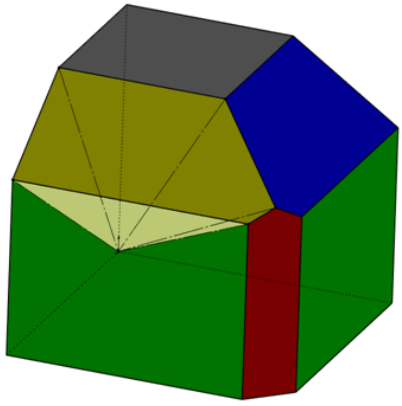

Figure 3.6c: Derivation of the Wulff parameter equivalent as function of the total surface energy (Es) and the given geometrical configuration volume (V). The highlighted step indicates the description on a polyhedral volume as the sum of pyramids volumes, which bases and heights are determined by the facets and distances from the model center, respectively.

The most favorable doping configuration for each incremental doping level was selected according to the minimum deviation between W_i and W* ($\sum (W_i - W^*)^2$). Table 3.6b exemplifies the most likely doping configuration selection for one dopant atom (n = 1) on the 13.9 $\%_{atom}$ Sb-doped SnO_2 nanocrystal geometry.

Table 3.6b: Evaluation of the most likely dopant configuration for a single dopant atom.

Distribution Candidates				**Surface Energy Density**					
$\mathbf{n_{100}}$	$\mathbf{n_{001}}$	$\mathbf{n_{110}}$	$\mathbf{n_{101}}$	$\mathbf{E_{100}}$	$\mathbf{E_{001}}$	$\mathbf{E_{110}}$	$\mathbf{E_{101}}$	**W***	$\mathbf{\sum [W_i - W^*]^2}$
1	0	0	0	2.1785	3.13	2.04	2.56	0.8947	0.208773
0	0	1	0	2.12	3.13	2.0751	2.56	0.8949	0.211092
0	0	0	1	2.12	3.13	2.04	2.5826	0.8945	0.215925
0	1	0	0	2.12	3.2722	2.04	2.56	0.8963	0.265924

e) Iteration and Results output

The steps c) and d) are iteratively repeated by the increase of dopant atoms number n and the generation of new possible dopant atoms distributions according to the DOF parameter. In this work we performed the calculations for both the 4.5 and 13.9 $\%_{atom}$ Sb-doped SnO_2 nanocrystals geometries until configurations with overall dopant contents similar to the experimentally measured were reached for both cases.

The proposed methodology output indicates the most likely dopant segregation configuration for every doping level given the unitary increment on n parameter during the iterations. Figure 3.6d presents the graphic outputs from the calculations for both crystal geometries.

A comparison between the dopant segregation behavior evaluated by the proposed methodology and the previous results by a semi-empirical approach is presented on Table 3.6c. It is indicated the methodologies are equivalent and the results deviation is probably due to the quantized dimensions used in this study, while the previously reported characterization considered the nanocrystals dimensions directly measured from HRTEM experiments.

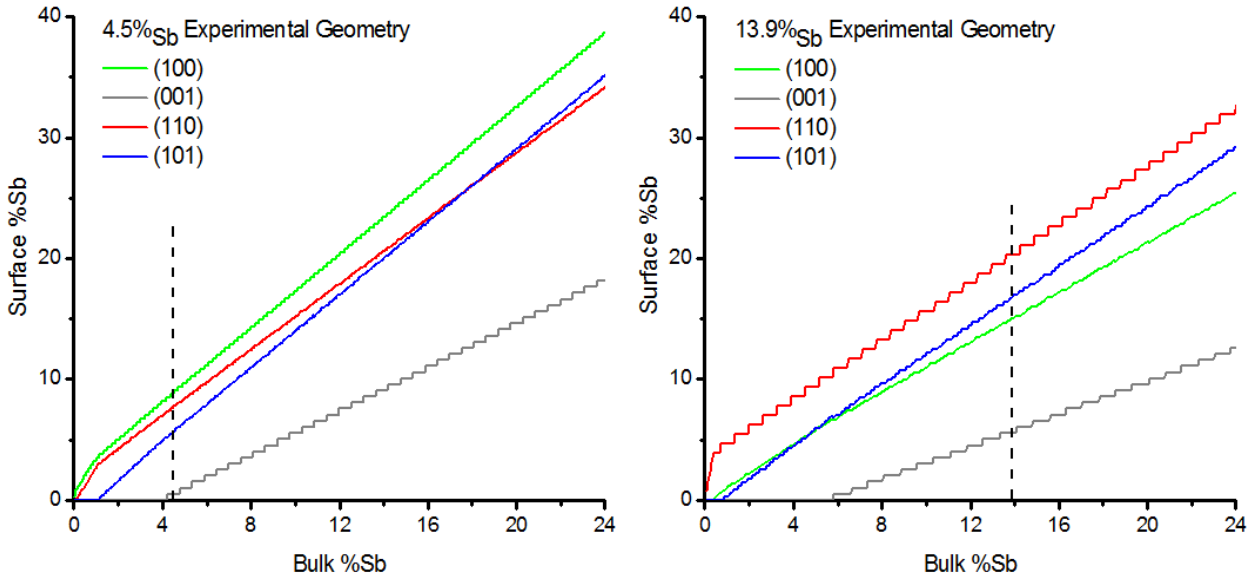

Figure 3.6d: Results from the proposed methodology for the evaluated nanocrystals geometry. The x axes represent the total dopant atomic concentration and the y axes represent the dopant concentration for each of the analyzed facets. The dashed lines indicate the 4.5 and 13.9 overall dopant contents, respectively.

Table 3.6c: Proposed methodology and semi-empirical approach comparison (STROPPAb *et al.*, 2011)

Facet	Expected Content (%)	Expected Sb atoms	Measured Content (%)	Sb atoms Equivalent	Sb atoms Deviation
4.5 $\%_{atom}$ Sb-doped SnO_2 nanocrystal geometry					
Bulk	**4.5**	**120**	**4.5**	**120**	**-**
[100]	8.5	29	8.3	28	-1
[001]	0.5	1	0.0	0	-1
[110]	7.4	45	4.7	48	+3
[101]	5.4	45	4.2	44	-1
13.9 $\%_{atom}$ Sb-doped SnO_2 nanocrystal geometry					
Bulk	**13.9**	**172**	**13.9**	**172**	**-**
[100]	14.8	76	15.3	87	+11
[001]	5.5	11	8.0	10	-1
[110]	20.3	26	16.1	15	-11
[101]	16.7	59	14.2	60	+1

The overall deviation between the atomic distributions can be evaluated by the proportion of misplaced and total number of dopant atoms considered for each system. This overall deviation is below 7% for both systems and may be partially due to the difference on the geometrical configuration used on the proposed model and the semi-empirical approach.

The described methodology is shown to be a valid first principle approach for the prediction of dopant atoms segregation on nanocrystals and equivalent to reported semi-empirical methods. As it relies on the nanocrystals geometric configuration and the surface energy evolution of different crystallographic facets as function of dopant content, its application is mostly restricted by the possibility of an accurate system description in such aspects. However, continuous improvements on characterization methods and on theoretical tools which allow the surface energy assessment indicate that this proposed methodology will provide increasingly accurate results about dopant segregation behavior, which can be decisive on nanomaterials features understanding and design.

The authors acknowledge the financial support of the research funding agencies FAPESP and DAAD. The authors would like to thank the C. Ospina, L. F. Zagonel and J. Bettini for the fruitful discussions.

3.7. Novas Ferramentas para a Análise Quantitativa em HRTEM

Conforme introduzido no Capitulo 2, a possibilidade de um amplo controle da configuração experimental em técnicas TEM pela implementação de dispositivos corretores de aberrações ópticas resultou na possibilidade de novas abordagens para a obtenção de imagens com alta resolução espacial. A mais notável dentre elas é o NCSI-HRTEM (JIA *et al.*, 2004b), na qual o uso de um coeficiente negativo de Cs propicia um notável aumento de contraste para colunas contendo espécies atômicas leves. Estas usualmente geram uma pequena variação na fase da função de onda dos elétrons quando comparadas a espécies atômicas mais pesadas. Neste contexto, a utilização do NCSI-HRTEM suporta a análise quantitativa de materiais que apresentem elementos com pesos atômicos significativamente diferentes, em especial óxidos de metais pesados. Um exemplo de aplicação é a avaliação de vacâncias de O em óxidos nanoestruturados utilizados para transporte iônico.

A Figura 3.7a apresenta exemplos de imagens obtidos pela técnica NCSI-HRTEM para amostras de Gd:CeO_2 indicando contraste para colunas atômicas contendo O.

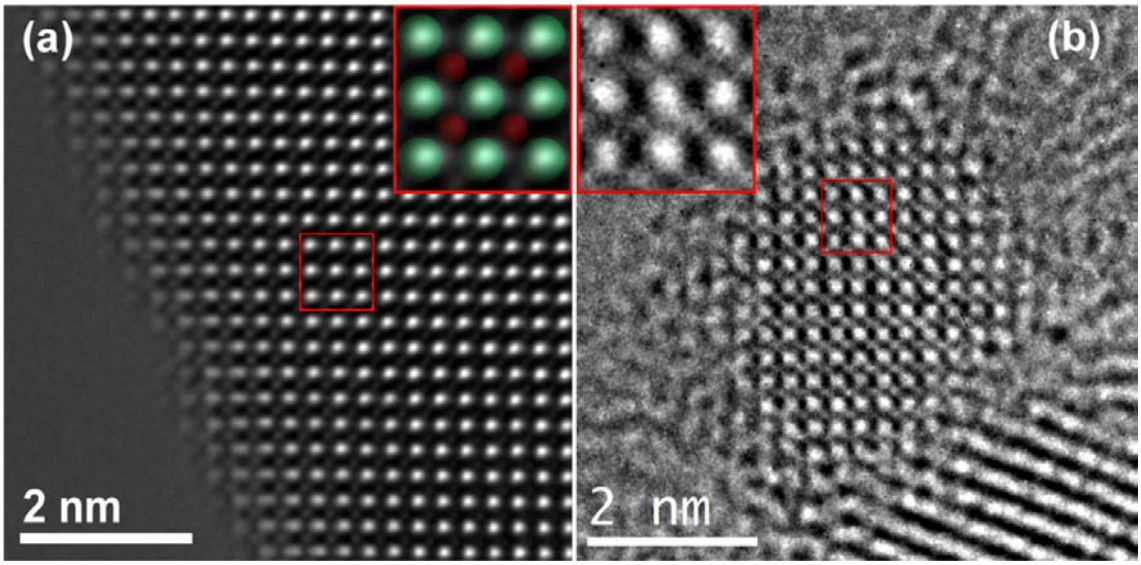

Figure 3.7a: Imagens NCSI-HRTEM de amostras a) *bulk* e b) nanocristalinas de Gd:CeO_2 no eixo de zona [100]. Os insets representam visualizações magnificadas da região de uma célula unitária e a estrutura projetada da celula unitária ao longo do eixo de zona [100]. As esferas vermelhas indicam as colunas atômicas que contem O.

Apesar do notável contraste, a avaliação quantitativa das colunas de oxigênio a partir de tais imagens é experimentalmente inviável devido às incertezas referentes às condições experimentais nas quais as imagens foram obtidas e à espessura da amostra. Com relação ao primeiro aspecto, dado que a função de transferência de contraste é dependente das aberrações ópticas, como discutido no Capítulo 2.1, são necessárias informações precisas a respeito da configuração do sistema óptico para a realização de análises quantitativas confiáveis. Com relação ao segundo aspecto, o contraste de fase em HRTEM é altamente dependente da espessura da amostra (WILLIANS *et al.*, 1996). Tal fato pode ser observado na Figura 3.7aa pela variação de intensidade do sinal nas posições de colunas atômicas de O conforme a proximidade da borda do cristal, ou seja, em função da espessura.

Uma possível alternativa para a quantificação em tais sistemas é dada pela reconstrução de séries focais (FSR) (THUST *et al.*, 1996). A realização de FSR a partir de imagens obtidas em modo NCSI permite a avaliação da função de onda dos elétrons do feixe após a interação com a amostra e a determinação acurada dos parâmetros experimentais relacionados à instrumentação. As vantagens do uso do modo NCSI em procedimentos de FSR são essencialmente relacionadas à inexistência de inversões na CTF para baixos valores de Cs, como indicado na Figura 2.1bc, e à maior facilidade de visualização das colunas atômicas de O durante os experimentos, tornando assim mais simples a localização de nanocristais orientados. É importante ressaltar que a primeira vantagem citada remete a reconstruções mais confiáveis e à determinação dos parâmetros experimentais de forma mais eficaz.

A Figura 3.7b apresenta resultados obtidos por um procedimento de FSR aplicado a imagens obtidas no modo NCSI. O procedimento experimental inclui a obtenção de 30 imagens NCSI-HRTEM (FEI TITAN 80-300 a 300kV, Cs = - 0.012 mm) com diferentes valores de defocus, sendo utilizado um passo nominal de 3 nm de defocus entre cada uma das imagens. O procedimento de reconstrução foi efetuando a metodologia Philips/Brite-Euram (software True Image) (COENE *et al.*, 1996). Vale ressaltar que, mesmo contando com o contraste aprimorado devido à utilização do modo NCSI, a realização de tal experimento para nanocristais mostrou-se extremamente trabalhosa. Os principais motivos para tal se referem à necessidade de localizar nanocristais dispersos e orientados em eixos de zona propícios e às estabilidades do filme suporte

e da amostra durante a aquisição das imagens. Tais fatores se mostraram proibitivos em relação à realização seriada de tal experimento.

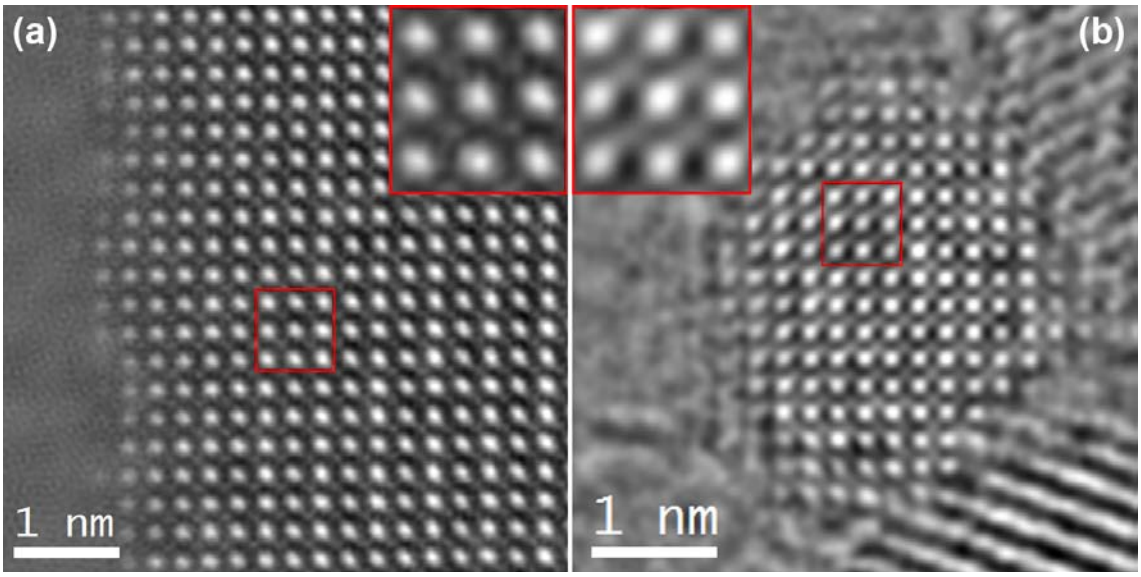

Figure 3.7b: Resultado do procedimento de FSR ilustrando a componente fase das funções de onda de saída dos elétrons para as condições experimentais que resultam na condição de mínima amplitude para amostras a) policristalinas e b) nanocristalinas de Gd:CeO_2 no eixo de zona [100]. Os insets representam visualizações magnificadas da região de uma célula unitária ao longo do eixo de zona [100].

A Tabela 3.7a sumariza os parâmetros experimentais obtidos pela reconstrução apresentada na Figura 3.7bb. É importante ressaltar que o menor espaçamento entre uma coluna atômica contendo átomos de O e a coluna atômica vizinha mais próxima é maior que 0.19 nm, assim sendo o limite de resolução da reconstrução, 0.14 nm, suficiente para resolver as colunas atômicas individuais.

Tabela 3.7a: Parâmetros experimentais estimados pelo procedimento de FSR

Parâmetro experimental	Valor estimado
Cs	- 0.010 mm
Defocus da imagem reconstruída	17.2 nm
Oscilação do defocus	2.4 nm
Astigmatismo de 2ª ordem	5.2 nm; 31.2º
Limite de resolução da reconstrução	0.14 nm

A extração de informações a partir da função de onda de saída dos elétrons que interagiram com a amostra é passível de ser realizada pelo uso da metodologia Multislice (COWLEY *et al.*, 1957) de simulação de imagens usando os parâmetros experimentais estimados pelo processo de FSR. Contudo, a metodologia Multislice requer como informação de entrada o modelo estrutural do sistema que interagiu com o feixe de elétrons, ou seja, as posições atômicas de cada um dos átomos que constituem a amostra. Tal problema poderia ser hipoteticamente resolvido pela geração e comparação entre modelos estruturais e as funções de onda de saída esperadas após a interação com a função de onda obtida experimentalmente, contudo esta abordagem é computacionalmente infactível devido ao número de variáveis presentes em um modelo estrutural que possa descrever a amostra.

Dada a complexidade da inversão da abordagem Multislice para se resolver um modelo estrutural com resolução atômica com base na função de onda de saída reconstruída a partir de uma interação durante o processo de HRTEM, uma abordagem possível é vista na comparação das variações da amplitude e da fase na interação do feixe com a amostra. De uma maneira simplificada, não considerando interações inelásticas, a solução da equação de Howie-Whelan indica que a amplitude da função de onda deve ser comportar de modo periódico em função da espessura, fato que resulta na distância de extinção, enquanto a variação absoluta da fase se dá de maneira monotônica neste mesmo regime (WILLIANS *et al.*, 1996; REIMER *et al.*, 2008). Dado tal comportamento, a representação gráfica das partes real e imaginária segundo o plot de Argand (ARGAND, 1806) da função de onda dos elétrons após a interação com a amostra contém

informações referentes à espessura, topografia e composição química de colunas atômicas individuais. (JINSCHEK *et al.*, 2004; LICHTE *et al.*, 2007; WANG *et al.*, 2010a).

A Figura 3.7c exemplifica o plot de Argand para a função de onda dos elétrons simulada para a interação com uma estrutura atômica modelo. Tal análise foi realizada pela comparação dos valores reais e imaginários da função de onda para os pixels centrais de cada uma das colunas atômicas. A realização desta mesma análise utilizando o valor médio dos pixels pertencentes às colunas atômicas após um procedimento de integração utilizando uma máscara de raio fixo (3 pixels) propiciou um resultado equivalente.

Em teoria, as espécies atômicas podem ser identificadas por passos angulares característicos entre os agrupamentos no plot de Argand, enquanto a número de átomos projetados ao longo da coluna pode ser avaliado segundo o número de grupos identificáveis. Adicionalmente, efeitos que levam à variação da topografia da amostra, como rugosidade superficial ou posicionamento dos átomos na célula unitária, levam à separação de grupos de mesma composição devido à diferença de fase na função de onda incidente na amostra. Tal efeito pode ser observado na Figura 3.7ce em decorrência do posicionamento dos átomos de Ce na célula unitária. Tal análise apresenta uma perspectiva otimista para a caracterização morfológica e quantitativa de nanocristais com resolução atômica.

No entanto, a análise de reconstruções a partir de resultados experimentais se apresenta restrita atualmente. A Figura 3.7d apresenta os plots de Argand construídos a partir das funções de onda dos elétrons obtidas experimentalmente via FSR. Os resultados indicam que o intervalo de variação das partes reais e imaginárias das funções de onda reconstruídas experimentalmente é menor que o observado para a reconstrução a partir da função de onda obtida pelo procedimento de simulação de imagens HRTEM. Tal fato pode ser justificado por uma combinação de fatores experimentais, como o limite de resolução da reconstrução e a ocorrência de absorção durante a interação entre o feixe e a amostra. Estes fatores levam à ocorrência de um padrão em forma de espiral cuja tendência se amplia com a diminuição do limite de resolução e com o aumento das interações inelásticas (WANG *et al.*, 2010a). Deste modo, os resultados presentes se justificam pela limitação experimental na obtenção de função de onda de saída dos elétrons com alta resolução espacial, sendo o limite atual superior a 0.05 nm.

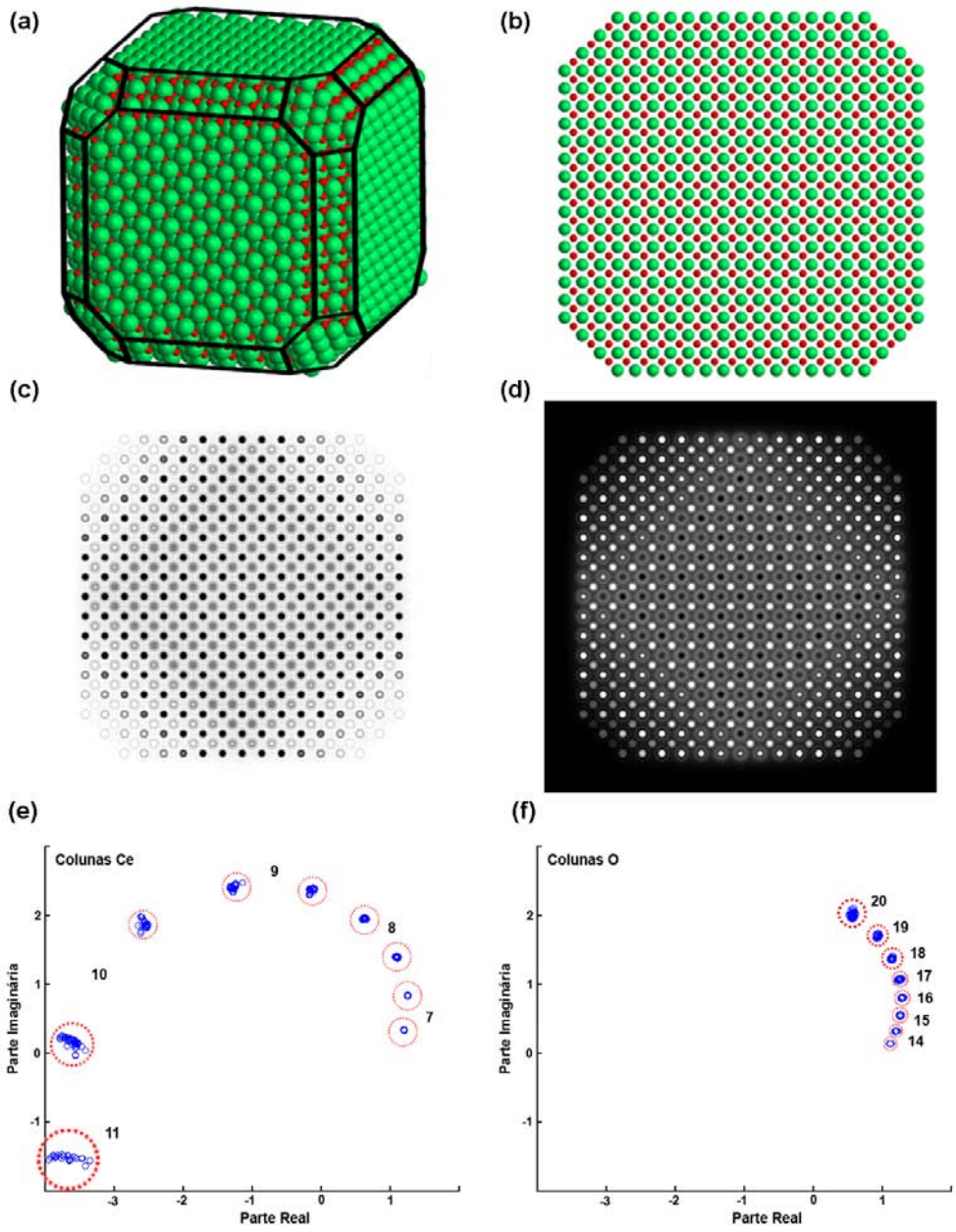

Figura 3.7c: a) Visualização isométrica e b) visão ao longo do eixo de zona [100] do nanocristal modelo utilizado no processo de simulação de imagem. c) Parte real e d) parte imaginária da função de onda obtida por simulação multislice de imagem HRTEM. Plot de Argand para os pixels centrais das colunas contendo e) átomos de Ce e f) átomos de O. Os círculos azuis representam os valores das partes reais e imaginárias dos pixels centrais das colunas analisadas, os círculos tracejados vermelhos indicam o agrupamento de colunas similares e os números adjacentes de referem ao número de átomos ao longo das colunas analisadas.

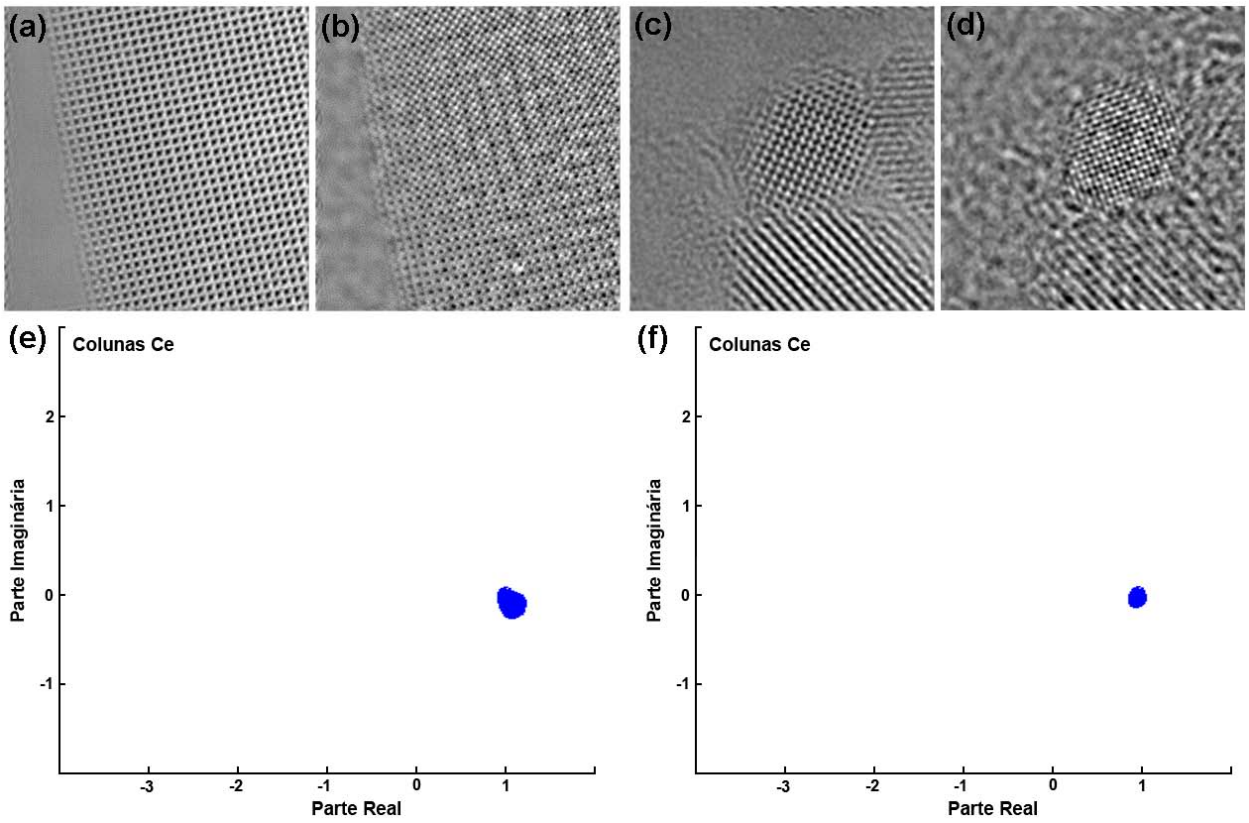

Figura 3.7d: a,c) Partes reais e b,d) partes imaginárias das funções de onda obtidas experimentalmente por meio de FSR para a,b) uma amostra *bulk* e c,d) um nanocristal de Gd:CeO_2. e,f) Respectivos plot de Argand para os pixels centrais das colunas contendo átomos de Ce. Os círculos azuis representam os valores das partes reais e imaginárias dos pixels centrais das colunas analisadas.

Em suma, os resultados apresentados indicam que a qualidade do procedimento de FSR é o fator limitante para a aplicação do plot de Argand na análise quantitativa de nanocristais em resolução atômica. Neste sentido, o aumento de resolução das reconstruções é fundamental para o avanço do uso de tal técnica. Dentre as possíveis melhorias no contexto da avaliação das funções de onda dos elétrons via FSR se destacam o aumento de estabilidade mecânica do filme suporte e o aumento da eficiência na aquisição de imagens visando a diminuição do tempo de exposição da amostra ao feixe de elétrons.

Alternativamente, o uso da holografia de elétrons em alta resolução (LICHTE *et al.*, 2007) apresenta possibilidades excepcionais na reconstrução da função de onda dos elétrons, contudo traz consigo novas dificuldades experimentais relacionadas à instrumentação, como o requerimento de uma lente do tipo *biprism* inserido na coluna, e ao preparo de amostra, como a necessidade de uma região de referência (vácuo) ao lado da amostra.

O desenvolvimento de dispositivos voltados à correção/manipulação de aberrações ópticas e de metodologias mais acuradas para os procedimentos de simulação de imagens e avaliação de funções de onda de elétrons é fundamental para ambas as metodologias baseadas em FSR e em holografia de elétrons de alta resolução. Tais aspectos devem ser determinantes para a evolução das técnicas HRTEM em direção à descrição quantitativa átomo-a-átomo de amostras cristalinas.

4. Análises Quantitativas pelo uso de HRSTEM

4.1. Reconstrução tridimensional a partir de imagens em regime HAADF

Como introduzido nos Capítulos 2.3 e 2.4, a formação de imagens a partir de elétrons espalhados em regime HAADF apresenta duas características vantajosas para a caracterização morfológica de sistemas nanoestruturados. A primeira delas é o caráter incoerente dos elétrons espalhados a alto ângulo, assim sendo desprezíveis os efeitos de contraste de difração para condições experimentais adequadas. Tais condições se referem basicamente à geometria do detector anular e ao comprimento de câmera empregado durante a análise.

A Figura 4.1a apresenta a difração de elétrons de uma amostra policristalina de SnO_2, sendo indicado em vermelho o ângulo de espalhamento de 80 mrad. Tal resultado indica que os ângulos típicos de difração em planos cristalinos são muito menores que os ângulos mínimos usados em configurações HAADF.

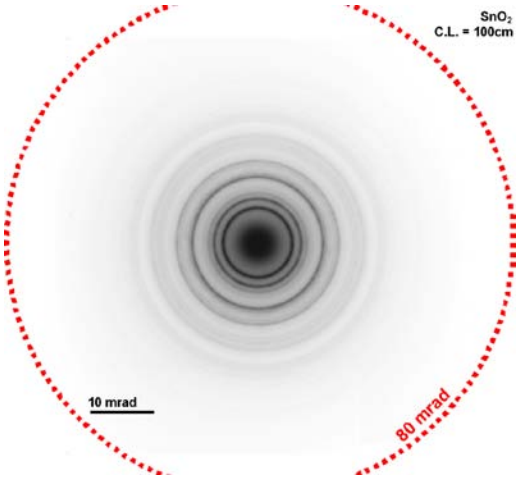

Figura 4.1a: Difração de elétrons de uma amostra de SnO_2 policristalino e indicação do limite angular de 80 mrad, usualmente utilizado como ângulo mínimo de coleção de elétrons para a formação de imagens em modo HAADF.

Dado o espalhamento no regime HAADF ser incoerente e majoritariamente elástico, os eventos de interação que o originam são decorrentes da interação do feixe de elétrons com os

núcleos dos átomos presentes na amostra. Uma primeira aproximação para a descrição destes eventos é dado pelo espalhamento Rutherford que apresenta seção de choque proporcional a Z^2. Experimentalmente, observa-se a potência de tal relação é significantemente alterada em decorrência do tunelamento eletrônico ao longo das colunas e do espalhamento difuso devido à moção térmica dos núcleos atômicos (HILLYARD *et al.*, 1995). Contudo, a dependência existente entre a seção de choque para espalhamento a altos ângulos e o peso atômico dos núcleos da amostra é a segunda característica fundamental do regime HAADF.

As propriedades do espalhamento HAADF o tornam ideal para o uso em tomografia (MIDGLEY *et al.*, 2003), técnica de reconstrução tridimensional baseada na análise de imagens obtidas em mais de uma orientação. Em tal metodologia, o uso do sinal HAADF minimiza a variação de contraste em situações que a amostra se encontra em um eixo de zona propício à ocorrência de difração, além de reduzir a contribuição do filme de suporte e eventuais espécies ligadas aos nanocristais, normalmente compostas de elementos leves, na formação das imagens.

Apesar das vantagens do uso de imagens obtidas em regime HAADF para a reconstrução tridimensional em tomografia, tal técnica apresenta restrições fundamentais em relação à obtenção de reconstruções com resolução atômica. A primeira é a limitação instrumental do intervalo de ângulos no qual a amostra pode ser inclinada para a obtenção de imagens projetadas, que leva a um artefato de reconstrução referido como ‘fatia faltante’ (*missing wedge*) (MIDGLEY *et al.*, 2003). A segunda é referente à estabilidade do microscópio e da amostra durante a aquisição das imagens, sendo neste sentido limitantes o deslocamento do sistema porta-amostra e a degradação da amostra e do filme suporte pela incidência do feixe de elétrons. Tais restrições tornam extremamente limitadas as aplicações de reconstrução tomográfica com alta resolução (VAN AERT *et al.*, 2011) e constituem um desafio atual para a evolução da técnica.

Dadas as restrições atuais em relação à tomografia em alta resolução, a aquisição de informações tridimensionais em sistema nanocristalinos, especialmente morfologia e localização de espécies atômicas, vêm sendo abordada por meio de metodologias alternativas. Em adição às metodologias baseadas em HRTEM, incluindo as mencionadas no Capitulo 3, a avaliação do sinal HAADF em conjunto com análises estatísticas e simulações de imagem tem apresentado notáveis resultados na caracterização de nanocristais.

O Capítulo 4.2 apresenta uma metodologia para a reconstrução tridimensional de nanocristais a partir de uma única imagem em modo HAADF. Neste procedimento, a extração da informação projetada ao longo do eixo de zona é efetuada pela análise do sinal integrado de cada uma das colunas atômicas, que posteriormente é relacionado ao número de átomos presentes nestas. Tal avaliação do sinal HAADF leva em conta o peso atômico Z acumulado em cada uma das colunas e resulta em um mapa de espessura (LEBEAU *et al.*, 2010). Finalmente, o posicionamento dos átomos ao longo do eixo de zona da imagem avaliada é realizado a partir da estrutura da cela unitária e das operações de simetria permitidas em relação ao eixo de zona. As imagens HAADF-HRSTEM presentes neste capítulo foram obtidas pelos colaboradores da Lehigh University, W. Weng e C. Kiely, enquanto a síntese dos nanocristais de CeO_2 foi realizada pelo colaborador do LIEC, M. A. L. Cordeiro.

Além da validação por meio de simulações HRSTEM, a metodologia apresentada no Capítulo 4.2 é suportada por resultados equivalentes obtidos pela caracterização das mesmas amostras por meio de HRTEM, como ilustrado na Figura 4.1b.

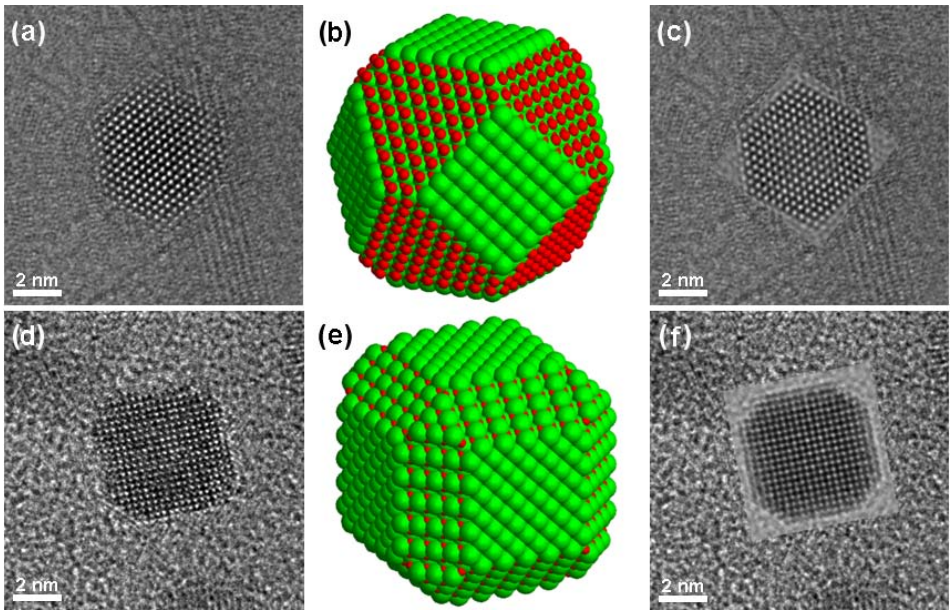

Figura 4.1b: a, d) Imagens HRTEM originais de nanocristais de CeO_2 sintetizados com diferentes adições de ácido oléico. b, e) Modelos 3D propostos a partir da simetria observada para os eixos de zona das imagens. c, f) Superposição das imagens HRTEM simuladas e experimentais.

4.2. HAADF-HRSTEM Applied to Three-Dimensional Nanocrystals Modeling

Three-Dimensional Reconstruction of Nanocrystals Morphology from Single HAADF-HRSTEM Images (STROPPA *et al.*, 2011f)

Daniel G. Stroppa, Ricardo D. Righetto, Luciano A. Montoro, Lothar Houben, Juri Barthel, Marco A. L. Cordeiro, Edson R. Leite, Weihao Weng, Christopher J. Kiely, Knut Urban, Antonio J. Ramirez

Submetido para publicação, **2011**.

Abstract

This work presents a methodology for the 3D morphological characterization of CeO_2 nanocrystals by the analysis of single unfiltered HAADF-HRSTEM images. The combined use of Gaussian mixture models, crystallographic symmetry operations and image simulations allows the reconstruction of nanocrystals at atomic resolution with a confidence level of ± 1 atom per atomic column. This procedure stands out as a remarkable tool for the morphological reconstruction of a wide range of nanostructured materials as it does not present major restrictions, such as the need to acquire multiple images from the same nanocrystal along different zone axes.

Introduction

The characterization of nanostructured systems is an important topic which is driven by the improved performances that can be achieved by the use of nanosized components. A key aspect in the effective use of the properties that arise at nanoscale lies in our ability to quantitatively characterize individual nanostructures, which is a vital step to understand their nucleation and growth mechanisms (CAO, 2004; BURDA *et al.*, 2005; STROPPA *et al.*, 2009; BARNARD *et al.*, 2010). In this context, it is necessary to develop reliable tools that can be used to describe the nanosized systems features as a function of their synthesis parameters.

Amongst the challenges for characterizing nanocrystalline systems is the acquisition of quantitative information with atomic resolution (TRASOBARES *et al.*, 2011; PENNYCOOK *et al.*, 2011). Elucidating the atomic arrangement of nanostructured materials is particularly important for the optimization of catalysis applications, in which the performance often depends on the nanocrystals faceting configuration (YANG *et al.*, 2008; DA SILVA *et al.*, 2011). Even though the most advanced characterization tools have provided significant advances in this direction, the three-dimensional (3D) morphological characterization of nanocrystals with atomic resolution still remains an important challenge.

The High Angle Annular Dark Field (HAADF) imaging mode on High Resolution Scanning Transmission Electron Microscopy (HRSTEM) is one of the most promising techniques for nanoparticles characterization as it allows the direct imaging of the projected atomic columns and provides information on their atomic weight and thickness (PENNYCOOK *et al.*, 1998; HILLYARD *et al.*, 1995; VOYLES *et al.*, 2002). This inherent feature of HAADF-HRSTEM is due to the high-angle incoherent electron scattering signal for each point scanned on the sample, which can be correlated to the atomic number (VAN AERT *et al.*, 2009; KRIVANEK *et al.*, 2010) and to the atomic columns thicknesses (ROSENAUER *et al.*, 2009) with a spatial resolution down to 500pm (PENNYCOOK *et al.*, 2011).

Recent reports have shown the successful thickness mapping of Au foils (LEBEAU *et al.*, 2010) and the 3D reconstruction of an Ag precipitate via discrete tomographic reconstruction (VAN AERT *et al.*, 2011). These studies describe the use of both HRSTEM multislice image simulation (COWLEY *et al.*, 1957; KIRKLAND, 1998) and Gaussian Mixture Models (GMMs) (MCLACHLAN *et al.*, 2000) arguments to associate the integrated signal from each atomic

column to their thicknesses. These approaches pointed out the feasibility of performing atomic resolution 3D morphological characterization of nanocrystals using HAADF-HRSTEM images with a ±1 atom confidence level. However, the requirement of model samples and/or the acquisition of multiple images from the same nanocrystal on different zone axes may restrict the practical application of these methodologies to a number of systems, especially those which cannot withstand long or multiple exposure times to the electron beam during data acquisition. In addition, environmental difficulties such as sample and microscope instabilities during sample tilting procedures may make the 3D morphological characterization of nanocrystalline samples by tomography approaches very difficult or even impractical.

This work presents an alternative approach for the atomic resolution 3D morphological reconstruction of nanocrystalline samples by the analysis of a single HAADF-HRSTEM image. The proposed methodology combines two steps, namely (i) the estimation of atomic columns thicknesses by GMM classification and (ii) 3D reconstruction using the crystallographic symmetry operations allowed by the unit cell of the examined nanocrystals. This approach has been applied to faceted CeO_2 nanocrystals displaying two different morphologies. In addition, HRSTEM multislice image simulations from symmetric faceted model structures have been used to evaluate the methodology accuracy.

Experimental Methods

CeO_2 nanocrystals were synthesized following a previously reported two phase approach (YANG *et al.*, 2006). In this method, 30 mL of a 0.085 mol/L cerium (III) nitrate aqueous solution was transferred to a 100 mL Teflon-lined stainless-steel autoclave, and then 30 mL of toluene and 0.30 mL of tert-butylamine were added under ambient conditions without stirring. CeO_2 nanocrystals with distinctly differing morphologies could be generated by manipulating the oleic acid concentration employed in the preparation. Polyhedral (labeled A) and cube-like (labeled B) CeO_2 nanocrystals were obtained by the use of low (3mL) and high (6mL) OA additions, respectively. A thermal treatment at 180 ^{o}C for 24 h was carried out for both variants of the synthesis process. Finally the material was washed several times and re-dispersed in non-polar solvents (e.g. toluene, hexane, chloroform) after the reaction.

Samples for electron microscopy analysis were prepared by dropping the diluted colloidal solution onto copper grids covered with a thin (~ 5 nm) continuous amorphous carbon film and allowing the solvent to evaporate. STEM characterization was carried out using a JEOL JEM-2200FS microscope equipped with CEOS probe corrector and a Schottky field-emission electron gun operating at 200kV. The HRSTEM imaging experiments were carried out using an electron beam with a 25 mrad convergence angle, 0.09 nm spot size, and a 64 μs/pixel dwell time during scanning. The bright field (BF) and HAADF signals were acquired simultaneously to ensure that the 110-300 mrad angular range of the HAADF detector included most of the incoherently scattered electrons.

The atomic columns peak detection and signal integration on the ‘as-obtained’ images were performed using Gaussian masks of fixed radii, whose size were selected with the aim of including approximately 80% of the peaks signal for each analyzed HAADF-HRSTEM image. A detailed description of these procedures can be found in the Appendix B.

The integrated intensities from the atomic columns were classified as a histogram and the data fitting procedure was performed by the use of multiple normal distributions according to the GMM (MCLACHLAN *et al.*, 2000). The histogram bin size, as well as the number of fitting Gaussian curves and their respective parameters was selected in such a way as to minimize the absolute values of residual error. After the fit, each atomic column was assigned to a Gaussian

distribution. The correlation between the fitting distributions and the atomic column thicknesses was performed by taking into account the periodicity of the mean value of the fitting curves and the integrated intensity of the isolated Ce atoms, which were used to assign the integrated intensity for a 'single-atom column'. The integrated intensity analysis from the isolated Ce atoms can be found in the Appendix B. Finally, the spacing between Ce atoms along the specific zone axes and the 3D topography of the examined nanocrystals were determined according to the allowed symmetry operations of the CeO_2 unit cell. Structural files of both 3D reconstructions (nanocrystals A and B) are available in the Appendix B.

Symmetric models of the nanocrystals morphologies A and B were constructed using the MEGACELL software (STROPPA *et al.*, 2011c) based on the HAADF images Fourier Transform (FT) indexing, the number of crystalline planes and the allowed symmetry operations for the Fm3m space group of CeO_2.

HRSTEM image simulations of the nanocrystal models were performed using the Dr. Probe software (BARTHEL *et al.*, 2011). The multislice algorithm considered an incident 200kV electron wave emanating from a source with 0.07 nm radius, and passing through 25 mrad radius condenser aperture. Spherical aberration (Cs) was the only optical aberration included in the calculation and this parameter was estimated to be 0.001 mm. The structural files employed for both symmetric models A and B can be found in the Appendix B. The models A and B were sectioned into 29 and 41 equally distributed slices, respectively, aiming at single-atom layers for a better adequacy to the weak phase object approximation (WPOA). In order to include the effects of thermal motion, 10 frozen-phonon configurations were calculated for every slice. The multislice calculations for models A and B were performed for each pixel (scanning point) on the 298 x 298 and 256 x 256 image matrices, respectively. Hence similar pixel sizes were obtained in relation to the experimental images for nanocrystals A and B, respectively. The resultant wavefunction amplitudes were evaluated within a 110-300 mrad annular range.

Results

Figure 4.2a presents representative ‘as-obtained’ HAADF-HRSTEM images of CeO_2 nanocrystals synthesized with a low oleic acid concentration (Fig. 4.2aa) and a high oleic acid concentration (Fig. 4.2ab). Previous HRTEM characterization of these systems indicated that they have polyhedral and cube-like morphologies. Due to the atomic weight dependence in the high angle incoherent electron scattering regime, and the experimental imaging configuration, only Ce atomic columns present distinguishable signal in respect to the background. Hence the signal from the oxygen atoms in these HAADF images is considered as a background component. Figure 4.2a insets present the FT pattern analyses, which allow the nanocrystals zone axis determination and the projected atomic planes indexation.

Quantitative analysis of these two particular HAADF-HRSTEM images was carried out via the signal integration of each peak, which is then related to the corresponding number of atoms in each column as shown later. Figure 4.2ba and 4.2bb show color maps of nanocrystals A and B, respectively, depicting the intensity of the integrated signal for each atomic column, and presenting a first insight into the CeO_2 nanocrystals 3D morphology.

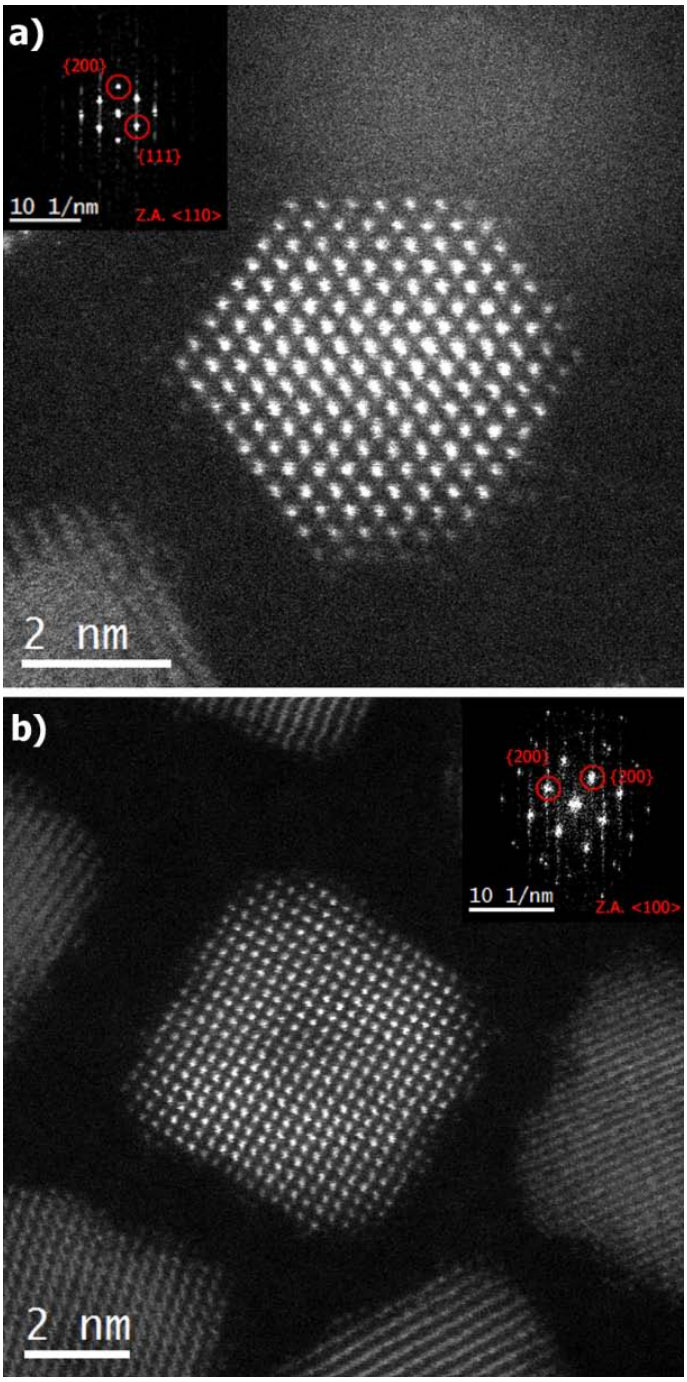

Figure 4.2a: 'As-obtained' HAADF-HRSTEM images from CeO_2 nanocrystals (a) A and (b) B. The insets present the images FT analysis including the zone axis and projected crystallographic plans indexation.

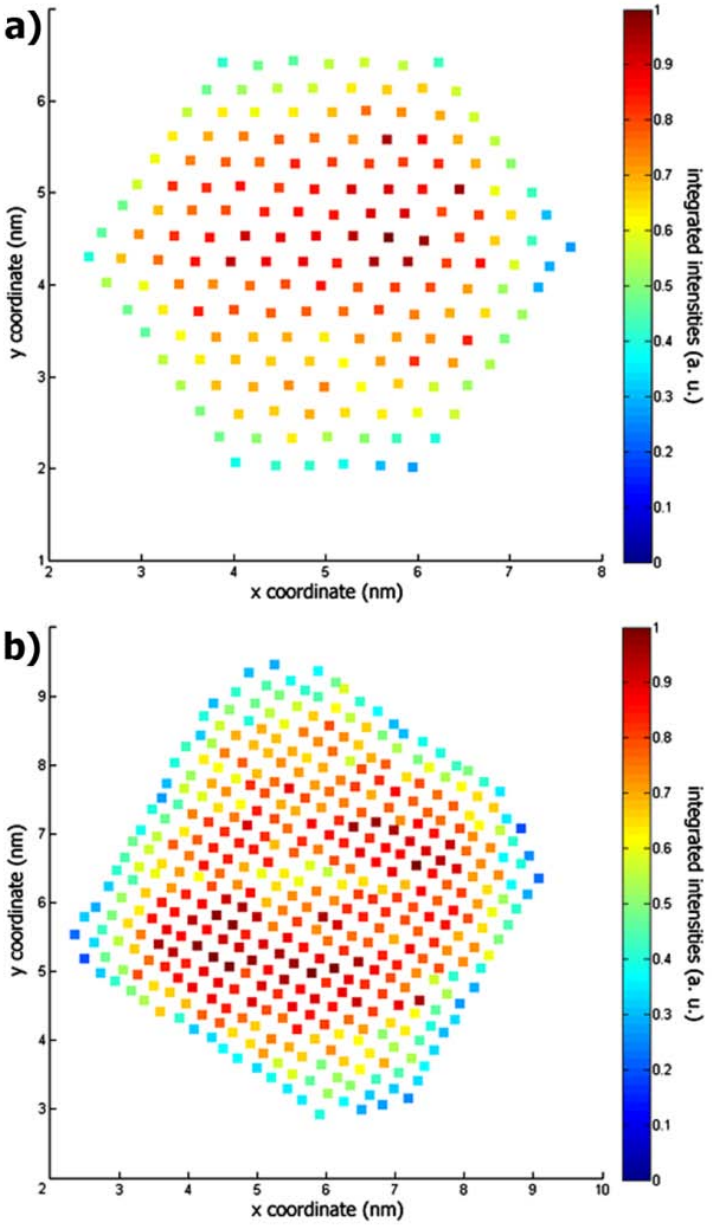

Figure 4.2b: Color maps obtained after the signal integration of the atomic column positions from the unfiltered HAADF-HRSTEM images of the nanocrystals A and B, shown in Figure 1. The *x* and *y* coordinates are referenced to the center of the integration masks center and the color coding refers to the normalized integrated intensity.

Although the 3D crystal morphology can be inferred by the combined analysis of the columns integrated signal intensities and the indexing of the projected crystallographic planes, a more accurate analysis can be achieved from a column-by-column thickness evaluation using the assumption of a quantized number of Ce atoms in each column. This approach minimizes the overall noise contributions to the atomic column signal quantification, such as the inherent noise of the detection system, electron channeling effects, and the background HAADF signal from (i) oxygen atoms in the CeO_2, (ii) the carbon support film and (iii) any residual ligand molecules attached to the nanoparticles.

In order to correlate the HAADF-HRSTEM spots integrated signal to the number of atoms in each column, an intensity histogram was calculated for both nanocrystals A and B images and then a fitting procedure was carried out using the GMM approach. This procedure describes the HAADF signal of the atomic columns as a mixture of Gaussian distributions, and allows grouping the atomic columns according to their integrated intensity. As a result, each quantized column thickness is represented by a Gaussian distribution and the experimentally integrated intensities are assigned to the one of them.

The number of Gaussian distributions was set as a limited parameter, ranging from 5 to 25, after a first estimate of the columns maximum thickness in atoms number given the nanocrystals lateral dimensions. The histograms bin sizes and the mean value, standard deviation and amplitudes of each Gaussian distribution were considered as free parameters during the fitting procedure. The best configurations to describe the analyzed systems were considered to be those which exhibit the minimum absolute value of residual errors.

Figure 4.2c shows the intensity histograms calculated from HAADF-HRSTEM images of particles A and B respectively. The results from the GMM fitting procedures and their residual errors for the analyzed images are also included. For both cases, the absolute residual errors were less than 10^{-14} for each sampling point.

The correlation between the index of distribution curves and the number of Ce atoms on the analyzed columns can be built by taking into account (i) a first estimate of the columns thickness given by the measured lateral nanocrystals dimensions and (ii) the allowed symmetry operations of the CeO_2 unit cell. Two relevant parameters were inspected in order to verify that an accurate

assignment of the number of atoms to each distribution curve shown in Figure 4.2c has been carried out. The first parameter was the mean periodicity value of the distribution curves as an approximately linear correlation is expected between the integrated signal and the number of atoms on the projected columns (VAN AERT *et al.*, 2011). The second parameter was the quantitative analysis of the integrated intensity of the peripheral atomic columns in each HAADF image, which supported the intensity distribution assignment for a single Ce atom.

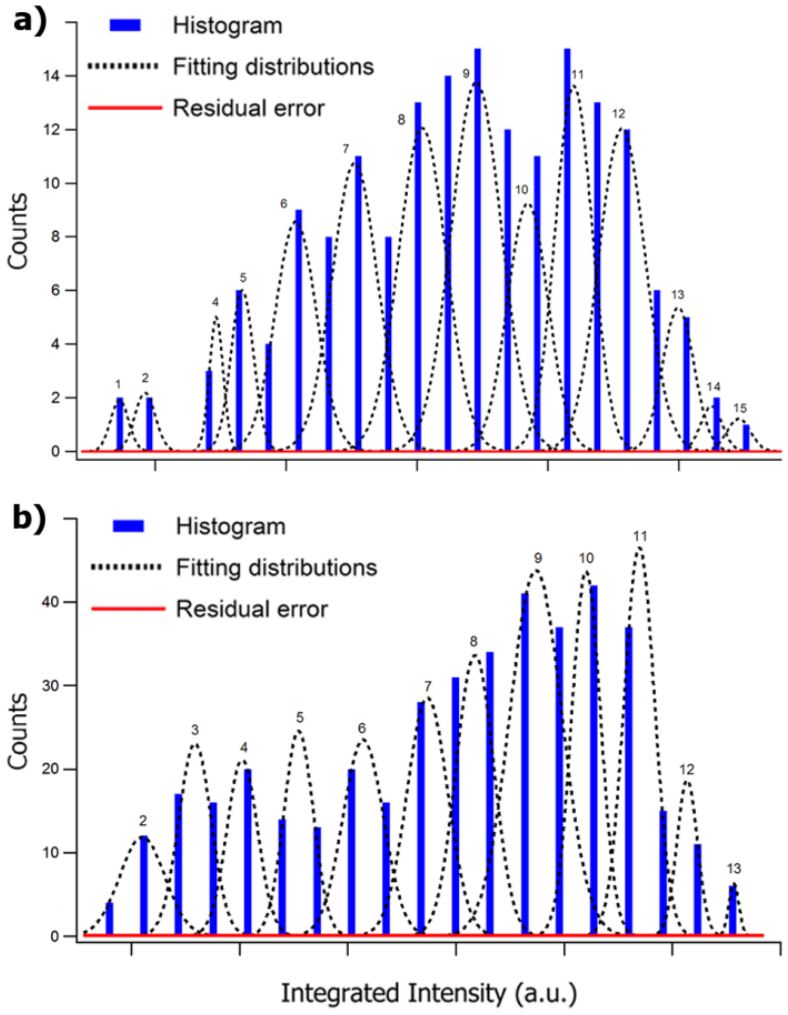

Figure 4.2c: Integrated intensity histograms derived from the HAADF-HRSTEM images of nanocrystals (a) A (Fig. 1(a)) and (b) B (Fig. 1(b)). The dashed lines indicate the optimal distribution curves given by the GMM fitting and the solid red curves indicate the residual errors. The number assigned to each distribution curve refers to the number of atoms along the atomic columns.

The standard deviation parameters from the fitting distributions can be related to a number of factors, such as the inherent noise of the HAADF-HRSTEM images, the scattering contribution from oxygen atoms, surfactant and/or adsorbed species on the nanocrystals surfaces, and signal fluctuations due to the channeling effect, which is highly dependent on the local environment of the atomic column. However, the extent of these effects cannot be quantitatively analyzed from the fitting results due to the low occurrence of some atomic columns groups. However, the assignment of each atomic column in the experimental images to the closest fitting distribution according to its integrated intensity value implicitly minimizes the afore-mentioned contributions to the standard deviation, and provides a quantized 3D map for the analyzed images. In addition, the precision of the thickness assignment can be initially estimated to be ± 1 atom from the maximum overlap of fitting distributions.

The quantized thickness maps for both CeO_2 nanocrystals morphologies A and B are shown in Fig. 4.2da and 4.2dc respectively, and their corresponding experimental 3D structural models are presented in Figs. 4.2db and 4.2dd. These models were constructed after GMM classification of the integrated intensities of each atomic column in the HAADF-HRSTEM images. The surface coordinates of atoms in the 3D models were calculated considering the zone axis and the mirror operations that are allowed for both the ⟨100⟩ and ⟨110⟩ direction families according to the Fm3m symmetry of the CeO_2 unit cell. A movie and an interactive 3D model for each analyzed nanocrystal type are available in the Appendix B. It should be noted that the green spheres in Figures 4.2db and 4.2dd, which represent Ce atoms in the nanocrystals are illustrative, in that their radii and positions are not in complete agreement with the unit cell structure.

The reconstructed 3D morphologies successfully highlight few structural characteristics which were expected from observing the projected facets termination on the HAADF-HRSTEM images, such as the {111} and {200} for nanocrystal A (Fig. 4.2aa) and the {111}, {220} and {200} facets for nanocrystal B (Fig. 4.2ab). However, the obtained results also indicate that the actual nanocrystals exhibit asymmetric features such as vacant Ce sites at the surface, and isolated Ce atoms on surface terraces.

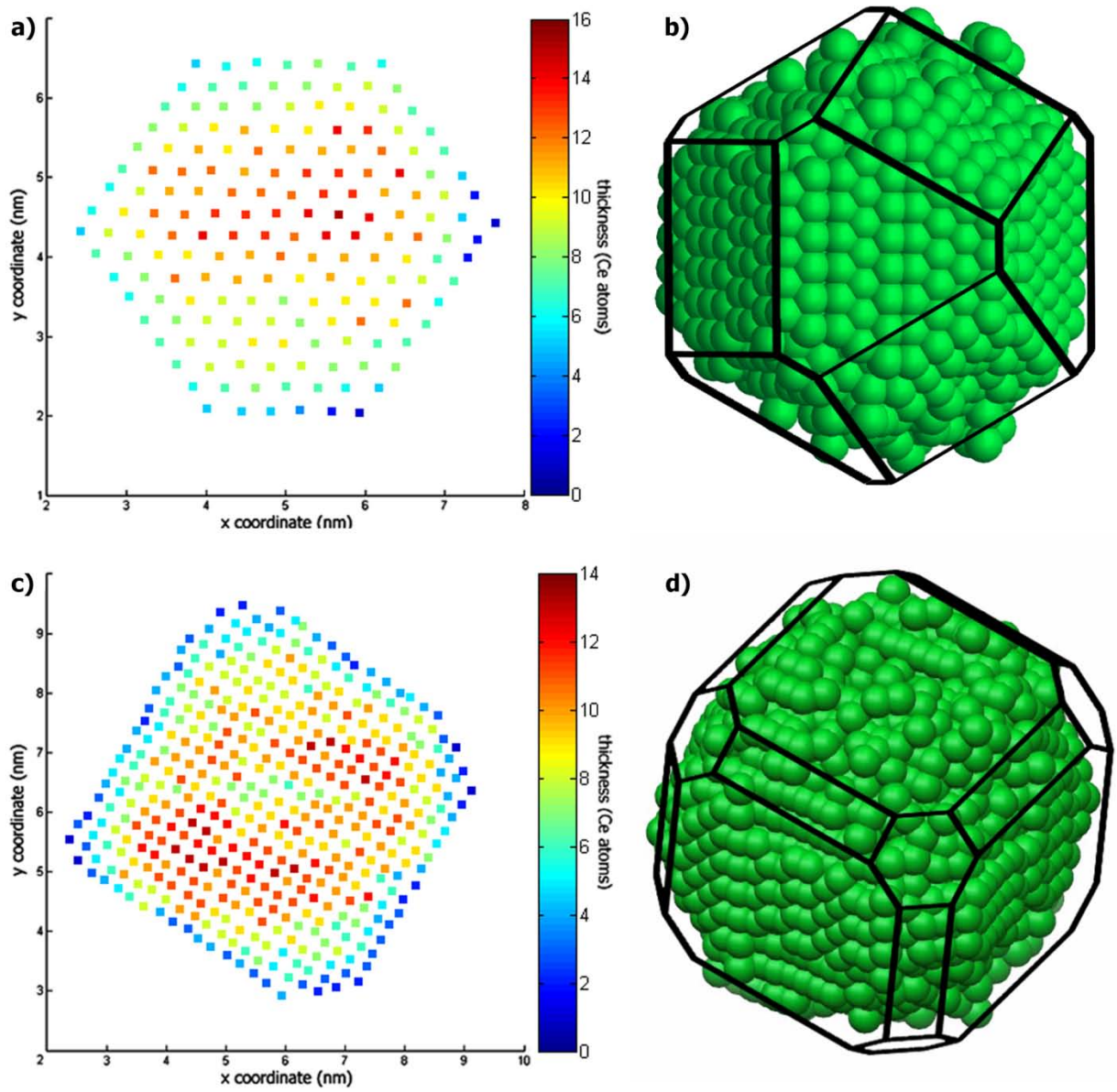

Figure 4.2d: a, c) Color maps generated after thickness map quantization by the GMM fitting procedure for the nanocrystals A and B, respectively. The color coding now represents the number of Ce atoms along each atomic column position. b, d) 3D morphology reconstructions based on the calculated column thicknesses and on the symmetry operations allowed by the CeO_2 nanocrystal structure.

In order to verify the accuracy of the quantification method and to provide a deeper insight into the deviations from Fm3m symmetry exhibited by the proposed 3D model structures (i.e. Figs. 4.2db and 4.2dd), HAADF-HRSTEM image simulations of perfectly symmetric CeO_2 model structures were also carried out. Figure 4.2ea presents the symmetric models constructed from the analysis of the symmetry operations allowed by the CeO_2 unit cell and the experimental HAADF-HRSTEM images without including surface defects. The relevant projections of the symmetric models A and B, as observed in experimental HAADF images are presented in Figure 4.2eb and their corresponding simulated HAADF-HRSTEM images are shown in Fig. 4.2ec.

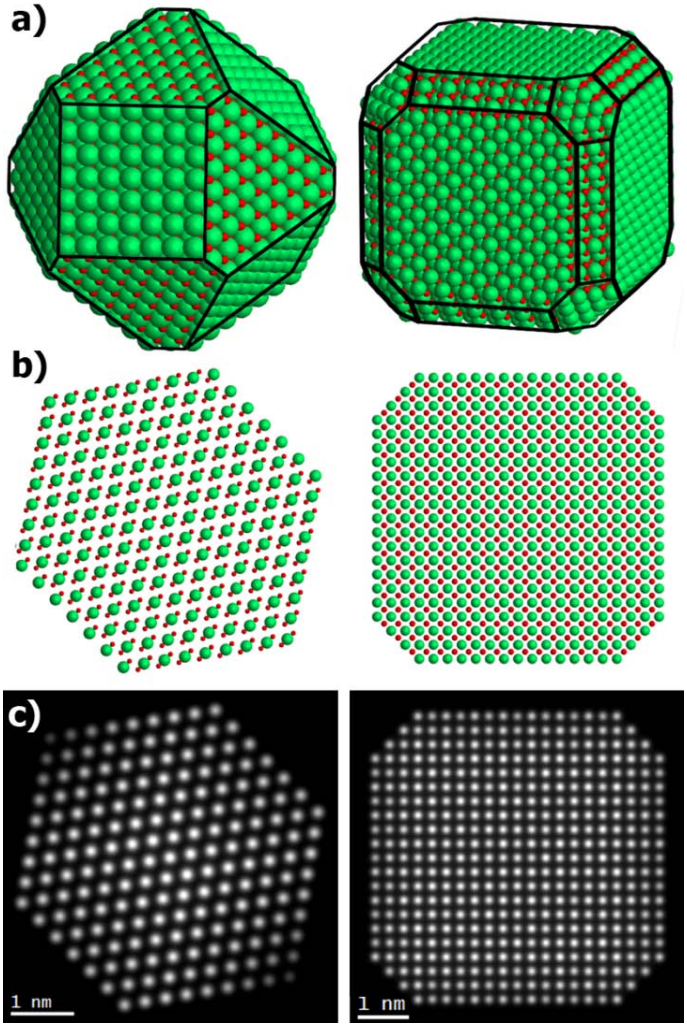

Figure 4.2e: a) 3D representations of perfectly symmetric CeO_2 nanocrystals models with morphologies A and B. b) [110] and [100] projected views of the model structures A and B; c) the corresponding HAADF-HRSTEM image simulations from the models presented in (b).

A qualitative comparison between the simulated and experimental HAADF-HRSTEM images is available in the Appendix B. This analysis points out that the actual nanocrystals present significant deviations from the symmetric construction, which extent can be up to an entire crystalline plane. This could be due to several reasons, including (i) the highly specific number of atoms required to construct a regular structure with a complete number of unit cells, (ii) the crystal growth process, (iii) the migration of atoms from highly unstable sites such as edges and kinks and (iv) a real surface reconstruction effect due to the presence of adsorbed ligands. However, in spite of the fact that the actual nanocrystals appear to be defective, the symmetric models still represent a reasonably good approximation for describing the overall nanocrystals morphologies.

A quantitative analysis of the simulated HAADF-HRSTEM images demonstrates a direct correlation between the integrated intensity from atomic column signal in the experimental images to the simulated ones, as shown in Figure 4.2f for the nanocrystal A.

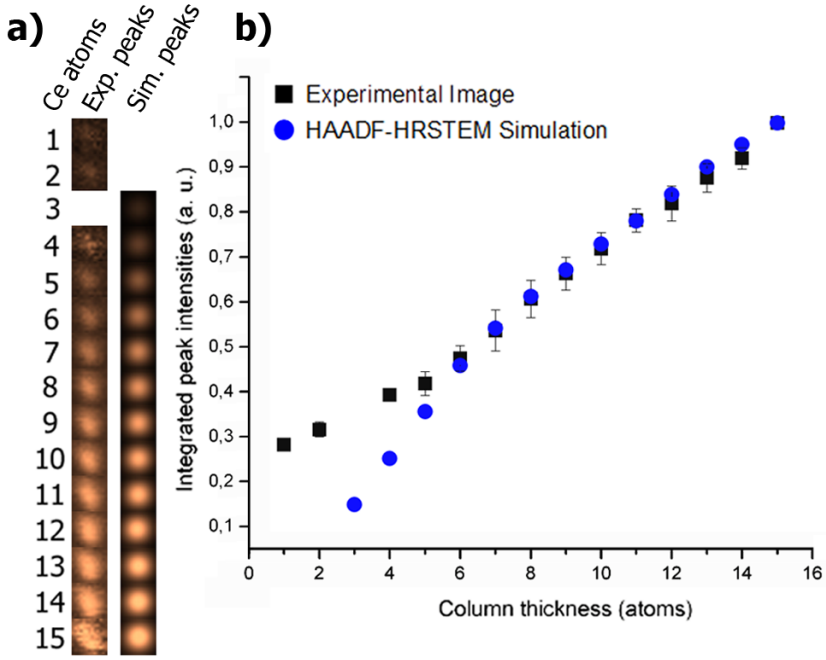

Figure 4.2f: a) Comparison between the averaged peaks images for different atomic column thicknesses on experimental and simulated images from nanocrystal A. b) Correlation between the normalized intensities value for experimental and simulated images peaks.

Figure 4.2fa presents a fair agreement between the experimental and simulated averaged peaks images for different column thicknesses in the CeO_2 nanocrystal A. The minor differences between these can be justified by a number of factors which were not taken into account in the HAADF-HRSTEM image simulation, such as the electron beam broadening due to interactions with low atomic number atoms from surfactants and the carbon support film, the residual sample tilt, residual optical aberrations, and any artifacts related to the scan stability. However, the better agreement between the normalized peak intensity values from the experimental and simulated images (Fig. 4.2fb) indicates the correct assignment of fitting distributions during the nanocrystals analysis procedure. In addition, the correlation between the integrated peak signals and the atomic column thickness is verified to be approximately linear within the measurement regime, as supported by the HAADF-HRSTEM simulation results (Fig. 4.2fb). The deviation noted for atomic column thicknesses below 5 atoms in Figure 4.2fb is probably due to the poorer signal-to-noise ratio and the greater influence on HAADF signal from lower atomic number elements in this ultra-thin regime.

Finally, it should be noted that the integrated peak intensity plot shown in Fig 4.2fb includes error bars based on standard deviation measurements which allows us to estimate the maximum error to be ± 1 atom within a 90% confidence level. The observed error bar variation as a function of the number of projected atoms is related to the low number of events in the image of crystal A for some atomic columns thickness groupings, (i.e. namely the lower occurrence of atomic columns with 1, 3, 4 and 15 cerium atoms). However, a more representative deviation is seen on the other column thicknesses where better sampling statistics exist.

Conclusions

An accurate determination of 3D nanocrystal morphology with atomic resolution is presented after the quantitative analysis of single HAADF-HRSTEM images using the GMM classification approach. This procedure allows direct thickness mapping, which can be used in conjunction with symmetry information pertinent to the unit cell of the material under investigation for evaluating the atoms positions along the zone axis. The comparison between the experimental and simulated HAADF-HRSTEM images indicates that a correct assignment of the

number of atoms in each atomic column is feasible after the GMM classification procedure and that this quantification methodology provides local thickness measurements within the ± 1 atom confidence level.

Even though the 3D morphological reconstruction relies upon knowing the symmetry operations of a specific unit cell and requires the images to be recorded along specific zone axes depending on the analyzed material, the use of single unfiltered HAADF-HRSTEM images improves its applicability or, at least provides a thickness map of the examined nanocrystal with a high level of precision. In this sense, this methodology is an alternative to tomographic reconstruction approaches (KANEKO *et al.*, 2007; VAN AERT *et al.*, 2011) which tend to require a much greater experimental effort and a lot of post data processing and which may be prohibitive in practice due to electron beam sensitivity limitations of the nanocrystalline material under examination.

From the perspective of quantitative characterization of nanocrystals at atomic resolution the HAADF-HRSTEM technique is still unmatched and will probably be improved in the near future by the development of other STEM based techniques that can provide further complementary information. These techniques may either provide a better perspective on the atomic coordinates along the zone axis, for example through the use of confocal-STEM, or complementary spectroscopic information for compositional analysis though atomically resolved EELS and/or XEDS spectrum imaging.

Acknowledgement

The authors would like to thank the STEM Group at Paris Sud Université, L. F. Zagonel and J. Bettini for the fruitful discussions. The authors also acknowledge the financial support of FAPESP and DAAD. WW and CJK gratefully acknowledge financial support from the NSF/EPSRC - Materials World Network Program (Grant # DMR-0709887).

4.3. EELS-HRSTEM aplicado à avaliação quantitativa direta da segregação de dopantes

Adicionalmente à possibilidade da caracterização morfológica em resolução atômica propiciada por HRSTEM, técnicas espectroscópicas associadas indicam a possibilidade de análises elementares quantitativas com alta resolução espacial, como abordado no Capítulo 2.4.

Embora seja um ramo com notáveis desenvolvimentos recentes, são escassas as técnicas de caracterização quantitativa com resolução atômica. No âmbito de técnicas que possibilitam análises diretas, são demonstrados resultados bem-sucedidos obtidas por meio de Atom Probe Field Ion Microscopy (APFIM) (HONO, 2002), Scanning Tunneling Microscopy (SPM) (BAER *et al.*, 2010), XEDS-HRSTEM (D'ALFONSO *et al.*, 2010) e EELS-HRSTEM (EGERTON, 2010). Contudo, tais métodos apresentam restrições, especialmente em relação aos tipos de amostras analisáveis e o preparo requerido para a adequação destas aos aparatos experimentais.

As técnicas baseadas em HRSTEM apresentam inicialmente a vantagem de possibilitarem a análise simultânea de diversos sinais de espalhamento, sendo a complementaridade das informações extraídas um fator positivo em relação à confiabilidade das análises. Em decorrência dos avanços instrumentais em HRSTEM apresentados no Capítulo 2.4, o uso de XEDS e EELS em análises quantitativas com alta resolução espacial tem se intensificado e parte das restrições apresentadas na Tabela 2.2a tem sido superadas. No entanto, algumas características específicas de tais técnicas as favorecem em diferentes casos. A Tabela 4.3a apresenta uma resumida comparação entre XEDS e EELS em relação a análises quantitativas em alta resolução em modo HRSTEM. Embora ambas as técnicas apresentem atualmente a possibilidade de análises com alta resolução espacial, a EELS-HRSTEM é mais explorada neste âmbito atualmente devido à melhor SNR e pelo apenas recente desenvolvimento de detectores XEDS suficientemente eficientes.

Diversos casos científicos têm sido abordados por meio da aplicação de EELS-HRSTEM na análise de segregação de espécies atômicas com alta resolução. Dentre estes podem ser citados a caracterização da segregação de espécies químicas na interface de filmes finos (PEI *et al.*, 2008), a caracterização de estruturas *core-shell* (WANG *et al.*, 2009; ABEL *et al.*, 2011; DEEPAK *et al.*, 2011), e a investigação da segregação e do estado de oxidação de espécies dopantes em nanopartículas (SUN *et al.*, 2005).

Tabela 4.3a: Comparativo entre XEDS e EELS aplicados em HRSTEM

Característica	XEDS	EELS
Eficiência na coleção do sinal e relação sinal-ruído	Baixa: raios X gerados se propagam em todas as direções	Alta: elétrons inelásticos espalham a baixos ângulos
Background, qualidade dos picos e interpretabilidade	Interpretação direta devido a reduzido bkg e picos definidos	Elevado bkg e picos irregulares dificultam interpretação
Informações disponíveis	Quantificação de espécies químicas	Idem XEDS, estrutura eletrônica e outras excitações
Delocalização do sinal	Mínima	Baixa (Å) para CLR, significativa (nm) para LLR
Restrição em relação a espécies químicas	Dependente da construção do detector	Dependente dos picos característicos

O Capítulo 4.4 apresenta a aplicação de EELS-HRSTEM na caracterização de amostras de CeO_2 e Gd:CeO_2 com o intuito de investigar a segregação de dopantes em nanocristais individuais. A síntese dos nanocristais de Gd:CeO_2 foi realizada pelo colaborador do LIEC, C. J. Dalmaschio. A aquisição de espectros EELS foi realizada por meio de *line profiles* devido à impossibilidade da obtenção de mapas 2D pelo uso da metodologia *spectral imaging* (EGERTON, 2010), dados os tempos necessários para a aquisição dos mapas e a conseqüente degradação das amostras. A análise quantitativa dos espectros individuais foi realizada pela integração de picos de Ce, Gd e O localizados na CLR após a subtração do fundo.

A fim de possibilitar a correlação entre a segregação de espécies e as direções cristalográficas, os espectros foram preferencialmente obtidos para nanocristais semi-orientados, sendo a direção do *line profile* ao longo dos planos atômicos resolvidos. Contudo, o requerimento de um alinhamento do sistema óptico que propiciasse alta corrente restringiu parcialmente a resolução espacial, sendo assim inviável a reconstrução 3D referente à segregação de dopantes. Contudo, tal prática reduziu a oscilação da intensidade total de espalhamentos inelásticos nos espectros ao longo do *line profile*, assim reduzindo flutuações de erro na quantificação.

4.4. Dopant Atoms Segregation Analysis on Gd:CeO_2 Nanocrystals

Dopant Atoms Segregation and Oxygen Vacancies Analysis on individual Gd:CeO_2 Nanocrystals by EELS-STEM (STROPPA *et al.*, 2011h)

Daniel G. Stroppa, Lothar Houben, Luciano A. Montoro, Cleocir J. Dalmaschio, Edson R. Leite, Knut Urban, Antonio J. Ramirez

Submetido para publicação, **2011**.

Abstract: This work presents the quantitative characterization of individual Gd:CeO_2 and CeO_2 nanocrystals by STEM-EELS with 0.29 nm spatial resolution. The EELS spectra quantification pointed out to a dopant enrichment at the Gd:CeO_2 nanocrystals surface, as well as a hydroxyl capping layer on both systems. In addition, the Oxygen quantification on the studied systems indicated the dopant atoms role on the vacancies generation. The above-mentioned characteristics are closely linked to the material ionic oxygen transport performance and efficiency as catalyst.

Introduction

High resolution quantitative characterization of materials represents a fundamental step on the development of functional materials with improved performance. As the perspective on nanosized components use increases due to the remarkable properties that can be obtained at nanoscale, the required description of nanostructures features is continuously pushed towards the atomic resolution level.

Nanocrystalline systems properties and stability are determined by their atomic-level configuration. Among the relevant aspects in this scenario are the nanoparticles morphology, atomic species distribution, and interactions with the environment (CAO, 2004). All of these factors are intrinsically related to resultant surface energy distribution, which governs most of the unique properties at nanoscale (BARNARD, 2010).

In recent years, significant efforts have been made in order to understand and control nanomaterials characteristics aiming the improvement of catalytic properties. Several studies related to the synthesis configuration optimization and the nanocrystals morphology control (BURDA *et al.*, 2005; XIA *et al.*, 2009a) have reported successful results. However, few results regarding the atomic species distribution evaluation on doped nanocrystals have been presented (ABEL *et al.*, 2001, DEEPAK *et al.*, 2011).

Few techniques can provide a high spatial resolution characterization including atomic species distribution on nanocrystalline systems. The most common approaches for such task are X-Ray Energy Dispersive Spectroscopy (XEDS) (D'ALFONSO *et al.*, 2010) and Electron Energy-Loss Spectroscopy (EELS) (EGERTON, 2010), both of them usually associated to Scanning Transmission Electron Microscopy (STEM) (STROPPA *et al.*, 2011e) due to the possibility of simultaneous spectroscopy analysis and imaging. More recently, Atom Probe Field Ion Microscopy (APFIM) (HONO, 2002) presented atomic species quantification with high spatial resolution for a limited number of systems due to sample preparation issues. Alternatively, the evaluation of atomic species segregation on nanocrystals has been carried out by indirect methodologies based on the combination of high resolution (S)TEM imaging and simulation (KRIVANEK *et al.*, 2010), *ab initio* surface energy calculations (STROPPA *et al.*, 2009; STROPPA *et al.*; 2011d), and strain field analysis (MONTORO *et al.*, 2009).

Aiming the atomic species segregation and surface structure analysis on nanostructured Gd:CeO_2 (CGO), which is a promising material for catalysis (TROVARELLI, 2002; RAMIREZ-CABRERA *et al.*, 2004) and fuel cell applications (ORERA *et al.*, 2010; KHARTON *et al.*, 2011), this works presents the quantitative characterization of individual CeO_2 and CGO nanocrystals by the use EELS-STEM technique.

Experimental Section

CeO_2 and CGO nanocrystals were synthesized using a co-precipitation approach.

For the CeO_2 system, 6mL of a 1.0 mol/L NaOH solution was added to 20 mL of a 0.1mol/L cerium (III) nitrate aqueous solution. The resulting solution was transferred to a 100 mL Teflon autoclave and heated to 130^{o}C for 30 minutes using a microwave oven (Anton Paar – Synthos 3000). Finally the material was centrifuged, washed several times and re-dispersed deionized water.

For the CGO system, stoichiometric amounts of $Ce(NO_3)_3$ and $Gd(NO_3)_3$ were mixed in order to obtain a 30%$_{atom}$ Gd aqueous solution with 0.1mol/L cations concentration. 20 mL of such aqueous solution was added to 6mL of a 1.0 mol/L NaOH solution, and the resulting solution was processed in an identical way as described above for the CeO_2 sample.

Samples for STEM analysis were prepared by dropping the diluted CeO_2 and CGO solutions onto copper grids covered with a thin (~ 5 nm) continuous amorphous carbon film and allowing the water to evaporate. Prior to the STEM analysis, the samples were submitted to a heat treatment at 80 ^{o}C for 5 h into a vacuum chamber (10^{-5} Pa) in order to eliminate residual water and/or contaminants from the samples surfaces.

STEM characterization was carried out using a FEI TITAN 80-300 microscope equipped with probe corrector and a Schottky field-emission monochromated electron gun operating at 300 kV. The EELS and imaging experiments were carried out using an electron beam with a 25 mrad convergence angle, a 0.11 nm spot size and a 150 pA beam current. The images were acquired using the HAADF signal collected within the 80 to 300 mrad annular range. The EELS acquisition was performed in a line profile mode with a 10 s collection time for each spectrum.

The spectrometer entrance was limited with a 18 mrad aperture and a 0.5 eV energy discretization was used for recording the energy-loss spectrum within the 400 - 1023 eV interval.

The spectra treatment was performed by the background subtraction after a power-law fitting based on the pre-edges signal, followed by $Ce_{M4,5}$, $Gd_{M4,5}$, and O_K peaks integration. The integration windows parameters present on Table 4.4a were based on such peaks onset and their width.

Table 4.4a: EELS spectra quantification parameters

Peak	**Edge onset**	**Integration window width**	**Inelastic cross-section** (POWELL, 1989)
O_K	532 eV	22 eV	157 barns
$Ce_{M4,5}$	883 eV	45 eV	649 barns
$Gd_{M4,5}$	1185 eV	50 eV	216 barns

Results and Discussion

A representative EELS spectrum obtained during the line-profile analysis of a CGO nanocrystal is presented on Figure 4.4a, including the background signal estimation and the integration window. It indicates that the microscope and spectrometer configuration is suitable for the simultaneous acquisition of O, Ce, and Gd core-loss peaks with a sufficient signal-to-noise ratio (SNR) for the chemical species quantification.

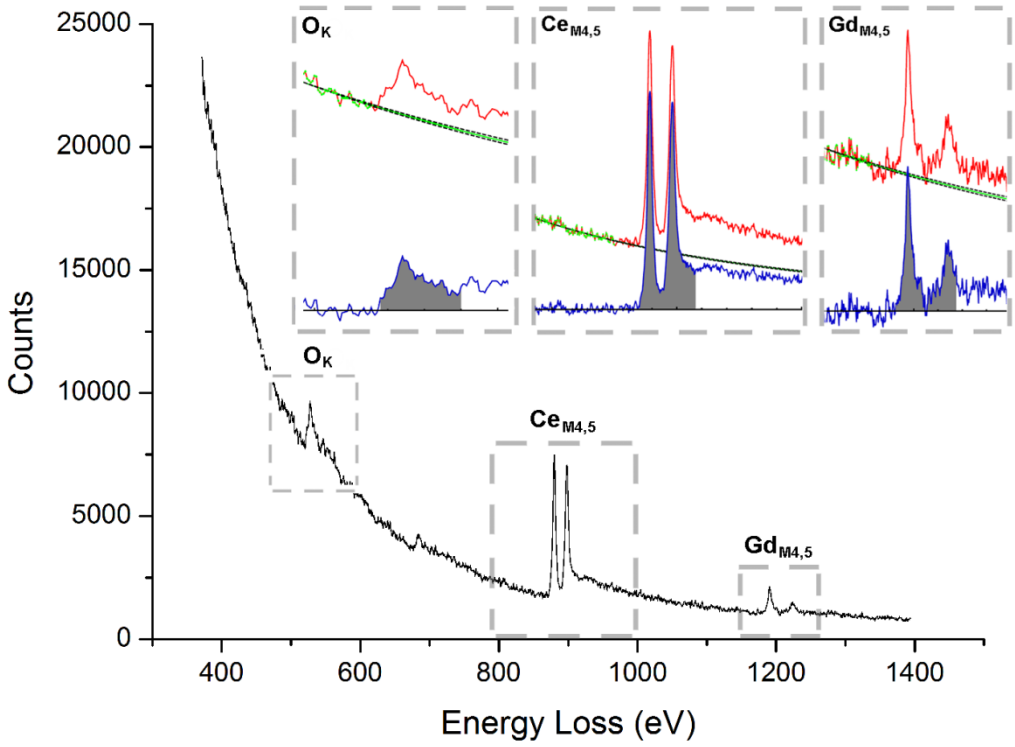

Figure 4.4a: EELS spectrum extracted from the line profile measurement, indicating the successful simultaneous acquisition of O_K, $Ce_{M4,5}$ and $Gd_{M4,5}$ peaks with an adequate SNR. The insets present the background curves estimation (dashed lines) based on the pre-peak signals (green dots). The integration windows (grey regions) are also indicated on the background-subtracted signal (blue lines).

The relative quantification results of the obtained line profile spectra are shown on Figure 4.4b. The HAADF image shown on Figure 4.4ba indicates the approximate location of each of the collected spectrum along the line profile. Such measurement direction on a semi-oriented nanocrystal was chosen in order to minimize the total inelastic signal fluctuation which would occur for positions in between atomic columns on an oriented nanocrystal, thus allowing a similar SNR for all the collected spectra. In addition to avoid the variable error that would be induced by SNR fluctuation, this approach provides partial crystallographic orientation information that can be related to chemical species quantification afterwards.

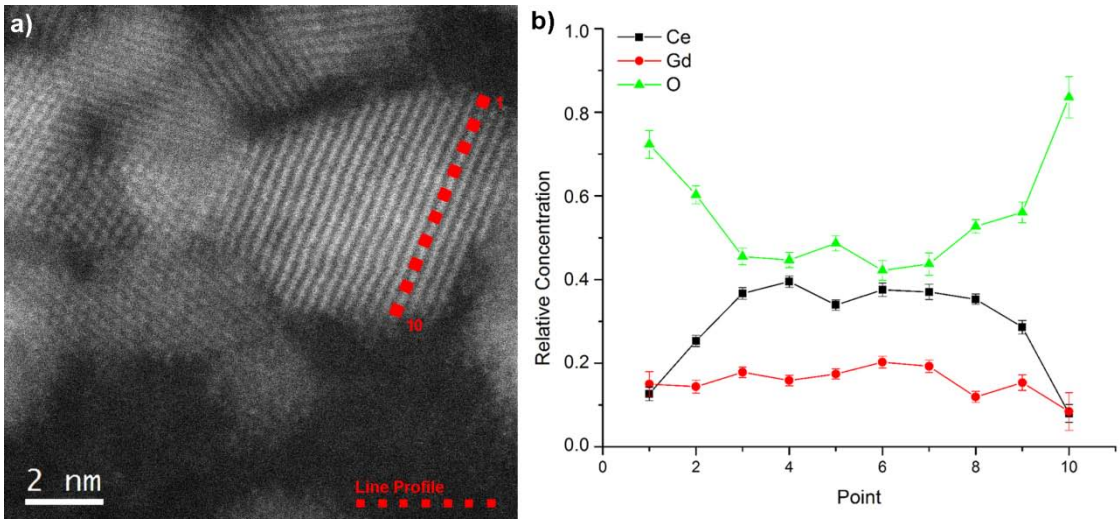

Figure 4.4b: a) CGO nanocrystal HAADF image acquired just before the EELS analysis including the approximate line profile location (red dashed line). b) Relative quantification of O, Ce, and Gd chemical species for each obtained spectra along the line profile.

The quantification error on Figure 4.4bb was estimated based on the background fitting maximum error. Although a significant deviation may exist for the given integration windows inelastic cross-sections, it is assumed that this error is minimized as the relative chemical species quantification is performed from a single spectrum, i. e. under the same experimental conditions. The direct quantitative analysis of the collected spectra is feasible due to the kinematic scattering regime existent on the experiment condition, considering the 105 nm estimated mean free path (MALIS *et al.*, 1989) for CeO_2 and the 5nm approximate thickness of the analyzed nanocrystal. The quantification spatial resolution can be estimated to be 0.29 nm after beam profile convolution with the characteristic length of core-loss signal delocalization (EGERTON, 1996), evaluated to be less than 0.2 nm for energy losses higher than 500 eV. The size of each of the line profile marks on Figure 4.4ba corresponds to maximum interaction area for the collected spectra.

The results shown on Figure 4.4bb indicate that a significant and approximately symmetric fluctuation on the relative composition occurs as function of the position along the nanocrystal, indicating that the chemical species distribution over the nanocrystal is not homogeneous. Figure 4.4c present the Gd relative concentration profile for the same measurement taking into account

only Ce and Gd atoms as scatter centers. It indicates that the Gd atoms tend to segregate preferentially towards the nanocrystal surface.

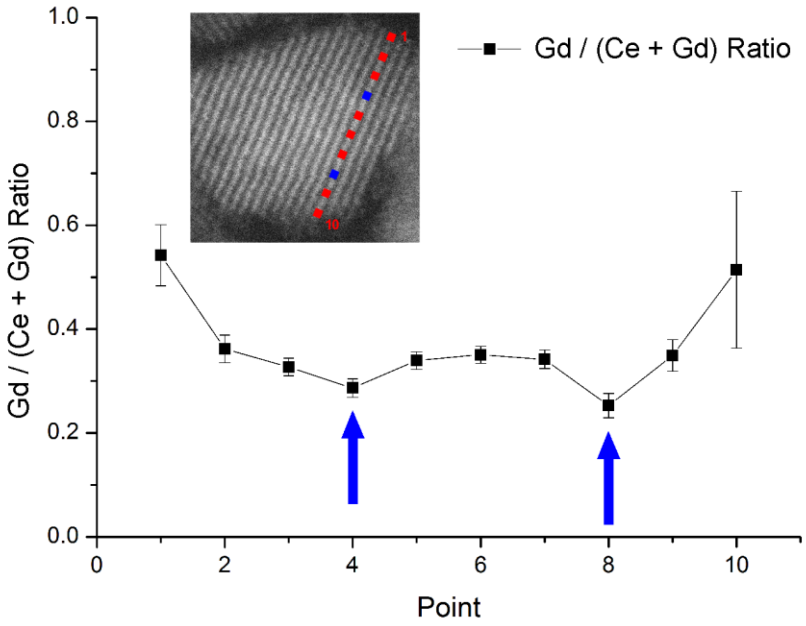

Figure 4.4c: Quantitative results on the Gd atomic ratio for each EELS spectrum on the line profile measurement. The blue arrows indicate Gd depletion zones in contrast to the enrichment observed on the CGO nanocrystal projected surface.

Qualitatively, the surface segregation of Gd atoms can be justified by the surface energy overall reduction due to the lower oxidation state for Gd (+3) in respect to Ce (+4) on the most stable oxide compounds. In this sense, the evidenced Gd atoms preferential migration will stabilize the system due to the reduction of unmet chemical bonds at the nanocrystal surface, similarly to the grain boundary segregation reported for polycrystalline materials (LI *et al.*, 2011).

Quantitatively, the total Gd / Ce ratio on the evaluated nanocrystal, 0.367 ± 0.037, agrees with the experimentally measured ratio for a large sample area (~300 nanocrystals), 0.340 ± 0.013, and is close to the nominal content expected from the synthesis procedure.

Figure 4.4d present the O relative concentration profile for the analyzed CGO nanocrystal and from a reference CeO_2 sample nanocrystal.

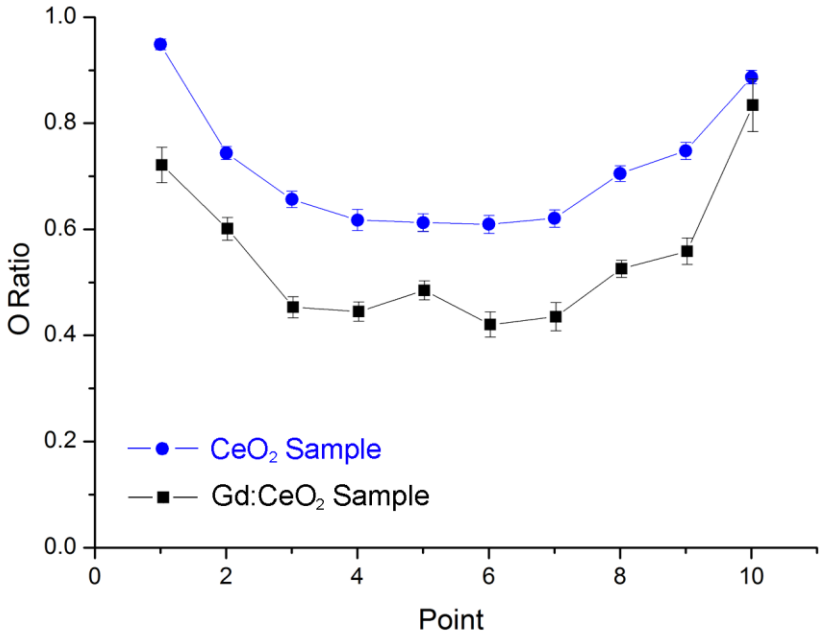

Figure 4.4d: Quantitative results on the O atomic ratio after the quantitative analysis of CGO (black squares) and CeO_2 (blue circles) nanocrystals.

The results present on Figure 4.4d indicate two key aspects on both the structure and the properties of functional materials at nanoscale, (i) the surface structure and (ii) the equilibrium defects.

The measured O enrichment at the nanocrystals projected surface that indicates a hydroxyl capping layer on both CeO_2 and CGO nanocrystalline systems. This feature can be justified due to the OH-rich basic synthesis environment as NaOH was used as precipitation agent. Despite the fact that this layer is only apparent on the chemical species quantification of very thin areas, such as the nanocrystals projected borders, it is probably distributed evenly along the nanocrystal surface. Consequently, the nanocrystals oxygen net content should be lower than the experimentally measured.

Regarding the equilibrium defects, the reduced O content from the doped material in comparison with the CeO_2 indicates the presence of equilibrium O vacancies on the nanostructure. Although the absolute quantification of the oxygen concentration is not possible due to both the atoms knock on during the analysis and the hydroxyl capping layer, the doping

effect on CeO_2 structure can be discussed as similar conditions were used on both the nanocrystals synthesis and the EELS analysis.

The nanocrystals average oxygen contents for CeO_2 and CGO nanocrystals within the points 2 to 9 range are 66.5 $\%_{atom}$ and 49.2 $\%_{atom}$, respectively. This result indicates that the approximate 34% $_{atom}$ Gd dopant addition represented a 26% relative decrease on O occupied sites. However, if only the difference between the most stable oxidation states from Ce and Gd is taken into account, the expected decrease on the O content from CeO_2 (66.67$\%_{atom}$ O) to the $Ce_{0.66}Gd_{0.34}O_{1.83}$ compound (64.66$\%_{atom}$ O) is approximately 3%. This discrepancy can be partially justified due to the induced Ce3+ content withing CGO (BABU *et al.*, 2009) and to the restrictions on the oxygen vacancies ordering (OU *et al.*, 2008) given the nanocrystals reduced dimensions.

Conclusions

The high resolution quantitative characterization of CGO and CeO_2 individual nanocrystals by EELS-STEM provided information on key aspects that determine these materials efficiency on ionic transport and catalysis applications. A direct evidence of Gd dopant atoms migration to the nanocrystal surface is provided, as well as the presence of a hydroxyl capping layer which acts as an additional surface energy reduction mechanism. Finally, the O quantification results comparison for doped and undoped CeO_2 systems provided further insights on the Gd dopant atoms effects on the structure of such materials.

Acknowledgement

The authors would like to thank the M. Heggen, C. Ospina and L. F. Zagonel for the fruitful discussions. The authors acknowledge the financial support of the research funding agencies FAPESP and DAAD.

5. Análise do Mecanismo de Crescimento de Nanocristais

5.1. Teorias Clássicas de Nucleação e Crescimento de Nanocristais

As possibilidades e as perspectivas na caracterização de sistemas nanocristalinos discutidas nos capítulos anteriores indicam a extração de informações fundamentais ao modelamento de nanocristais. Os aspectos tratados até o momento – morfologia, segregação de dopantes e distribuição de energia superficial – apresentam interdependência e estão diretamente correlacionados com os processos de formação e evolução do sistema ao longo tempo. Deste modo, a descrição da nucleação e do crescimento de cristais pode ser abordada com o suporte dos resultados experimentais obtidos por técnicas quantitativas de HR(S)TEM. Conseqüentemente, o desenvolvimento de tais técnicas traz consigo perspectivas a respeito da descrição mais acurada destes aspectos no modelamento de nanocristais.

A síntese de sistemas nanoestruturados é usualmente dividida segundo sua abordagem. Enquanto métodos físicos para a redução das dimensões dos materiais precursores, como técnicas litográficas e o uso de moinhos de alta energia, são denominados *top-down* (BAKKER *et al.*, 1995; XIA *et al.*, 1999), as metodologias baseadas na síntese de nanoestruturas a partir de espécies atômicas individuais são referidas como *bottom-up* (LEITE, 2004). Uma parcela significativa das técnicas existentes no contexto *bottom-up* é baseada em rotas de síntese em fase líquida, nas quais os compostos resultantes são obtidos pela redução química de sais precursores ou pela decomposição de precursores organometálicos metaestáveis sob condições controladas.

A formação de nanocristais neste contexto é iniciada pela etapa de nucleação, na quais núcleos de dimensões reduzidas são formados a partir dos monômeros provenientes da decomposição dos agentes precursores devido à supersaturação do ambiente reacional. A fase de nucleação é descrita como a formação e resolubilização de núcleos segundo o critério de estabilidade termodinâmica, existindo um raio crítico (r*) a partir do qual os núcleos tornam-se estáveis e inicia-se o processo de crescimento, segundo o diagrama apresentado na Figura 5.1a.

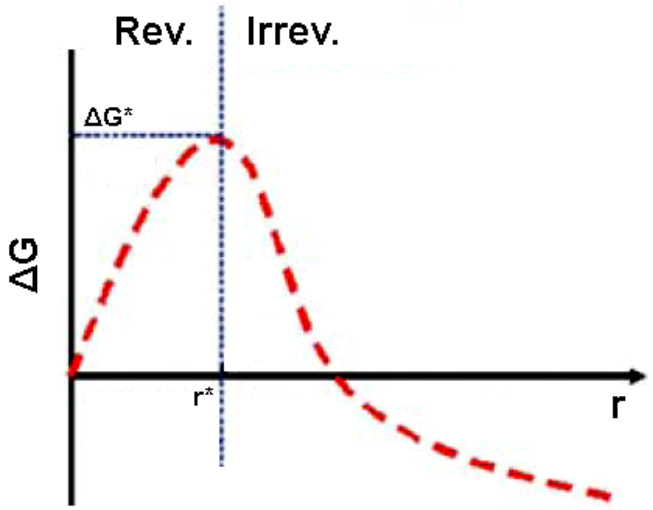

Figure 5.1a: Diagrama de estabilidade para a etapa de nucleação em função do raio dos núcleos formados. A partir do raio crítico r*, os núcleos formados são termodinamicamente estáveis e inicia-se o processo de crescimento.

A evolução de sistemas nanocristalinos a partir da formação dos núcleos se dá a partir dos mecanismos crescimento. De uma maneira simplificada, a combinação dos mecanismos Maturação de Ostwald (*Ostwald Ripening*) (OR) (RATKE *et al.*; 2002) e Coalescência Orientada (Oriented Attachment) (OA) (PENN *et al.*, 1998; PENN *et al.*, 1999) é utilizada para a descrição do crescimento de nanocristais. Em ambos os casos, o crescimento de partículas em sistemas nanocristalinos é motivado pela redução da energia livre, dada neste contexto pela minimização da área superficial por unidade de volume.

O mecanismo OR baseia-se na solubilização de núcleos ou de partículas menores e o transporte de massa para partículas maiores. Tal efeito é devido à dependência entre a solubilidade (S) e o tamanho de cristal (d), descrita pela Equação 5.1a em função da tensão superficial γ_{SL} e da temperatura T, e é favorecido nos caso em que o material apresenta um alto coeficiente de solubilidade no meio reacional e não existem restrições majoritárias no transporte de espécies atômicas.

$$S = S_0.\exp(4\gamma_{SL}.V_m/R.T.d) \qquad \textbf{Equação 5.1a}$$

Neste regime, a tendência é que os íons em solução migrem para sítios de maior energia nas partículas maiores, como defeitos cristalinos e superfícies mais energéticas, ocorrendo assim o crescimento preferencial ao longo da direção cristalográfica que apresente maior energia superficial (VOORHEES, 1985). A descrição cinética clássica do mecanismo de OR é dada segundo o modelo LSW (LIFSHITZ *et al.*, 1961; WAGNER, 1961).

O mecanismo OA é baseado na colisão entre os núcleos/nanocristais devido à movimentação térmica do sistema, ocorrendo a coalescência para os casos ocorram interações que resultem em uma orientação cristalográfica propicia e que apresentem energia cinética suficiente para promover a formação de um único domínio cristalino (LEE *et al.*, 2005). Dado o caráter estatístico da ocorrência de colisões orientadas (RIBEIRO *et al.*, 2005), uma primeira aproximação é a de que as colisões efetivas sejam proporcionais à áreas superficiais expostas de facetas de mesma família cristalográfica. Neste sentido, a direção de crescimento preferencial esperada é normal aos planos cristalográficos com a menor energia superficial, dado que segundo o critério termodinâmico estes devem estabilizar facetas com maiores áreas.

O Capítulo 5.2 apresenta a caracterização do crescimento de nanocristais de SnO_2 pelo mecanismo de OA, sendo evidenciado um comportamento anômalo em relação à descrição clássica presente na literatura. A síntese dos nanocristais de SnO_2 utilizados neste estudo foi realizada pelos colaboradores do LIEC, T. G. Conti e R. O. da Silva. A avaliação do crescimento anisotrópico em relação a duas direções cristalográficas idênticas é feita em função de argumentos termodinâmicos e cinéticos, sendo indicado que a descrição clássica do OA apresenta limitações em relação à descrição de sistemas específicos.

5.2. Anomalous Oriented Attachment Growth Behavior on SnO_2 Nanocrystals

Anomalous Oriented Attachment Growth Behavior on SnO_2 Nanocrystals (STROPPA *et al.*, 2011b)

Daniel G. Stroppa, Luciano A. Montoro, Armando Beltrán, Tiago G. Conti, Rafael O. da Silva, Juan Andrés, Edson R. Leite, Antonio J. Ramirez

Publicado na revista *Chemical Communications*, 47, 3117-3119, **2011**.

Abstract

This work reports a detailed characterization of an anomalous Oriented Attachment behaviour for SnO_2 nanocrystals. Our results evidenced an anisotropic growth for two identical ⟨110⟩ directions, which are equivalent according to the SnO_2 crystallographic structure symmetry. A hypothesis that considers edges energies contribution is proposed to describe this behaviour.

Introduction

Semiconductor nanomaterials have been intensively studied over the last decade due to a number of novel applications in a variety of technological fields. Tin Oxide (SnO_2) can be noticed among this group for its use on gas sensors, transparent conductive oxide and solar cell devices. Several works (NIEDERBERGER *et al.,* 2006b) report synthesis procedures for tailoring SnO_2 nanocrystals with controlled morphology and some studies (DA SILVA *et al.*, 2009) elucidated the crystal growth behavior for particular synthesis environments. Probing its low solubility on some typical solvents, some works (STROPPA *et al.*, 2009) further evaluated SnO_2 and its doped forms growth behavior to enhance the oriented attachment (OA) growth mechanism theory (PENN *et al.*, 1998; PENN *et al.*, 1999). The originally proposed OA mechanism regards the adjacent nanocrystals self-organization and coalescence, which can occur after the effective collision between particles either with mutual orientation or followed by a particle rotation step.

This communication regards an anomalous oriented attachment growth behavior that has been repeatedly observed for SnO_2 nanoparticles obtained by a non-aqueous solution synthesis procedure. These results could not be explained using the crystal growth descriptions available in the literature.

Experimental Section

The SnO_2 nanocrystals were synthesized in a glovebox under a controlled atmosphere. A total of 5.47 mmol $SnCl_4$ (99.995%) was stirred in a vessel with 40 ml of benzyl alcohol, after which the reaction vessel was removed from the glovebox and heated at 150^{o}C for about 48h in a silicone bath. SnO_2 nanoparticles were collected by centrifugation, washed twice with tetrahydrofuran, and stocked in a concentrated THF dispersion. TEM samples were prepared right after the synthesis procedure by dripping a diluted SnO_2 solution onto copper grids covered with a thin amorphous carbon film. HRTEM characterization was performed using a JEM-3010 URP TEM at 300 kV with a LaB_6 electron gun and equipped with a 1024×1024 thermoelectrically cooled CCD camera. HRTEM multislice simulation was performed using JEMS software (STADELMANN, 1987).

Results

XRD analysis of synthesized material indicated highly crystalline SnO_2 nanocrystals with cassiterite tetragonal P42/mnm structure (MCCARTHY *et al.*, 1989). Figure 5.2aa shows a representative TEM image depicting that the nonaqueous synthesis route produces dispersed and crystalline SnO_2 nanoparticles with elongated shape. The size distribution for 200 measurements shown in Figure 5.2ab reveals elongated particles with a mean length of 29.9 nm, mean width of 10.9 nm, and mean aspect ratio of 3.24.

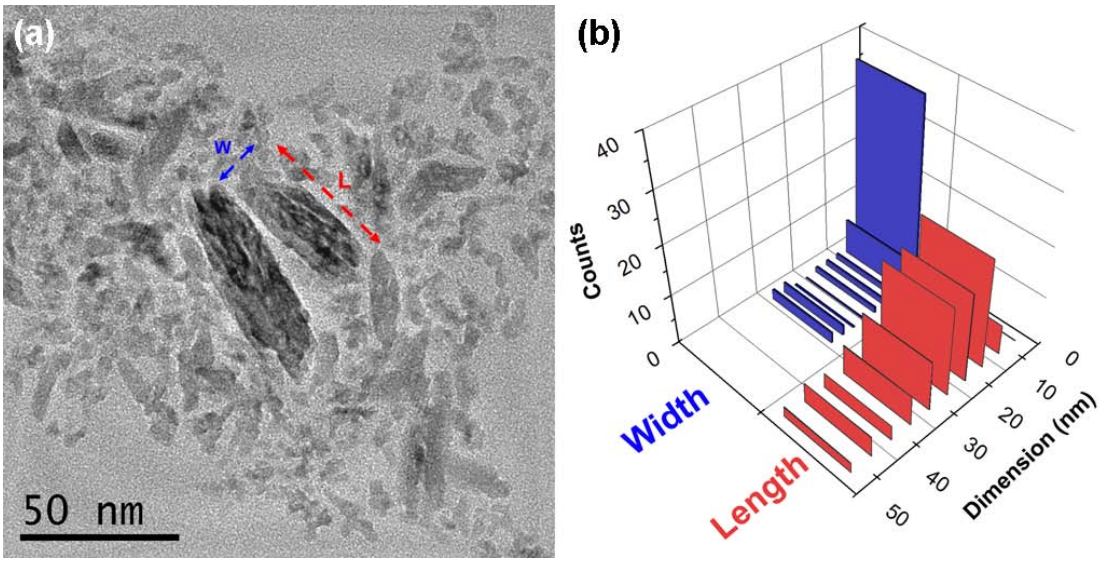

Figure 5.2a: (a) Low-magnification TEM micrograph illustrating SnO_2 nanocrystals with large aspect ratio, with can be noticed on the (b) particle size distribution plot for 200 counts.

Figures 5.2ba and 5.2bb depict SnO_2 nanocrystals HRTEM images which reveal some relevant features. It can be observed that the SnO_2 particles are single crystals elongated along the [110] direction, accordingly with the aspect ratio indicated by the particle size distribution plot. OA (PENN *et al.*, 1998; PENN *et al.*, 1999) is the expected main crystal growth mechanism due to SnO_2 low solubility on both benzyl alcohol and THF. A similar behavior was observed for SnO_2 nanoparticles synthesized in water solution, however with a different growth direction (LEITE *et al.*, 2003). Based on the [001] zone axis projection and the homogeneous contrast along the particle extension, as depicted on Figure 5.2bb, it is indicated that the {110} facets

were the most favorable OA growth sites. According to the allowed symmetry operations for this tetragonal crystalline structure, an identical growth rate would be expected for the four equivalent {110} facets. However, it is important to notice that the observed aspect ratio is related to the two ⟨110⟩ directions, configuring thus an anisotropic growth behavior for identical directions.

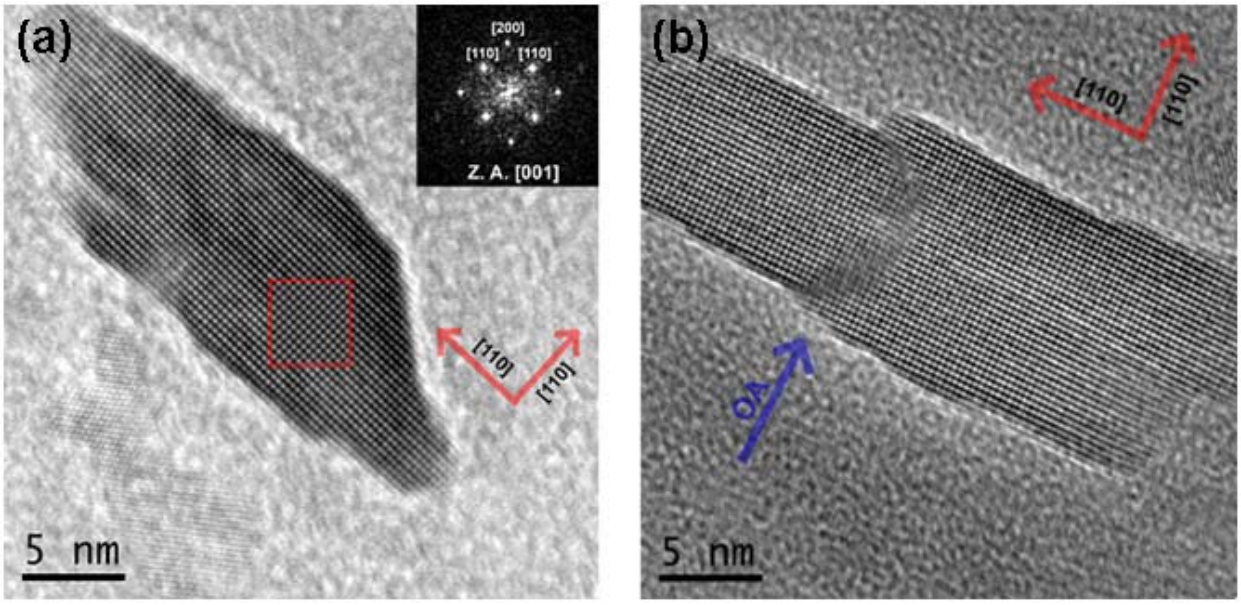

Figure 5.2b: (a) SnO_2 nanocrystal HRTEM micrograph with an indexed FFT inset (upper right corner) and a HRTEM multislice simulation (red square). Two ⟨110⟩ directions are identified either as lengthen and shorten nanocrystals axes. (b) O. A. along the [110] is identified as the main growth mechanism

The nanocrystals facets surface area for different crystallographic planes plays a major role on the OA events, which can be described as a statistical process that depends on the collision rate. The nanocrystals facets surface area can be determined either thermodynamically or kinetically.

Wulff theorem (HERRING *et al.*, 1951) describes the nanocrystals geometry at thermodynamic equilibrium as function of the surface energy distribution for different crystalline planes families, thus indicating the crystal shape for a given volume that would present the minimum surface energy. As the surface energy is related to the plane family bonding configuration, the crystallographic symmetry rules also apply to the surface energy

values and to the nanocrystal faceting. *Ab initio* calculation for surface energy (BELTRAN *et al.*, 2003) indicated that SnO_2 would present ⟨110⟩ directions family as the preferential oriented attachment growth direction due to the lower surface energy and higher surface area.

Capping agents can alter the thermodynamic equilibrium shape during the growth process since they stick to the nanocrystal surface in preferential facets, thus preventing the crystal growth along that direction. This capping agent selectivity for different facets is related to its polarity relationship with the exposed crystalline plane. A similar approach is valid to the pH role on the reaction kinetics since its influence depends on the surface charge distribution, which is related to the crystalline planes terminations. Other essential kinetic factors like temperature and pressure are isotropic.

As a consequence of the crystalline symmetry operations for the tetragonal $P4_2/mnm$ special group, it would be expected that the SnO_2 nanocrystals would present an identical faceting behavior for different crystalline planes within the {110} plane family both by thermodynamic and kinetic arguments. In addition this would ensure an identical OA growth rate along the ⟨110⟩ directions family since there is no other identified reason for anisotropic growth such as external polarization or orientation relationship.

A Monte Carlo based algorithm was used to simulate the oriented attachment process behavior for equivalent directions. A detailed description of this methodology can be found in Appendix B. Figure 5.2c depicts a comparison between the experimentally observed aspect ratio distribution for SnO_2 nanocrystals (red) and the expected aspect ratio distribution considering randomized attachment events for two identical directions in a 2D model, according to the Monte Carlo based calculation results (green). The aspect ratio distribution comparison showed in Figure 5.2c indicates that the SnO_2 nanocrystals present a higher aspect ratio than what would be expected for a statistical growth process along two identical directions. This result points out that a symmetry-breaking event occurs during the crystal growth, which leads to the nanocrystals anisotropic morphology.

This analysis strongly suggests that the observed OA behavior cannot be described as a statistical process controlled by the collision rate. Interactions between the particles, which may be the symmetry-breaking source during the OA events, are highly relevant for the growth mechanism. These interactions must be associated to the van der Walls forces (FRENCH *et al.*, 2000) such as Keesom, Debye, and London dispersion forces. However, the pairwise forces based on permanent dipoles interaction should not be responsible for the observed anisotropic growth behavior due to the dipoles symmetry concerning identical crystallographic directions. In addition, attractive forces involving interactions between charges and dipole/charge should not be imperative for the present study due to the use of an aprotic organic solvent.

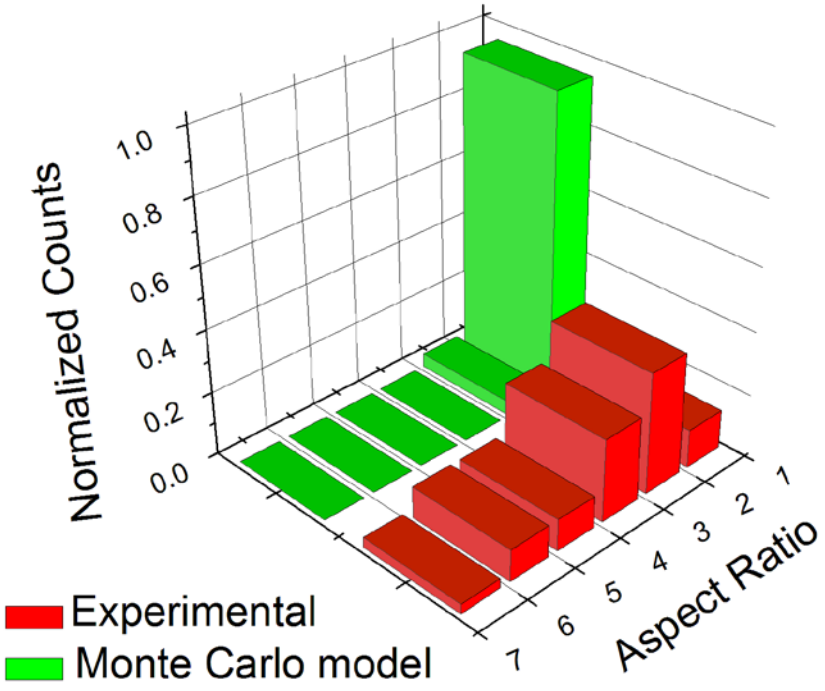

Figure 5.2c: Comparison between the experimental aspect ratio distribution (red) and the results from a Monte Carlo based algorithm considering equivalent growth directions (green).

Although a highly anisotropic growth behavior was also reported for metallic and semiconductor systems (CADEMARTIRI *et al.*, 2009), a comprehensive description for the OA mechanism in such cases was not achieved. Our findings point out that the observed growth behavior can be related to the excess energy from the nanocrystal assembly's edges and kinks (BARNARD *et al.*, 2004), which may have significant contribution during the OA growth mechanism steps. Considering the OA as a multistep growth mechanism, we believe that this excess energy can induce the nanoparticles rotation (DALMASCHIO *et al.*, 2011) at each coalescence event and lead to the preferential attachment on facets which would generate configurations with lower amount of edges and kinks. This effect would ensure a lower nanocrystals assembly overall energy. In this sense, intermediary steps with elongated configurations ("I-like" structures) could be more favorable than structures with isotropic OA events ("L-like" structures).

The effect of decreasing the overall system energy by the edges and kinks minimization from a smoothing process is reported for highly anysotropic metalic nanowires growth (HALDER *et al.*, 2007). The occurence of a smoothing process after attachment events supports our hypothesis as it indicates that the energy contribution from edges and kinks are significant for the crystal growth mechanism. In addition, as the mentioned smoothing process is not favored for ionic systems with reduced surface diffusion, the excess energy could be responsible for inducing a symmetry-breaking event, which would lead to different growth rates along equivalent crystallographic directions.

The HRTEM characterization indicated that the oriented attachment along the ⟨110⟩ directions family is the predominant growth mechanism for SnO_2 nanocrystals. However, it was noticed that different directions within the ⟨110⟩ direction family have different growth ratios and a mean aspect ratio value of 3.24 was observed. A Monte Carlo based simulation showed that this behavior is not likely for a statistical growth process along two identical directions according to the crystallographic symmetry operations.

The observed anomalous anisotropic growth along the ⟨110⟩ direction family could not be explained using neither the classical thermodynamic nor kinetic arguments. An OA growth model that includes the edges and kinks excess energies is currently under development and validation for describing these findings.

5.3. Considerações acerca do Crescimento Anisotrópico

A constatação do crescimento anisotrópico em relação a direções equivalentes discutido no Capítulo 5.2 remete à necessidade de uma abordagem mais elaborada para a descrição da evolução temporal de sistemas nanoestruturados. Neste sentido, dada a demonstração de que uma descrição baseada em eventos estatísticos de colisão orientada não é válida o sistema em questão, a consideração de eventos que levem a quebra de simetria no crescimento por OA é necessária.

Alguns fatores remetem à alteração da razão de aspecto entre as distâncias características no facetamento de nanocristais e até mesmo à formação de estruturas altamente anisotrópicas em relação a diferentes direções cristalográficas. Inicialmente podem ser mencionados os fatores discutidos nos capítulos anteriores, como a alteração da distribuição de energia superficial para diferentes planos cristalinos devido à distribuição de espécies dopantes (YANG *et al.*, 2008; STROPPA *et al.*, 2011d) e a presença de espécies químicas ligadas preferencialmente a diferentes facetas (BURDA *et al.*, 2005). Neste segundo caso, a consideração de um sistema de crescimento análogo à polimerização (RIBEIRO *et al.*, 2006) pode ser utilizada caso levados em consideração os sítios ativos para a coalescência, sendo contudo não elucidados os casos de anisotropia para planos cristalográficos equivalentes (STROPPA *et al.*, 2011b).

A descrição de eventos de coalescência anisotrópica para direções cristalográficas equivalentes no crescimento de nanocristais pode ser iniciada pela consideração de duas evidências experimentais. A primeira é a ocorrência de rotações durante eventos de interação entre nanocristais (MOLDOVAN *et al.*, 2002; RIBEIRO *et al.*, 2005; MOORE *et al.*, 2010), ocasionando assim a possibilidade do desvio em relação à natureza estocástica dos eventos de interação. A segunda é a ocorrência de difusão atômica e/ou movimentação de planos atômicos em um processo de *smoothing* de estruturas após um evento de OA (HALDER *et.al.*, 2007), que remete à atuação conjunta dos mecanismos de crescimento OR e OA e indica que a direção efetiva de crescimento pode diferir em relação à orientação da interação de coalescência devido ao transporte de massa na estrutura coalescida. Dados estes dois argumentos, sendo existente uma força motriz que possa levar à rotação de nanocristais durante eventos de interação ou a migração de átomos, via difusão superficial ou movimentação de defeitos, para uma condição de

crescimento preferencial, é factível a ocorrência de crescimento de estruturas anisotrópicas em relação a direções cristalográficas equivalentes. É importante ressaltar que estão sendo considerados sistemas sem a presença de restrições físicas (*i.e.templates*) (CADEMARTIRI *et al.*, 2009) e com concentração adequada concentração de precursores (*i.e.* não coagulados) (LEE *et. al.*, 2005; DALMASCHIO *et al.*, 2010).

Embora o Capítulo 5.2 justifique a desconsideração de interações dipolares como possíveis fontes de crescimento anisotrópico para direções equivalentes em função de argumentos de simetria, o surgimento de interações análogas durante eventos seqüenciais de coalescência de nanocristais poderia originar tal efeito. Neste caso, após um primeiro evento de coalescência estocástico, o nanocristal formado por dois "blocos", ilustrado na Figura 5.3a, apresentaria uma relação entre as taxas de crescimento efetivas por OA para as facetas indicadas em azul (1) e em vermelho (2) menor do que a proporção entre as áreas expostas (A) destas mesmas facetas.

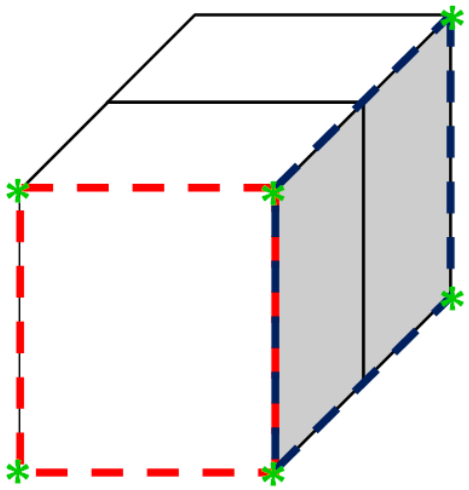

Figura 5.3a: Modelo para a coalescência composto de dois blocos modelos com geometria cúbica e facetas equivalentes. As facetas indicadas em azul (1) e em vermelho (2) apresentam, respectivamente, áreas expostas de 2A e A, comprimento de arestas 6L e 4L, e número de vértices 4V e 4V.

A representação ideal de um evento inicial de OA presente na Figura 5.3a indica que a densidade de energia relacionada às diferentes facetas associadas a planos cristalinos equivalentes pode ser relacionada ao comportamento de crescimento anisotrópico. Neste contexto, caso

considerados os excesso de energia associados às arestas (E_L) e aos vértices (E_V) como contribuições à energia superficial (E_A), as densidades de energia (D) são descritas pela Equação 5.3a e 5.3b.

$$D_1 = (2.E_A + 6.\ E_L + 4.E_V) / 2.A \qquad \textbf{Equação 5.3a}$$

$$D_2 = (1.E_A + 4.\ E_L + 4.E_V) / 1.A \qquad \textbf{Equação 5.3b}$$

Considerando que as contribuições de E_A, E_L, e E_V levam a um incremento positivo da energia associada à faceta devido ao aumento de ligações não satisfeitas na superfície, D_2 será maior que D_1 para a estrutura modelo proposta. Deste modo, a ocorrência de um subseqüente evento de coalescência na faceta 2 pode ser favorável se levada em conta a energia superficial desta. Tal argumento leva à formulação de uma hipótese que tem a densidade de energia superficial como fator fundamental na indução do crescimento anisotrópico para direções equivalentes. Contudo, a avaliação quantitativa por meio de cálculos *ab initio* referentes ao excesso de energia induzido pelos defeitos 1D e 0D não foi factível devido a restrições em relação aos modelos de cálculo empregados. Tal fato deve-se a dificuldades computacionais em relação ao cálculo de energia total para sistemas assimétricos e relativamente grandes, além do problema referente à consideração de construções com carga efetiva não nula.

Neste sentido, o Capítulo 5.4 aborda a mesma hipótese por meio de um modelo para a avaliação das taxas de crescimentos de direções equivalentes em um sistema nanocristalino. Neste caso, a relação entre as taxas de crescimento para facetas do tipo 1 e 2 é derivada em função da diferença entre as energias de ativação para tais eventos em um sistema considerando sucessivos eventos de OA. Sendo demonstrada a relação entre as taxas de crescimento e a temperatura, o modelo proposto é verificado por meio de dados experimentais de razão de aspecto de nanocristais de SnO_2 obtidos em diferentes condições de síntese. O equacionamento presente neste capítulo foi desenvolvido conjuntamente com o colaborador do LNNano, L. A. Montoro, enquanto a síntese dos nanocristais de SnO_2 foi realizada pelo colaborador do LIEC, C. F. Ferreira.

5.4. Relação entre Taxas de Crescimento em Eventos de Coalescência Orientada

A descrição quantitativa das taxas de crescimento por OA para diferentes facetas pertencentes a uma mesma família cristalográfica pode ser abordada segundo a energia de ativação para eventos de coalescência bem-sucedida. O desenvolvimento de tal abordagem leva em conta a tendência para eventos de coalescência subseqüentes ao primeiro, conforme abordado anteriormente, e as direções de crescimento 1 e 2 são consideradas em relação a facetas cristalograficamente equivalentes conforme ilustrado na Figura 5.3a.

As Equações 5.4a e 5.4b descrevem a constante cinética (K_i) segundo a energia de ativação para eventos de coalêscencia efetiva (Ea_i), a seção de choque (σ_i), o fator estérico (P_i) e a temperatura do sistema (T).

$$K_i = A_i \cdot \exp(-Ea_i / k_b \cdot T) \qquad \textbf{Equação 5.4a}$$

$$A_i = P_i \cdot N_A^2 \cdot \sigma_i \cdot [\,(8 \cdot k_b \cdot T) / (\pi \cdot \mu)\,]^{0.5} \qquad \textbf{Equação 5.4b}$$

A razão entre as constantes cinéticas para crescimento nas direções 1 e 2 é descrita pela Equação 5.4c, obtida a partir da substituição da Equação 5.4b na Equação 5.4a. Dada a consideração de que os eventos de coalescência ocorrem de maneira discreta no tempo, a massa reduzida resultante (μ) é equivalente para ambas as distintas direções de crescimento avaliadas para um determinado momento entre dois eventos de coalescência.

$$K_1 / K_2 = (\sigma_1 / \sigma_2) \cdot (P_1 / P_2) \cdot \exp[(Ea_2 - Ea_1)/ k_b \cdot T] \qquad \textbf{Equação 5.4c}$$

Alternativamente, as constantes cinéticas podem ser relacionadas à taxa de formação de estruturas coalescidas (r_i) segundo as direções de crescimento estabelecidas no modelo, conforme descrito pela equação cinética de primeira ordem presente na Equação 5.4d.

$$r_i = K_i \,.\, [A] \,.\, [B] \qquad \textbf{Equação 5.4d}$$

Como a concentração de núcleos ([A]) e a concentração de estruturas com um evento de coalescência ([B]) são equivalentes em relação ao evento subseqüente de coalescência independentemente da direção de crescimento, a razão entre r_i é diretamente relacionada à razão entre K_i, como indicado na Equação 5.4e.

$$r_1 / r_2 = K_1 / K_2 \qquad \textbf{Equação 5.4e}$$

A taxa de formação de estruturas coalescidas (r_i) pode ser em termos de variação temporal da concentração de produto, como indicado na Equação 5.4f. Tal relação pode ser desenvolvida para a avaliação da taxa de crescimento ($\Delta L_i/\Delta t$) conforme a Equação 5.4g, sendo consideradas (i) a equivalência entre a área superficial exposta (A_i) e a seção de choque (σ_i), e (ii) a invariância da sessão de choque durante um evento discreto de choque orientado.

$$r_i = \Delta[C_i] / \Delta t \qquad \textbf{Equação 5.4f}$$

$$r_i = \sigma_i \,.\, (\Delta L_i / \Delta t) / V_g \qquad \textbf{Equação 5.4g}$$

A razão entre as taxas de formação para estruturas coalescidas em diferentes direções é dada pela Equação 5.4h, sendo considerado um valor de volume global (V_g) idêntico para ambas as direções de crescimento. Adicionalmente, a taxa de crescimento ($\Delta L_i / \Delta t$) passa a ser descrita como v_j, sendo a inversão do índice justificada pela representação da geométrica ilustrada na Figura 5.4a.

$$r_1 / r_2 = (\sigma_1 \, . \, v_2) / (\sigma_2 \, . \, v_1) \qquad \textbf{Equação 5.4h}$$

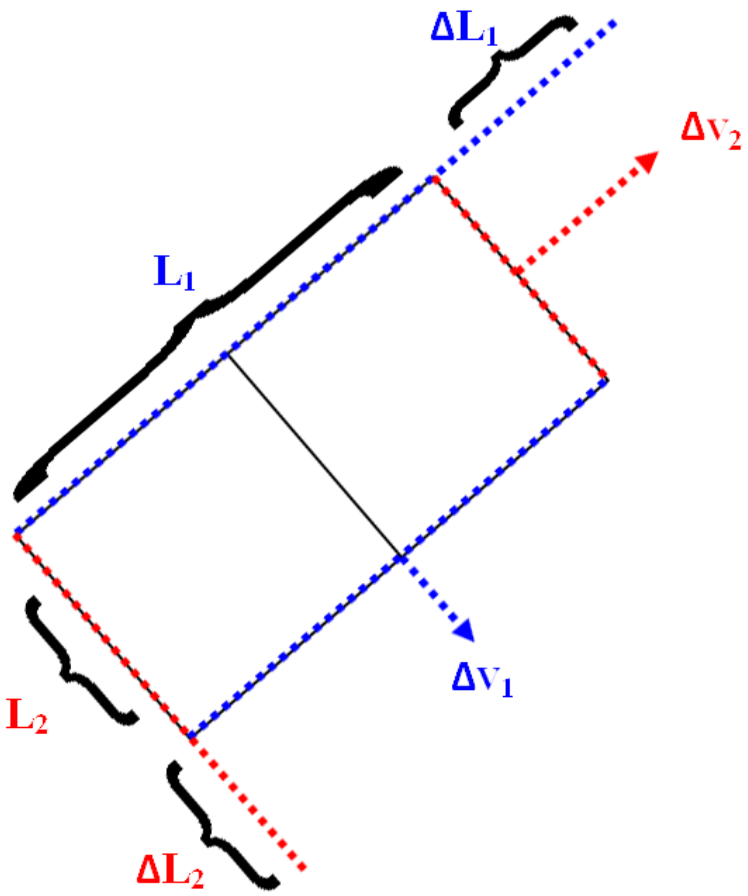

Figura 5.4a: Ilustração da relação ortogonal entre a variação de dimensão (L_i) e a velocidade de crescimento (v_j) para o modelo proposto.

Pela combinação das Equações 5.4c, 5.4e e 5.4h é obtida a Equação 5.4i, que relaciona a velocidade de crescimento (v_i) para duas direções equivalentes em função dos respectivos fatores estéricos (P_i), da diferença entre as energias de ativação (Ea_i) e da temperatura T.

$$\ln (v_1 / v_2) = \ln (P_1 / P_2) + [(Ea_2 - Ea_1)/ k_b \, . \, T] \qquad \textbf{Equação 5.4i}$$

Dada a relação entre a razão de velocidades de crescimento (v_1 / v_2) e a temperatura de crescimento (T), a verificação experimental da hipótese proposta foi realizada por meio da avaliação da evolução da razão de aspecto (AR) média de amostras nanocristalinas padrão após a aplicação de diferentes tratamentos térmicos.

Nanocristais de SnO_2 foram sintetizados por meio de uma rota de síntese em meio orgânico (NIEDERBERGER at al., 2006b). Neste método, 1 mL de uma solução de $SnCl_4$ a a 0.21 $mol.L^{-1}$ foi adicionada a 40.0 mL de álcool benzílico sob agitação vigorosa dentro de uma *glovebox*. O frasco reacional foi vedado hermeticamente e submetido a um banho térmico a 125^oC em silicone. Em seguida, os nanocristais foram coletados por meio de centrifugação, lavados e estocados em uma solução diluída (0.025 $mol.L^{-1}$) de THF.

O procedimento de crescimento controlado foi iniciado pela preparação de quatro frascos reacionais idênticos pela adição de 0.1131g da solução previamente obtida a 30 mL de THF e 0.015 mL de oleamina sob agitação vigorosa. Enquanto uma das soluções resultantes (identificada como amostra A) foi separada como amostra controle, as outras três (identificadas como amostras B, C e D) foram submetidas a tratamentos térmicos com duração de 24h em diferentes temperaturas, 50 ^oC, 100 ^oC e 150 ^oC, respectivamente.

As amostras para análise HRTEM foram preparadas a partir das quatro soluções resultantes pela diluição em THF e sucessivo gotejamento sobre uma grade de cobre coberta com uma fina camada de carbono amorfo (~5 nm). A caracterização HRTEM foi realizada com o uso de um microscópio JEM-3010 URP TEM a 300 kV equipado com um canhão de elétrons LaB_6 e uma câmera CCD com 1024×1024 pixels.

A Figura 5.4b apresenta exemplos de imagens HRTEM das amostras avaliadas. Em concordância com os resultados apresentados no Capítulo 5.2, o OA ao longo da direção [110] foi observado como mecanismo de crescimento predominante nas amostras avaliadas. Adicionalmente, foi observada a presença majoritária de nanocristais elongados e o incremento da consolidação de nanocristais anisotrópicos para tratamento de maior temperatura.

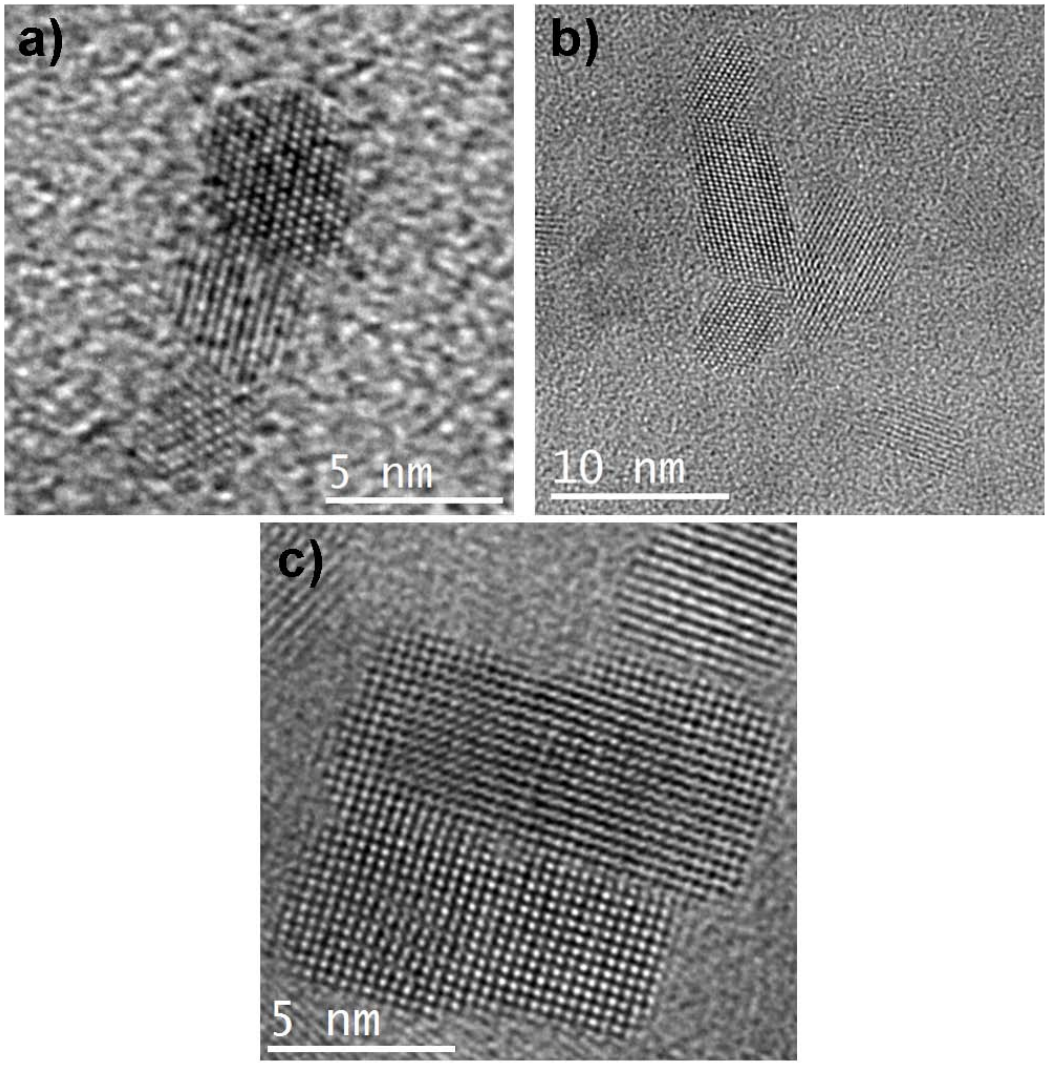

Figura 5.4b: Exemplos de imagens HRTEM obtidas para as amostras de SnO_2 submetidas a diferentes condições de tratamento térmico. a) Observação de OA anisotrópico na amostra A, b) a acentuação deste na amostra B e c) a consolidação de nanocristais anisotrópicos por meio da orientação mútua em condições de tratamento com maior temperatura (C).

A Figura 5.4c apresenta uma representação estatística das dimensões resultantes dos nanocristais submetidos a tratamentos térmicos com diferentes configurações. Os histogramas apresentados se referem à distribuição da razão de aspecto para as quatro amostras avaliadas. A análise foi realizada para aproximadamente 150 nanocristais em cada uma das amostras, sendo medidos diretamente a partir de imagens HRTEM os dois eixos principais de cada nanocristal.

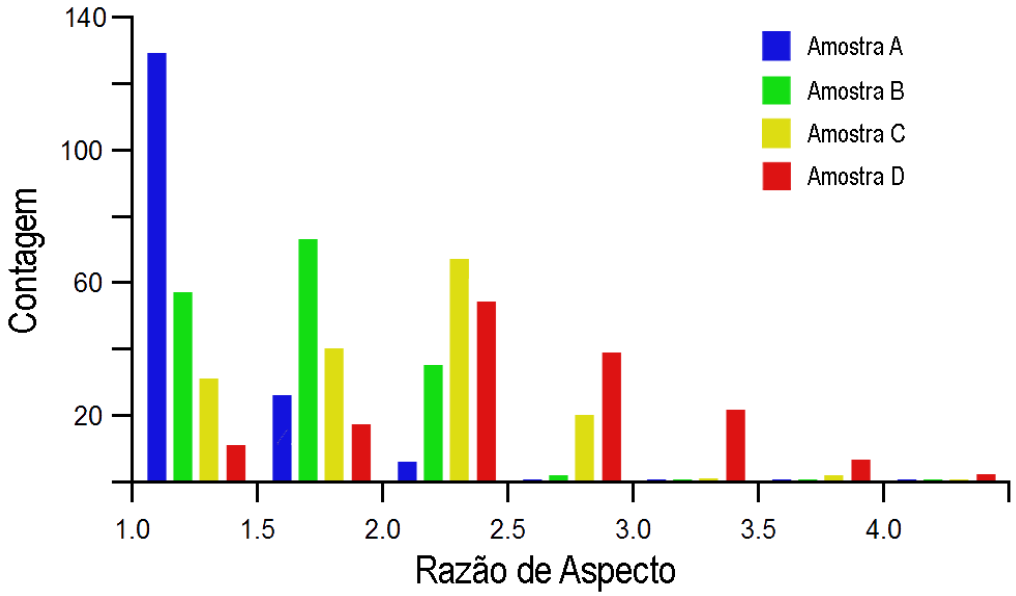

Figura 5.4c: Histogramas referentes à ditribuição de razão de aspecto de nanocristais submetidos a tratamentos térmicos com diferentes temperaturas.

Os resultados apresentados na Figura 5.4c indicam a evolução da razão de aspecto média dos sistemas avaliados em função da temperatura de tratamento térmico. Tal comportamento pode ser inferido a partir Equação 5.4i, que prevê a dependência entre a razão das velocidades de crescimento (v_1 / v_2) e da temperatura do sistema. Deste modo, a diferença entre as energia de ativação (Ea_2 - Ea_1) e a razão entre os fatores estéricos (P1 / P2) nos eventos de OA relativos às direções 1 e 2 podem ser quantificados pela análise do gráfica da dependência entre ln(AR) e 1/T, exibida na Figura 5.4d.

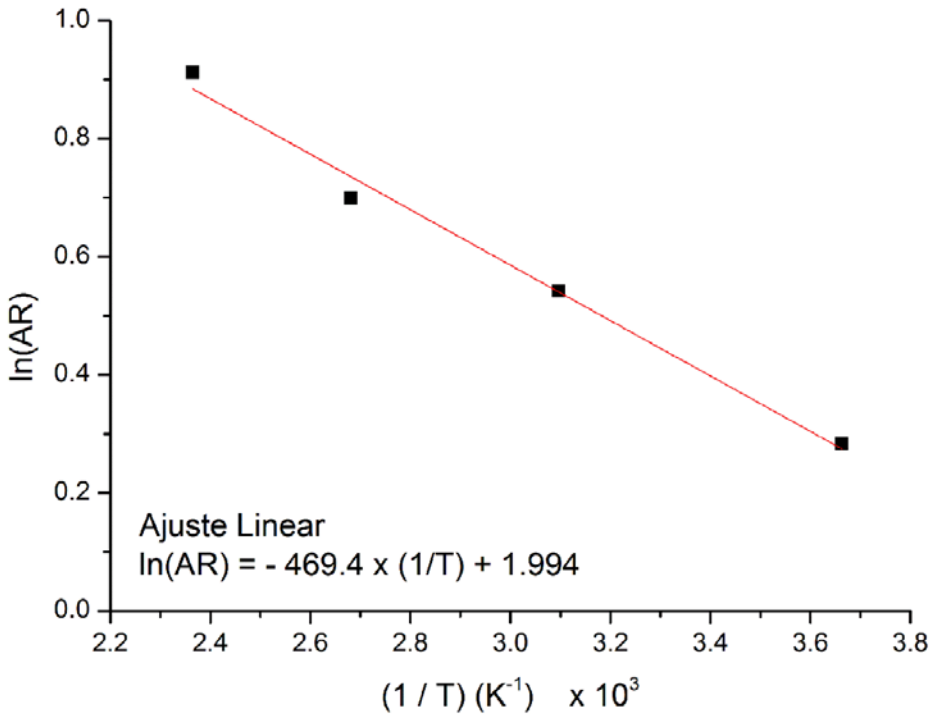

Figura 5.4d: Apresentação gráfica da relação experimental existente entre a razão de aspecto (AR) e a temperatura (T) de tratamento térmico empregado.

A partir da correlação entre a Equação 5.4h e os parâmetros do ajuste linear obtido a partir dos dados experimentais, apresentados na Figura 5.4d, duas grandezas podem ser estimadas.

A primeira é a razão entre os fatores estéricos para eventos de OA relativos às direções 1 e 2 (P_1 / P_2), com valor aproximado de 7.34. Tal resultado remete ao comportamento estatístico das colisões no sistema nanocristalino, sendo favorecido o crescimento normal à facetas de maior área superficial disponível dada a maior probabilidade de colisões com orientação efetiva. Deste modo, tal fator representa a tendência de crescimento isotrópico do sistema.

A segunda é a diferença na energia de ativação (Ea_2 - Ea_1) eventos de OA relativos às direções 1 e 2, sendo esta aproximadamente -6.48×10^{-21} J por nanocristal. Tal valor indica o crescimento favorável ao longo da direção 2, remetendo assim a um comportamento anisotrópico de crescimento em relação a direções isotrópicas. Uma possível interpretação para este resultado é dado pelo diagrama de energia potencial do sistema, ilustrado na Figura 5.4e.

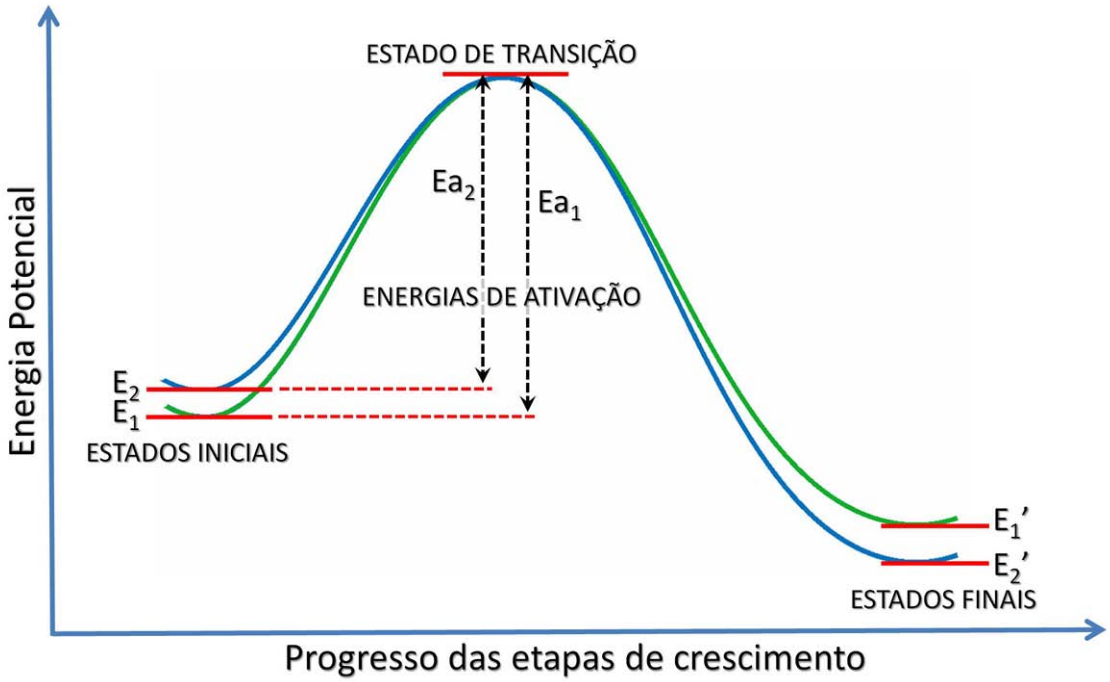

Figura 5.4e: Diagrama de energia potencial para as condições de crescimento ao longo da direção 1 e 2.

O diagrama de energia potencial presente na Figura 5.4e indica que a configuração de crescimento anisotrópico (Ea_2) pode ser favorecida em decorrência da maior energia inicial (E_2), justificada nas Equações 5.3a e 5.3b, sendo assim necessária uma menor energia de ativação para que o estado de transição seja atingido. Neste sentido, é indicado que contribuições de energia superficial provenientes de arestas e vértices podem representar variação de energia suficiente no estado inicial para deslocar o regime de crescimento em direção a eventos de coalescência fora do regime estocástico, previsto pela teoria de colisões.

5.5. Considerações finais

Os resultados apresentados no Capítulo 5.4 evidenciam a influência do excesso de energia proveniente de defeitos 1D e 0D no padrão de crescimento de nanocristais por OA. Tal efeito pode ser descrito qualitativamente como a diferença entre as energias de ativação necessárias para a ocorrência de eventos eficazes de coalescência, dado que estas dependem das energias no estado inicial. Deste modo, uma faceta do tipo 2, ilustrada na Figura 5.3a, pode apresentar uma taxa de crescimento ampliado caso apresente uma maior densidade de energia, promovendo assim uma compensação de sua reduzida seção de choque efetiva, incluído o fator estérico, pela menor energia de ativação requerida para a ocorrência de eventos bem sucedidos de coalescência. Adicionalmente, o excesso em densidade de energia pode também atuar na indução à rotação de nanocristais nos eventos de coalescência subseqüente.

É válido retomar os demais efeitos que atuam como mecanismos de redução de energia total durante o crescimento, como a difusão superficial levando ao *smoothing* da estrutura, o deslocamento relativo entre planos cristalinos visando a movimentação de defeitos e a segregação de espécies dopantes. Embora os dois primeiros efeitos sejam reduzidos no sistema estudado Sb:SnO_2, é visível a influência do terceiro no crescimento de nanoestruturas devido a não ocorrência do crescimento anisotrópico anômalo nas estruturas dopadas sintetizadas, abordadas nos Capítulos 3.2 e 3.4. Tal comportamento pode ser justificado pela consideração da migração de espécies atômicas como um mecanismo ativo para a redução de energia superficial efetiva. Neste caso, a difusão interna de átomos dopantes atuaria equilibrando os excessos de energia provenientes de defeitos estruturais. Tal justificativa é factível segundo a cinética dos sistemas avaliados, dado que o tempo característico para a difusão interna de espécies atômicas, estimado na ordem de nanosegundos (RATSCH *et al.*, 1998), é muito menor que o tempo característico para a ocorrência de eventos de coalescência orientada, estimado em milisegundos (RIBEIRO *et al.*, 2005). Neste caso, a migração de átomos dopantes estabilizaria os eventuais desbalanços na densidade de energia superficial de facetas específicas em respeito à contribuição de defeitos estruturais gerado em eventos de coalescência prévios.

Adicionalmente ao efeito dos átomos dopantes no mecanismo de crescimento por OA, os resultados experimentais obtidos remetem à influência destes na fase de nucleação. Nesta direção, a alteração da tensão superficial γ_{SL} decorrente da concentração de dopantes promove a alteração da solubilidade dos núcleos, segundo a Equação 5.1a, e conseqüentemente leva a alteração no raio crítico durante a nucleação. Deste modo, uma explicação qualitativa para a diferença de tamanho médio para nanocristais com diferentes conteúdos de dopante pode ser obtida.

Uma visão alternativa do aspecto de nucleação pode ser inferida após a análise dos dados presentes na Figura 3.4d, que indica que as duas composições do $Sb:SnO_2$ apresentam similar valor de energia superficial total, aproximadamente $3.6x10^{-16}$J por nanocristal. Tendo em vista que tal valor apenas depende das dimensões do nanocristal e da energia superficial das facetas existentes, a obtenção de um valor constante indica que o tamanho de cristal é intrinsecamente relacionado à distribuição de energias superficiais no estágio de nucleação e a tensão superficial do meio reacional. Tal efeito pode ser correlacionado com a curvatura de uma gota em um ensaio de gota séssil, sendo esta determinada pela relação das tensões superficiais das fases envolvidas (ERBIL, 2006). Curiosamente, a avaliação deste ângulo de contato pode ser realizada por meio de imagens projetadas (STROPPA *et al.*, 2010), remetendo assim a uma similaridade com tal característica intrínseca das técnicas TEM.

A avaliação criteriosa da correlação entre a presença de dopantes e os mecanismos de nucleação e crescimento é uma das sugestões de trabalho futuro.

6. Conclusões

6.1. Conclusões

Os temas tratados nesta tese indicam a aplicabilidade de diferentes metodologias de microscopia eletrônica de transmissão quantitativa na caracterização de materiais nanocristalinos visando a extração de informações quantitativas e com alta resolução espacial, sendo as abordagens e as avaliações sumarizadas na Tabela 6.1a. Os resultados obtidos incluem elementos fundamentais ao modelamento de nanocristais, como a estrutura tridimensional dos mesmos, a distribuição de energia superficial para diferentes planos cristalográficos e a distribuição de átomos dopantes. Neste sentido, as técnicas abordadas se mostram extremamente valiosas na caracterização de nanomateriais e na proposição de modelos que possam ser utilizados para a posterior descrição de sistemas a partir de blocos de construção nanocristalinos.

Table 6.1a: Sumário das metodologias avaliadas neste projeto

Característica	Técnica	Abordagem	Avaliação
Morfologia	HRTEM	Construção de modelos e simulação de imagens	Versátil e reprodutível Precisão dependente de simetria
//	HRSTEM	Intensidade HAADF integrada	Precisão de ± 1 átomo Simetria ao longo do eixo de zona
Segregação de dopantes	HRTEM	Comparação com construção de Wulff	Distribuição 3D de dopantes Assume equilíbrio termodinâmico Cálculos *ab initio* representativos
//	STEM	Medidas de EELS-STEM em perfil de linha	Quantificação direta de espécies Resolução espacial x SNR Dano na amostra
Morfologia + Segregação de dopantes	HRTEM	Análise de função de onda de saída por FSR de imagens NCSI	Modelo inclui informação completa Complexa aquisição de dados Restrições instrumentais

Além do fornecimento de informações diretamente aplicadas ao desenvolvimento de dispositivos, a possibilidade de caracterização de nanocristais de modo quantitativo e com alta resolução suporta a análise de mecanismos que determinam a estrutura, a evolução e as propriedades dos sistemas nanoestruturados. Neste âmbito, os estudos realizados suportam o entendimento da interdependência entre a morfologia, distribuição de energia superficial e a segregação de dopantes, como discutido no modelo proposto no Capítulo 3.6, além de proverem informações fundamentais acerca da teoria de nucleação e crescimento de nanocristais, como apresentado no modelo proposto no Capítulo 5.4.

Adicionalmente, os estudos desenvolvidos na tese contribuíram na consolidação e na expansão do conhecimento relacionado à caracterização de sistemas nanocristalinos por meio de abordagens HR(S)STEM em âmbito nacional. Neste contexto, colaborações com grupos especialistas em microscopia (Ernst Ruska Center no Forschungszentrum Jülich, Nanocharacterization Laboratory na Lehigh University, STEMgroup na Paris Sud Université) e com grupos especialistas em áreas correlatas, como síntese de nanostruturas (LIEC na UFSCar) e cálculos teórios (QFA na Universitat Jaume I), promoveram a incorporação de ferramentas avançadas de caracterização de materiais às atualmente disponíveis em um centro multiusuário com abrangência nacional (LNNano no CNPEM). É importante mencionar que o *software* MEGACELL, desenvolvido em conjunto com o colaborador R. D. Righetto do LNNano e descrito no Anexo A, apresenta-se disponível livremente à comunidade científica e em processo de registro com relação à propriedade intelectual.

Em suma, o uso complementar de diferentes técnicas de microscopia eletrônica de transmissão quantitativa e de cálculos teóricos diversos suportou com sucesso a caracterização morfológica e a avaliação da segregação de dopantes. Os resultados obtidos pelas abordagens propostas suportaram o desenvolvimento de um modelo para a predição da distribuição de dopantes em nanocristais e a extensão dos modelos de nucleação e crescimento de nanocristais presentes na literatura. Desta forma, os objetivos inicialmente propostos para esta tese foram atingidos em sua totalidade.

6.2. Sugestões para Trabalhos Futuros

Com base nos resultados obtidos nos estudos realizados nesta tese e nas perspectivas decorrentes destes, duas classes de sugestão de trabalhos futuro são propostas.

A primeira refere-se ao uso de demais técnicas experimentais para a confirmação e extensão dos resultados presentes. Dentre estas podem ser listadas:

- **Avaliação da segregação de dopantes em nanocristais por meio de técnicas emergentes com resolução atômica, como XEDS-HRSTEM ou APFIM.** A comparação dos resultados obtidos por estas técnicas quantitativas diretas e pelas metodologias de análise propostas no Capítulo 3 indicaria a aplicabilidade destas na predição da distribuição de espécies em nanocristais, além de apresentar uma estimativa do erro associado a esta quantificação. Adicionalmente, tal comparação indicaria a viabilidade das considereções referentes ao equilíbrio termodinâmico e à adequação da metodologia de cálculo de energia superficial.

- **Obtenção de funções de onda com melhores resoluções espaciais, via NCSI-HRTEM ou holografia de elétrons em HRTEM, para a realização de construções de plots de Argand com melhor definição.** Embora exista atualmente a restrição em relação à resolução espacial que pode ser alcançada em análises HRTEM (50 pm), existe um acréscimo na resolução obtida pelo procedimento de FSR em relação às imagens individuais, principalmente devido à instabilidade da amostra ao longo da aquisição da série de imagens. Deste modo a obtenção de imagens em um regime mais estável e o desenvolvimento de procedimentos mais precisos para a realização da FSR seriam fundamentais para o desenvolvimento desta metodologia.

- **Realização de experimentos HRTEM *in situ* contando com o uso de célula líquida** (ZHENG *et. al.*, 2009) **e temperatura controlada, visando o monitoramento em tempo real dos estágios de nucleação de crescimento de cristais.** Os resultados provenientes de procedimentos *in situ* com alto controle sobre as condições ambientais apontam para a verificação em tempo real dos eventos relacionados à evolução temporal de sistemas nanocristalinos, assim propiciando a validação dos modelos teóricos existentes e a obtenção de informações mais acuradas que podem ser utilizadas na melhoria destes.

A segunda refere-se ao aprimoramento dos modelos propostos e a extensão destes para demais sistemas nanoestruturados. Dentre estas estão:

- **Aprimoramento do modelo de predição de segregação de dopante pelo uso das dimensões do nanocristal como variáveis livres.** Dada a quantização das possíveis geometrias para os modelos de nanocristais em função dos planos cristalinos considerados para o facetamento, é possível a inclusão da morfologia como uma variável adicional na geração de candidatos segundo o procedimento proposto no Capítulo 3.6. Deste modo, pela adequação do critério de seleção, é indicada a possibilidade de verificação da geometria mais provável e da configuração de segregação de dopantes simultaneamente.

- **Desenvolvimento de um modelo baseado em dinâmica molecular para a descrição do efeito da presença de dopantes nas fases de nucleação dos nanocristais.** Tendo em vista a influência de átomos dopantes na morfologia e no crescimento dos sistemas nanocristalinos, observada experimentalmente por meio de técnicas HRTEM e brevemente discutida no Capítulo 5.5, é indicada a avaliação da formação e estabilização de núcleos por meio de metodologias teóricas. A análise da variação de energia superficial decorrente da possível segregação de dopantes durante a fase de nucleação poderia trazer informações fundamentais acerca da estabilidade dos núcleos formados e da morfologia resultante ao longo dos estágios de crescimento.

7. Referências Bibliográficas

ABEL, K. A.; BOYER, J. -C.;ANDREI, C. M.; VAN VEGGEL, F. C. J. M.; Analysis of the shell thickness distribution on NaYF4/NaGdF 4 core/shell nanocrystals by EELS and EDS. **J. Phys. Chem. Lett.**, 2, 3, 185-189, 2011.

ALLEN, J. E.; HEMESATH, E. R.; PEREA, D. E.; LENSCH-FALK, J. L.; LI, Z. Y.; YIN, F.; GASS, M. H.; WANG, P.; BLELOCH, A. L.; PALMER, R. E.; L. J.; LAUHON, High-resolution detection of Au catalyst atoms in Si nanowires. **Nat. Nanotechnol.**, 3, 168-173, 2008.

ARENAL, R.; DE LA PEÑA, F.; STÉPHAN, O.; WALLS, M.; TENCÉ, M.; LOISEAU, A.; COLLIEX, C.; Extending the analysis of EELS spectrum-imaging data, from elemental to bond mapping in complex nanostructures. **Ultramicroscopy**, 109, 32-38, 2008.

ARGAND, J. R.; **Essai sur une manière de représenter les quantités imaginaires dans les constructions géométriques**, Paris: Albert Blanchard,1806.

ARSLAN, I.; YATES, T. V. J.; Embedded nanostructures revealed in three dimensions. **Science**, 309, 2195-2198, 2005.

BA, J. H.; POLLEUX, J.; ANTONIETTI, M.; NIEDERBERGER, M.; Non-aqueous Synthesis of Tin Oxide. Nanocrystals and Their Assembly into Ordered Porous Mesostructures. **Adv. Mat.**, 17, 20, 2509-2512, 2005.

BABU, S.; THANNEERU, R.; INERBAEV, T.; DAY, R.; MASUNOV, A. E.; SCHULTE, A.;

SEAL, S.; Dopant-mediated oxygen vacancy tuning in ceria nanoparticles, **Nanotechnology**, 20, 085713, 2009.

BAER, D. R.; GASPAR, D.J.; NACHIMUTHU, P.; TECHANE, S. D.; CASTNER, D. G.; Application of surface chemical analysis tools for characterization of nanoparticles. **Anal. Bioanal. Chem.**, 396, 3, 983-1002, 2010.

BAKKER, H.; ZHOU, G. F.; YANG, H.; Mechanically driven disorder and phase transformations in alloys **Prog. Mater. Sci.**, 39, 159-241, 1995.

BARNARD, A. S.; ZAPOL, P.; Effects of particle morphology and surface hydrogenation on the phase stability of TiO_2. **J. Chem. Phys.**, 121, 4276, 2004.

BARNARD, A. S.; YEREDLA, R. R.; XU, H.F.; Modeling the Formation of High Aspect CdSe Quantum Wires: Axial-Growth versus Oriented-Attachment Mechanisms. **Nanotechnology**, 17, 12, 3039-3047, 2006.

BARNARD, A. S.; KIRKLAND, A. I.; Combining Theory and Experiment in Determining the Surface Chemistry of Nanocrystals. **Chem. Mater.**, 20, 17, 5460-5463, 2008.

BARNARD, A. S.; Modelling of Nanoparticles: Approaches to Morphology and Evolution; **Rep. Prog. Phys.**, 73, 1-52, 2010.

BARTHEL, J.; THUST, A.; Quantification of the Information Limit of Transmission Electron Microscopes. **Phys. Rev. Lett.**, 101, 200801, 2008.

BARTHEL J.; WEIRICH T. E.; COX, G.; HIBST, H.; THUST, A.; Structure of $Cs_{0.5}[Nb_{2.5}W_{2.5}O_{14}]$ analysed by focal-series reconstruction and crystallographic image processing; **Acta Materialia**, 58, 10, 3764-3772, 2010.

BARTHEL, J.; **Software Dr. Probe**, http://www.er-c.org/centre/software/drprobe.htm, acessado em 10/10/2011.

BATSON, P. E.; DELLBY, N.; KRIVANEK, O. L.; Sub-ångstrom resolution using aberration corrected electron optics. **Nature**, 418, 617-620. 2002.

BECKE, A. D.; Density-functional thermochemistry. III. The role of exact exchange. **J. Chem. Phys.,** 98 (7), 5648-5652, 1993.

BELTRÁN, A.; ANDRÉS, J.; LONGO, E.; LEITE, E. R.; Thermodynamic argument about SnO2 nanoribbon growth. **Appl. Phys. Lett.**, 83 (4), 635-637, 2003.

BERTONI, G.; VERBEECK, J.; Accuracy and precision in model based EELS quantification. **Ultramicroscopy**, 108, 782-790, 2008.

BIGGEMANN, D.; DA SILVA, M. H. P.; ROSSI, A. M.; RAMIREZ, A. J.; High-Resolution Transmission Electron Microscopy Study of Nanostructured Hydroxyapatite. **Microscopy and Microanalysis**, 14, 433-438, 2008.

BORISEVICH, A. Y.; LUPINI, A. R.; TRAVAGLINI, S.; PENNYCOOK, S. J.; Depth sectioning of aligned crystals with the aberration-corrected scanning transmission electron microscope. **Journal of Electron Microscopy**, 55, 1, 7-12, 2006.

BOSMAN, M.; WATANABE, M.; ALEXANDER, D. T. L.; KEAST, V. J.; Mapping chemical and bonding information using multivariate analysis of electron energy-loss spectrum images. **Ultramicroscopy**, 106, 1024-1032, 2006.

BOSMAN, M.; KEAST, V. J.; WATANABE, M.; MCCULLOCH, D. G.; SHAKERZADEH, M.; TEO, E. H. T.; TAY, B. K.; Quantitative, nanoscale mapping of sp^2 percentage and crystal orientation in carbon multilayers. **Carbon**, 47, 94-101, 2009.

BRUNDLE, C. R.; EVANS, C. A.; WILSON, S.; **Encyclopedia of Materials Characterization**, Reed Publishing, 1992.

BRUNE, H.; GIOVANNINI, M.; BROMANN, K.; KERN, K.; Self-organized growth of nanostructure arrays on strain-relief patterns. **Nature**, 394, 451-453, 1998.

BURDA, C.; CHEN, X.; NARAYANAN, R.; EL-SAYED, M. A.; Chemistry and properties of nanocrystals of different shapes. **Chem. Rev.**, 105, 4, 1025-1102, 2005.

CADEMARTIRI, L.; OZIN, G. A.; Ultrathin Nanowires – A Materials Chemistry Perspective. **Adv. Mater.**, 20, 1013- 1020, 2009.

CALLISTER, W. D.; **Fundamentals of Materials Science and Engineering**. New York: John Wiley & Sons, 2001.

CAO, G.; **Nanostructures & Nanomaterials: Synthesis, Properties & Applications**, London: Imperial College Press, 2004.

CHU, M.-W.; LIOU, S. C.; CHANG, C.-P.; CHOA, F.-S.; CHEN, C. H.; Emergent chemical mapping at atomic-column resolution by energy-dispersive x-ray spectroscopy in an aberration-corrected electron microscope. **Phys. Rev. Lett.**, 104, 196101, 2010.

COENE, W. M. J.; THUST, A.; DEBEECK, M.; VAN DYCK, D.; Maximum-likelihood method for focus-variation image reconstruction in high resolution transmission electron microscopy. **Ultramicroscopy**, 64, 109-135, 1996.

COLFEN, H.; ANTONIETTI, M.; Mesocrystals: Inorganic Superstructures Made by Highly Parallel Crystallization and Controlled Alignment. **Angew. Chem. Int. Ed.**, 44, 5576-5591, **2005**.

COLLIEX, C.; BRUN, N.; GLOTER, A.; IMHOFF, D.; KOCIAK, M.; MARCH, K.; MORY, C.; STÉPHAN, O.; TENCÉ, M.; WALLS, M.; Multi-dimensional and multi-signal approaches in scanning transmission electron microscopes. **Phil. Trans. R. Soc. A.**, 367, 3845-3858, 2009.

COLLIEX, C.; BOCHER, L.; DE LA PEŇA, F.; GLOTER, A.; MARCH, K.; WALLS, M.; Atomic-scale STEM-EELS mapping across functional interfaces. **JOM**, 62, 53-57, 2010.

COWLEY, J. M.; MOODIE, A. F.; The Scattering of Electrons by Atoms and Crystal. **Acta Crystal.**, 10, 10, 609-619, 1957.

CROZIER, P.; CHENNA, S.; In situ analysis of gas composition by electron energy-loss spectroscopy for environmental transmission electron microscopy. **Ultramicroscopy**, 111, 177-185, 2011.

D'ALFONSO, A. J.; FREITAG, B.; KLENOV, D.; ALLEN, L. J.; Atomic-resolution chemical mapping using energy-dispersive x-ray spectroscopy. **Phys. Rev. B**, 81, 100101, 2010.

DA SILVA, R. O.; CONTI, T. G.; DE MOURA, A. F.; STROPPA, D. G.; FREITAS, L. C. G.; RIBEIRO, C.; CAMARGO, E. R.; LONGO, E.; LEITE, E. R.; Antimony-doped tin oxide nanocrystals: synthesis and solubility behavior in organic solvents. **ChemPhysChem**, 10, 5, 841-846, 2009.

DA SILVA, R. O.; GONÇALVES, R. H.; STROPPA, D. G.; RAMIREZ, A. J.; LEITE, E. R.; Synthesis of recrystallized anatase TiO2 mesocrystals with Wulff shape assisted by oriented attachment. **Nanoscale** 3, 1910-1916, 2011.

DALMASCHIO, C. J.; RIBEIRO, C.; LEITE, E. R.; Impact of the colloidal state on the oriented attachment growth mechanism. **Nanoscale**, 2, 2336-2345, 2010.

DASGUPTA, S.; GOTTSCHALK, S.; KRUK, R.; HAHN, H.; A nanoparticulate indium tin oxide field-effect transistor with solid electrolyte gating. **Nanotechnology**, 19, 43, 435203, 2008.

DEEPAK, F. L.; CASILLAS-GARCIA, G.; ESPARZA, R.; BARRON, H.; JOSE-YACAMAN, M.; New insights into the structure of PdAu nanoparticles as revealed by aberration-corrected STEM. **J. Cryst. Growth**, 325, 1, 60-67, 2011.

DIERCKS, D.; LIAN, G.; CHUG, J.; KAUFMAN, M.; Comparison of convergent beam electron diffraction and geometric phase analysis for strain measurement in a strained silicon device. **Journal of Microscopy**, 241(2), 195–199, 2011.

DILANIAN, R. A.; IZUMI, F.; **VESTA Software** - http://www.geocities.jp/kmo_mma/crystal/en/vesta.html, acessado em 10/10/2011.

DOVESI, R.; ORLANDO, R.; CIVALLERI, B.; ROETTI, C.; SAUNDERS, V. R.; ZICOVICH-WILSON, C. M.; CRYSTAL: a computational tool for the ab initio study of the electronic properties of crystals. **Z. Kristallogr.**, 220, 571-573, 2005.

DU, N.; ZHANG, H.; CHEN, B.; MA, X.; YANG, D.; Ligand-free self-assembly of ceria nanocrystals into nanorods by oriented attachment at low temperature. **J. Phys. Chem. C**, 111, 12677-12680, 2007.

DURAND, P.; BARTHELAT, J. C.; A theoretical method to determine atomic pseudopotentials for electronic structure calculations of molecules and solids. **Theoret. Chim. Acta**, 38 (4), 283-302, 1975.

EGERTON, R. F.; Electron energy-loss spectroscopy in the TEM. **Rep. Prog. Phys.**, 72, 1-25, 2009.

EGERTON, R.; **Electron Energy-Loss Spectroscopy in the Electron Microscope**, New York: Plenum Press, 339.

EINSPAHR, J. J.; VOYLES, P. M.; Prospects for 3D, nanometer-resolution imaging by confocal STEM. **Ultramicroscopy**, 2006, 106, 1041-1052.

ERBIL, H. Y.; **Surface Chemistry of Solid and Liquid Interfaces**; Oxford: Wiley-Blackwell, 2006.

ESPINOSA-MAGANA, F.; ROSAS, A.; ESPARZA-PONCE, H. E.; OCHOA-LARA, M. T.; AGUILAR-ELGUEZABAL, A.; In situ study of the metal-insulator transition in VO(2) by EELS and ab initio calculations. **Micron**, 40, 787-792, 2009.

FANG, J. X.; MA, X. N.; CAI, H. H.; SONG, X. P.; DING, B. J.; Nanoparticle-aggregated 3D monocrystalline gold dendritic nanostructures. **Nanotechnology**, 17, 5841-5845, 2006.

FEI - **ChemiSTEM Technology** - http://www.fei.com/products/transmission-electron-microscopes/chemistem.aspx, verificado em 10/10/2011.

FERRER, D.; TORRES-CASTRO, A.; GAO, X.; SEPULVEDA-GUZMAN, S.; ORTIZ-MENDEZ, U.; JOSE-YACAMAN, M.; Three-layer core/shell structure in Au-Pd bimetallic nanoparticles. **Nano Lett.**, 7, 6, 1701-1705, 2007.

FEYNMAN, R. P.; There's plenty of room at the bottom. **Eng. Sci.**, 23, 5, 22-36, 1960.

FINDLAY, S. D.; AZUMA, S.; SHIBATA, N.; OKUNISHI, E.; IKUHARA, Y.; Direct oxygen imaging within a ceramic interface, with some observations upon the dark contrast at the grain boundary. **Ultramicroscopy**, 111, 285-289, 2011a.

FINDLAY, S. D.; SAITO, T.; SHIBATA, N.; SATO, Y.; MATSUDA, J.; ASANO, K.; AKIBA, E.; HIRAYAMA, T.; IKUHARA, Y.; Direct imaging of hydrogen within a crystalline environment. **Appl. Phys. Express**, 3, 116603, 2011b.

FITTING KOURKOUTIS, L.; PARKER, M. K.; VAITHYANATHAN, V.; SCHLOM, D. G.; MULLER, D. A.; Direct measurement of electron channeling in a crystal using scanning transmission electron microscopy. **Phys. Rev. B**, 84, 075485, 2011.

FRENCH, R. H.; Origins and applications of London dispersion forces and Hamaker constants in ceramics. **J. Am. Ceram. Soc.**, 83, 2117-2146, 2000.

GANESH, K. J.; KAWASAKI, M.; ZHOU, J. P.; FERREIRA, P. J.; D-STEM: A Parallel Electron Diffraction Technique Applied to Nanomaterials. **Microsc. Microanal.**, 16, 614-621, 2010.

GLOTER, A.; DOUIRI, A.; TENCÉ, M.; COLLIEX, C.; Improving energy resolution of EELS spectra: an alternative to the monochromator solution. **Ultramicroscopy**, 96, 385-400, 2003.

GOMEZ-RODRIGUEZ, A.; BELTRAN-DEL-RIO, L. M.; HERRERA-BECERRA, R.; SimulaTEM: multislice simulations for general objects. **Ultramicroscopy**, 110, 95-104, 2010.

GONG, X.-Q.; SELLONI, A.; BATZILL, M.; DIEBOLD, U.; Steps on anatase TiO2(101). **Nature Materials**, 5, 665-670, 2006.

GRANQVIST, C. G.; HULTAKER, A.; Transparent and conducting ITO films: new developments and applications. **Thin Solid Films**, 411, 1, 1-5, 2002.

GRUBBS, R. B.; Nanoparticle assembly - Solvent-tuned structures. **Nat. Mater.**, 6, 8, 553-555, 2007.

GUSTAFSSON, A.; BOLINSSON, J.; SKÖLD, N.; SAMUELSON, L.; Determination of diffusion lengths in nanowires using cathodoluminescence. **Appl. Phys. Lett.**, 97, 072114, 2010.

HAIDER, M.; UHLEMANN, S.; SCHWAN, E.; ROSE, H.; KABIUS, B.; URBAN, K.; Electron Microscopy Image Enhanced; **Nature**, 392, 768-769, 1998.

HALDER, A. RAVISHANKAR, N.; Ultrafine single-crystalline gold nanowire arrays by oriented attachment. **Adv. Mater.**, 19, 14, 1854-1858, 2007.

HANSEN, P. L.; WAGNER, J. B.; HELVEG, S.; ROSTRUP-NIELSEN, J. R.; CLAUSEN, B. S.; TOPSOE, H.; Atom-Resolved Imaging of Dynamic Shape Changes in Supported Copper Nanocrystals. **Science**, 295, 2053-2055, 2002.

HASHIMOTO, A.; MITSUISHI, K.; SHIMOJO, M.; ZHU, Y.; TAKEGUCHI, M.; Experimental examination of the characteristics of bright-field scanning confocal electron microscopy images **J. Electron Microsc.**, 60, 227-234, 2011.

HAWKES, P.; **Advances in Imaging and Electron Physics: Aberration-corrected Electron Microscopy**. Elsevier, 153, 2008.

HEIDELMANN, M.; BARTHEL, J.; HOUBEN, L.; StripeSTEM, a technique for the isochronous acquisition of high angle annular dark-field images and monolayer resolved electron energy loss spectra. **Ultramicroscopy**, 102, 1447-1452, 2009.

HERRING, C.; Some Theorems on the Free Energies of Crystal Surfaces. **Phys. Rev.**, 82, 1, 87-93, 1951.

HILLYARD, S.; SILCOX, J.; Detector geometry, thermal diffuse scattering and strain effects in ADF STEM imaging. **Ultramicroscopy**, 58, 6-17, 1995.

HITCHCOCK, A. P.; DYNES, J. J.; JOHANSSON, G.; WANG, J.; BOTTON, G.; Comparison of NEXAFS microscopy and TEM-EELS for studies of soft matter. **Micron**, 39, 741-748, 2008.

HOFMANN, S.; SHARMA, R.; DUCATI, C.; DU, G.; MATTEVI, C.; CEPEK, C.; CANTORO, M.; PISANA, S.; PARVEZ, A.; CERVANTES-SODI, F.; FERRARI, A. C.; DUNIN-BORKOWSKI, R.; LIZZIT, S.; PETACCIA, L.; GOLDONI, A.; ROBERTSON, J.; In situ observations of catalyst dynamics during surface-bound carbon nanotube nucleation. **Nano Letters**, 7, 602, 2007.

HONO, K.; Nanoscale microstructural analysis of metallic materials by atom probe field ion microscopy. **Prog. Mat. Sci.**, 47, 6, 621-729, 2002.

HOVDEN, R.; XIN, H. L.; MULLER, D. A.; Extended Depth of Field for High-Resolution Scanning Transmission Electron Microscopy. **Microsc. Microanal.**, 17, 75-80, 2011.

HUANG, F. T.; GLOTER, A.; CHU, M. W.; CHOU, F. C.; SHU, G. J.; LIU, L. K.; CHEN, C. H.; COLLIEX, C.; Scanning transmission electron microscopy using selective high-order laue zones: three-dimensional atomic ordering in sodium cobaltate. **Phys. Rev. Lett.**, 105, 125502, 2010.

HUANG, W. J.; ZUO, J. M.; JIANG, B.; KWON, K. W.; SHIM, M.; Sub-ångström-resolution diffractive imaging of single nanocrystals. **Nat. Phys.**, 5, 2, 129-133, 2009.

HUE, F.; HYTCH, M.; BENDER, H.; HOUDELLIER, F.; CLAVERIE, A.; Direct mapping of strain in a strained silicon transistor by high-resolution electron microscopy; **Phys. Rev. Lett.**, 100, 15, 1-4, 2008.

HYTCH, M. J.; PUTAUX, J. M.; PENISSON, J. M. ; Measurement of the displacement field of dislocations to 0.03 angstrom by electron microscopy. **Nature**, 423, 270-273, 2003.

HYTCH, M.; HOUDELLIER, F.; HÜE, F.; SNOECK, E.; Nanoscale holographic interferometry for strain measurements in electronic devices. **Nature**, 453, 1086-1089, 2008.

IAKOUBOVSKII, K.; MITSUISHI, K.; NAKAYAMA, Y.; FURUYA, K.; Thickness measurements with electron energy loss spectroscopy. **Microscopy Research and Technique**, 71, 626-631, 2008.

ISHIKAWA, R.; OKUNISHI, E.; SAWADA, H.; KONDO, Y.; HOSOKAWA, F.; ABE, E.; Direct imaging of hydrogen-atom columns in a crystal by annular bright-field electron microscopy. **Nat. Mater.**, 10, 278-281, 2011.

ISHIZUKA, K.; KIMOTO, K.; BANDO, Y.; Improving Energy Resolution of EELS Spectra by Deconvolution using Maximum-Entropy and Richardson-Lucy Algorithms. **Microsc. Microanal.**, 9(2), 832-833, 2003.

JAMES, E. M.; BROWNING, N. D.; Practical aspects of atomic resolution imaging and analysis in STEM. **Ultramicroscopy**, 78, 125-139, 1999.

JIA, C. L.; LENTZEN, M.; URBAN, K.; Atomic-resolution imaging of oxygen in perovskite ceramics. **Science**, 299, 870-873, 2003.

JIA, C. L.; LENTZEN, M.; URBAN, K.; High-resolution transmission electron microscopy using negative spherical aberration; **Microscopy and Microanalysis**, 10, 2, 174-184, 2004a.

JIA, C. L.; URBAN, K.; Atomic-Resolution Measurement of Oxygen Concentration in Oxide Materials. **Science**, 303, 2001-2004, 2004b.

JIA, C. L.; MI, S. B.; URBAN, K.; VREJOIU, I.; ALEXE, M.; HESSE, D.; Atomic-scale study of electric dipoles near charged and uncharged domain walls in ferroelectric films. **Nature Materials**, **7**, 57-61, 2008.

JIA, C. L.; HOUBEN, L.; THUST, A.; BARTHEL, J.; On the benefit of the negative-spherical-aberration imaging technique for quantitative HRTEM, **Ultramicroscopy**, 110, 5, 500-505, 2010.

JINSCHEK, J. R.; KISIELOWSKI, C.; VAN DYCK, D.; GEUENS, P.; Measurement of the indium segregation in InGaN based LEDs with single atom sensitivity. **Proceedings of the SPIE**, 5187, 54-63, 2004.

JINSCHEK, J. R.; BATENBURG, K. J.; CALDERON, H. A.; KILAAS, R.; RADMILOVIC, V.; KISIELOWSKI, C.; 3-D reconstruction of the atomic positions in a simulated gold nanocrystal based on discrete tomography: prospects of atomic resolution electron tomography. **Ultramicroscopy**, 108, 589-604 2008.

JOHNSON, C. L.; SNOECK, E.; EZCURDIA, M.; RODRIGUEZ-GONZALEZ, B.; PASTORIZA-SANTOS, I.; LIZ-MARZAN, L. M.; HYTCH, M. J.; Effects of elastic anisotropy on strain distributions in decahedral gold nanoparticles. **Nature Materials**, **7**, 120-124, 2008.

KANEKO, K.; INOKE, K.; FREITAG, B.; HUNGRIA, A. B.; MIDGLEY, P. A.; HANSEN, T. W.; ZHANG, J.; OHARA, S.; ADSCHIRI, T.; Structural and morphological characterization of cerium oxide nanocrystals prepared by hydrothermal synthesis. **Nano Lett.**, 7, 421-425, 2007.

KHARTON, V. V.; FIGUEIREDO, F. M.; NAVARRO, L.; NAUMOVICH, E. N.; KOVALEVSKY, A. V.; YAREMCHENKO, A. A.; VISKUP, A. P.; CARNEIRO, A.; MARQUES, F. M. B.; FRADE, J. R.; Ceria-Based Materials for Solid Oxide Fuel Cells. **Journal Of Materials Science**, 36, 5, 1105-1117, 2001.

KILAAS, R.; RADMILOVIC, V.; Structure determination and structure refinement of Al_2CuMg precipitates by quantitative high-resolution electron microscopy. **Ultramicroscopy**, 88, 1, 63-72, 2001.

KIMOTO, K.; ASAKA, T.; NAGAI, T.; SAITO, M.; MATSUI, Y.; ISHIZUKA, K.; Element-selective imaging of atomic columns in a crystal using STEM and EELS. **Nature**, 450, 702-704, 2007.

KIMOTO, K.; ISHIZUKA, K.; MATSUI, Y.; Decisive factors for realizing atomic-column resolution using STEM and EELS. **Micron**, 39, 257-262, 2008.

KIMOTO, K.; ISHIZUKA, K.; Spatially resolved diffractometry with atomic-column resolution. **Ultramicroscopy**, 111, 1111-1116, 2011.

KIRKLAND, A. I.; MEYER, R. R.; "Indirect" high-resolution transmission electron microscopy: Aberration measurement and wavefunction reconstruction. **Microscopy and Microanalysis**, 10, 4, 401-413, 2004.

KIRKLAND, E. J.; **Advanced Computing in Electron Microscopy**, New York: Plenum, 1998.

KITTEL, C.; **Introduction to Solid State Physics**, New York: John Wiley and Sons, 2004.

KOCH, C.; **QSTEM software**, http://www.christophtkoch.com/stem/index.html, acessado em 10/10/2011.

KOLMAKOV, A.; MOSKOVITS, M.; Chemical Sensing and Catalysis by One-Dimensional Metal-Oxide Nanostructures. **Annu. Rev. Mater. Res.**, 34, 151-180, 2004.

KOWAL, A.; LI, M.; SHAO, M.; SASAKI, K.; VUKMIROVIC, M. B.; ZHANG, J.; MARINKOVIC, N. S.; LIU, P.; FRENKEL, A. I.; ADZIC, R. R.; Ternary Pt/Rh/SnO2 electrocatalysts for oxidizing ethanol to CO2. **Nat. Mat.**, 8, 4, 325-330, 2009.

KRET, S.; RUTERANA, P.; ROSENAUER, A.; GERTHSEN, D.; Extracting quantitative information from high resolution electron microscopy; **Phys. Stat. Sol.**, 227, 1, 247-295, 2001.

KRIVANEK, O. L.; DELLBY, N.; LUPINI, A. R.; Towards sub-Å electron beams, **Ultramicroscopy**, 78, 1 -11, 1999.

KRIVANEK, O. L.; URSIN, J. P.; BACON, N. J.; CORBIN, G. J.; DELLBY, N.; HRNCIRIK, P.; MURFITT, M. F.; OWN, C. S.; SZILAGYI, Z. S.; High-energy-resolution monochromator for aberration-corrected scanning transmission electron microscopy/electron energy-loss spectroscopy. **Phil. Trans. R. Soc. A.**, 367, 3683-3697, 2009.

KRIVANEK, O. L.; CHISHOLM, M. F.; NICOLOSI, V.; PENNYCOOK, T. J.; CORBIN, G. J.; DELLBY, N.; MURFITT, M. F.; OWN, C. S.; SZILAGYI, Z. S.; OXLEY, M. P.; PANTELIDES, S. T.; PENNYCOOK, S. J.; Atom-by-atom structural and chemical analysis by annular dark-field electron microscopy. **Nature**, 464, 571-574, 2010.

KURATA, H.; ISOJIMA, S.; KAWAI, M.; SHIMAKAWA, Y.; ISODA, S.; Local analysis of the edge dislocation core in BaTiO(3) thin film by STEM-EELS. **J. Microscopy**, 2009, 236, 128-131.

LAZAR, S.; SHAO, Y.; GUNAWAN, L.; NECHACHE, R.; PIGNOLET, A.; BOTTON, G. A.; Imaging, Core-Loss, and Low-Loss Electron-Energy-Loss Spectroscopy Mapping in Aberration-Corrected STEM. **Microscopy and Microanalysis**, 16, 416-424, 2010.

LEBEAU, J. M.; FINDLAY, S. D.; ALLEN, L. J.; STEMMER, S.; Standardless Atom Counting in Scanning Transmission Electron Microscopy. **Nano Lett.**, 10, 4405-4408, 2010.

LEE, C.; YANG, W.; PARR, R. G.; Development of the Colle-Salvetti correlation-energy formula into a functional of the electron density. **Phys. Rev. B**, 37, 2, 785-789, 1988.

LEE, E. J. H.; RIBEIRO C.; LONGO, E.; LEITE, E. R.; Oriented Attachment: An Effective Mechanism in the Formation of Anisotropic Nanocrystals. **J. Phys. Chem. B**, 109, 20842-20846, 2005.

LEE, K. S.; PARK, I. S.; CHO, Y. H.; JUNG, D. S.; JUNG, N.; PARK, H. Y., SUNG, Y.E.; Electrocatalytic activity and stability of Pt supported on Sb-doped SnO2 nanoparticles for direct alcohol fuel cells. **J. Catal.**, 258 (1), 143-152, 2008.

LEITE, E. R.; GIRALDI, T. R.; PONTES, F. M.; LONGO, E.; BELTRAN, A.; ANDRES, J.; Crystal growth in colloidal tin oxide nanocrystals induced by coalescence at room. **Appl. Phys. Lett**., 83, 1566-1568, 2003.

LEITE, E. R. In: **Encyclopedia of Nanoscience and Nanotechnology**, Los Angeles: ASP, 2004, 6.

LENTZEN, M.; THUST, A.; URBAN, K.; The error of aberration measurements in HRTEM using Zemlin tableaus. **Microscopy Microanal.**, 10, 980-981, 2004.

LEVI, A. C.; SUHL, H.; Quantum theory of atom-surface scattering: Debye-Waller factor. **Surface Science**, 88, 1, 221-254, 1979.

LEWIS, G. N.; RANDALL, M.; **Thermodynamics**, New York: McGraw-Hill, 1961.

LI, Z.-P.; MORI, T.; AUCHTERLONIE, G. J.; ZOU, J.; DRENNAN J.; Direct evidence of dopant segregation in Gd-doped ceria. **Appl. Phys. Lett.**, 98, 093104, 2011.

LICHTE, H.; FORMANEK, P.; LENK, A.; LINCK, M.; MATZECK, C.; LEHMANN, M.; SIMON, P.; Electron Holography: Applications to Materials Questions, **Annu. Rev. Mater. Res.**, 37, 539-588, 2007.

LIFSHITZ, I. M.; SLYOZOV, V. V.; The kinetics of precipitation from supersaturated solid solutions. J**. Phys. Chem. Sol.**, 19, 35-50, 1961.

LIM, S. K.; BREWSTER, M.; QIAN, F.; LI, Y.; LIEBER, C. M.; GRADECAK, S.; Direct Correlation between Structural and Optical Properties of III-V Nitride Nanowire Heterostructures with Nanoscale Resolution. **Nano Lett.**, 9, 3940-3944, 2009.

LONGO, V. M.; GRACIA, L.; STROPPA, D. G.; CAVALCANTE, L. S.; ORLANDI, M. O.; RAMIREZ, A. J; LEITE, E. R.; ANDRÉS, J.; BELTRAN, A.; VARELA, J. A.; LONGO, E.; A Joint Experimental and Theoretical Study on the Nanomorphology of CaWO4 Nanocrystals. **J. Phys. Chem. C**, DOI: 10.1021/jp205764s, 2011.

LU, K.; SOURTY, E.; LOOS, J.; Annular dark-field scanning transmission electron microscopy (ADF-STEM) tomography of polymer systems. **J. Electron Microsc.,** 59, 39-44, 2010.

LUFF, B. J.; WILKINSON, J. S.; PERRONE, G.; Indium tin oxide overlayered waveguides for sensor applications. **Applied Optics**, 36, 27, 7066-7072, 1997.

LUYSBERG, M.; HEIDELMANN, M.; HOUBEN, L.; BOESE, M.; HEEG, T.; SCHUBERT, J.; ROECKERATH, M.; Intermixing and charge neutrality at DyScO3/SrTiO3 interfaces. **Acta Mater.**, 57(11), 3192-3198, 2009.

MA, Y; NAVROTSKY A; Calorimetric Study of Heats of Mixing in SnxTi1-xO2 Rutile Solid Solutions. **J. Am. Cer. Soc.**, 93, 3432, 2010.

MALIS, T.; CHENG, S. C.; EGERTON, R. F.; EELS log-ratio Technique for Specimen-thickness Measurement in the TEM. **J. Electron Microsc. Techn.**, 8, 193-200, 1988.

MARKS, L. D.; Modified Wulff constructions for twinned particles. **J. Cryst. Growth**, 61, 3, 556-566, 1983.

MCCARTHY, G. J.; WELTON, J. M.; X-Ray Diffraction Data for SnO2. An Illustration of the New Powder Data Evaluation Methods. **Powder Diffr.**, 4, 3, 156-160, 1989.

MCLACHLAN, G.; PEEL, D.; **Finite Mixtures Models**, New York: John Wiley and Sons, 2000.

MELDRUM, F. C.; COLFEN, H.; Controlling Mineral Morphologies and Structures in Biological and Synthetic Systems. **Chem. Rev.**, 108, 4332-4432, 2008.

MIDGLEY, P. A.; WEYLAND, M.; THOMAS, J. M.; JOHNSON, B. F. G; Z-contrast tomography: A technique in three-dimensional nanostructural analysis based on Rutherford scattering. **Chem. Comm.**, 10, 907-908, 2001.

MIDGLEY, P. A.; WEYLAND M.; 3D electron microscopy in the physical sciences: the development of Z-contrast and EFTEM tomography, **Ultramicroscopy**, 903, 413-431, 2003.

MINAMI, T.; Transparent conducting oxide semiconductors for transparent electrodes. **Semicond. Sci. Tech.**, 20, 4, S35-S44, 2005.

MITSUISHI, K.; HASHIMOTO, A.; TAKEGUCHI, M.; SHIMOJO, M.; ISHIZUKA, K.; Imaging properties of bright-field and annular-dark-field scanning confocal electron microscopy. **Ultramicroscopy**, 111, 20-26, 2010.

MITTAL, A.; MKHOYAN, K. A.; Limits in detecting an individual dopant atom embedded in a crystal. **Ultramicroscopy**, 111, 1101-1110, 2011.

MÖBUS, G.; Tese de doutorado, University of Stuttgart, Alemanha, 1994.

MOECK, P.; ROUVIMOV, S.; RAUCH, E. F.; VÉRON, M.; KIRMSE, H.; HÄUSLER, I.; NEUMANN, W.; BULTREYS, D.; MANIETTE, Y.; NICOLOPOULOS, S.; High spatial resolution semi-automatic crystallite orientation and phase mapping of nanocrystals in transmission electron microscopes. **Cryst. Res. Technol.**, 46, 589-606, 2011.

MOLDOVAN, D.; YAMAKOV, V.; WOLF, D.; PHILLPOT, S. R.; Scaling behavior of grain-rotation-induced grain growth. **Phys. Rev. Lett.**, 89, 20, 206101, 2002.

MOLINA, S. I.; SALES, D. L.; GALINDO, P. L.; FUSTER, D.; GONZÁLEZ, Y.; ALÉN, B.; GONZÁLEZ, L.; VARELA, M.; PENNYCOOK, S. J.; Column-by-column compositional mapping by Z-contrast imaging. **Ultramicroscopy**, 109, 172-176, 2009.

MONTORO, L. A.; LEITE, M. S.; BIGGEMANN, D.; PETERNELLA, F. G.; BATENBURG, K. J.; MEDEIROS-RIBEIRO, G.; RAMIREZ, A. J.; Revealing Quantitative 3D Chemical Arrangement on Ge-Si Nanostructures. **J. Phys. Chem. C.**, 113, 21, 9018-9022, 2009.

MONTORO, L. A.; MEDEIROS-RIBEIRO, G.; RAMIREZ, A. J.; Novel Approach for High-Resolution Elastic Behavior Assessment of Alloyed Strained Nanostructures. **J. Phys. Chem. C.**, 114, 29, 12409-12415, 2010.

MOOK, H. W.; KRUIT, P. P.; Construction and characterization of the fringe field monochromator for a field emission gun. **Ultramicroscopy**, 81,129-139, 2000.

MOORE, L. J.; DEAR, R. D.; SUMMERS, M. D.; DULLENS, R. P. A.; RITCHIE, G. A. D.; Direct observation of grain rotation-induced grain coalescence in two-dimensional colloidal crystals. **Nano Lett.**, 10, 10, 4266-4272, 2010.

MORALES, E. H.; HE, Y.; VINNICHENKO, M.; DELLEY, B.; DIEBOLD, U.; Surface structure of Sn-doped In2O3 (111) thin films by STM. **New Journal of Physics**, 10, 125030, 2008.

MULLER, D. A.; SILCOX, J.; Delocalization in inelastic scattering. **Ultramicroscopy**, 59, 195-213, 1995.

MULLER, D. A.; KOURKOUTIS, L. F.; MURFITT, M.; SONG, J. H.; HWANG, H. Y.; SILCOX, J.; DELLBY, N.; KRIVANEK, O. L.; Atomic-scale chemical imaging of composition and bonding by aberration-corrected microscopy. **Science**, 319, 1073-1076, 2008.

NELAYAH, J.; KOCIAK, M.; STEPHAN, O.; DE ABAJO, F. J. G.; TENCE, M.; HENRARD, L.; D.; TAVERNA, PASTORIZA-SANTOS, I.; LIZ-MARZAN, L. M.; COLLIEX, C.; Mapping surface plasmons on a single metallic nanoparticle. **Nature Physics**, 3, 348-353, 2007.

NIEDERBERGER, M.; COLFEN, H.; Oriented attachment and mesocrystals: Non-classical crystallization mechanisms based on nanoparticle assembly. **Phys. Chem. Chem. Phys.**, 8, 3271-3287, 2006a.

NIEDERBERGER, M.; GARNWEITNER, G.; Organic reaction pathways in the nonaqueous synthesis of metal oxide nanoparticles. **Chem. Eur. J.**, 12, 28, 7282-7302, 2006b.

NÜTZENADEL, C.; ZÜTTEL, A.; CHARTOUNI, D.; SCHMID, G.; SCHLAPBACH, L.; Critical size and surface effect of the hydrogen interaction of palladium clusters. **Eur. Phys. J. D**, 8, 2, 245-250, 2000.

O'KEEFE, M.A.; ALLARD, L. F.; BLOM, D. A.; HRTEM imaging of atoms at sub-Ångström resolution. **J. Electron Microsc.**, 54, 3, 169-180, 2005.

OHNISHI, I.; OKUNISHI, E.; YAMAZAKI, K.; AOTA, N.; MIYATAKE, K.; NAKANISHI, M.; OHKURA, Y.; KONDO, Y.; YASUNAGA, K.; TOH, S.; MATSUMURA, S.; **Microscopy & Microanalysis 2011 Meeting**, 2011.

ORERA, A.; SLATER, P. R.; New Chemical Systems for Solid Oxide Fuel Cells. **Chem. Mater.**, 22, 675-690, 2010.

OU, D. R.; MORI, T.; YE, F.; ZOU, J.; AUCHTERLONIE, G.; DRENNAN, J.; Oxygen-vacancy ordering in lanthanide-doped ceria: Dopant-type dependence and structure model. **Phys. Rev. B**, 77, 024108, 2008.

PEI, L.; DUSCHER, G.; STEEN, C.; PICHLER, P.; RYSSEL, H.; NAPOLITANI, E.; DE SALVADOR, D.; PIRO, A. M.; TERRASI, A.; SEVERAC, F.; CRISTIANO, F.; RAVICHANDRAN, K.; GUPTA, N.; WINDL W.; Detailed arsenic concentration profiles at Si/SiO2 interfaces. **J. Apl. Phys.**, 104, 043507, 2008.

PENN, R. L.; BANFIELD, J. F.; Imperfect oriented attachment: Dislocation generation in defect-free nanocrystals. **Science,** 281, 969-971, 1998a.

PENN, R. L.; BANFIELD, J. F.; Oriented attachment and growth, twinning, polytypism, and formation of metastable phases: Insights from nanocrystalline TiO2. **Am. Mineral.,** 83, 1077-1082, 1998b.

PENN, R. L.; BANFIELD, J. F.; Morphology development and crystal growth in nanocrystalline aggregates under hydrothermal conditions: Insights from titania. **Geochim. Cosmochin. Acta**, 63, 1549-1557, 1999.

PENNYCOOK, S. J.; BOATNER, L. A.; Chemically sensitive structure-imaging with a scanning transmission electron microscope **Nature**, 336, 565-567, 1988.

PENNYCOOK, S. J.; JESSON, D. E.; High-resolution Z-contrast imaging of crystals. **Ultramicroscopy**, 37, 14-38, 1991.

PENNYCOOK, S. J.; JESSON, D. E.; MCGIBBON, A. J.; NELLIST, P. D.; High Angle Dark Field STEM for Advanced Materials. **J. Electron Microsc.**, 45, 36-43, 1996.

PENNYCOOK, S. J.; CHISHOLM, M. F.; LUPINI, A. R.; VARELA, M.; BORISEVICH, A. Y.; OXLEY, M. P.; LUO, W. D.; VAN BENTHEM, K.; OH, S.-H.; SALES, D. L.; MOLINA, S. I.; GARCÍA-BARRIOCANAL, J.; LEON, C.; SANTAMARÍA, J.; RASHKEEV, S. N.; PANTELIDES, S. T.; Aberration-corrected scanning transmission electron microscopy: from atomic imaging and analysis to solving energy problems. **Phil. Trans. R. Soc. A.**, 367, 3709-3733, 2009.

PENNYCOOK, S. J.; NELLIST, P. D.; **Scanning Transmission Electron Microscopy: Imaging and Analysis**, New York: Springer, 2011.

PETTERSEN, E. F.; GODDARD, T. D.; HUANG, C. C.; COUCH, G. S.; GREENBLATT, D. M.; MENG, E. C.; FERRIN, T. E.; UCSF Chimera--a visualization system for exploratory research and analysis. **J. Comput. Chem.**, 25, 13, 1605-1612, 2004.

POLLEUX, J.; PINNA, N.; ANTONIETTI, M.; HESS, C.; WILD, U.; SCHLOGL, R.; NIEDERBERGER, M.; Ligand functionality as a versatile tool to control the assembly behavior of preformed titania nanocrystals. **Chem. Eur. J.**, 11, 3541-3551, 2005.

POWELL, C. J.; Cross sections for inelastic electron scattering in solids, **Ultramicroscopy**, 28, 24-31, 1989.

PUNTES, V. F.; KRISHNAN, K. M.; ALIVISATOS, A. P.; Colloidal nanocrystal shape and size control: The case of cobalt. **Science**, 291, 2115-2117, 2001.

RAKHSHANI, A. E.; MAKDISI, Y.; RAMAZANIYAN, H. A.; Electronic and optical properties of fluorine-doped tin oxide films. **J. Appl. Phys.**, 83, 2, 1049-1057, 1998.

RAMÍREZ-CABRERA, E.; ATKINSON, A.; CHADWICK, D.; Catalytic Steam Reforming Of Methane Over $Ce_{0.9}Gd_{0.1}O_{2-X}$. Appl. Catal. B-Environ, 47, 2, 127-131, 2004.

RATKE, L.; VOORHEES, P. W.; **Growth and Coarsening: Ostwald Ripening in Material Processing**, Berlin: Springer, 2002.

RATKOVICH, A. S.; PENN, R. L.; Controlling Nanosized ZnO Growth Kinetics Using Various Zn:OH Concentration Ratios. **J. Phys. Chem. C**, 111, 14098-14104, 2007.

RATSCH, C.; SCHEFFLER, M.; Density-functional theory calculations of hopping rates of surface diffusion. **Phys. Rev. B,** 58, 13163-13166, 1998.

REIMER, L.; KOHL, H.; **Transmission electron microscopy: physics of image formation**, New York: Springer, 2008.

RENAUD, G; LAZARI, R.; REVENANT, C.; BARBIER, A.; NOBLET, M.; ULRICH, O.; LEROY, F.; JUPILLE, J.; BORENSZTEIN, Y.; HENRY, C. R.; DEVILLE, J. P.; SCHEURER, F.; MANE-MANE, J.; FRUCHART, O.; Real-time monitoring of growing nanoparticles. **Science**, 300, 1416-1419, 2003.

RIBEIRO C.; LEE, E. J. H.; LONGO, E.; LEITE, E. R.; A kinetic model to describe nanocrystal growth by the oriented attachment mechanism. **ChemPhysChem**, 6, 690-696, 2005.

RIBEIRO C.; LEE, E. J. H.; LONGO, E.; LEITE, E. R.; Oriented Attachment Mechanism in Anisotropic Nanocrystals: A “Polimerization“ approach. **ChemPhysChem**, 7, 664-670, 2006.

RIEGLER, K.; KOTHLEITNER, G.; EELS detection limits revisited: Ruby - a case study. **Ultramicroscopy**, 110, 8, 1004-1013, 2010.

ROSENAUER, A.; GRIES, K.; MÜLLER, K.; PRETORIUS, A.; SCHOWALTER, M.; AVRAMESCU, A.; ENGL, K.; LUTGEN, S.; Measurement of specimen thickness and composition in Al(x)Ga(1-x)N/GaN using high-angle annular dark field images. **Ultramicroscopy**, 109, 1171-1182, 2009.

ROSSOUW, D.; COUILLARD, M.; VICKERY, J.; KUMACHEVA, E.; BOTTON, G. A.; Multipolar Plasmonic Resonances in Silver Nanowire Antennas Imaged with a Subnanometer Electron Probe. **Nano Lett.**, 11, 4, 1499-1504, 2011.

RUH, E.; MUELLER, E.; MUSSLER, G.; SIGG, H. C.; GRUETZMACHER, D.; Investigation of the local Ge concentration in Si/SiGe nanostructures by convergent-beam electron diffraction. **Ultramicroscopy**, 2010, 110, 1255-1266.

RÜHLE, M.; ERNST, F.; **High Resolution imaging and Spectroscopy of Materials**. Berlin: Springer, 2003.

SCHAMM, S.; BONAFOS, C.; COFFIN, H.; CHERKASHIN, N.; CARRADA, M.; BEN ASSAYAG, G.; CLAVERIE, A.; TENCE, M.; COLLIEX, C.; Imaging Si nanoparticles embedded in SiO2 layers by (S)TEM-EELS, **Ultramicroscopy**, 108, 346-357, 2008.

SCHERZER, O.; The Theoretical Resolution Limit of the Electron Microscope. **J. Appl. Phys.**, 20, 1, 20-29, 1949.

SEYRING, M.; SONG, X.; RETTENMAYR, M.; Advance in orientation microscopy: Quantitative analysis of nanocrystalline structures. **ACS Nano**, 5(4), 2580-2586, 2011.

SHARP, J. H.; BARNARD, J. S.; KANEKO, K.; HIGASHIDA, K.; MIDGLEY, P. A.; Dislocation tomography made easy: a reconstruction from ADF STEM images obtained using automated image shift correction. **Journal of Physics: Conference Series**, 126, 012013, 2008.

SHCHUKIN, V. A.; LEDENTSOV, N. N.; KOP'EV, P. S.; BIMBERG, D.; Spontaneous Ordering of Arrays of Coherent Strained Islands. **Phys. Rev. Lett.**, 1995, 75(16), 2968-2971.

SHIBATA, N.; PENNYCOOK, S. J.; GOSNELL, T. R.; PAINTER, G. S.; SHELTON, W. A.; BECHER, P. F.; Observation of rare-earth segregation in silicon nitride ceramics at subnanometre dimensions. **Nature**, 428, 730-733, 2004.

SINGH, T.; MOUNTZIARIS, T. J.; MAROUDAS, D.; On the transition-metal doping efficiency of zinc oxide nanocrystals. **Appl. Phys. Lett.**, 97, 073120, 2010.

SLATER, B.; CATLOW, C. R. A.; GAY, D. H.; WILLIAMS, D. E.; DUSASTRE, V.; Study of Surface Segregation of Antimony on SnO2 Surfaces by Computer Simulation Techniques. **J. Phys. Chem. B**, 103, 10644, 1999.

SOHLBERG, K.; RASHKEEV, S.; BORISEVICH, A. Y.; PENNYCOOK, S. J.; PANTELIDES, S. T.; Origin of Anomalous Pt–Pt Distances in the Pt/Alumina Catalytic System. **ChemPhysChem**, 5, 1893-1897, 2004.

STADELMANN, P. A.; EMS - A Software Package for Electron Diffraction Analysis and HREM Image Simulation in Materials Science. **Ultramicroscopy**, 21, 2, 131-145, 1987.

STEINECKER, A.; MADER, W.; Measurement of lens aberrations by means of image displacements in beam-tilt series. **Ultramicroscopy**, 81, 149-161, 2000.

STÖGER-POLLACH, M.; Optical properties and bandgaps from low loss EELS: Pitfalls and solutions. **Micron**, 39, 1092-1110, 2008.

STROPPA, D. G.; MONTORO, L. A.; BELTRAN, A.; CONTI, T. G.; SILVA, R. O.; ANDRES, J.; LONGO, E.; LEITE, E. R.; RAMIREZ, A. J.; Unveiling the Chemical and Morphological Features of Sb:SnO_2 Nanocrystals by the Combined Use of HRTEM and ab initio Surface Energy Calculations. **J. Am. Chem. Soc.**, 131, 14544-14548, 2009.

STROPPA, D. G.; UNFRIED S., J.; HERMENEGILDO, T.; RAMIREZ A. J.; Projected Area Method for the Evaluation of Contact Angle on Sessile Drop Test. **Welding Journal**, 89, 3, 47-49, 2010.

STROPPA, D. G.; MONTORO, LEITE, E. R.; RAMIREZ, A. J.; HRTEM techniques applied to nanocrystal modeling: towards an “atom-by-atom” description. **Material Characterisation V**, WIT Press, 2011a.

STROPPA, D. G.; MONTORO, L. A.; BELTRAN, A.; CONTI, T. G.; SILVA, R. O.; ANDRES, J.; LEITE, E. R.; RAMIREZ, A. J.; Anomalous oriented attachment growth behavior on SnO_2 nanocrystals. **Chem. Commun.**, 47, 3117-3119, 2011b.

STROPPA, D. G.; MONTORO, L. A.; RIGHETTO, R. D.; RAMIREZ, A. J.; MEGACELL: A nanocrystals models construction software for HRTEM multislice simulation. **Ultramicroscopy**, 111, 1077-1082, 2011c.

STROPPA, D. G.; MONTORO, L. A.; BELTRAN, A.; CONTI, T. G.; SILVA, R. O.; ANDRES, J.; LEITE, E. R.; RAMIREZ, A. J.; Dopants segregation analysis on $Sb:SnO_2$ nanocrystals. **Chem. Eur. J.**, 17, 11515-11519, 2011d.

STROPPA, D. G.; ZAGONEL, L. F.; MONTORO, LEITE, E. R.; RAMIREZ, A. J.; HRSTEM techniques - High Resolution Imaging and Spectroscopy Side by Side, **ChemPhysChem**, aceito para publicação, 2011e.

STROPPA, D. G.; RIGHETTO, R. D.; MONTORO, L. A.; HOUBEN, L.; BARTHEL, J.; CORDEIRO, M. A. L.; LEITE, E. R.; WENG, W.; KIELY, C. J.; URBAN, K.; RAMIREZ, A. J.; Nanocrystals Three-Dimensional Reconstruction from HAADF-HRSTEM single images, submetido para publicação, 2011f.

STROPPA, D. G.; MONTORO, L. A.; CAMPELO, A.; GRACIA, L.; BELTRÁN, A.; ANDRÉS, J.; LEITE, E. R.; RAMIREZ, A. J.; Thermodynamic approach to predict dopant atoms segregation on nanocrystals, submetido para publicação, 2011g.

STROPPA, D. G.; MONTORO, L. A.; DALMASCHIO, C. J.; HOUBEN, L.; URBAN, K.; LEITE, E. R.; RAMIREZ, A. J.; Dopant Atoms Segregation and Oxygen Vacancies Analysis on individual $Gd:CeO_2$ Nanocrystals by EELS-STEM, submetido para publicação, 2011h.

SUENAGA, K.; TENCE, T.; MORY, C.; COLLIEX, C.; KATO, H.; OKAZAKI, T.; SHINOHARA, H.; HIRAHARA, K.; BANDOW, S.; IIJIMA, S.; Element-Selective Single Atom Imaging. **Science**, 290, 2280-2282, 2000.

SUN, K.; LIU, J.; BROWNING, N. D.; Correlated atomic resolution microscopy and spectroscopy studies of Sn(Sb)O2 nanophase materials. **J. Catal.**, 205, 266-277, 2002.

TAKEGUCHI, M.; HASHIMOTO, A.; SHIMOJO, M.; MITSUISHI, K.; FURUYA, K.; Development of a stage-scanning system for high-resolution confocal STEM. **J. Electron Microsc.**, 57, 123-127, 2008.

TANG, Z. Y.; KOTOV, N. A.; GIERSIG, M.; Spontaneous Organization of Single CdTe Nanoparticles Into Luminescent Nanowires. **Science**, 297, 237, 2002.

TANUMA, S.; POWELL, C. J.; PENN, D. R.; Calculations of electron inelastic mean free paths. **Surf. Interface Anal.**, 43, 689-713, 2011.

TERRIER, C.; CHATELON, J. P.; ROGER, J. A.; Electrical and optical properties of Sb:SnO2 thin films obtained by the sol-gel method. **Thin Solid Films**, 295, 95-100, 1997.

THUST, A.; COENE, W. M. J.; de BEECK, M. O.; Van DYCK, D.; Focal-series reconstruction in HRTEM: simulation studies on non-periodic objects; **Ultramicroscopy**, 64, 1, 211-230, 1996.

THUST, A.; High-Resolution Transmission Electron Microscopy on an Absolute Contrast Scale. **Phys. Rev. Lett.**, 102, 22, 1-4, 2009.

TILLMANN, K.; LUYSBERG, M.; SPECHT, P.; WEBER, E. R.; Direct compositional analysis of AlGaAs/GaAs heterostructures. **Ultramicroscopy**, 93, 123-137, 2002.

TITILOYE, J.O.; PARKER, S.C.; MANN, S.; Atomistic simulation of calcite surfaces and the influence of growth additives on their morphology, **J. Cryst. Growth**, 131, 533-545, 1993.

TIZEI, L. H. G.; CRAVEN, A. J.; ZAGONEL, L. F.; TENCÉ, M.; STÉPHAN, O.; CHIARAMONTE, T.; COTTA, M. A.; UGARTE, D.; Enhanced Eshelby twist on thin wurtzite InP nanowires and measurement of local crystal rotation. **Phys. Rev. Lett.**, aceito para publicação, 2011.

TRASOBARES, S.; LÓPEZ-HARO, M.; KOCIAK, M.; MARCH, K.; DE LA PEÑA, F.; PEREZ-OMIL, J. A.; CALVINO, J. J.; LUGG, N. R.; D'ALFONSO, A. J.; ALLEN, L. J.; COLLIEX, C.; Chemical Imaging at Atomic Resolution as a unique tool to Refine the Structure of Nanocrystals. **Angew. Chem. Int. Ed.**, 50, 1-6, 2011.

TROVARELLI, A.; **Catalysis by Ceria And Related Materials**, London: Imperial College Press, 2002.

TUTUIANU, M.; INDERWILDI, O.; BESSLER, W. G.; WARNATZ, J.; Competitive adsorption of NO, NO2, CO2, and H2O on BaO(100): A quantum chemical study. **J. Phys. Chem. B,** 110, 17484-17492, 2006.

UESUGI, F.; HOKAZONO, A.; TAKENO, S.; Evaluation of two-dimensional strain distribution by STEM/NBD. **Ultramicroscopy**, 111, 995-998, 2011.

UHLEMANN, S.; HAIDER, M.; Residual wave aberrations in the first spherical aberration corrected transmission electron microscope. **Ultramicroscopy**, 72, 109-119, 1998.

URBAN, K. W.; Studying atomic structures by aberration-corrected transmission electron microscopy. **Science**, 321, 506-510, 2008.

VAN AERT, S.; VERBEECK, J.; ERNI, R.; BALS, S.; LUYSBERG, M.; VAN DYCK, D.; VAN TENDELOO, G.; Quantitative atomic resolution mapping using high-angle annular dark field scanning transmission electron microscopy. **Ultramicroscopy**, 109, 1236-1244, 2009.

VAN AERT, S.; BATENBURG, K. J.; ROSSELL, M. D.; ERNI, R.; TENDELOO, G. V.; Three-dimensional atomic imaging of crystalline nanoparticles. **Nature**, 470, 374-377, 2011.

VERLEYSEN, E.; BENDER, H.; RICHARD, O.; SCHRYVERS, D.; VANDERVORST, W.; Characterization of nickel silicides using EELS-based methods. **J. Microscopy**, 240, 75-82, 2010.

VOORHEES, P. W.; The theory of Ostwald ripening. **Journal of Statistical Physics**, 38, 231-252, 1985.

VOYLES, P. M.; MULLER, D. A.; GRAZUL, J. L.; CITRIN, P. H.; GOSSMANN, H. -J. L.; Atomic-scale imaging of individual dopant atoms and clusters in highly n-type bulk S. **Nature**, 416, 826-829, 2002.

WAGNER, C.; Theorie der Alterung von Niederschlägen durch Umlösen (Ostwald-Reifung). **Z. Electrochem.**, 65, 581-591, 1961.

WALSH, A.; CATLOW, C. R. A.; Structure, stability and work functions of the low index surfaces of pure indium oxide and Sn-doped indium oxide (ITO) from density functional theory. **J. Mater. Chem.**, 20, 10438, 2010.

WALTON, A. J.; The Abbe theory of imaging: an alternative derivation of the resolution limit. **Eur. J. Phys.**, 7, 62-63, 1986

WANG, A.; CHEN, F. R.; VAN AERT, S.; VAN DYCK, D.; Direct structure inversion from exit waves Part I: Theory and simulations, **Ultramicroscopy**, 110, 527-534, 2010a.

WANG, C. M.; BAER, D. R.; AMONETTE, J. E.; ENGELHARD, M. H ; ANTONY, J.; QIANG, Y.; Morphology and Electronic Structure of the Oxide Shell on the Surface of Iron Nanoparticles. **J. Am. Chem. Soc.**, 131, 25, 8824-8832, 2009.

WANG, X.; SONG, F.; CHEN, Q.; WANG, T.; WANG, J.; LIU, P.; SHEN, M.; WAN, J.; WANG, G.; XU, J.; Scaling dopant states in a semiconducting nanostructure by chemically resolved electron energy-loss spectroscopy: a case study on Co-doped ZnO. **J. Am. Chem. Soc.**, 132, 6492-6497, 2010b.

WANG, Y. D.; DJERDJ, I.; ANTONIETTI, M.; SMARSLY, B.; Polymer-Assisted Generation of Antimony-Doped SnO2 Nanoparticles with High Crystallinity for Application in Gas Sensors. **Small**, 4, 10, 1656-1660, 2008.

WANG, Z. L.; FENG, X. *J.*; Polyhedral shapes of CeO_2 nanoparticles. **J. Phys. Chem. B.**, 107, 13563-13566, 2003.

WATANABE, M.; WILLIANS, D. B.; The quantitative analysis of thin specimens: a review of progress from the Cliff-Lorimer to the new ζ-factor methods. **Journal of Microscopy**, 221, 2, 89-109, 2006.

WATANABE, M.; **Progress on X-ray Analysis of Materials in Aberration-Corrected Scanning Transmission Electron Microscopes**, 17th International Microscopy Congress, 2010.

WILLIANS, D. B.; CARTER, C. B.; **Transmission Electron Microscopy**, New York: Plenum Press, 1996.

WULFF, G. *Z.*; Zur Frage der Geschwindigkeit des Wachstums und der Auflösung der Krystallflagen. **Kryst. Mineral.**, 34, 449-530, 1901.

XIA, X.; OLDMAN, R.; CATLOW R.; Computational Modeling Study of Bulk and Surface of Yttria-Stabilized Cubic Zirconia. **Chem. Mater.**, 21, 3576-3585, 2009b.

XIA, Y.; ROGERS, J. A.; PAUL, K. E.; WHITESIDES, G. M.; Unconventional Methods for Fabricating and Patterning Nanostructures. **Chem. Rev.**, 99, 7, 1823-1848, 1999.

XIA, Y.; XIONG, Y.; LIM, B.; SKRABALAK, S.E.; Shape-controlled synthesis of metal nanocrystals: Simple chemistry meets complex physics? **Angew. Chem. Int. Ed.**, 48, 1, 60-103, 2009a.

XIN, H. L.; MULLER, D. A.; Aberration-corrected ADF-STEM depth sectioning and prospects for reliable 3D imaging in S/TEM. **J. Electron Microsc.**, 58, 157-165, 2009.

XIN, H. L.; MULLER, D. A.; Three-Dimensional Imaging in Aberration-Corrected Electron Microscopes. **Microsc. Microanal.**, 16, 445-455, 2010.

XU, P.; LOANE, R. F.; SILCOX, J.; Energy-filtered convergent-beam electron diffraction in STEM. **Ultramicroscopy**, 38, 2, 127-133, 1991.

YAKOVLEV, S.; MISRA, M.; SHI, S.; FIRLAR, E.; LIBERA, M.; Nanoscale water mapping in hydrated biological materials by low-loss electron energy-loss spectroscopy. **Ultramicroscopy**, 110, 866-876, 2010.

YAMAZAKI, T.; KOTAKA, Y.; KATAOKA, Y.; Analysis of eel spectrum of low-loss region using the c(s)-corrected stem-eels method and multivariate analysis. **Ultramicroscopy**, 111, 303-308, 2011.

YANG, H. G.; SUN, C. H.; QIAO, S. Z.; ZOU, J.; LIU, G.; SMITH, S. C.; CHENG, H. M.; LU, G. Q.; Anatase TiO2 single crystals with a large percentage of reactive facets. **Nature**, 453, 638-641, 2008.

YANG, S.; GAO L. J.; Controlled synthesis and self-assembly of CeO_2 nanocubes. **J. Am. Chem. Soc.**, 128, 9330-9331, 2006.

YU, W. W.; WANG, Y. A.; PENG, X.; Formation and Stability of CdTe Nanocrystals. **Chem. Mater.**, 15, 4300-4308, 2003.

ZAGONEL, L. F.; MAZZUCCO, S.; TENCÉ, M.; MARCH, K.; BERNARD, R.; LASLIER, B.; JACOPIN, G.; TCHERNYCHEVA, M.; RIGUTTI, L.; JULIEN, F. H.; SONGMUANG, R.; KOCIAK, M.; Nanometer scale spectral imaging of quantum emitters in nanowires and its correlation to their atomically resolved structure. **Nano Lett.**, 11, 568-573, 2011.

ZEMLIN, F.; WEISS, K.; SCHISKE, P.; KUNATH, W.; HERRMANN, K. H.; Coma-free alignment of high resolution electron microscopes with the aid of optical diffractograms. **Ultramicroscopy**, 3, 49-60, 1978.

ZHANG, H. Z.; BANFIELD, J. F.; Aggregation, coarsening, and phase transformation in ZnS nanoparticles studied by molecular dynamics simulations. **Nano Lett.**, 4, 713-718, 2004.

ZHANG, L.; TURNER, S.; BROSENS, F.; VERBEECK, J.; Model-based determination of dielectric function by STEM low-loss EELS. **Phys. Rev. B**, 81, 035102, 2010.

ZHENG, H.; SMITH, R. K.; JUN, Y. -W.; KISIELOWSKI, C.; DAHMEN, U.; PAUL ALIVISATOS, A.; Observation of single colloidal platinum nanocrystal growth trajectories. **Science**, 324, 1309-1312, 2009.

ZHOU, L.; O´BRIEN P.; Mesocrystals: A New Class of Solid Materials, **Small**, 4, 1566-1577, 2008.

8. Extras

8.1. Lista de Atividades Acadêmicas

8.1.1. Publicações

Stroppa, D. G.; Zagonel, L. F.; Montoro, L. A.; Leite, E. R.; Ramirez, A. J. HRSTEM techniques - High Resolution Imaging and Spectroscopy Side by Side. *ChemPhysChem*, aceito para publicação, **2011**.

Stroppa, D. G.; Montoro, L. A.; Beltrán, A.; Conti, T. G.; da Silva, R. O.; Andrés, J.; Leite, E. R.; Ramirez, A. J. Dopant Segregation Analysis on Sb:SnO_2 Nanocrystals. *Chemistry A - European Journal*, 17, 11515, **2011**.

Stroppa, D. G.; Righetto, R. D.; Montoro, L. A.; Ramirez, A. J.; MEGACELL: A nanocrystal model construction software for HRTEM multislice simulation. *Ultramicroscopy*; 111, 1077, **2011**.

da Silva, R. O. ; Gonçalves, R. H. ; Stroppa, D. G. ; Ramirez, A. J. ; Leite, Edson R.; Synthesis of recrystallized anatase TiO_2 mesocrystals with Wulff shape assisted by oriented attachment. *Nanoscale*; 3, 1910, **2011**.

Stroppa, D. G.; Montoro, L. A.; Beltrán, A.; Conti, T. G.; da Silva, R. O.; Andrés, J.; Leite, E. R.; Ramirez, A. J.; Anomalous oriented attachment growth behavior on SnO_2 nanocrystals. *Chem. Commun.*; 47(11), 3117, **2011**.

Longo, V. M.; Gracia, L.; Stroppa, D. G.; Cavalcante, L. S.; Orlandi, M. O.; Ramirez, A. J; Leite, E. R.; Andrés, J.; Beltran, A.; Varela, J. A.; Longo, E. A Joint Experimental and Theoretical Study on the Nanomorphology of $CaWO_4$ Nanocrystals. *J. Phys. Chem. C*, DOI: 10.1021/jp205764s, **2011**.

Stroppa, D. G.; Montoro, L. A.; Leite, E. R.; Ramirez, A. J.; HRTEM techniques applied to nanocrystal modeling: towards an atom-by-atom description. *In: Materials Characterization V*. 1, WIT Press, 41. **2011**.

Arantes, T. M.; Mambrini, G. P.; Stroppa, D. G.; Leite, E. R.; Longo, E.; Ramirez, A. J.; Camargo, E. R.; Stable colloidal suspensions of nanostructured zirconium oxide synthesized by hydrothermal process. *J. Nanopart. Res.*, 12(8), 3105, **2010**.

Damaschio, C. J.; Berengue, O. M.; Stroppa, D. G.; Simon, R. A.; Ramirez, A. J. ; Schreiner, W. H.; Chiquito, A. J.; Leite, E. R.; Sn_3O_4 single crystal nanobelts grown by carbothermal reduction process. *J. Cryst. Growth*, 312 (20), 2881, **2010**.

Moura, A. P.; Cavalcante, L. S.; Sczancoski, J. C.; Stroppa, D. G.; Paris, E. C.; Ramirez, A. J.; Varela, J. A.; Longo, E.; Structure and growth mechanism of CuO plates obtained by microwave-hydrothermal without surfactants. *Advanced Powder Technology*, 21, 197, **2010**.

Stroppa, D. G.; J. Unfried S.; Hermenegildo, T. F. C.; Ramirez, A. J.; Projected Area Method for the Evaluation of Contact Angle on Sessile Drop Test. *Welding Journal*, 89, 47, **2010**.

Stroppa, D. G.; Hermenegildo, T. F. C.; J. Unfried S.; Oliveira, N.; Ramirez, A. J.; Joint Clearance Calculation at Brazing Temperature. *Welding Journal*, 89, 32, **2010**.

Stroppa, D. G., Montoro, L. A., Beltran, A., Conti, T. G., da Silva, R. O., Andres, J., Longo, E., Leite, E. R., Ramirez, A. J.; Unveiling the Chemical and Morphological Features of $Sb:SnO_2$ Nanocrystals by the Combined Use of HRTEM and *ab initio* Surface Energy Calculations. *J. Am. Chem. Soc.*, 131 (40), 14544, **2009**.

da Silva, R. O., Conti, T. G., de Moura, A. F., Stroppa, D. G., Freitas, L. C. G., Ribeiro, C., Camargo, E. R., Longo, E., Leite, E. R.; Antimony-Doped Tin Oxide Nanocrystals: Synthesis and Solubility Behavior in Organic Solvents. *ChemPhysChem*, 10(5), 841, **2009**.

Stroppa, D. G.; Giraldi, T. R.; Leite, E. R.; Varela, J. A.; Longo, E.; Obtenção de filmes finos de TiO_2 nanostruturado pelo método dos precursores poliméricos. *Química Nova*, 31, 1706, **2008**.

Ribeiro, C., Vila, C., Stroppa, D. G., Mastelaro, V. R., Bettini, J., Longo, E., Leite, E. R.; Anisotropic Growth of Oxide Nanocrystals: Insights into the Rutile TiO2 Phase. *J. Phys. Chem. C*, 111 (16), 5871, **2007**.

8.1.2. Trabalhos apresentados em Congressos/Reuniões Científicas

Stroppa, D. G.; Righetto, R. D.; Montoro, L. A.; Leite, E. R.; Ramirez, A. J.; Reconstruction of Nanocrystals 3D Morphology by HAADF-HRSTEM, *X SBPMat Meeting*, Gramado - Brasil, **2011**. (oral)

Stroppa, D. G.; Houben, L.; Montoro, L. A.; Leite, E. R.; Urban, K.; Ramirez, A. J.; Negative Cs Imaging HRTEM: Perspectives and Challenges in the Oxide Nanocrystals Quantitative Analysis. ICXOM 21, Campinas – Brazil, **2011**. (pôster)

Stroppa, D. G.; Montoro, L. A.; Leite, E. R.; Ramirez, A. J.; HRTEM techniques applied to nanocrystal modeling: towards an "atom-by-atom" description, 2011. *Materials Characterisation V*, Kos – Grécia, **2011**. (oral)

Stroppa, D. G.; Righetto, R. D.; Montoro, L. A.; Ramirez, A. J.; MEGACELL: A nanocrystal models construction software for HRTEM multislice simulation, *International Microscopy Conference 17*, Rio de Janeiro - Brazil, **2010**. (oral)

Stroppa, D. G.; Montoro, L. A.; Campello, A.; Beltran, A.; Andres, J.; Leite, E. R.; Ramirez, A. J.; A thermodynamic approach to predict dopant atoms segregation on nanocrystals. *E-MRS Fall Meeting*, Warsaw – Polônia, **2010** (pôster)

Stroppa, D. G.; Cs- Corrected HRTEM applied to Gd:CeO_2 Nanocrystals Modeling; *Université Paris Sud*, Paris – França, **2010**. (seminário)

Stroppa, D. G.; Montoro, L. A.; Beltran, A.; Silva, R. O.; Andres, J.; Leite, E. R.; Ramirez, A. J.; Dopants segregation analysis on Sb:SnO_2 nanocrystals. *E-MRS Spring Meeting*, Strasbourg – França, **2010**. (oral)

Stroppa, D. G.; Nanocrystals Modeling; *LNLS Summer TEM-STEM course*, Campinas – Brasil, **2010**. (seminário)

Stroppa, D. G.; Oxide nanocrystals modeling: Combined HRTEM and *ab initio* calculation approach; *ER-C Centre*, Jülich – Alemanha, **2010**. (seminário)

Stroppa, D. G., Montoro, L. A., Beltran, A., Conti, T. G., da Silva, Rafael O., Andres, J., Longo, E., Leite, E. R., Ramirez, A. J.; Analysis of Sb dopant influence on SnO2 nanoparticles morphology and growth mechanism; *International Conference on Advanced Materials 2009*, Rio de Janeiro – Brasil, **2009**. (oral)

Stroppa, D. G.; Oxide Nanocrystals Modeling: Combined HRTEM and *ab initio* Calculation Approach; *Universitat Jaume I*; Castellón de la Plana – Espanha, **2009**. (seminário)

Stroppa, D. G., Montoro, L. A., Beltran, A., Conti, T. G., da Silva, Rafael O., Andres, J., Longo, E., Leite, E. R., Ramirez, A. J.; Oxide nanocrystals modeling: Combined HRTEM and *ab initio* calculation approach; *MRS Spring Meeting*, San Francisco – EUA, **2009**. (pôster)

Stroppa, D. G. ; J. Unfried S. ; Hermenegildo, T. F. C. ; Ramirez, A. J.; Projected Area Method for the Evaluation of Contact Angle on Sessile Drop Test; *III COBEF*, Belo Horizonte – Brasil, **2009**. (pôster)

Stroppa, D. G., Silva, R. O., Conti, T. G., Montoro, L. A., Leite, E. R., Ramirez, A. J.; HRTEM evaluation of oriented attachment growth mechanism on ATO nanoparticles; *VII SBPMat Meeting*, Guarujá – Brasil, **2008**. (oral)

Stroppa, D. G. ; Goto, A. Y. ; Ramirez, A. J.; Thermodynamic Evaluation of Nitrogen Addition on Brazing Atmospheres; *IIW International Congress*, São Paulo – Brasil, **2008**. (oral)

8.1.3. Treinamentos e Participações em Escolas

2011 - Developments in the Field of Synchroton Radiation; Escola São Paulo de Ciência Avançada (ESPCA); Campinas – Brasil.

2010 - Theoretical and Computational Nanotechnology; Instituto Nacional de Ciência e Tecnologia dos Materiais em Nanotecnologia (INCTMN); São Carlos – Brasil.

2010 – Treinamento em Cs-corrected HRSTEM; Ernst Ruska Centre – Forschungszentrum Jülich; Jülich – Alemanha.

2009 - European School on Nanoscience and Nanotechnology (ESONN); Centre National de la Recherche Scientifique (CNRS); Grenoble – França.

2009 – Treinamento em Cs-corrected HRTEM; Ernst Ruska Centre – Forschungszentrum Jülich; Jülich – Alemanha.

2009 - Quantitative Electron Microscopy (QEM); Enabling Science and Technology through European Electron Microscopy (ESTEEM); Saint Aygulf – França.

2009 - High Resolution Electron Microscopy; Arizona State University (ASU); Tempe – EUA.

2008 - Microscopy Techniques for Nanomaterials; Pan-American Advanced Studies Institute (PASI); Cancun – México.

2007 – Treinamento em Microscopia Eletrônica de Transmissão; Laboratório Nacional de Luz Síncrotron (LNLS); Campinas – Brasil.

2007 - Treinamento em Microscopia Eletrônica de Varredura (SEM-FEG); Laboratório Nacional de Luz Síncrotron (LNLS); Campinas – Brasil.

9. Anexos

Anexo A - MEGACELL: A nanocrystal model construction software

MEGACELL: A nanocrystal model construction software for HRTEM multislice simulation (STROPPA *et al.*, 2011c)

Daniel G. Stroppa, Ricardo D. Righetto, Luciano A. Montoro, Antonio J. Ramirez

Publicado na revista *Ultramicroscopy*, 111, 1077-1082, **2011**.

Abstract

Image simulation has an invaluable importance for the accurate analysis of High Resolution Transmission Electron Microscopy (HRTEM) results, especially due to its non-linear image formation mechanism. Because the as-obtained images cannot be interpreted in a straightforward fashion, the retrieval of both qualitative and quantitative information from HRTEM micrographs requires an iterative process including the simulation of a nanocrystal model and its comparison with experimental images. However, most of the available image simulation software requires atom-by-atom coordinates as input for the calculations, which can be prohibitive for large finite crystals and/or low-symmetry systems and zone axis orientations. This paper presents an open source citation-ware tool named MEGACELL that was developed to assist on the construction of nanocrystals models. It allows the user to build nanocrystals with virtually any convex polyhedral geometry and to retrieve its atomic positions either as a plain text file or as an output compatible with EMS (Electron Microscopy Software) input protocol. In addition to the description of this tool features, some construction examples and its application for scientific studies are presented. Those studies show MEGACELL as a handy tool, which allows an easier construction of complex nanocrystal models and improves the quantitative information extraction from HRTEM images.

Introduction

A wide variety of scientific areas have been increasingly taking advantage from High Resolution Transmission Electron Microscopy (HRTEM). Its application is a fundamental part of a number of groundbreaking scientific advances, as well as a complimentary tool for almost every development in nanosciences (SUENAGA *et al.*, 2000; MIDGLEY *et al.*, 2001; JIA *et al.*, 2003; HOFMANN *et al.*, 2007; MULLER *et al.*, 2008; HYTCH *et al.*, 2008). However, differently from other imaging techniques such as scanning electron microscopy (SEM) and scanning probe microscopy (SPM), the data extraction from HRTEM images is not straightforward due to the complex image formation mechanism. Consequently, serious misinterpretations may occur if the imaging conditions are not taken into account.

HRTEM image simulation (KIRKLAND *et al.*, 2008) is a fundamental step in HRTEM characterization that supports the atomic structure analysis in an unambiguous way. The image simulation process consists in the exit-plane wave function calculation after the incident electrons interaction with the crystalline structure projected potential. In addition, imaging distortions and modifications due to the lens system aberrations, microscope instabilities, and image registration system are also taken into account to reproduce the experimental imaging conditions.

Multislice method (COWLEY, 1957) is the most commonly used approach for HRTEM image simulation. It consists in sectioning the crystal structure in a number of thin layers, which allows the weak phase object approximation within the kinematical diffraction regime for the interaction calculation at each layer. Therefore, a HRTEM multislice image simulation of a thick crystal structure can be performed by successive calculations of electron wave function interaction with thin slices and the further propagation to the next slice. An illustrative diagram of HRTEM multislice image simulation is presented on Figure Aa.

The HRTEM multislice image simulation process requires the complete description of both the sample and imaging system. The Incident Electron Wave Function (1) information is mainly related to the microscope illumination system. The Slice Projected Potential (2) depends on a number of factors including the atomic species and positions within the slices, and the Propagation Step (3) is dependent on the slices geometrical configuration. The Instrumental Factors (4) include several experimental conditions that modify the exit-plane electron wave

function, such as objective lens aberrations (SCHERZER, 1949; UHLEMANN *et al.*, 1998), spatial and temporal coherence, beam divergence and tilt, physical apertures, sample vibration and drift, and the image registration system influence (THUST *et al.*, 2009).

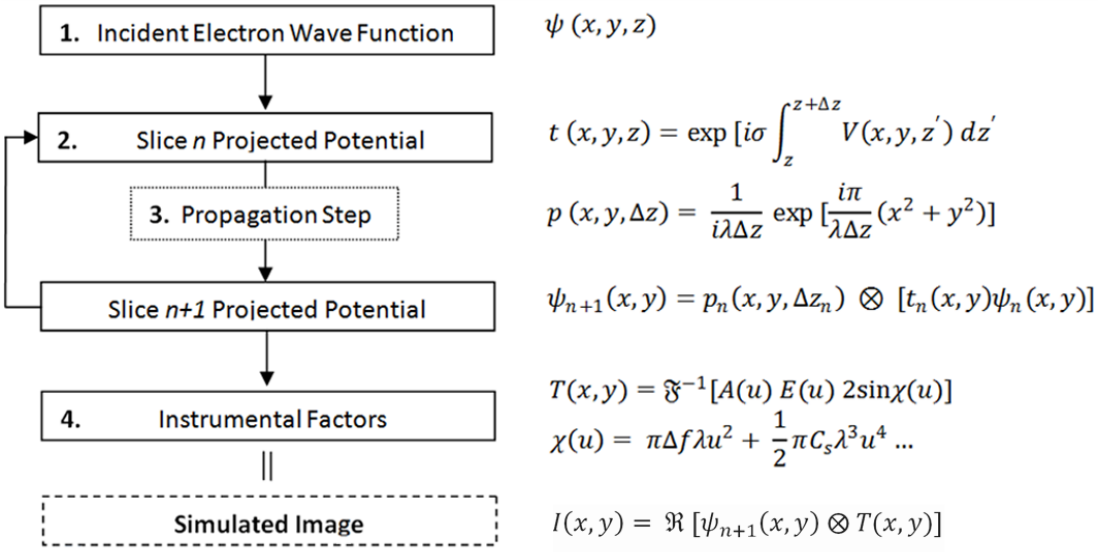

Figure Aa: Multislice image calculation simplified flow chart including the calculations performed on each step. The Instrumental Factors only presents the contrast transfer function (T), which modulates the exit-plane wave function. Although the contribution of the image acquisition system is not shown in this figure, it must be taken into account for HRTEM multislice image simulation (THUST *et al.*, 2011).

As the microscope imaging parameters can be determined after some careful characterization steps (ZEMLIN *et al.*, 1978; STEINECKER *et al.*, 2000; LENTZEN *et al.*, 2004), the most exhaustive procedure on HRTEM multislice simulation is related to the sample description. The atomic type and position of each atom in the structure is required in order to determine both the Slices Projected Potential (2) and the Propagation Step (3) geometrical parameters, which is a critical issue for large structures and for low-symmetry systems and zone axes.

A preliminary step on HRTEM image simulation is usually performed for semi-infinite structures considering the unit cell repetition along the axes that are normal to the zone axis.

Although this approach simplifies the HRTEM multislice simulation input regarding the atoms information and allows the direct verification of thickness and defocus dependence on the phase contrast, it is not adequate to describe nonlinear thicknesses profiles and border effects that are present on finite nanocrystalline structures, as nanowires and nanoparticles. This paper describes the developed tool named MEGACELL, which is a nanocrystal model construction software that supports finite crystals HRTEM multislice simulation by other available softwares (STADELMANN *et al.*, 1987; BARTHEL *et al.*, 2010; GOMEZ-RODRIGUEZ *et al.*, 2010). Some construction examples are depicted as well as the main software features.

Description

The crystal model construction is performed using a text file input containing the material crystallographic information and geometrical construction. This input file is divided into sections identified by brackets, as shown in the example file included in the supplementary material. Figure Ab illustrates the MEGACELL workflow indicating the routine main steps and Figure Ac present construction results for each step. A comprehensive tutorial is also presented on the supplementary material.

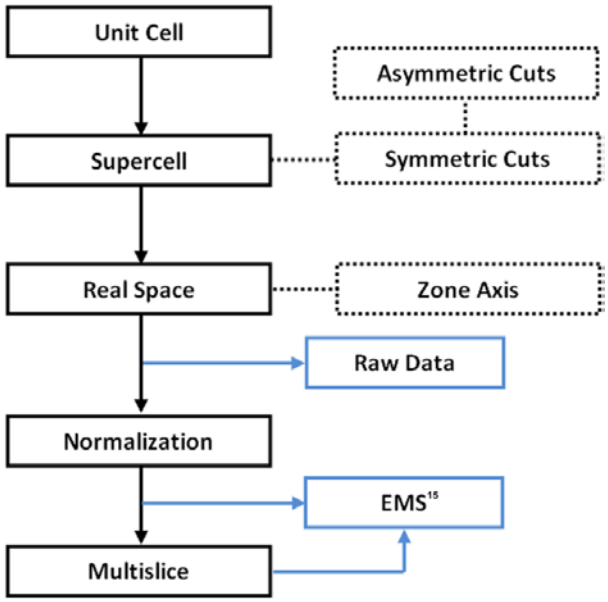

Figure Ab: Flow chart indicating MEGACELL main operations. The dashed line indicates optional steps and the blue line indicates the data output steps.

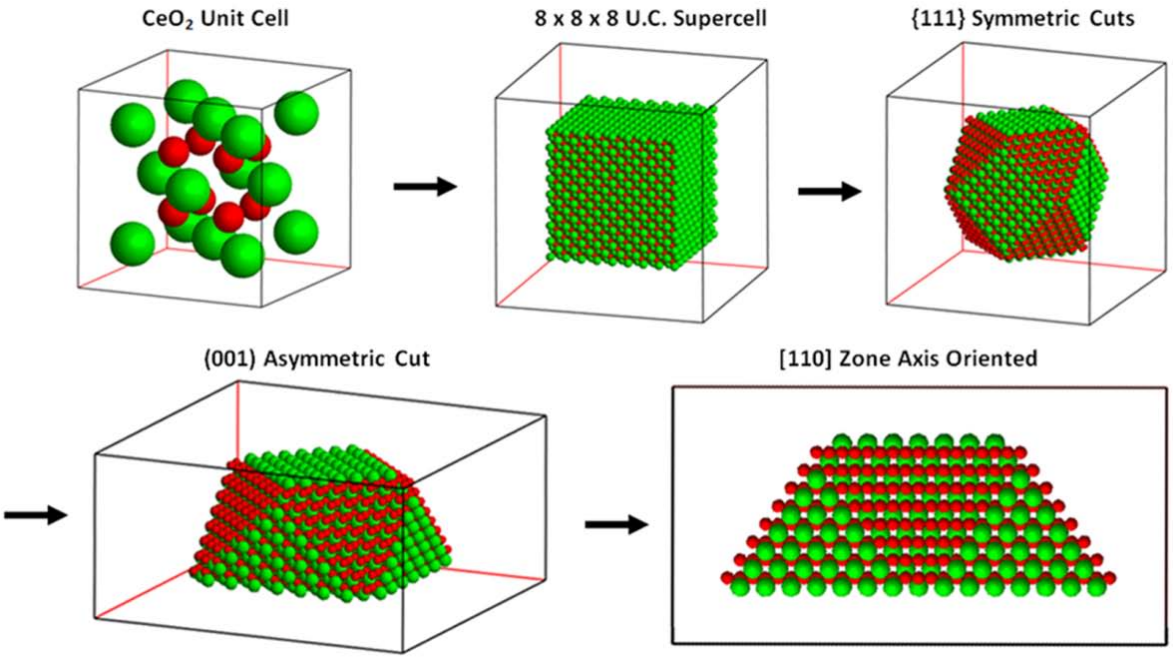

Figure Ac: Construction example at each operation step.

The Unit Cell operation stores the atoms relative positions within the unit cell, as informed on [Atoms Coordinates] section in the input file. Each atom coordinates are informed relatively to the lattice parameters and range from 0 to 1 for each axis, resulting in an orthonormal unit cell.

The Supercell operation builds a supercell centered on (0,0,0) by repeating the unit cell along the three orthonormal axes and eliminating duplicated atomic position entries. The supercell dimensions are specified by the number of unit cell repetitions along each axis on the [Supercell] section in the input file. Afterwards, two routines are available for shaping the crystal model. Those can be specified in order to generate any convex polyhedral shape with a given faceting and the desired atomic layers exposed on each facet.

The Symmetric Cuts operation defines cut planes in the orthonormal points space and crops the atomic positions located outside the delimited boundaries. The geometrical information for the cut planes is informed on the [Symmetric Cuts] section in the input file and includes each plane's Miller indices (h,k,l) and the relative distance from the origin in the orthonormal points space in unit cell units. This operation only requires the input regarding the planes that define the crystal model within the first octant boundaries as the 4m symmetry operations relative to YZ,

ZX, XY planes are automatically performed to the inputted planes. The Asymmetric Cuts operation defines cut planes in the orthonormal point space using the point space coordinates of three non-collinear points informed on the [Asymmetric Cuts] section in the input file. This routine allows the user to perform independent cuts on each one of the crystal octants and therefore to obtain any asymmetric convex polyhedral shape.

The Real Space operation applies the real space geometry to the previously used orthonormal point space crystal model, accordingly to the unit cell information provided on [Unit Cell] section in the input file, which includes the lattice parameters (a, b, c) and the lattice angles (α, β, γ). This step is followed by the Zone Axis operation, which rotates the crystal to the orientation informed on the [Zone Axis] section in the input file. After these steps, a text file with xyz format including the supercell dimensions and each atom position in real space can be exported using the Raw Data output. The standard length unit is nm.

The Normalization operation rewrites each atom position coordinates as a fraction of the supercell dimensions. The Multislice operation segments the crystal model along the Z axis and prepares n slice files for HRTEM multislice image simulation. The n value is provided on the [Multislice] section in the input file and the thickness of each slice is given by the oriented supercell Z dimension divided by the number of slices. Both the complete supercell file and the set of slices can be exported into text files in compliance to the EMS (STADELMANN *et al.*, 1987) input format.

Results A - Construction examples

Some model examples generated by MEGACELL and their correspondent HRTEM multislice simulated images are depicted to illustrate the construction possibilities. Complete information about those models and their respective image simulation results can be found in the supplementary material.

Faceted nanocrystal with 4m symmetry

Figure Ad illustrates the atomic structure of a faceted nanocrystal model with CeO_2 cubic structure (ICSD 72155). This model was constructed from an 8 x 8 x 8 CeO_2 unit cells arrangement and {100}, {110} and {111} facets with arbitrary distances from the origin. As a consequence of the 4m symmetry operations automatically performed during the Symmetric Cuts step, the input parameter file only included the cutting information for the first octant, which was given by the planes indexes and the relative distances from the origin.

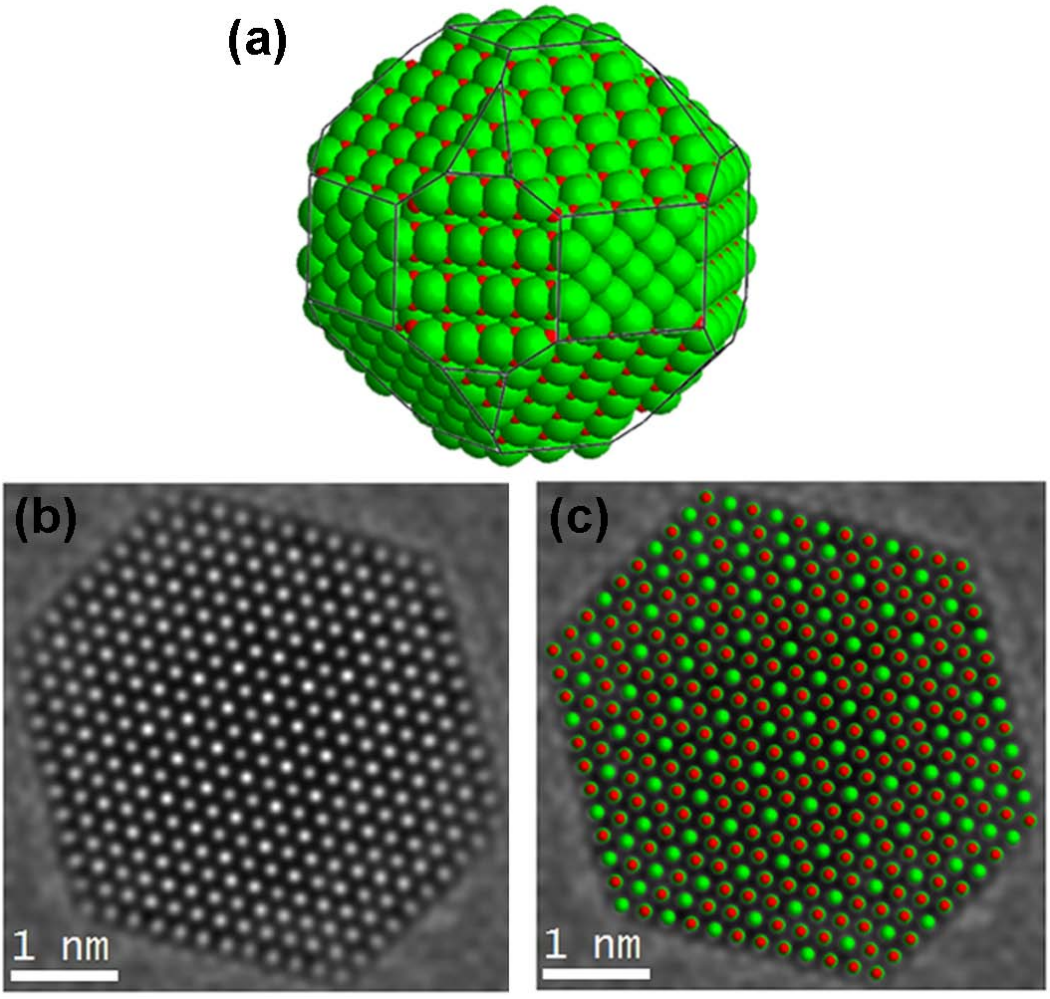

Figure Ad: a) Trimetric view of a CeO_2 faceted nanocrystal model (Example 1, Ce atoms in green), b) <111> Zone Axis HRTEM multislice simulation (300kV, Cs = 0.7mm, dF = -64nm), c) simulated image and model structure superimposition.

Wedge

Figure Ae illustrates a model for a wedge-like structure based on a Si unit cell (ICSD 51688). The HRTEM multislice image simulation of this kind of structure can be used to directly evaluate the HRTEM phase contrast dependence with the nanocrystal thickness for a given defocus value. This model was constructed from an initial 16 x 16 x 16 unit cells supercell by the combination of {110} Symmetric Cuts to generate a parallelogram block with a rectangular projection on the [110] zone axis and Asymmetric Cuts to generate the wedge-like geometry.

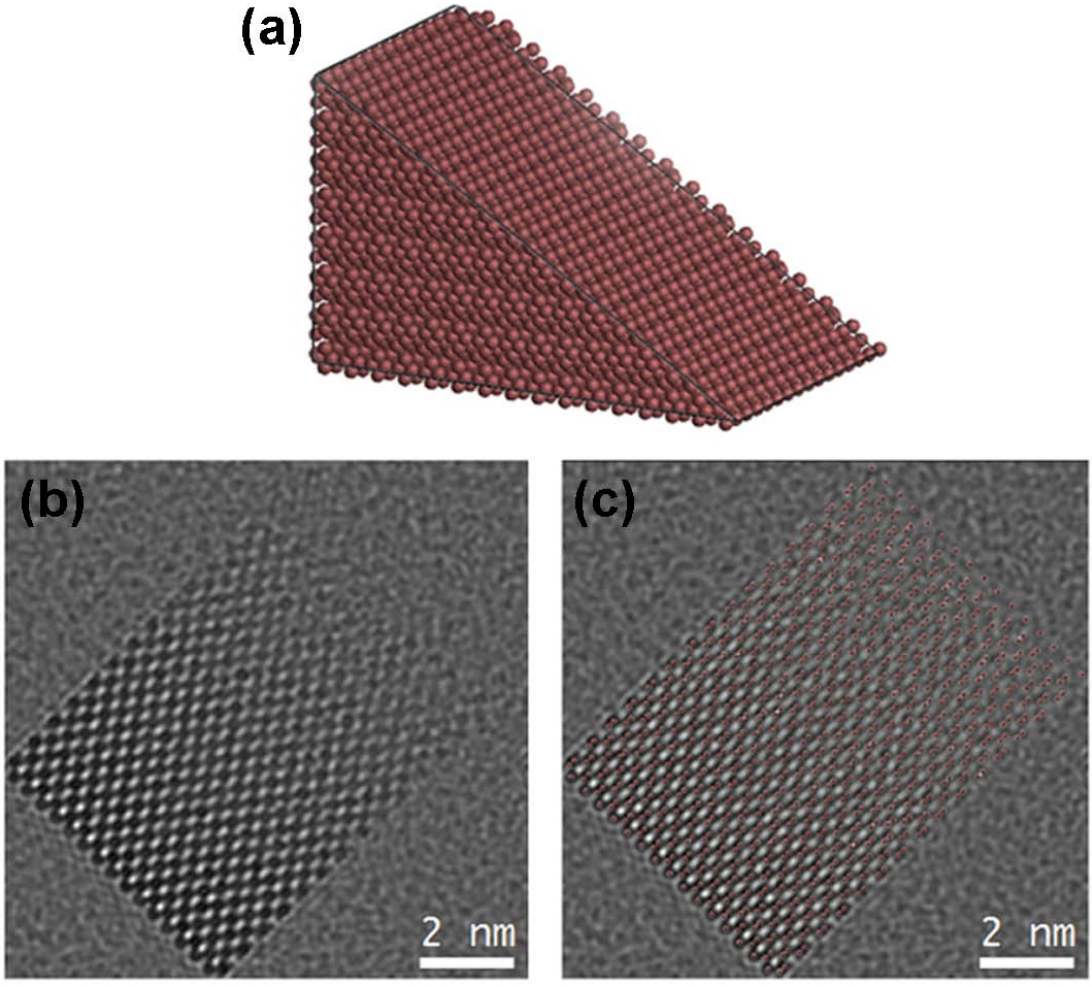

Figure Ae: a) Trimetric view of a Si wedge model (Example 2, Si atoms in purple), b) <110> Zone Axis HRTEM multislice simulation (300kV, Cs 0.7mm, dF = -25nm), c) simulated image and model structure superimposition. This model thickness along the <110> zone axis ranges from 1 to 16 Si atoms.

Faceted nanocrystal with arbitrary symmetry:

Figure Af present construction examples of nanocrystals models by the combined use of Symmetric cuts and Asymmetric cuts. Due to the latter's geometrical properties, any convex polyhedral shape can be obtained from the combination of these cut operations.

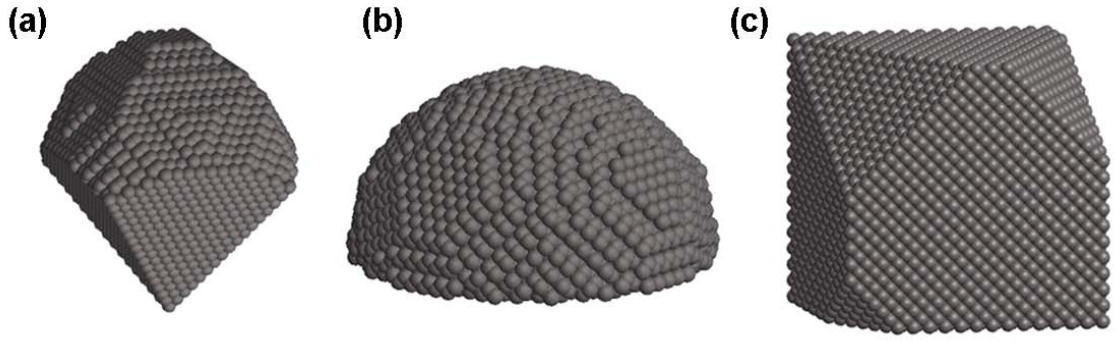

Figure Af: Trimetric views of complex nanocrystal models; a) Diamond-like structure (example file 3a), b) Dome-like structure (example file 3b) and c) Asymmetric convex polyhedron (example file 3c).

Complex constructions: Attachment models and crystalline defects evaluation

Complex nanocrystal models, either with non-convex shapes or with crystalline defects, can be obtained with MEGACELL support. As an unlimited number of configurations may be interesting for the users, their direct specification on the program input parameters is not feasible. For such cases it is possible to use MEGACELL to obtain starting convex geometries, then export these models using the Raw Data output, and finally manipulate the atomic coordinates from each atom afterwards. The resultant file in xyz file format can then be imported to MEGACELL for further manipulation and conversion to other supported supercell formats. An example where two simple crystalline models were merged in order to obtain a complex non-convex model is depicted in Figure Ag.

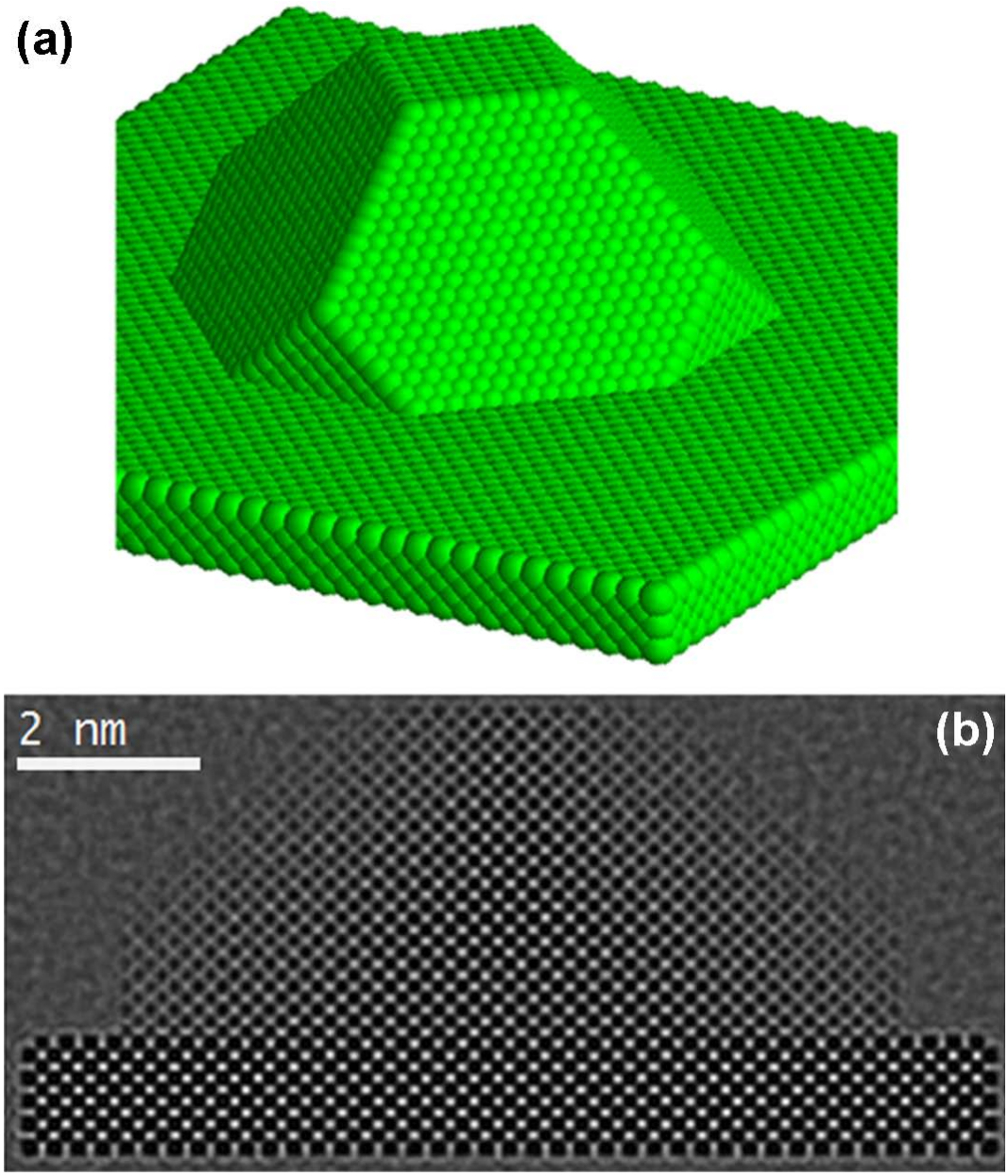

Figure Ag: a) Trimetric view of a hypothetical model containing a Si nanocrystal epitaxially grown over a Si substrate (example files 4a, 4b and 4c) (ICSD 51688) and HRTEM multislice image simulation for [100] zone axis (300kV, Cs -0.012mm, dF = -10nm).

Results B - Applications The following sub-sections present results from scientific works that used nanocrystals models generated by MEGACELL.

Faceting determination for CeO_2 nanocrystals

The construction of reliable geometric models for nanocrystals has an evident importance for the development of catalysts, whose properties are closely linked to the surface area of different crystallographic facets. For example, CeO_2 nanocrystals models constructed using MEGACELL after HRTEM characterization supported the morphological characterization in an unambiguous way for CeO_2 nanocrystals obtained by a low-temperature synthesis route (DU *et al.*, 2007), as indicated in Figure Ah. The obtained results led to an improvement on the understanding of the synthesis parameters role on the CeO_2 structure regarding the exposed crystallographic facets and the resultant surface energy configuration, which are directly related to the catalytic performance of this material.

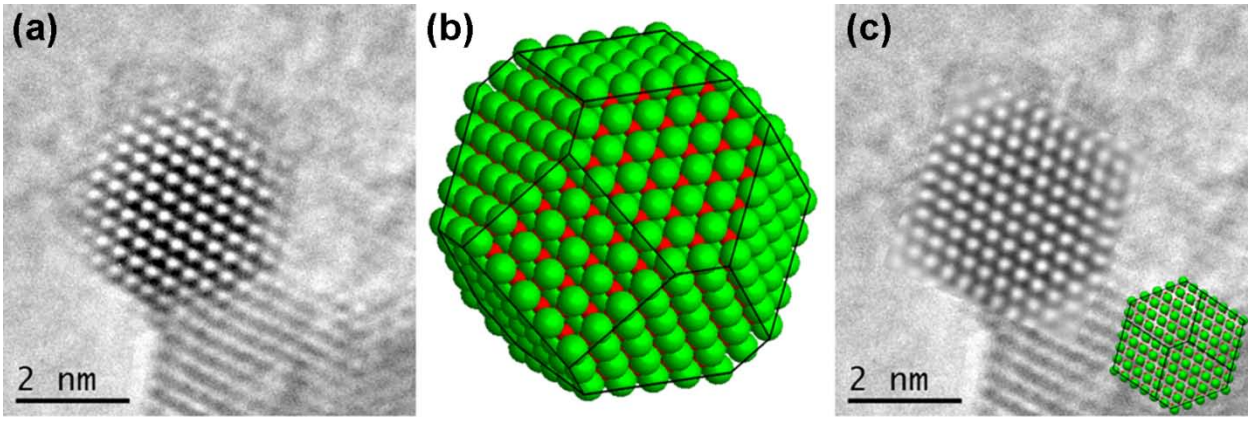

Figure Ah: CeO_2 nanocrystal characterization supported by MEGACELL. The geometrical analysis of the original HRTEM image (left) supported the construction of geometrical models (center), whose adequacy was tested by the superimposition of the simulated frames and the original HRTEM images (right). The surface area ratio between the exposed {100} and {111} facets could be retrieved from the geometrical model and its value is approximately 0.66.

Dopant segregation and growth mechanism analysis for Sb:SnO_2 nanocrystals

The accurate nanocrystals morphology determination has been also used for the indirect extraction of quantitative information on dopant segregation for nanocrystalline systems in which direct quantitative techniques are impracticable due to experimental restrictions. (STROPPA *et al.*, 2009) MEGACELL was successfully employed to generate a geometrical models for representing Sb:SnO_2 nanocrystals based on the dimensions retrieved from HRTEM experimental images, as depicted in Figure Ai. The comparison between the model and the Wulff (HERRING, 2011) constructions based on *ab initio* calculated surface energies elucidated the dopant atoms segregation behavior for individual particles. In addition, the growth mechanism analysis of this system (STROPPA *et al.*, 2011) was significantly improved by the HRTEM multislice image simulation of the attached nanocrystals model, which was also obtained using MEGACELL.

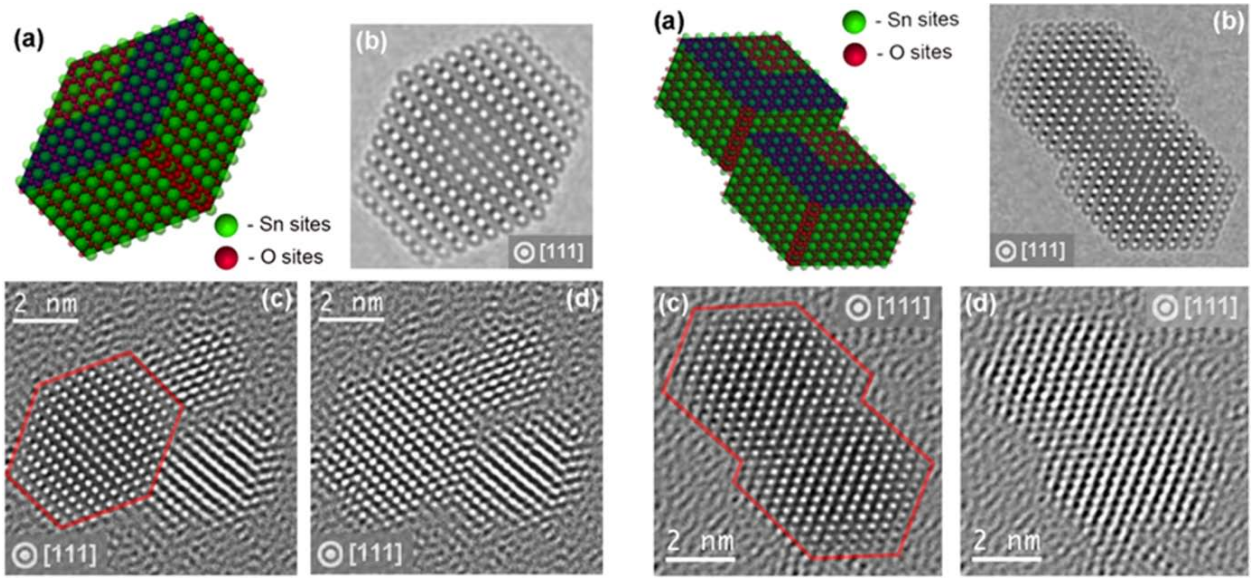

Figure Ai: Sb:SnO_2 nanocrystal (left side) and nanocrystals attachment (right side) modeling supported by MEGACELL. Models (a) constructed after HRTEM characterization were simulated using the multislice approach (b). The models adequacy was tested by the comparison between the simulated frames and the original HRTEM images superimposition (c, d).

HRTEM multislice simulation supporting strain and composition analysis on SiGe islands

The quantitative strain state analysis from HRTEM images present several difficulties that have been associated to the phase-contrast image formation. Multiple scattering, dynamical effects, and lens aberrations may induce inaccuracy to the strain state analysis results. In order to evaluate and minimize the contribution of these effects on the quantitative analysis, the use of 3D models is essential.

HRTEM images of cross-sectioned Si_xGe_{1-x}:Si(001) epitaxial alloyed islands were used to calculate the local chemical composition and the strain/stress state in a self-consistent way. Such experiments allowed a two-dimensional chemical composition mapping from two different cross-sectioned (zone axis) views, [100] and [110] (MONTORO *et al.*, 2009; MONTORO *et al.*, 2010). In addition, from these chemical maps it was possible to infer the chemical composition in a three-dimensional fashion. However, these epitaxial 3D nanostructures with a multifaceted dome shape have an inherent and complex thickness variation which can induce contrast inversions and abrupt modifications on the HRTEM pattern, which could induce errors on the images analyses. MEGACELL was employed to generate the Si_xGe_{1-x} islands 3D model, which allowed the HRTEM images simulation at different zone axis and defocus values, as exemplified on Figure Aj.

The HRTEM multislice image simulation of the generated models allowed the determination of the ideal island imaging conditions in order to improve the accuracy and precision for quantitative displacement fields mapping and to check that the image formation process doesn't induce errors on the corresponding atomic column position at the HRTEM images.

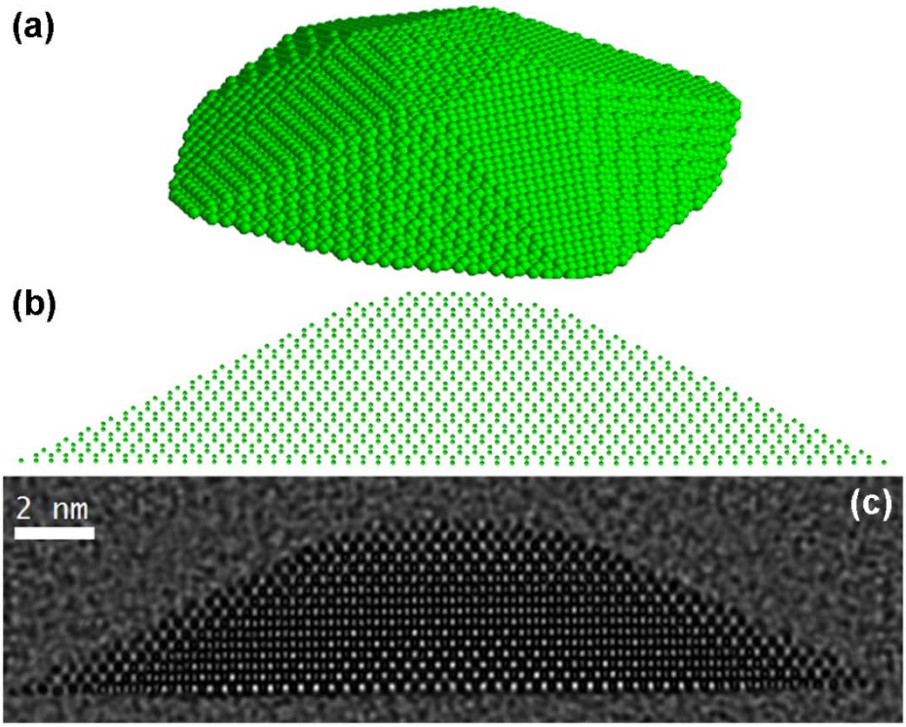

Figure Aj: Trimetric view of a SiGe island model with {113}, {15,3,23} and {105} faceting (top), model projection along the <110> zone axis (center) and HRTEM multislice simulated image (300kV, Cs 0.7mm, dF = -25nm).

Conclusions

The previous examples illustrate how the construction and multislice image simulation of nanocrystals models can be an advantageous procedure to support quantitative information retrieving from HRTEM images. In this context, MEGACELL is presented as an effective tool to construct such models and to export the supercell files to currently available HRTEM multislice simulation software. As this task would be unfeasible to be manually performed for most of the real nanocrystalline systems, MEGACELL can be an invaluable

Supplementary material

A detailed tutorial containing comprehensive instructions on MEGACELL operation, examples and software files are available at http://megacell.lnls.br.

Anexo B - Informações Suplementares

B.1. Unveiling the Chemical and Morphological Features of Sb:SnO_2 Nanocrystals

Unveiling the Chemical and Morphological Features of Sb-SnO_2 Nanocrystals by the Combined Use of High Resolution Transmission Electron Microscopy and *ab initio* Surface Energy Calculations (STROPPA *et al.*, 2009)

Daniel G. Stroppa, Luciano A. Montoro, Armando Beltran, Tiago G. Conti, Rafael O. da Silva, Juan Andres, Elson Longo, Edson R. Leite, Antonio J. Ramirez.

Publicado na revista *Journal of the American Chemical Society*, 131, 14544-14548, **2009**

Content:

S1 - XRD Characterization

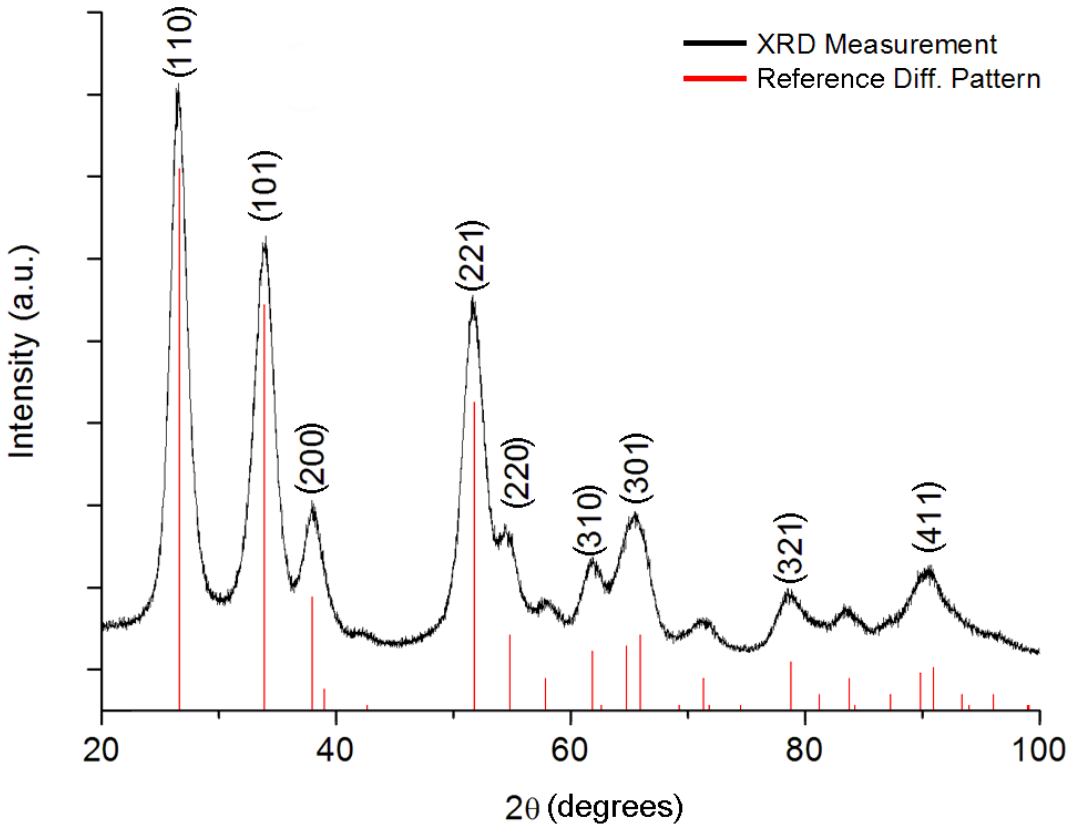

Figure B1a: Indexed X-ray diffraction pattern of dry ATO powder sample obtained with a rotary anode Rigaku D/MAX 2500 PC diffractometer using Cu-Kα radiation. Red lines denote the reference spectrum accordingly to JCPDS 41-1445 (MCCARTHY *et al.*, 1989).

S2 - HRTEM Image Simulation for (001) Facets

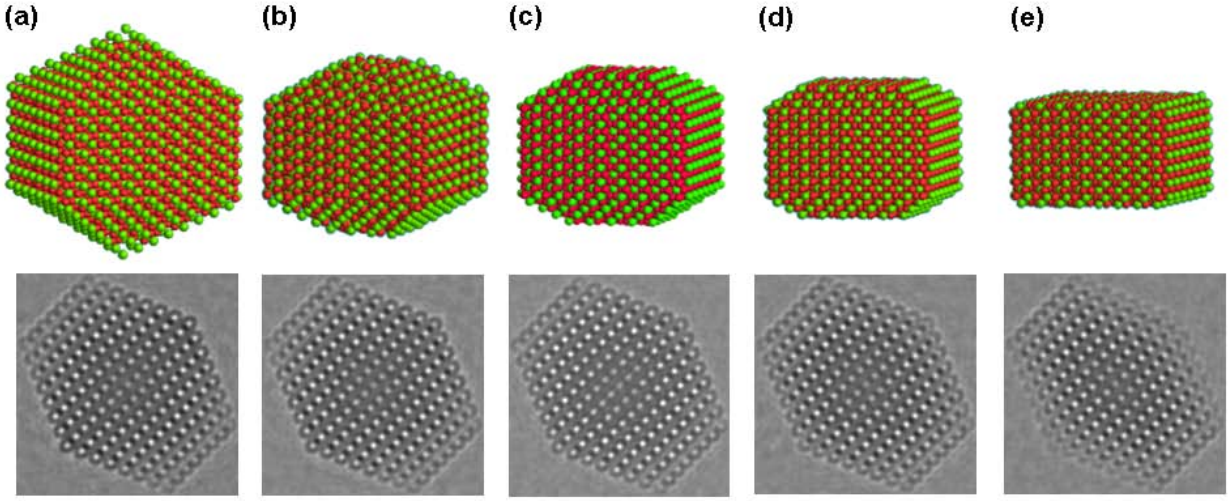

Figure B1b: Atomic arrangement of ATO nanocrystals with different (001) faceting and their respective simulated HRTEM images. These results show that the contrast at the edges of the HRTEM simulated images is strongly dependent on the (001) facets dimension.

S3- XEDS Measurements and Dopant Localization Analysis: ATO 18% Sb

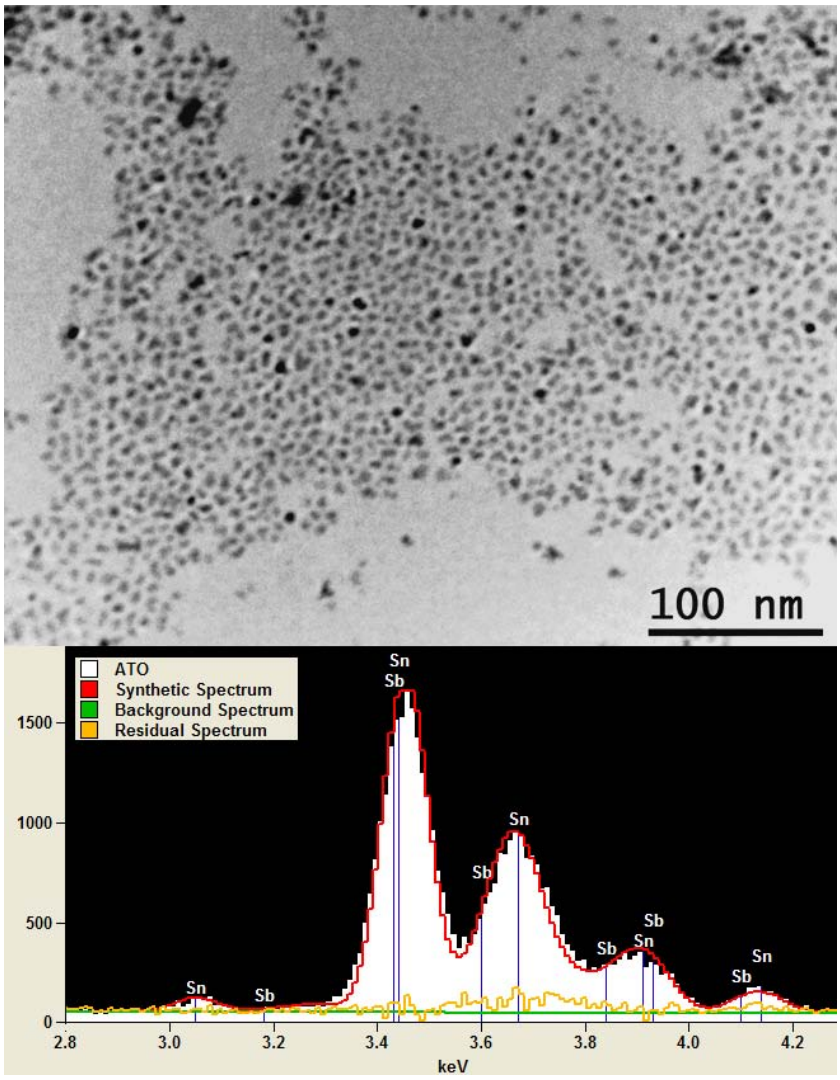

Figure B1c: TEM image and XEDS spectra of the measured region. The quantification indicates an average Sb content of 13.9 ± 1.4 % for approximately 500 particles. The spectra was recorded to assure 20000 accumulated counts on the region of interest (3.2 – 3.8 keV) and quantified using Cliff-Lorimer k-factors without absorbance ($k_{Sb\text{-}L}$ =1.752; $k_{Sn\text{-}L}$=1.750). The XEDS spectrometer was calibrated with the CuKα X-Ray line and a dark spectrum was recorded for background correction. The quantification was performed by subtracting standard Sn and Sb peaks from the recorded spectrum in order to minimize the residual spectrum.

The surface area fraction of nanocrystal facets was considered as the weighting factor on the determination of Sb content on ATO nanoparticles. This assumption is justified considering the large total surface area to bulk volume fraction due to the small particle size.

$$\sum_n C_n.A_n = C_{total}.A_{total}$$

where **C** stands for Sb concentration and **A** stands for surface area for each specific facet (**n**). The surface area values (**A**) were retrieved from the Wulff construction after the HRTEM images analysis and the $\mathbf{C_{total}}$ was considered 13.9% after the XEDS measurements.

As indicated on Figure B1c, the Sb content on a given facet is directly related to its surface energy. Consequently the variable **C** was replaced with the surface energy (**E**) after the linear fit of surface energy versus Sb content chart (**a** and **b** are the linear fit constants)

$$E_n = a_n.C_n + b_n$$

$$\sum_n (E_n - b_n).A_n / a_n = C_{total}.A_{total}$$

The Wulff rule states that the surface energy (**E**) for a given facet is proportional to its distance to the crystal center (**d**).

$$\alpha.\sum_n (d_n - b_n).A_n / a_n = C_{total}.A_{total}$$

where **α** denotes the proportionality constant from Wulff rule. The facets distances from the origin (**d**) were retrieved from the Wulff construction after the HRTEM images analysis.

Table B1a: Summary of ATO nanocrystal characteristics.

α	Facet	Surface Area (nm^2)	Distance (nm)	Energy (J/m^2)	Sb Content (%)
2.70466	[100]	32.16	1.90	5.18	15.3
	[001]	10.66	1.73	4.65	8.0
	[110]	3.80	2.50	6.87	16.1
	[101]	21.60	2.08	5.54	14.2

S4 - Oriented Attachment Evaluation

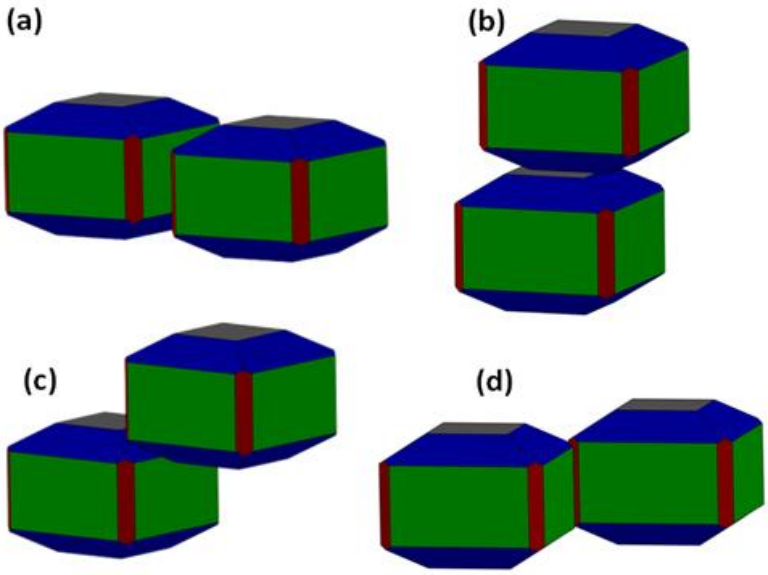

Facet	Fraction (%)
(100)	47.1
(001)	15.6
(110)	5.6
(101)	31.7

Figure B1d: Predicted oriented attachment configurations for the modeled ATO nanocrystal for (a) (100), (b) (001), (c) (101), and (d) (110) facets. The inset table indicates the color code for the nanocrystals facets and the respective surface area fraction.

B.2. Dopants segregation analysis on Sb:SnO_2 nanocrystals

Dopants segregation analysis on Sb:SnO_2 nanocrystals (STROPPA *et al.*, 2011d)

Daniel G. Stroppa, Luciano A. Montoro, Armando Beltran, Tiago G. Conti, Rafael O. da Silva, Juan Andres, Edson R. Leite, Antonio J. Ramirez.

Publicado na revista *Chemistry: A European Journal*, 17, 11515-11519, **2011**.

Content:

S1 - XRD and Electron Diffraction Analysis

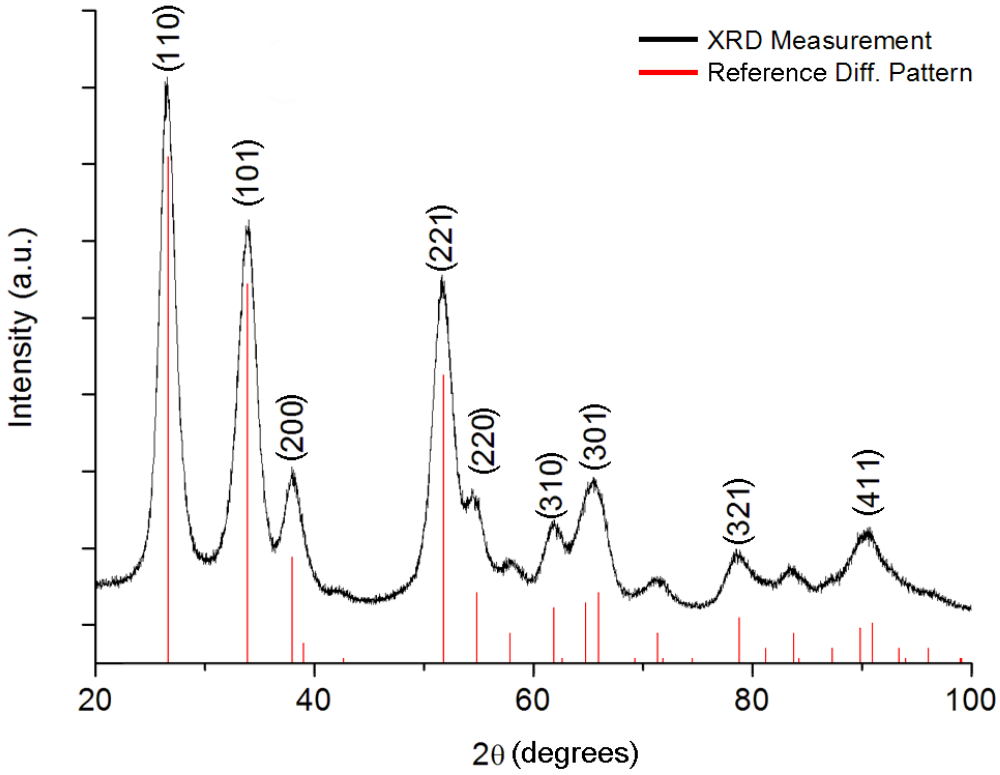

Figure B2a: Example of indexed X-ray diffraction pattern of dry Sb:SnO_2 powder sample obtained with a rotary anode Rigaku D/MAX 2500 PC diffractometer using Cu-Kα radiation. Red lines denote the reference spectrum (MCCARTHY *et al.*, 1989).

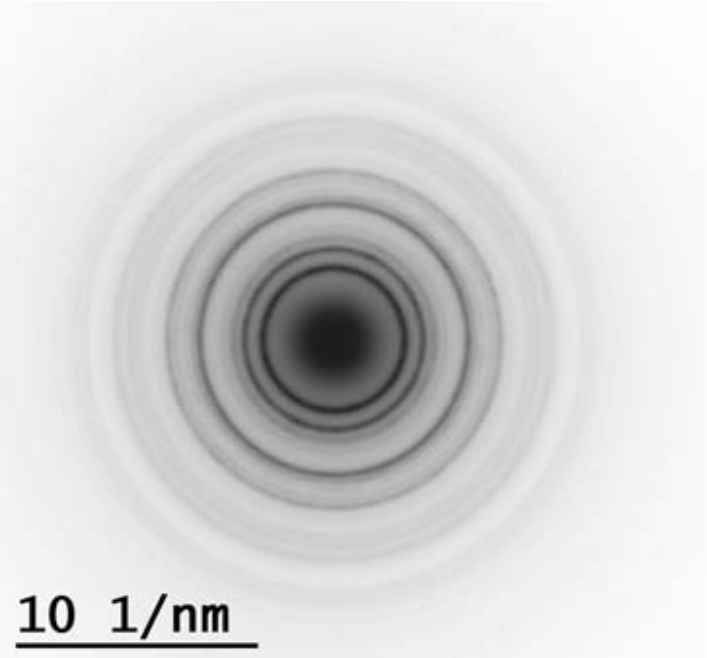

R (1/nm)	d (Å)	Ref. JCPDS (Å)	(hkl)
2.95	3,39	3,36	110
3.72	2,69	2,65	101
4.22	2,37	2,38	200
4.67	2,14	2,13	210
5.59	1,79	1,77	211
5.99	1,67	1,68	220
6.33	1,58	1,60	002
6.67	1,50	1,50	310
7.04	1,42	1,42	301
7.52	1,33	1,33	202
8.20	1,22	1,22	321
8.70	1,15	1,16	222
9.17	1,09	1,10	312

SnO_2 - $P4_2/mnm$ Spatial Group

Figure B2b: Example of Sb:SnO_2 polycrystalline sample electron diffraction pattern. The second column indicates measured interplanar values and the third column denote the reference interplanar spacing accordingly to JCPDS 41-1445.

S2- XEDS Measurements

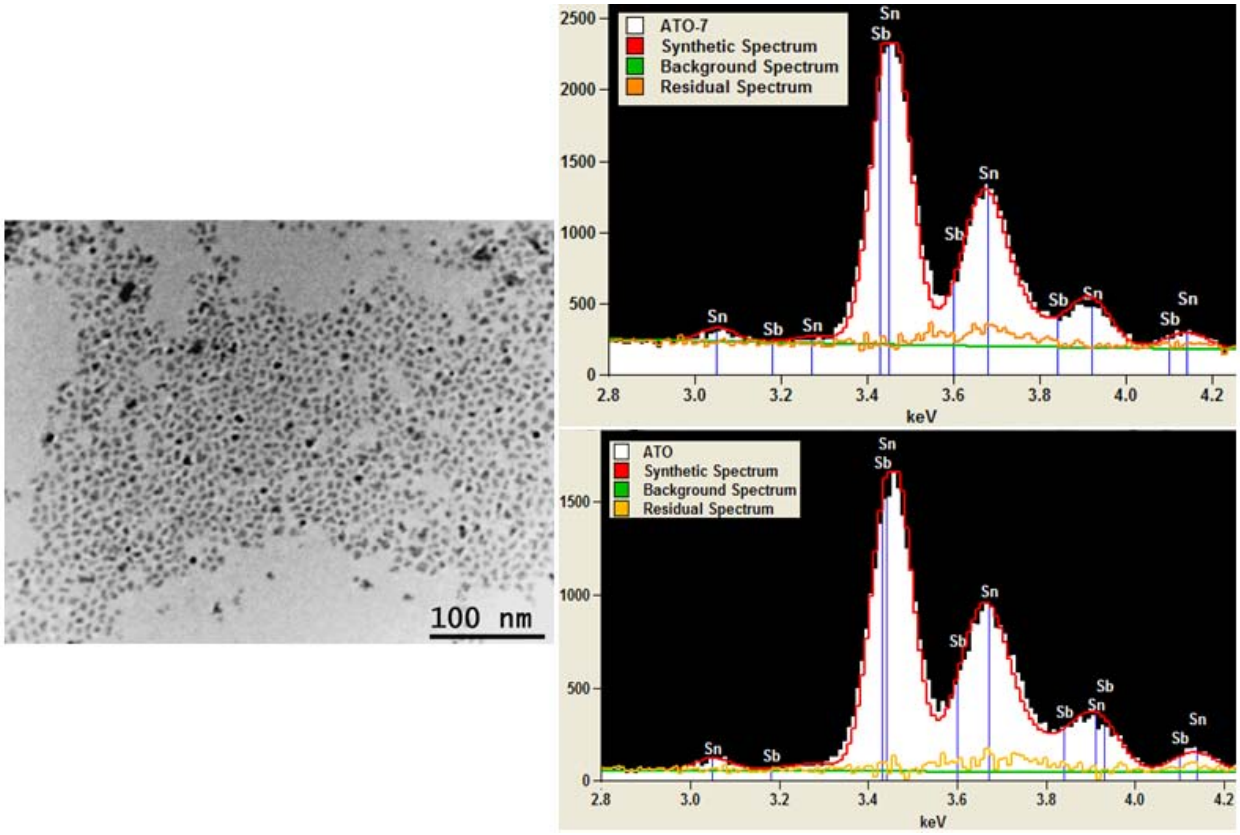

Figure B2c: Example of a low-magnification TEM image of a representative Sb:SnO_2 sample region. The XEDS spectra were recorded to assure 20000 accumulated counts on the region of interest (3.2 – 3.8 keV) and quantified using Cliff-Lorimer k-factors without absorbance ($k_{Sb\text{-}L}$ =1.752; $k_{Sn\text{-}L}$=1.750). The XEDS spectrometer was calibrated with the CuKα X-Ray line and a dark spectrum was recorded for background correction. The quantification was performed by subtracting standard Sn and Sb peaks from the recorded spectrum in order to minimize the residual spectrum. The quantification results indicate average Sb contents of 4.5 ± 0.8% and 13.9 ± 1.4% for the ATO samples with nominal composition of $7\%_{atom}$ and $18\%_{atom}$ Sb, respectively. The averaging area for the XEDS spectra included approximately 500 particles for each sample.

S3 - Geometrical Analysis

The theoretical value for the total surface energy (Es) per volume (V) unit can be derived as presented on Figure B2d.

$$\frac{E_s}{V} = \frac{\sum E_i A_i}{\sum \frac{A_i d_i}{3}} = \frac{3\sum E_i A_i}{\sum \frac{E_i A_i}{w}} = 3.W$$

Figure Bd: Wulff constant geometrical derivation. Ei, Ai and di represent the surface energy densities, surface areas and absolute distances from the center for the *i* index facet, respectively, and W represents the Wulff parameter. The first operation describes the polyhedral volume as a sum of pyramids volumes, as highlighted in yellow on the Figure B2e. The second operation uses the Wulff relationship (Ei = W.di) and assumes W as constant.

Figure B2.e presents the comparison between experimental and expected values for the Es/(V.W) parameter for both evaluated compositions. The concordance between these values indicates that the proposed nanocrystals models after the combined HRTEM characterization and *ab initio* calculation approach are in close agreement with the theoretical thermodynamic equilibrium conditions, which were assumed initially.

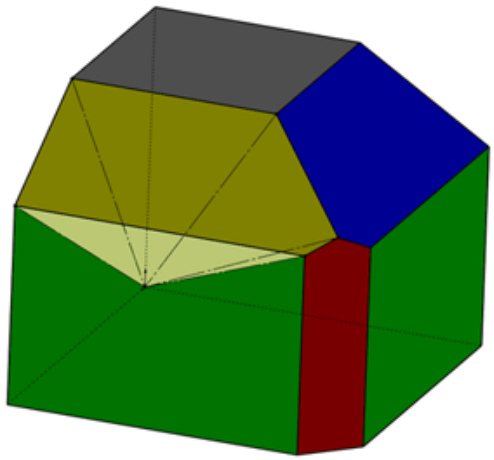

ATO 7%$_{atom}$ Sb			
Es/V	W	Es/(V.W)	Expected Value
3.94	1.3159	2.9941	3
ATO 18%$_{atom}$ Sb			
Es/V	W	Es/(V.W)	Expected Value
8.10	2.7047	2.9947	3

Figure B2e: A convex polyhedron first octant representation. Its total volume can be described as a sum of pyramid volumes, each one with a facet as base and the facet-center distance as height.

S4 - Particle Size Distribution Analysis

Figure B2f presents the nanoparticles size distribution after HRTEM imaging for the 7%$_{atom}$ Sb-doped and 18%atom Sb-doped samples. The size measurements including oriented and non-oriented nanocrystals were performed by an automated routine after the images contrast enhancement.

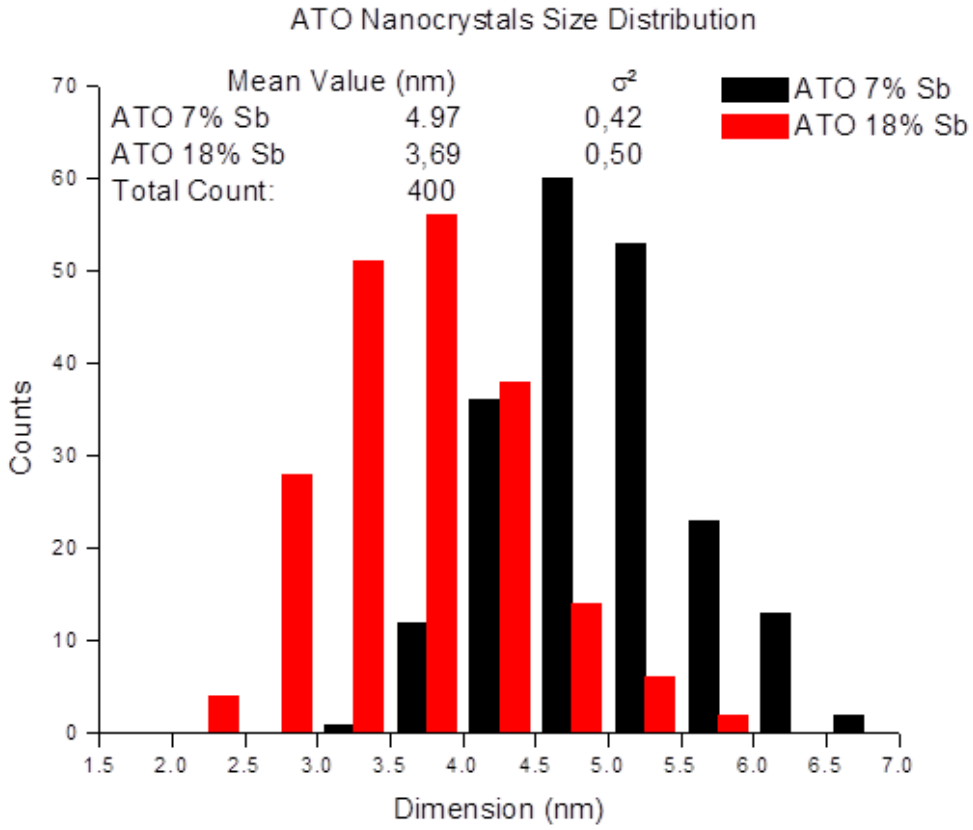

Figure B2f: Nanocrystals size distribution diagram from the 7%$_{atom}$ Sb-doped and 18%atom Sb-doped samples.

Figure B2g summarizes the geometrical characterization from the 3D models proposed after the HRTEM imaging and image simulation. The projected dimensions regard the distance between the facets. The low deviation values indicate that the analyzed particles for the model construction are close to the systems' mean particle sizes.

Sample	Facets	Distance from Origin (nm)	Projected Dimension (nm)	Mean Value - Model (nm)	Deviation (%)
$7\%_{atom}$ Sb	[100]	2.85	5.71	5.25	5.7
	[001]	2.40	4.80		
	[110]	2.62	5.23	**Mean Value - Experiment (nm)**	
	[101]	2.63	5.27	4.97	

Sample	Facets	Distance from Origin (nm)	Projected Dimension (nm)	Mean Value - Model (nm)	Deviation (%)
$18\%_{atom}$ Sb	[100]	1.90	3.80	4.11	11.3
	[001]	1.73	3.46		
	[110]	2.50	5.00	**Mean Value - Experiment (nm)**	
	[101]	2.08	4.16	3.69	

Figure B2g: Comparison between experimental particles size distributions and the models geometrical parameters.

B.3. HAADF-HRSTEM Applied to Three-Dimensional Nanocrystals Modeling

Three-Dimensional Reconstruction of Nanocrystals Morphology from Single HAADF-HRSTEM Images (STROPPA *et al.*, 2011f)

Daniel G. Stroppa, Ricardo D. Righetto, Luciano A. Montoro, Lothar Houben, Juri Barthel, Marco A. L. Cordeiro, Edson R. Leite, Weihao Weng, Christopher J. Kiely, Knut Urban, Antonio J. Ramirez

Submetido para publicação, ***2011***.

Content:

- Section S1 – Peak detection and masking algorithm
- Section S2 – Integrated intensity analysis of single atoms
- Section S3 – Experimental derived models and symmetric models
- Section S4 – Movies and interactive models
- Section S5 – Comparison of experimental and simulated HAADF-HRSTEM images

Section S1 – Peak detection and masking algorithm

Peak detection on the as-obtained HAADF-HRSTEM images was performed using a custom algorithm for detecting the atomic column positions by correlating the image with Gaussian masks of different radii. The integration mask radius was selected so as to capture approximately 80% of the peak signal. Such a configuration was chosen as it did not present overlaps between the signals from adjacent atomic columns and provided a reduced amount of inherent background during the peak integration. Finally, a refinement of estimate of the center position for each atomic column was achieved by shifting the center of each mask within a ±2 pixel interval along the *x* and *y* directions. The center positions of atomic columns were considered to be the *x*,*y* coordinates with the maximum integrated value of pixels within the shifting range. Typical results from the peak detection procedure are presented in Figure B3a.

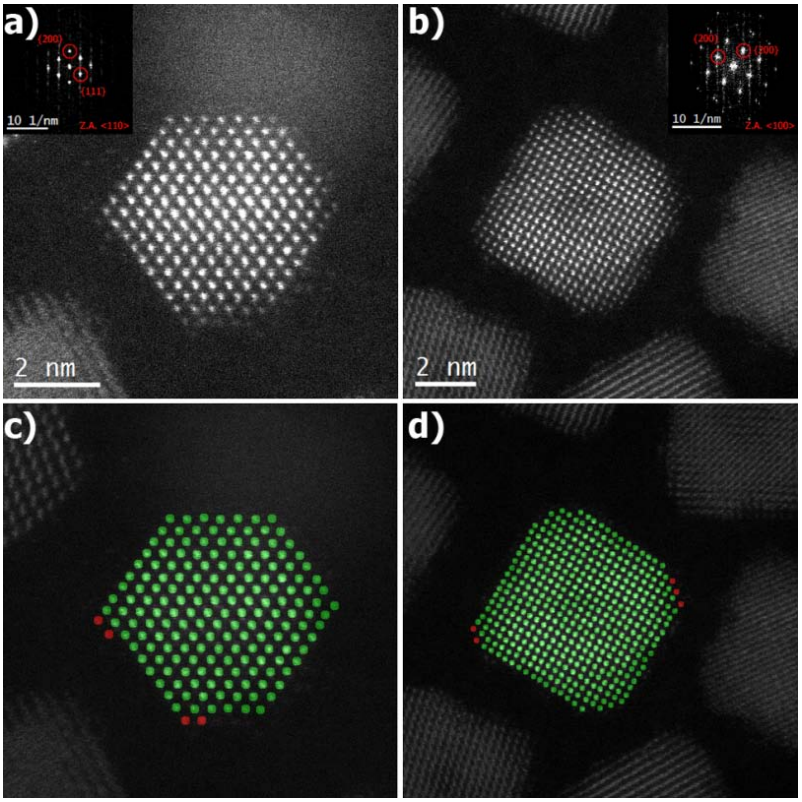

Figure B3a: a, b) Experimental HAADF images from nanocrystals A and B, respectively. c, d) Superimposition of the integration masks over the corresponding experimental images after the refinement step. The masks indicated by the green color show which spots which were used for the 3D morphological reconstruction. The red color masks were used for verifying the assignment of the HAADF signal level from a single Ce atom during the GMM analysis.

Section S2 – Integrated intensity analysis of single atoms

A preliminary inspection of HAADF-STEM images for nanocrystals A and B (Fig. 1(a),(b)) indicated that a few bright spots at the edge of the nanocrystal might possibly have arisen from a single or possible two Ce atoms, as indicated by the red colored masks in Figure S1(c)(d). This supposition was based on the lack of symmetry of those positions in comparison with the well developed surface facets of the nanocrystals.

The integrated values from these periphery atoms were compared to the integrated intensity histograms in order to verify this single atom thickness assignment after the GMM fitting procedure. Figure B3b presents the intensity of the periphery atoms and their spatial locations on the histograms according to the overall integrated intensity.

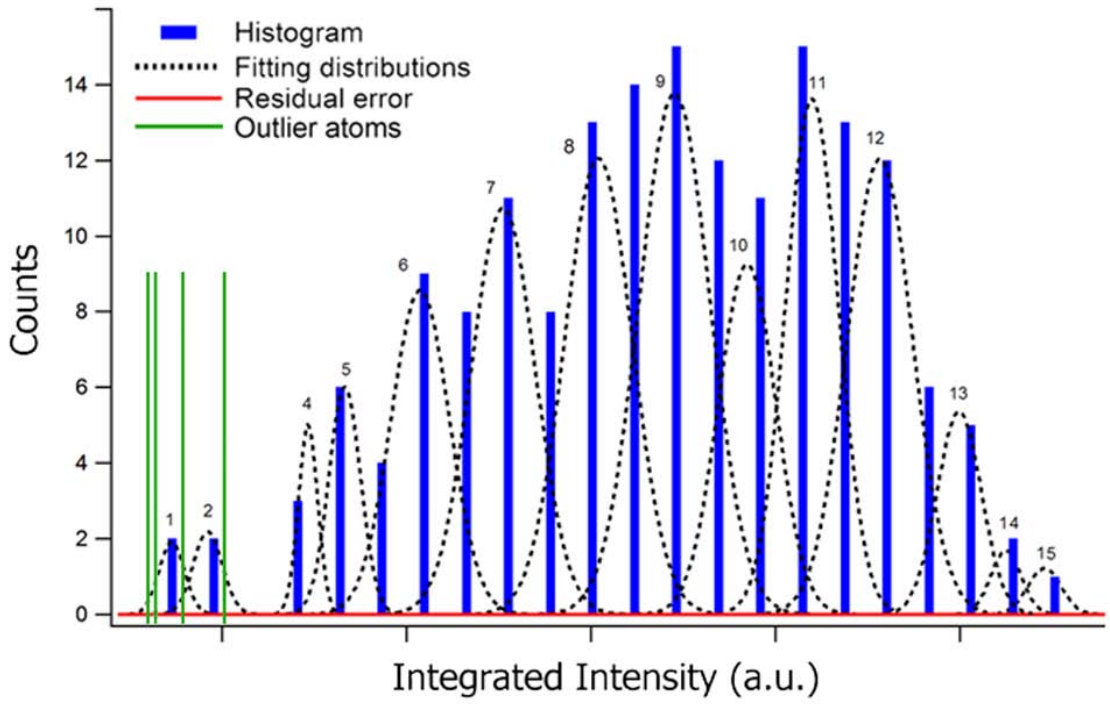

Figure B3b: Intensity histogram and GMM fitting from nanocrystal A atomic columns. The integrated intensities from periphery atoms (see B3ac) are indicated as green lines.

As the integrated intensities* of the peripheral atoms are relatively close to the minimum atomic column intensity included in the 3D reconstruction, the assignment of the first fitting Gaussian curve to a single-atom atomic column is justified. Although a small discrepancy between the values from the GMM fitting for a single-atom atomic column and the peripheral atoms is acknowledged, its mean value is less than 55% of the average step between two adjacent fitting curves. Consequently, the integrated intensities from these peripheral atoms can be classified in the same fitting curve as the minimum measured atomic column in the 3D reconstruction.

* - except for the most intense one, which was associated to the 2-atoms columns classification.

Section S3 – Experimental derived models and symmetric models

Both the experimentally derived and symmetric 3D theoretical models depicted in Figure B3c are available as plain text (.cif) files. These files can be downloaded from http://megacell.lnls (provisional address) and visualized/manipulated using various software packages, such as VESTA (DILANIAN *et al.*, 2002) and MEGACELL (STROPPA *et al.*, 2011).

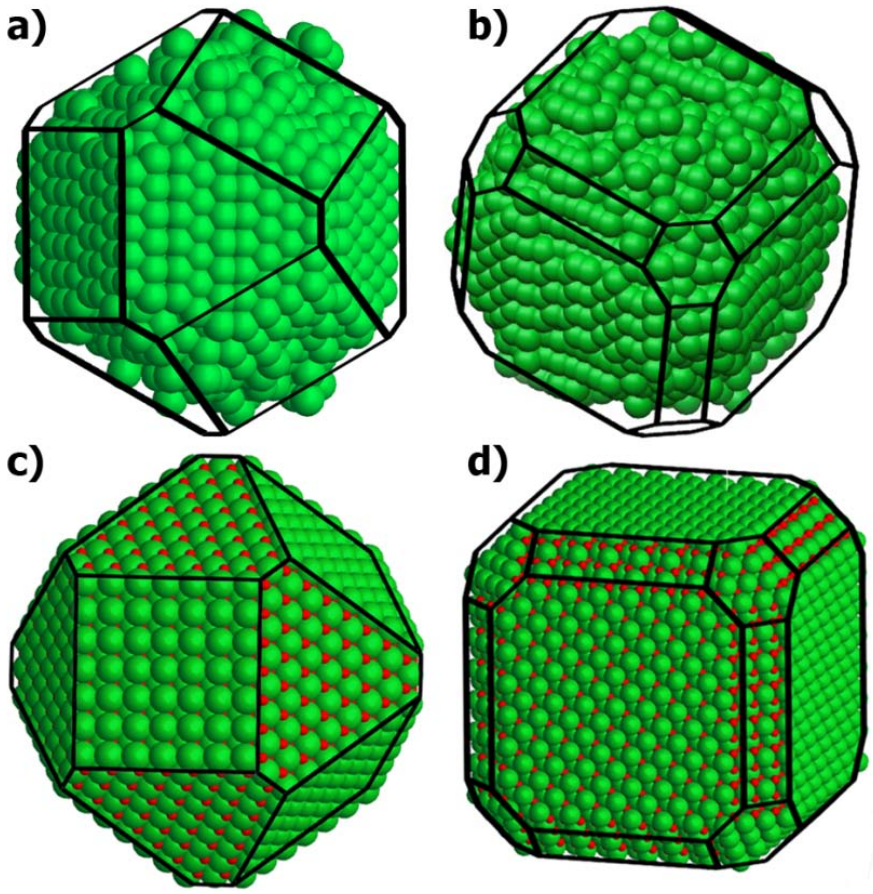

Figure B3c: a,b) Experimentally derived and c,d) symmetric 3D morphological reconstruction from A and B-type nanocrystals after the HAADF-HRSTEM image analysis.

Section S4 – Movies and interactive models

Figure B3d presents compressed videos from the experimental 3D models retrieved from both A and B-type nanocrystals. Higher quality videos can be found on http://megacell.lnls (provisional address). The videos were generated with the aid of CHIMERA software (PETTERSEN *et al.*, 2004).

Figure B3d: Videos showing experimentally derived 3D models of a) A-type and b) B-type nanocrystals, respectively. The wireframe structures indicate the faceting of symmetric models at different viewing angles (only available on .pdf version).

Section S5 – Comparison of experimental and simulated HAADF-HRSTEM images

Although the experimental HAADF-HRSTEM images presented well-faceted nanocrystals with a reasonably high degree of symmetry, a careful analysis after the counting of atomic rows indicate a few asymmetric features, as depicted in Figure B3e.

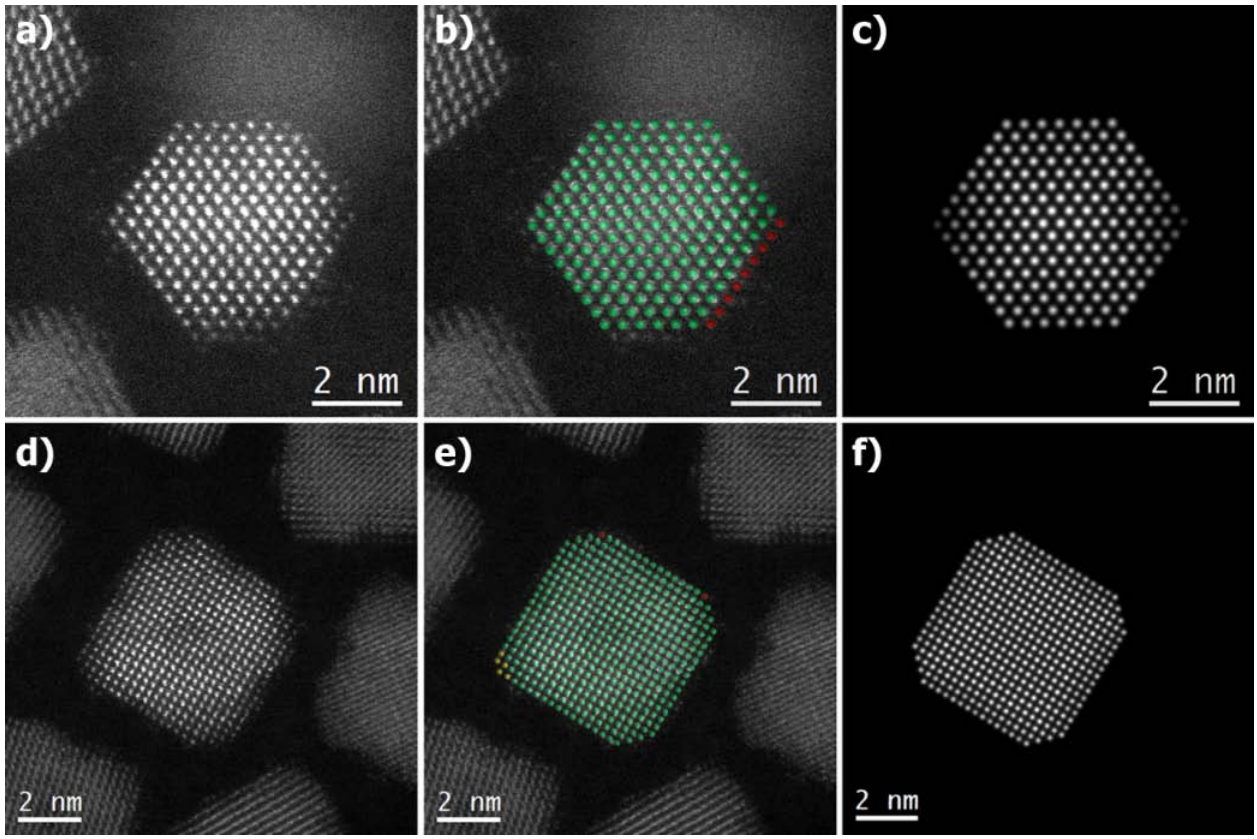

Figure B3e: Qualitative comparison of a,d) experimental HAADF-HRSTEM images, b,e) symmetric models and c,f) simulated images from the symmetric models for nanocrystals A (*row 1*) and B (*row 2*), respectively. The atomic positions marked in red and yellow represent missing and extra atomic columns in the actual nanocrystals, respectively.

B.4. Anomalous Oriented Attachment Growth Behavior on SnO_2 Nanocrystals

Anomalous Oriented Attachment Growth Behavior on SnO_2 Nanocrystals (STROPPA *et al.*, 2011b)

Daniel G. Stroppa, Luciano A. Montoro, Armando Beltrán, Tiago G. Conti, Rafael O. da Silva, Juan Andrés, Edson R. Leite, Antonio J. Ramirez

Publicado na revista *Chemical Communications*, 47, 3117-3119, **2011**.

Content:

S1 - XRD Characterization

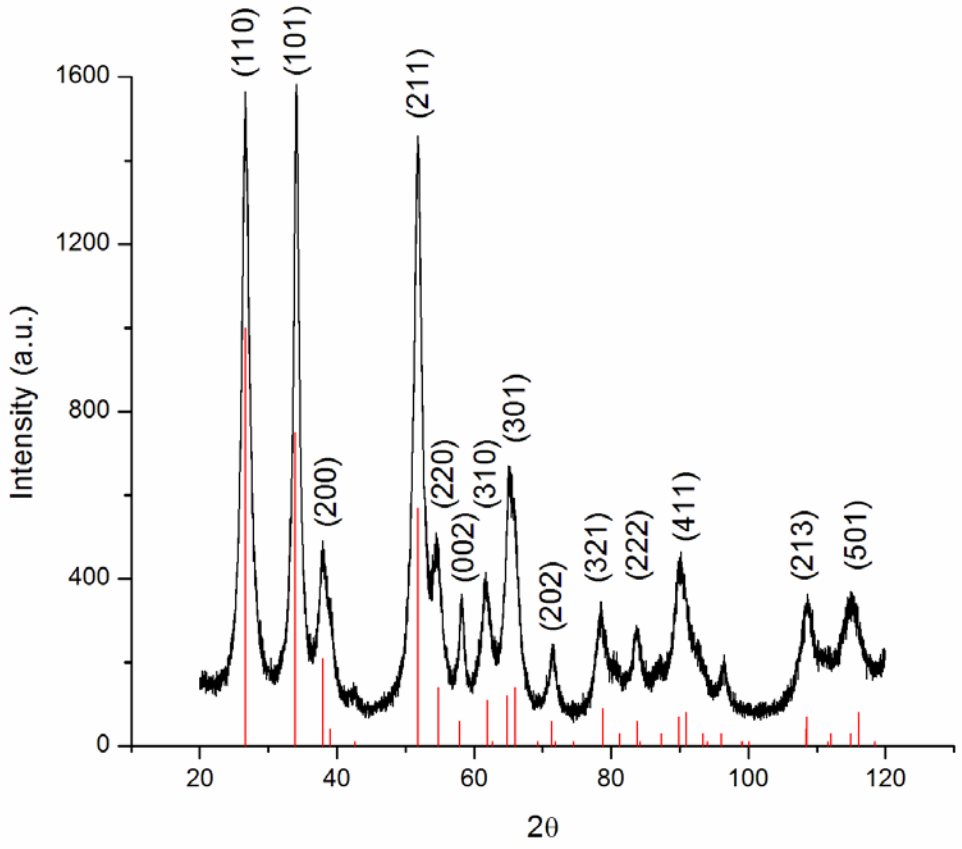

Figure B4a: Indexed X-ray diffraction pattern of dry SnO_2 powder sample obtained with a rotary anode Rigaku D/MAX 2500 PC diffractometer using Cu-Kα radiation. Red lines denote the reference spectrum accordingly to JCPDS 41-1445. The XRD peaks indicate small crystalline domains with dimensions of approximately 12 and 16 nm for (110) and (101) planes, respectively, as evaluated by Scherrer's equation.

S2 – SnO_2 Surface Energy *ab initio* Calculation

Surface energy calculations (BELTRAN *et al.*, 2003) for SnO_2 nanocrystals were performed with the CRYSTAL06 program package. Oxygen atoms were described by the standard 6-31G* basis sets and the Tin centers in the PS-21G* scheme, where PS stands for Durand-Barthelat's non-relativistic large effective core potential. Becke's three-parameter hybrid nonlocal exchange functional combined with the Lee-Yang-Parr gradient-corrected correlation functional (B3LYP) was used. Full optimization of the cell parameters (a and c) and internal coordinate (u) for the bulk SnO_2 was carried out. The low index (110), (101), (100) and (001) surfaces were modeled by unreconstructed (truncated bulk) slab models using the calculated equilibrium geometry. Because these surfaces have a different number of atoms in each layer, the low-index surfaces were modeled with different thicknesses in the z-direction but periodic in x- and y-directions. After the corresponding convergence test, slab models containing nine SnO_2 layers for the (110), (100), and (101) surfaces and eleven layers for the (001) one were selected. A complete relaxation of all the atoms in each model was performed.

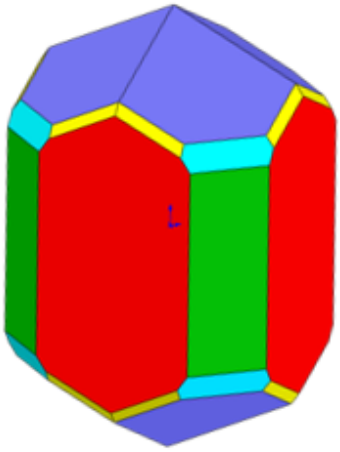

Tetragonal SnO_2 - $P4_2/mnm$		
(hkl)	Surface Energy (J/m^2)	Relative Distance
100	1.74	1.000
001	2.71	1.557
110	1.56	0.897
101	2.11	1.213
111	4.07	2.339
211	2.18	1.253
301	2.08	1.195

Figure B4b: Wulff geometry (HERRING *et al.*, 1951) for SnO_2 nanocrystal after the *ab initio* surface energy calculations.

S3 – Monte Carlo Model

A custom Monte Carlo based algorithm was implemented using Microsoft Visual Basic programming language for the evaluation of aspect ratio distribution for a system with 2D isotropic attachment behavior. Firstly, a 20x20 matrix M_{ij} with a seed in its center was built, according to Figure B4c. Then, two random integer numbers ranging from 1 to 20 were drawn denoting the *i* and *j* matrix coordinates. The applied selection rule was determined by the neighborhood: for the *ij* drawn coordinates just next to the seed, it would be integrated to the seed; otherwise, other random *ij* coordinates would be drawn.

This process was repeated iteratively until the seed reached 20 blocks, as depicted in Figure B4c. This process was repeated 50000 times in order to assure a statistical representativeness for L and W dimensions measurements. The aspect ratio was considered as the ratio between lengthen and shorten directions on *i* and *j* axes. The results indicated 1.308 and 0.081 as the mean aspect ratio value and variance, respectively.

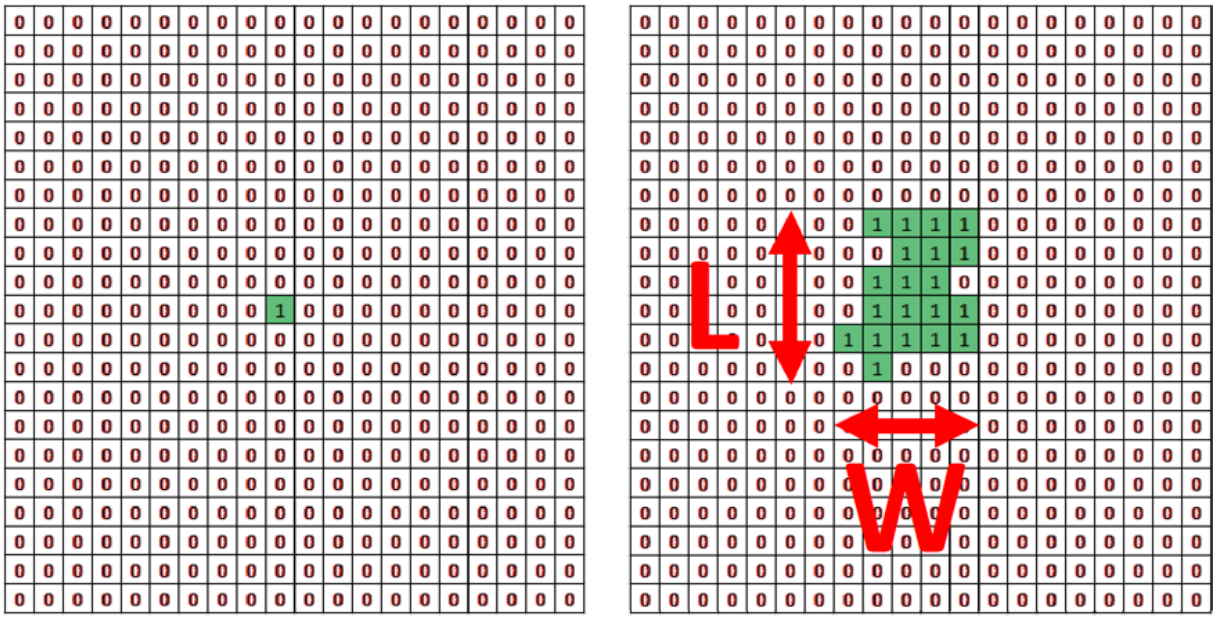

Figure B4c: (left) Initial M_{ij} matrix with a seed and (right) result after the iterative calculation until 20 neighbor blocks. The L and W refer to the maximum dimensions along *i* and *j* directions.